

SINGLE AND MULTIPHASE FLOW AND TRANSPORT IN FRACTURED POROUS MEDIA

A DISSERTATION SUBMITTED TO THE DEPARTMENT OF
CIVIL ENGINEERING AND THE COMMITTEE ON
GRADUATE STUDIES OF STANFORD UNIVERSITY IN
PARTIAL FULFILLMENT OF THE REQUIREMENTS FOR
THE DEGREE OF DOCTOR OF PHILOSOPHY

By

Arturo Alejandro Keller

© Copyright by Arturo Alejandro Keller, 1996

SINGLE AND MULTIPHASE FLOW AND TRANSPORT IN FRACTURED POROUS MEDIA

© Copyright by Arturo Alejandro Keller, 1996

Abstract

This dissertation summarizes an experimental investigation of flow and transport of non-aqueous phase liquids (NAPLs) in fractured porous media, either in their own phase or as dissolved contaminants. We observed displacement mechanisms at the pore scale when two and three phases are present, using a micromodel, to test the presence of NAPL layers and double displacements. We also conducted single phase tracer experiments, as well as two- and three-phase displacements in real fractured granite and sandstone cores, at a larger scale, using a CAT-scanner. We characterized the fracture aperture distribution at high resolution, to determine the geometry of the pore space, and its influence on flow behavior. The pore space in the micromodels is a simile of a sandstone, which was etched onto a silicon wafer. The sizes of the pores are in the range 3-30 μm , the same as observed in the rock. We conducted the experiments at low capillary numbers (in the order of 10^{-7}). We observed stable NAPL layers between water and air for the water-decane-air system, even though it has a negative equilibrium spreading coefficient (as do many environmentally significant NAPLs), as well as four different types of double displacements. The NAPL layers are important because they result in very low NAPL saturations at large time scales (months to years). These results are valid for both NAPLs that are less dense than water (LNAPLs) and denser than water NAPLs (DNAPLs), since the formation of the NAPL layers depends only on the contact angles of the interfaces and the angle of the crevices where they are formed, and capillary forces dominate at the pore scale, relative to gravity and viscous forces. The large variation in fracture aperture results in preferential paths for contaminant transport, which results in very early breakthrough. For multiphase flow, capillary forces play a significant role in determining the movement of NAPL from the fracture to the porous matrix and vice versa. These issues, as well as the complex geometry of a network of fractures, have to be taken into consideration when designing a remediation scheme for fractured porous media.

Acknowledgments

First and foremost I would like to thank my wife, Brigitte, who supported my decision to make a radical turn in my life to embark in graduate studies and fulfill my career goals, despite the significant changes it involved in our lives. She has also endured many long hours waiting for me to come home from the lab, and has provided stability to our family by taking charge of our home and our daughters' education. I thank my daughters, Michelle and Nathalie, for their understanding and encouragement to finish this dissertation. I also thank my father and sisters for their support both in my decision to go on to graduate studies and to start my new career. My thanks also to Paul Roberts and Martin Blunt, who provided me with many ideas, insights and comments to help me find a path between the original research proposal and this dissertation. They have been great role models for my future plans. I also thank Lynn Orr and Peter Kitanidis for their comments and suggestions, as well as their encouragement. Last but not least I thank Charlie Werth, for his continuous competitive motivation to finish the Ph. D. I leave Stanford with many good friends.

Table of Contents

Abstract

Acknowledgments

1. Introduction

- 1.1 Problem Statement
- 1.2 Research Objectives
- 1.3 Approach
- 1.4 Dissertation Overview
- 1.5 References

2. Measurement and Characterization of Fracture Aperture

- 2.1 Introduction
- 2.2 Theory
- 2.3 Method
- 2.4 Imaging the Fracture Aperture Distribution
- 2.5 Characterization of the Fracture Aperture Distribution
- 2.6 Discussion
- 2.7 References

3. Single-phase Flow and Transport in Fractured Media

- 3.1 Introduction
- 3.2 Theory
- 3.3 Experimental Determination of Flow and Transport Parameters
 - 3.3.1 Analysis of Breakthrough Curves
 - 3.3.2 Imaging of Tracer Flow in Fractured Media
- 3.4 Modeling of Single Phase Flow and Transport in Fractures
 - 3.4.1 Stochastic Analysis
 - 3.4.2 Numerical Modeling
- 3.5 Summary and Conclusions
- 3.6 References

4. Two- and Three-Phase Flow at the Pore Scale

- 4.1 Introduction
- 4.2 Theory
 - 4.2.1 Spreading Coefficient
 - 4.2.2 NAPL Layers
 - 4.2.3 Double Displacement Mechanisms
- 4.3 Experimental Setup
- 4.4 Experimental Results
 - 4.4.1 Two-Phase Flow

- 4.4.2 Three-Phase Flow
 - 4.4.2.1 Equilibrium Spreading Coefficient
 - 4.4.2.2 Micromodel Observations
- 4.5 Discussion and Conclusions
- 4.6 References

- 5. Two-Phase Flow in Fractured Media
 - 5.1 Introduction
 - 5.2 Theory
 - 5.2.1 Continuum Model
 - 5.2.2 Discrete Fracture Network Model
 - 5.3 Modeling Results of Two-Phase Flow in Fractured Porous Media
 - 5.3.1 Capillary Pressure
 - 5.3.2 Relative Permeabilities
 - 5.3.3 Fracture Flow in a Porous Matrix
 - 5.4 Experimental Observation of Two-Phase Flow
 - 5.4.1 Experimental Method
 - 5.4.2 Absolute Permeability Measurements
 - 5.4.3 Saturation Profiles
 - 5.4.3.1 Water Imbibition into Dry Cores
 - 5.4.3.2 Primary Drainage: NAPL Displacing Water
 - 5.4.3.3 Secondary Imbibition: Water Displacing NAPL
 - 5.5 Discussion
 - 5.6 Summary and Conclusions
 - 5.7 References

- 6. Three-Phase Flow in Fractured Media
 - 6.1 Introduction
 - 6.2 Theory
 - 6.2.1 Capillary Pressure
 - 6.2.2 Relative Permeability
 - 6.3 Experimental Observation of Three-Phase Flow
 - 6.3.1 Experimental Method
 - 6.3.2 Saturation Profiles
 - 6.3.3 Steam Injection
 - 6.4 Modeling of Three-Phase Flow in Fractured Media
 - 6.5 Summary and Conclusions
 - 6.6 References

- 7. Engineering Significance
 - 7.1 Pore Scale Observations
 - 7.2 Fracture Aperture
 - 7.3 Single Phase Flow in Fractures
 - 7.4 Multiphase Flow in Fractures
 - 7.5 Conclusions
 - 7.6 Future Work

Chapter 1

Introduction

1.1 Problem Statement

Fractures are prevalent in natural and synthetic structural media, even in the best engineered materials. We find fractures in bedrock, in sandstone aquifers and oil reservoirs, in clay layers and even in unconsolidated materials (Figures 1.1 to 1.4). Fractures are also common in concrete, used either as a structural material or as a liner for storage tanks (Figure 1.5). Clay liners used in landfills, sludge and brine disposal pits or for underground storage tanks can fracture, releasing their liquid contents to the subsurface (Figure 1.6). Even “flexible” materials such as asphalt fracture with time (Figure 1.7). The fact that fractures are inevitable has led to spending billions of research dollars to construct “safe” long-term (10,000 years or more) storage for high-level nuclear waste (Savage, 1995; IAEA, 1995), both to determine which construction techniques are least likely to result in failure and what are the implications of a failure, in terms of release to the environment and potential contamination of ground water sources or exposure of humans to high levels of radioactivity.

Why do materials fail? In most cases, the material is flawed from its genesis. In crystalline materials, it may be the inclusion of one different atom or molecule in the structure of the growing crystal, or simply the juncture of two crystal planes. In depositional materials, different grain types and sizes may be laid down, resulting in layering which then becomes the initiation plane for the fracture. Most materials fail because of mechanical stresses, for example the weight of the overburden, or heaving (Atkinson, 1989; Heard *et al.*, 1972). Some mechanical stresses are applied constantly

until the material fails, others are delivered in a sudden event. Other causes of failure are thermal stresses, drying and wetting cycles and chemical dissolution.

After a material fractures, the two faces of the fracture may be subject to additional stresses which either close or open the fracture, or may subject it to shear. Other materials may temporarily or permanently deposit in the fracture, partially or totally blocking it for subsequent fluid flow. The fracture may be almost shut for millions of years, but if the material becomes exposed to the surface or near surface environment, the resulting loss of overburden or weathering may allow the fractures to open.

In some cases, we are actually interested in introducing fractures in the subsurface, via hydraulic (Warpinski, 1991) or pneumatic fracturing (Schuring *et al.*, 1995), or more powerful means, to increase fluid flow in oil reservoirs or at contaminated sites.

Our particular focus in this study is the role that fractures play in the movement of contaminants in the subsurface. Water supply from fractured bedrock aquifers is common in the United States (Mutch and Scott, 1994). With increasing frequency contaminated fractured aquifers are detected (NRC, 1990). In many cases, the source of the contamination is a Non-Aqueous Phase Liquid (NAPL) which is either in pools or as residual ganglia in the fractures of the porous matrix. Dissolution of the NAPL may occur over several decades, resulting in a growing plume of dissolved contaminants which is transported through the fractured aquifer due to natural or imposed hydraulic gradients. Fractures in aquitards may allow the seepage of contaminants, either dissolved or in their own phase, into water sources.

Fluid flow in the fractured porous media is of significance not only in the context of contaminant transport, but also in the production of oil from reservoirs, the generation of steam for power from geothermal reservoirs, and the prediction of structural integrity or failure of large geotechnical structures, such as dams or foundations. Thus, the results of this study have a wide range of applications.

The conceptual model of a typical contaminant spill into porous media has been put forward by Abriola (1989), Mercer and Cohen (1990), Kueper and McWhorter (1991) and Parker *et al.* (1994). In some cases, the contaminant is dissolved in water and thus

travels in a fractured aquifer or aquitard as a solute. Fractures provide a fast channel for widely distributing the contaminant throughout the aquifer and also result in contaminant transport in somewhat unpredictable directions, depending on the fracture planes that are intersected (Hsieh *et al.*, 1985).

More typically a contaminant enters the subsurface as a liquid phase separate from the gaseous or aqueous phases present (Figure 1.8). The NAPL may be leaking from a damaged or decaying storage vessel (e.g. in a gasoline station or a refinery) or a disposal pond, or may be spilt during transport and use in a manufacturing process (e.g. during degreasing of metal parts, in the electronics industry to clean semiconductors, or in an airfield for cleaning jet engines). The NAPL travels first through the unsaturated zone, under three-phase flow conditions, displacing air and water. The variations in matrix permeability, due to the heterogeneity of the porous medium, result in additional deviations from vertical flow. If the NAPL encounters layers of slightly less permeable materials (e.g. silt or clay lenses, or even tightly packed sand), or materials with smaller pores and thus a higher capillary entry pressure (e.g. NAPL entering a tight, water-filled porous medium), it will tend to flow mostly in the horizontal direction until it encounters a path of less resistance, either more permeable or with larger pores. Microfractures in the matrix are also important in allowing the NAPL to flow through these low-permeability lenses.

When the NAPL reaches the capillary fringe, two scenarios may arise. First, if the NAPL is less dense than water (LNAPL, e.g. gasoline, most hydrocarbons), then buoyancy forces will allow it to “float” on top of the water table. The NAPL first forms a small mound, which quickly spreads horizontally over the water table (Figure 1.9). When the water table rises due to recharge of the aquifer, it displaces the NAPL pool upward, but by that time the saturation of NAPL may be so low that it becomes disconnected. Disconnected NAPL will usually not flow under two-phase (water and NAPL) conditions. Connected NAPL will move up and down with the movements of the water table, being smeared until becomes disconnected. If the water table goes above the disconnected NAPL, it will begin to slowly dissolve. NAPL in the unsaturated zone will

slowly volatilize. The rates of dissolution and volatilization are controlled by the flow of water or air, respectively (Powers *et al.*, 1991; Miller *et al.*, 1990; Wilkins *et al.*, 1995; Gierke *et al.*, 1990). A plume of dissolved NAPL will form in the ground water, as well as a plume of volatilized NAPL in the unsaturated zone.

If the NAPL is denser than water (DNAPL, e.g. chlorinated organic solvents, polychlorinated biphenyls, tars and creosotes), then once it reaches the water table it begins to form a mound and spread horizontally until either there is enough mass to overcome the capillary entry pressure (DNAPL into a water saturated matrix) or it finds a path of less resistance into the water-saturated matrix, either a fracture or a more porous/permeable region. Once in the saturated zone, the DNAPL travels downward until either it reaches a low enough saturation to become disconnected (forming drops or “ganglia”) and immobile, or it finds a low-permeability layer. If the layer does not extend very far, the DNAPL will flow horizontally around it. In many cases, the DNAPL reaches bedrock (Figure 1.10). The rock usually contains fractures into which the DNAPL flows readily, displacing water. The capillary entry pressure into most fractures is quite low, on the order of a few centimeters of DNAPL head (Kueper and McWhorter, 1991). Flow into the fractures continues until either the fracture becomes highly DNAPL saturated, or the fracture is filled or closed below, or the DNAPL spreads thin enough to become disconnected. The DNAPL may flow into horizontal fractures within the fracture network.

In terms of remediation strategies, DNAPLs in fractured bedrock are probably one of the most intractable problems (National Research Council, 1994). They are a continuous source of dissolved contaminants for years or decades, making any pumping or active bioremediation alternative a very long term and costly proposition. Excavation down to the fractured bedrock is very expensive in most cases, and removal of the contaminated bedrock even more so. Potential remediation alternatives for consideration, include dewatering the contaminated zone via high-rate pumping and then applying Soil Vapor Extraction to remove volatile DNAPLs, or applying steam to mobilize and volatilize the DNAPL towards a collection well. An additional option is to use

surfactants, either to increase the dissolution of DNAPL or to reduce its interfacial tension and thus remobilize it (Abdul et al., 1992). An issue with remobilizing via surfactants is the potential to drive the DNAPLs further down in the aquifer or bedrock, complicating the removal.

If an effective remediation scheme is to be engineered, such as Soil Vapor Extraction, steam injection or surfactant-enhanced dissolution or mobilization, we need to understand how DNAPLs flow through fractures. Flow may be either as a solute in the aqueous phase, as two separate phases (DNAPL-water) or as three phases (DNAPL, water and gas, either air or steam). Another complication in any remediation scheme, not addressed in this study, is how to characterize the fracture network. Which are the fractures that carry most of the flow? What is their aperture and direction? What is the density of fracturing in a particular medium? Are the fractures connected to other fractures, probably in other planes? How does one sample enough of the subsurface to generate a good idea of the complexity involved? Some techniques are beginning to emerge to determine some of the most important parameters. For example, pumping and tracer tests (McKay et al., 1993; Hsieh *et al.*, 1983) may provide enough information to determine the mean mechanical and hydraulic aperture of a fracture, as well as its main orientation. Geophysical techniques like seismic imaging, ground-penetrating radar and electrical conductivity tests are being improved to assist in the determination of fracture zones (National Research Council, 1996). However, there is room for significant improvement in our current ability to characterize fractures in the subsurface.

Even if we come to understand how single and multiphase flow occurs in a fracture, and the interactions between the fracture and the porous matrix surrounding it, how do we describe all these phenomena in a modeling framework? Clearly, we cannot describe every fracture in a model that may consider scales of tens, hundreds or thousands of meters in one or more directions. One approach is to consider the medium as an “equivalent continuum” (Long, 1985), where the small-scale properties are somehow averaged in the macroscopic scale. Probably the best solution for averaging properties is to use a stochastic description of properties such as permeability (or

hydraulic conductivity) including the effect of fractures on overall permeability, diffusivity, sorption capacity, grain size, wettability, etc. Another approach, first developed in the petroleum industry, is to consider a “dual porosity/dual permeability” medium (Bai *et al.*, 1993; Zimmerman *et al.*, 1993; Johns and Roberts, 1991; Warren and Root, 1963), referring to the porosity and permeability of the matrix and the fracture. Diffusive or capillary forces drive the contaminants, or the oil and its components, into or out of the matrix, and most advective flow occurs in the fractures. None of these models has yet been validated through controlled experiments.

1.2 Research Objectives

The objectives of this research are:

- To characterize the fracture aperture distribution of several fractured porous media at high resolution;
- To study the transport of a contaminant dissolved in water through fractured media, via experimental observation;
- To study the physical processes involved in two- and three-phase displacements at the pore scale;
- To observe two- and three-phase displacements in real fractured porous media;
- To bring the experimental observations into a modeling framework for predictive purposes.

1.3 Approach

To understand single and multiphase flow and transport processes in fractures, I first decided to characterize at a high level of resolution the fracture aperture distribution of a number of fractured rock cores using CAT-scanning. With this information, I determined the geometry and permeability of the fractures, which I then use to construct a numerical flow model. I also use this information to test the validity of predictive models that are based on the assumed statistics of the aperture distribution. For example, stochastic models (Gelhar, 1986) use the geometric mean of the aperture distribution to predict the transmissivity of a fracture, and show that the aperture variance and correlation length can be used to predict the dispersivity of a solute through a fracture. These models have not been, to my knowledge, been tested experimentally prior to this study. I compare these theoretical predictions of fracture transmissivity and dispersivity of a contaminant, with experimental results, both from the interpretation of the breakthrough curve of a non-sorbing tracer and from CAT-scans of the tracer movement through the fractured cores.

To study multiphase displacements at the pore scale, we use a physical “micromodel”, which is a simile of a real pore space in two dimensions, etched onto a silicon substrate. The advantage of having a realistic pore space, which for the first time has the correct pore body and pore throat dimensions in a micromodel, is that we can observe multiphase displacements under realistic conditions in terms of the balance between capillary and viscous forces. I conduct two- and three-phase displacements to observe the role that water and NAPL layers play in the mobilization of the various phases. The micromodels are also used to study the possible combinations of double displacements, where one phase displaces another which displaces a third phase. The pore scale observations have been captured by Fenwick and Blunt (1996) in a three-dimensional, three-phase network model which considers flow in layers and allows for double displacements. This network model then can produce three-phase relative permeabilities as a function of phase saturation(s) and the displacement path (drainage, imbibition or a series of drainage and imbibition steps).

In addition, I use the fracture aperture information to construct capillary pressure-saturation curves for two phase (Pruess and Tsang, 1990) and three phases (Parker and Lenhard, 1987), as well as three-phase relative permeabilities (Parker and Lenhard, 1990). The fracture aperture distribution is also an input to a fracture network model which I use to study two-phase displacements (drainage and imbibition) under the assumption of capillary-dominated flow.

To observe two- and three-phase displacements at a larger scale, in real fractured cores, I use the CAT-scanner. I can observe the displacements at various time steps, in permeable (e.g. sandstones) and impermeable (e.g. granites) fractured media, determining the paths that the different phases follow. These observations are then compared with the results of the network model as well as with more conventional numerical simulation.

1.4 Dissertation Overview

The work is presented in self-contained chapters. Chapter 2 deals with the high resolution measurement and subsequent statistical characterization of fracture aperture. Chapter 3 uses the fracture aperture geostatistics to predict transmissivity and diffusivity of a solute in single-phase flow through a fracture, which is then tested experimentally. We also observe the flow of a tracer inside the fracture using the CAT-scanner, and relate the observations to numerical modeling results.

Chapter 4 presents the theory behind the flow characteristics at the pore scale as well as the micromodel observations of two- and three-phase flow. In Chapter 5, two-phase flow in fractured and unfractured porous media is presented, comparing CAT-scanned observations of various two-phase flow combinations (imbibition, drainage and water flooding) against numerical modeling results. Chapter 6 presents three-phase flow

in fractures, comparing numerical results against CAT-scanner observations. Finally, Chapter 7 considers the engineering relevance of these studies.

1.5 References

- Atkinson, B. K., 1989: Fracture Mechanics of Rock, Academic Press, New York, pp. 548
- Abdul, A. S., T. L. Gibson, C. C. Ang, J. C. Smith and R. E. Sobczynski, 1992: Pilot test of in situ surfactant washing of polychlorinated biphenyls and oils from a contaminated site, *Ground Water*, **30**:2, 219-231
- Abriola, L., 1989: Modeling multiphase migration of organic chemicals in groundwater systems - A review and assessment, *Environmental Health Perspectives*, **83**, 117-143
- Bai, M., D. Elsworth, J-C. Roegiers, 1993: Multiporosity/multipermeability approach to the simulation of naturally fractured reservoirs, *Water Resources Research*, **29**:6, 1621-1633
- Fenwick, D. H. and M. J. Blunt: 1996, Three Dimensional Modeling of Three Phase Imbibition and Drainage, *Advances in Water Resources*, (in press)
- Gelhar, L. W., 1986: Stochastic subsurface hydrology: From theory to applications., *Water Resources Res.*, **22**(9), 1355-1455.
- Gierke, J. S., N. J. Hutzler and J. C. Crittenden, Modeling the movement of volatile organic chemicals in columns of unsaturated soil, *Water Resources Research*, **26**:7, 1529-1547
- Heard, H. C., I. Y. Borg, N. L. Carter and C. B. Raleigh, 1972: *Flow and fracture of rocks*, *Geophysical Monograph 16*, American Geophysical Union, Washington, D. C.
- Hsieh, P. A., S. P. Neuman, G. K. Stiles and E. S. Simpson, 1985: Field determination of the three-dimensional hydraulic conductivity of anisotropic media: 2. Methodology and application to fracture rocks, *Water Resources Research*, **21**:11, 1667-1676
- Hsieh, P. A., S. P. Neuman and E. S. Simpson, 1983: Pressure testing of fractured rocks- A methodology employing three-dimensional cross-hole tests, Report NUREG/CR-3213 RW, Dept. of Hydrology and Water Resources, *University of Arizona*, Tucson, AZ 85721
- IAEA, 1995: *The principles of radioactive waste management*, International Atomic Energy Agency, Vienna
- Johns, R. A. and P. V. Roberts, 1991: A solute transport model for channelized flow in a fracture. *Water Resources Res.* **27**(8): 1797-1808.
- Kueper, B. H. and D. B. McWhorter, 1991: The behavior of dense, nonaqueous phase liquids in fractured clay and rock, *Ground Water*, **29**:5, 716-728
- Long, J. C. S., 1985: Verification and characterization of continuum behavior of fractured rock at AECL Underground Research Laboratory, *Report BMI/OCRD-17, LBL-14975*, Batelle Memorial Institute, Ohio
- McKay, L. D., J. A. Cherry and R. W. Gillham, 1993: Field experiments in a fractured clay till, 1. Hydraulic conductivity and fracture aperture, *Water Resources Research*, **29**:4, 1149-1162
- Mercer, J. W. and R. M. Cohen, 1990: A review of immiscible fluids in the subsurface: properties, models, characterization and remediation, *J. of Contaminant Hydrology*, **6**, 107-163
- Miller, C. T., M. M. Poirier-McNeill and A. S. Mayer, 1990: Dissolution of trapped nonaqueous phase liquids: mass transfer characteristics, *Water Resources Research*, **26**:11, 2783-2796
- Mutch, R. D. and J. I. Scott, 1994: Problems with the Remediation of Diffusion-Limited Fractured Rock Systems. *Hazardous Waste Site Soil Remediation: Theory and Application of Innovative Technologies*. New York, Marcel Dekker, Inc.
- National Research Council, 1994: *Alternatives for ground water cleanup*, National Academy Press, Washington, D. C.
- National Research Council, 1996: *Rock Fracture and Fracture Flow: Contemporary Understanding and Applications*, *Committee on Fracture Characterization and Fluid Flow*, National Academy Press, Washington, D. C. (in press).
- Parker, J. C. and R. J. Lenhard, 1987: A model for hysteretic constitutive relations governing multiphase flow: 1. Saturation-pressure relations, *Water Resources Research*, **23**:12, 2187-2196

- Parker, J. C. and R. J. Lenhard, 1990: Determining three-phase permeability-saturation-pressure relations from two-phase system measurements, *J. Pet. Sci. and Eng.*, **4**, 57-65
- Parker, B. L., R. W. Gillham and J. A. Cherry, 1994: Diffusive disappearance of immiscible-phase organic liquids in fractured geologic media, *Ground Water*, **32**:5, 805-820
- Powers, S. E., C. O. Loureiro, L. M. Abriola and W. J. Weber, Jr., 1991: Theoretical study of the significance of nonequilibrium dissolution of nonaqueous phase liquids in subsurface systems, *Water Resources Research*, **27**:4, 463-477
- Pruess, K. and Y. W. Tsang, 1990: On two-phase relative permeability and capillary pressure of rough-walled rock fractures, *Water Resources Research*, **26**:9, 1915-1926
- Reitsma, S. and B. H. Kueper, 1994: Laboratory measurement of capillary pressure-saturation relationships in a rock fracture, *Water Resources Research*, **30**:4, 865-878
- Savage, D., 1995: *The scientific and regulatory basis for the geological disposal of radioactive waste*, John Wiley, New York
- Schuring, J. R., P. C. Chan and T. M. Boland, 1995: Using pneumatic fracturing for in-situ remediation of contaminated sites, *Remediation*, **5**:2, 77-90
- Norman R. Warpinski, 1991: Hydraulic fracturing in tight, fissured media, SPE 20154, *J. Petroleum Technology*, 43:2, 146-209
- Warren, J. E. and P. J. Root, 1963: The behavior of naturally fractured reservoirs, *Soc. Pet. Eng. J.*, **3**, 245-255
- Wilkins, M. D., L. M. Abriola and K. D. Pennell, 1995: An experimental investigation of rate-limited nonaqueous phase liquid volatilization in unsaturated porous media: Steady state mass transfer, *Water Resources Research*, **31**:9, 2159-2172
- Zimmerman, R. W., G. Chen, T. Hadgu and G S. Bodvarsson, 1993: A numerical dual-porosity model with semianalytical treatment of fracture/matrix flow, *Water Resources Research*, **29**:7, 2127-2137

Figure 1.1 Complex fracture network in bedrock.



Figure 1.2 Heavily fractured exposed bedrock.



Figure 1.3 Horizontal fractures in layered sandstone, as well as vertical fractures shearing the exposed face.



Figure 1.4 Fractures in unconsolidated porous media.

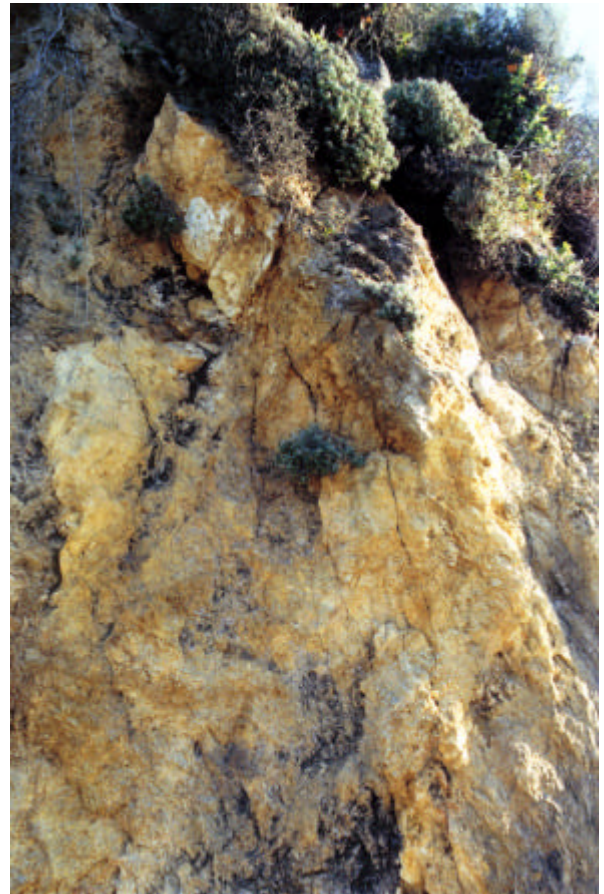


Figure 1.5 Fracture in concrete storage tank base.



Figure 1.6 Fracture in clay matrix due to wetting and drying cycles.



Figure 1.7 Fracture in asphalt liner.



Figure 1.8 Schematic of DNAPL spill from an underground storage tank. Horizontal movement of DNAPL is due to less permeable/porous layer.

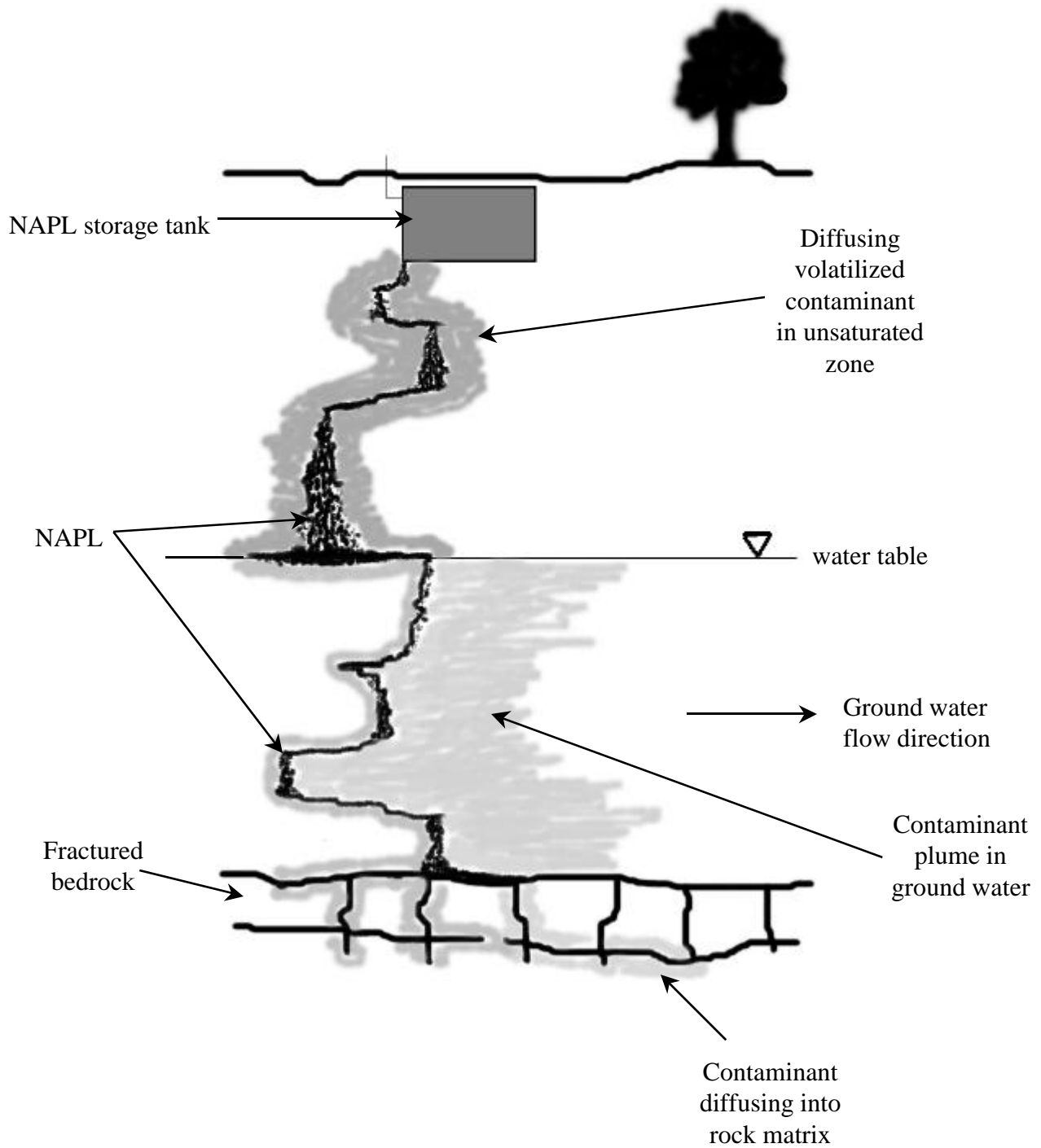


Figure 1.9 Schematic of LNAPL spill which reaches the water table after passing through a fractured clay lens. Note the smearing of LNAPL due to seasonal fluctuations of the water table.

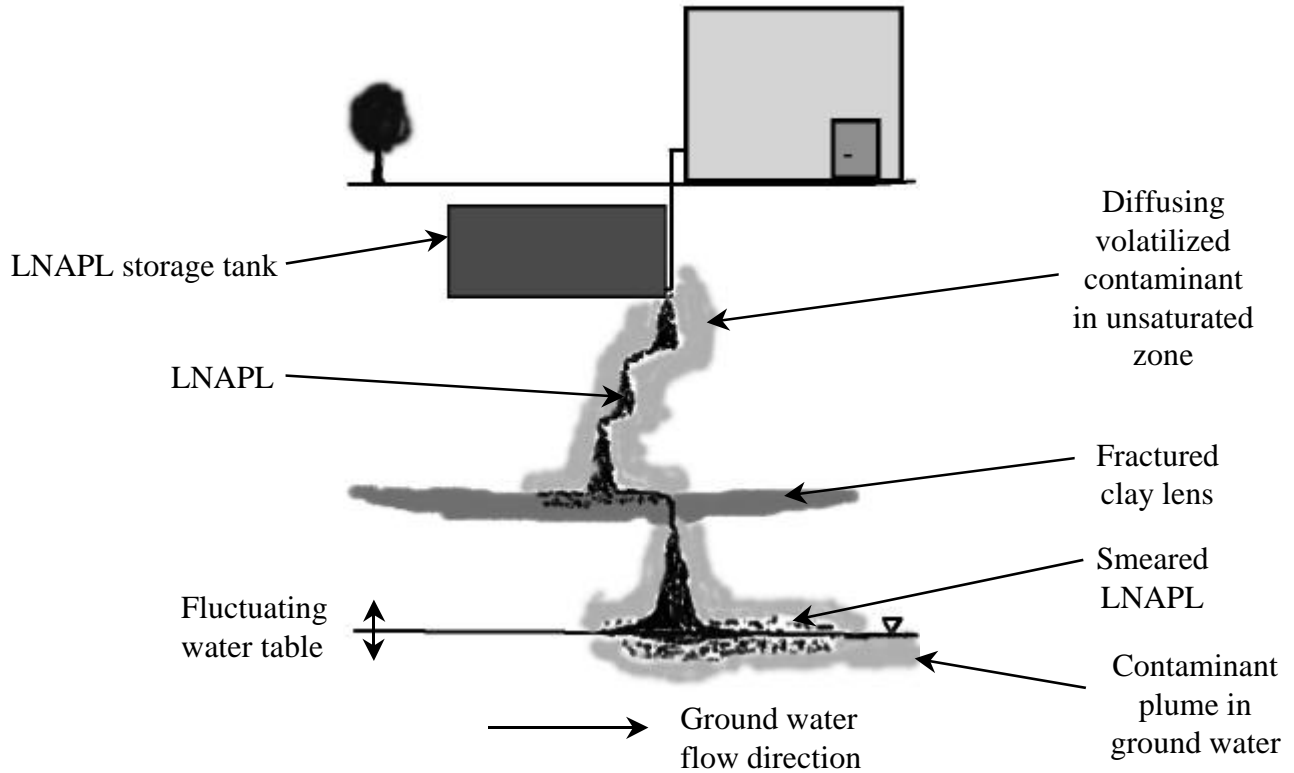
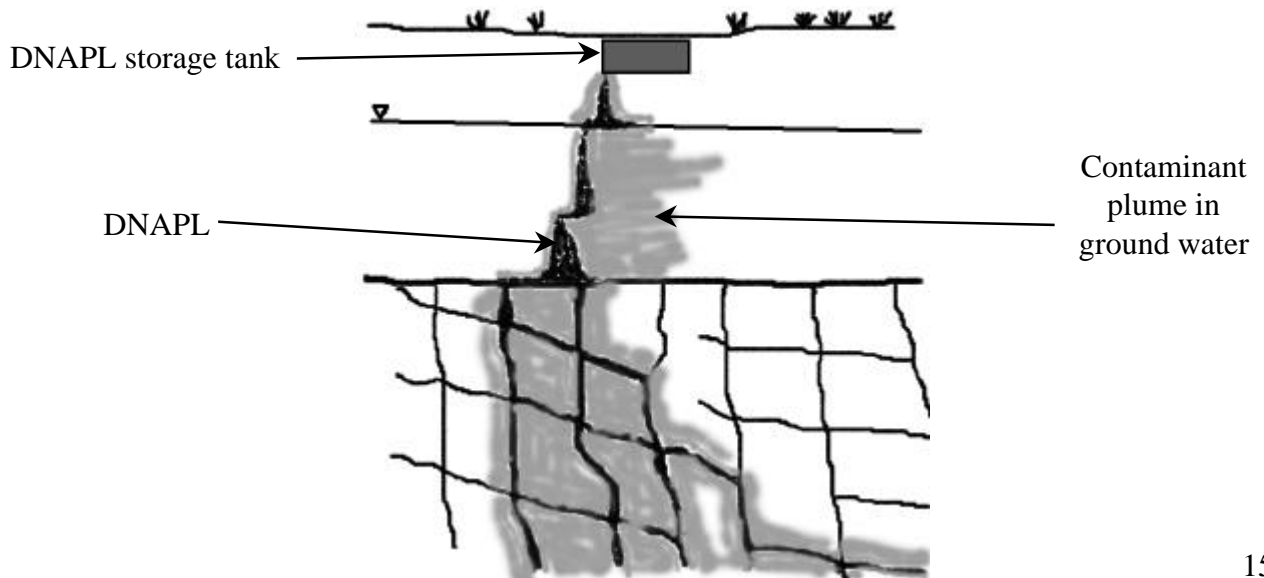


Figure 1.10 Schematic of DNAPL spill into a heavily fractured bedrock matrix with dissolution of contaminant which then diffuses into the matrix.



Chapter 2

Measurement and Characterization of Fracture Aperture

2.1 Introduction

Fracture aperture is the key parameter in determining the flow and transport characteristics of fractured media. In natural fractures there is usually a large distribution of fracture apertures even within a single fracture. The fracture aperture distribution is controlled by a number of factors, among them the flaws and inclusions in the material and the history of mechanical, thermal and chemical stresses on the material, from before it fractured, through the primary fracturing process and the subsequent fracturing episodes on to its current state (Atkinson, 1989; Lawn and Wilshaw, 1975). A sudden release of the confining pressure may result in a widening of the fractures. The strength of the porous media, as well as that of inclusions, is a key factor in determining whether the material will fail, and under what stresses, and plays a role in determining the fracture aperture, deciding whether the material holds together or crumbles after failure. Fracture spacing, which may be a result of both material strength and stress history, also affects the fracture aperture distribution. Other materials, such as calcites, may exhibit dissolution channels in addition to fractures, generated by a totally different set of circumstances.

Prediction of the fracture aperture distribution given the material properties and stress history (even if it could be somehow precisely determined over millions of years) is next to impossible, since the material is likely to fail at flaws or inclusions in the matrix, which cannot be captured in the averaged material properties. Field determination of the fracture aperture distribution, or even simply mean aperture, is currently an area of active research. Several direct techniques for detecting and imaging fractures are under development. Small-scale features can be imaged using video imaging inside the well

(Palmer and Sparks, 1991; Overbey et al., 1988, Darilek, 1986), which of course only provides an image of the fracture aperture in the immediate vicinity of the well, where the aperture of the fractures is most likely affected by the well boring process. For larger scales, geophysical imaging techniques include (National Research Council, 1996): (1) seismic reflection, where seismic waves are generated at one location and measured at several points for 3D imaging, measuring the reflection of the seismic energy at discontinuities; (2) electrical methods, which rely on the fact that water-filled fractures have a higher conductivity than unfractured rock and can mobilize ions in solution; and (3) ground-penetrating radar, in which electromagnetic radiation is applied in a similar manner as with seismic imaging but at much higher frequencies (10 to 1000 MHz), with propagation of the radar signal depending on the dielectric constant and electrical conductivity of the materials and reflection of the signal at discontinuities. At present, these geophysical imaging methods are successful only in detecting only very large features, with resolution at best of the same order as the dominant wavelength of the input signal for radar and seismic imaging (0.1 to 10's of meters), and 1 to 10 m for electric profiling.

Indirect techniques of measuring the statistics of the fracture aperture distribution (arithmetic mean, geometric mean and standard deviation) include pumping and tracer injection tests. These are currently the most accurate means of assessing fracture aperture and its distribution in the field. Pumping tests are performed by first isolating the fracture (or a small interval in the well containing fractures) using packers. The pumping tests at one or more wells provide the transmissivity of the fracture (or fractured interval), from which the geometric mean of the fracture aperture, a_{gm} , can be inferred using the Boussinesq or “cubic” law (Dagan, 1989; Witherspoon *et al.*, 1980; Dagan, 1979) for linear flow in an “equivalent” parallel plate fracture with constant aperture, a_{gm} , fracture plane width W and flow path length L :

$$Q = -\frac{\Delta P}{12\mathbf{mL}} a_{gm}^3 W \quad (2.1)$$

where Q is the volumetric flow rate, \mathbf{m} is the fluid's dynamic viscosity and ΔP is the pressure difference. Pumping at one well and monitoring the effect on pressure head at other wells, which have also been packed to isolate a given fracture, can provide information about the extent of the fracture, the inclination of the fracture plane and its transmissivity over a wider area (Piggott *et al.*, 1991; Paillet and Kapucu, 1989; Silliman and Robinson, 1989; Hsieh *et al.*, 1985; Hsieh *et al.* 1983; Ramirez *et al.*, 1982). Tracer tests (Novakowski and Lapcevic, 1994; Raven *et al.*, 1988; Novakowski *et al.*, 1985) can be used to determine the arithmetic mean of fracture aperture, a_m , (Tsang, 1992), obtained from a mass balance for the tracer:

$$Q = \frac{LW a_m}{t_m} \quad (2.2)$$

where t_m is the mean residence time of the tracer, assuming a linear geometry.

At the laboratory scale, much higher resolution can be attained in the determination of the fracture aperture distribution. The higher resolution can be used to increase our understanding of the controlling mechanisms and key parameters for flow and transport in fractured porous media, and thus make better predictions of the infiltration path of a contaminant, the location of trapped ganglia of NAPLs in the fracture, the effect of containment or mobilization techniques, and the remediation of a contaminated fractured aquifer or aquitard. The knowledge can also be used to improve the efficiency of crude oil extraction from a fractured reservoir, leaving behind the lowest possible oil saturation.

Several techniques have been applied to determine fracture aperture in the laboratory. The two surfaces of an open fracture can be scanned using a surface profiler (Brown *et al.*, 1986; Keller and Bonner, 1985; Brown and Scholz, 1985), providing a map of the surface roughness at a theoretical resolution of 10 μm for surface features. The two

halves are then closed using a precise guidance mechanism. The fracture aperture distribution is computed indirectly by knowing the distance between the two halves. Although this technique can in principle be very precise, there is a high probability that the confining pressure may change during a flow experiment, or that the referencing between the two halves may not be adequate, resulting in an error in the estimated fracture aperture distribution. In addition, the surface profiling process may affect the surface due to the direct application of mechanical force.

The fracture aperture distribution can also be determined by injecting a fluid into the fracture that can be solidified, such as resins (Gentier *et al.*, 1989; Gale, 1987) or low melting point metals (Pyrak-Nolte *et al.*, 1987). These methods may yield the desired aperture information but render the fracture useless for flow experiments. The fracture aperture distribution is still useful for numerical modeling of flow and transport in the fracture.

Non-intrusive methods of determining the in-situ fracture aperture, within a core holder, at a given confining pressure, are thus more desirable. High energies are required to probe inside the rock. X-ray and gamma radiation are currently used to image porous media. If the fractured media is thin, on the order of a few millimeters, X-rays or gamma rays can be applied on a single plane, and the fracture aperture can then be mapped to a one-dimensional “channel”. However, for a real two-dimensional fracture in a three-dimensional porous medium, a complete representation can only be obtained if the X-ray source is rotated around the core and the signals received by the X-ray detectors are then processed to reconstruct the X-ray beam attenuation. This technique is referred to as Computer Aided Tomography (CAT) X-ray scanning, and will be discussed more fully in the next section. CAT-scanning has been applied to studying porous media and the flow of fluids in the medium (Peters *et al.*, 1992; Vinegar and Wellington, 1991; Lenormand *et al.*, 1990; Tollner *et al.*, 1989; Chatzis *et al.*, 1988; Withjack, 1988; Hunt *et al.*, 1987). The feasibility of using CAT-scanning to study fluid flow in fractured granite rocks was demonstrated by Johns (1991), using a scanner with a maximum resolution of 1.465 x

1.465 mm. The smallest fracture apertures determined by Johns *et al.*, (1993) were on the order of 50 μm . With the new generation of scanner used in this work, the resolution is 0.27 x 0.27 mm. The current fracture aperture resolution with CAT-scanning is around 38 μm , which is somewhat larger than the dimensions of pore throats (~ 1 to 30 μm) in typical porous media, but is adequate for observing most flow and transport processes in natural fractures.

This chapter presents the theory behind CAT-scanning, which is used throughout most of these flow and transport studies, as well as its application to obtain the fracture aperture distribution in naturally fractured cores of consolidated material. The technique is used to map the aperture distribution in three cores: (1) a relatively simple single fracture in a granite core; (2) a complex set of fractures in a granite core; and (3) a simple fracture in a sandstone core. These materials were chosen to represent extremes in matrix porosity and permeability for the subsequent flow and transport studies. The fracture aperture distribution is then characterized using a set of statistical parameters which relate to the variability of the distribution, reflecting the “surface roughness” and its impact in flow behavior.

2.2 Theory

When a material is exposed to a beam of X-rays, the incoming radiation is either reflected and scattered (Compton scattering), absorbed and reemitted as lower energy electromagnetic radiation (Photoelectric effect) or transmitted through the material. The percentage of incoming radiation transmitted is a function of material thickness, density and chemical composition. Beers’ law (Wellington and Vinegar, 1987) is used to relate the intensity of the transmitted radiation, I , to the material properties lumped in the attenuation coefficient, μ , and the distance traveled through the material, x :

$$I = I_o e^{-m x} \quad (2.3)$$

This empirical relation is valid for a single wavelength, i.e. a “monochromatic” or monoenergetic beam. The attenuation coefficient is also a function of the wavelength of the incoming radiation, with the lower energy photons absorbed more easily. This is of consequence, since most X-ray sources generate a polyenergetic beam, and as the beam penetrates the material, the attenuation coefficient varies. This effect is called beam hardening (since the higher energies are transmitted farther into the sample) and generates a noticeable pattern in the scanned image, if the material is not uniform in thickness, that must be corrected via post-scan processing.

The transmitted radiation is received by an array of detectors located around the sample. In the current generation of CAT-scanners, the X-ray source is rotated around the sample at very fast speeds (typically 1-5 seconds for a 360° scan), as shown in Figure 2.1. Due to the scanner’s geometry, the sample should be placed as close as possible to the center of the field of view, and the core and core holder should be cylindrical if possible. The Picker 1200x scanner used for these studies has 1,200 detectors. Although the beam is narrowly focused, each detector may receive the transmitted radiation (signal) from slightly different X-ray source positions. The information from the detectors is processed by the CAT-scanner’s computer to generate the image using the signal from several detectors to generate a two-dimensional image of the cross-section. The resulting image in the Picker 1200x scanner is a 512 x 512 matrix, or 262,144 “pixels”. Typically, the signal in each pixel is expressed in CT units:

$$CT = 1000 \frac{(\mu - \mu_w)}{\mu_w} \quad (2.4)$$

where μ_w is the attenuation of pure water. The scanner is usually calibrated to result in a $CT_{\text{water}} = 0$ and $CT_{\text{air}} = -1000$.

The x-ray attenuation for a mixed sample (e.g. water in a porous matrix, or air in a fracture) is empirically modeled using (Wellington and Vinegar, 1987):

$$\mu_{mix} = \sum_i \mu_i S_i \quad (2.5)$$

where μ_{mix} refers to the attenuation of the mixed material, and μ_i and S_i to the attenuation and saturation of the i^{th} component. This relation is useful for interpreting the small fracture apertures, where within a given pixel there are both rock and air present. In effect, the measured attenuation is a volume averaged response of the contributions from the various materials present.

2.3 Method

The Picker 1200x scanner parameters were set to optimize the resolution of the scanned images, after a series of studies with different parameter combinations and typical granite and sandstone samples. The parameters used for this study are shown in Table 2.1. Field size refers to the region within the scanning field which is considered in the image processing. For the Picker 1200x, the field size can range up to 48 cm, for very large samples. Using a large field size results in reduced spatial resolution. The largest image matrix is 512 x 512, which gives the best resolution (0.27 mm x 0.27 mm). The scan angle refers to the total angle of rotation of the X-ray source. For the Picker 1200x, it is actually possible to scan 1.1 rotations (398°), to ensure that all the detectors receive a full signal. The image processing algorithm compensates for the overscanning at these detectors. The algorithm is also chosen to give the best contrast for hard samples (e.g. rocks, bones) as opposed to soft samples (e.g. tissue).

The total power delivered in a scan is a combination of voltage and current, as well as scan time. For the best contrast, a high power delivery is desirable. The combination of 140 kV x 80 mA x 3 s was chosen to deliver a relatively large amount of energy but

without unduly overheating the lamp filament. A constraint in the total scanning time is the frequent cooling periods required (usually every 5 to 6 scans) for the lamp filament. Some of the studies involve up to 240 scans, which implies more than 40 cooling periods. In addition, the same settings are used for the flow and transport experiments, and in order to capture the displacement of phases as they occur, it is necessary to complete the scanning in a relatively short time, with few cooling periods.

Table 2.1 Picker 1200x Scanner parameter values (Protocol 18)

Parameter	Value	Parameter	Value
Field size	16 cm	Voltage	140 kV
Image matrix	512 x 512	Current	80 mA
Sampling	1024	Scan time	5.09 sec
Scan Angle	398°	Thickness	3 mm
X-ray Filter	1	Resolution	UHR
Anode Speed	automatic	Focal spot	small
Image algorithm	7		

The thickness or width of the X-ray beam can be adjusted using an aperture control, from 1 to 10 mm. However, if the aperture is set very low (1-2 mm), the amount of energy projected onto the sample is too small, since the beam is not actually focused through the smaller aperture but simply cut-off. If the aperture is large, then the thickness of the slice through the sample is large, so that the final two-dimensional image is actually an average of the three-dimensional slice. When the sample is homogeneous, this may actually be desirable, but for heterogeneous samples, e.g. fractured rock cores, a smaller aperture is necessary. For the best resolution (Ultra High Resolution, UHR), the focal spot must be set to small. This collimates the X-ray beam, to enhance the fine resolution of small details, for example very thin fractures.

Large features can be measured directly from the scanned image, by counting the number of pixels they encompass. This is useful in determining the overall width of a sample, or the length of a fracture. However, for small features less than one pixel in size, e.g. fracture aperture, a different approach must be undertaken. Thin fractures will be

discernible as a reduction of the CT number for the pixel containing the fracture, relative to pixels which are 100% rock. Since the images are usually seen as monochromatic, with the lowest CT number set to black and the highest to white, the reduction in CT number is seen as a darker gray, as shown in Figure 2.2 . This image presents a typical scan of a fractured granite. Air is seen as black, with $CT_{\text{air}} = -1000$. The solid plastic core holder has an average CT greater than water, around 580. The low viscosity epoxy used in between the core holder and the granite core has a CT slightly lower than water ($CT_{\text{low v epoxy}} = -60$). The granite has an average CT value of around 1680, but with considerably more variability than the other materials. The variability in the rock CT numbers is due to differences in chemical composition for this granite, with denser regions shown as a whiter region and less dense regions slightly darker. A thin fracture is also noticeable in this scan.

Fracture aperture calibration standards were constructed from granite and sandstone samples. The calibration standard comprises two halves of the same rock type. The adjoining flat surfaces are polished, to reduce surface roughness as much as possible. To produce a “fracture” of known aperture, two metal feeler gauges of calibrated thickness are placed between the two flat surfaces, as shown in Figure 2.3. The two halves are firmly held together with a clamp during scanning, and the lower polished surface is leveled, to produce a horizontal fracture plane. The scan is done perpendicular to the longitudinal axis of the calibration standard, between the two feeler gauges. Fracture apertures ranging from 38 μm to 6.375 mm are scanned for each rock type, to obtain a calibration curve. Several apertures were scanned again at a later date to test the reproducibility of the method, with excellent results.

A section perpendicular to the fracture plane is shown in Figure 2.4 . The variability in the granite CT numbers is seen in this figure. Although the mean rock CT is 1680, there is a dense region centered around a pixel value of 25 (i.e. the position along the vertical axis in this case) with CT peaking at 1960. The minimum rock CT by contrast is 1618. For most fractures, the signal from a fracture is easily discernible as a sharp drop

in CT number (e.g. signal at pixel number 118). However, fractures less than around 35 to 40 μm are within the noise observed in the granite CT values.

To find a suitable method of measuring fracture aperture, several approaches were undertaken. One was to simply measure minimum CT number for a given fracture aperture. This was valid for the smaller fractures, but was not useful throughout the whole range of fracture apertures studied, since at large fracture apertures it became considerably non-linear and asymptotic. Large fractures are spread out over several pixels, so several pixels must be added. By integrating the dashed area (Figure 2.5), i.e. the “missing rock mass”, we can obtain an adequate predictor for fracture aperture for both small and large apertures (which may be larger than one pixel). The integration is done by subtracting the CT values in the pixel(s) from the minimum CT number for the rock matrix and then summing all those pixels with a positive value within a section. The calibration curve for granite is shown in Figure 2.6 and for sandstone in Figure 2.7. In Figure 2.6a we present all the apertures sampled for the granite core. In Figure 2.6b, only the small apertures ($a < 0.4 \text{ mm}$) are presented, which still exhibit a linear behavior. This can also be seen in the logarithmic plot of the integrated CT signal vs. aperture (Figure 2.6c). The statistics of the linear fit are shown in Table 2.2, indicating a very good correlation. These statistics actually represent the average fit of 50 sections for each thickness, with very good reproducibility. The coefficient of variation of 0.9% is for all the apertures sampled; for some of the smaller apertures, the coefficient of variation was as large as 7.3%. The discrepancies become large when a high density region in the rock matrix is very near the fracture. Because of the variability in the rock CT values, very small fractures ($< 35 \mu\text{m}$) cannot be accurately distinguished with the current CAT-scan resolution. However, we assume that the linear relationship still holds for small apertures.

Table 2.2 Statistics of calibration of fracture aperture from integrated CT signal

Rock Type	Conversion Factor	Standard Deviation	Coefficient of Variation
-----------	-------------------	--------------------	--------------------------

Sandstone	0.991×10^{-4} mm/CT	0.036×10^{-4} mm/CT	3.6 %
Granite	1.17×10^{-4} mm/CT	0.010×10^{-4} mm/CT	0.9 %

To ensure that the fracture aperture distributions measured in this study were valid for the subsequent flow experiments, the naturally fractured rock cores were first covered with a thin layer of high viscosity epoxy (Duralco 4525), then placed inside a polycarbonate cylindrical core holder. The space between the rock and the core holder was filled with a low viscosity epoxy (Duralco 4461). A granite sample similar to that used in the experiments is shown in Figures 2.8 and 2.9. This core was used in earlier experiments (Core A). For illustrative purposes, a piece of the rock is removed for the photo in Figure 3.9. This core actually had three main fractures, one longitudinal and two transverse to the longitudinal axis. All the cores are cylindrical, with diameters ranging from 52 to 76 mm. The main fracture is along the length of the cylinder. Although the two surfaces may have shifted from their original position, they match quite well and are carefully set before applying epoxy to the core. The fracture aperture is seen in Figure 2.9 to be quite small, on the order of 0.5 mm. A typical sandstone sample is shown in Figures 2.10 and 2.11. The relatively large fracture apertures along the sides of the core were filled with high viscosity epoxy, to avoid a very large channel along the edges of the fracture plane. The high viscosity epoxy has a very high CT number (>2000); thus it is equivalent to having a very high density, impermeable rock region. The rocks are then scanned inside the core holder. The scans are essentially perpendicular to the longitudinal axis of the cores.

2.4 Imaging the Fracture Aperture Distribution

All the cores scanned contain variable aperture fractures. The granite cores were obtained from a nearby quarry by Johns (1991), by coring naturally fractured blocks. The

sandstone cores were fractured in the laboratory using a hydraulic press, applying a pressure of 5 tons along a scored line on the longitudinal axis of the core. In both cases, granites and sandstone, the original fracture opening was not preserved, due to the method of coring or fracture generation, but the two faces of the fracture were carefully matched. In a realistic situation, it is likely that after the initial fracturing the faces of a fracture will be mismatched due to subsequent displacements, so we feel that we have a setup which closely matches the natural conditions. It can be argued that these fractures are not exactly as they might be found in their original setting, but we have not found a better method for obtaining fractured cores with realistic variations in aperture.

The first core scanned (identified as core C) is a granite core with a single fracture plane, and a diameter of 52.5 mm. The core was scanned every millimeter, from inlet to outlet, for a total of 166 scans. Figure 2.12 presents six of the slices, selected as representative images of the fracture aperture along the core. The entire set of slices is available in Appendix A. Figure 2.13 shows three different views of the fracture aperture distribution: (a) a “top view”, i.e. looking down perpendicular to the fracture plane; (b) a “side view”, reconstructed from the 166 scans and (c) a projection at an angle. The first and last three slices have been removed from the images in Figure 2.13, since they are mostly of the epoxy around the inlet and outlet.

As can be seen in the top view, most of the fracture has an aperture between 300 and 500 μm , but there are two main regions where the aperture is relatively large, up to around 4.5 mm, and there are some features that suggest channels within the fracture plane. To better delineate the extent of the fracture plane, in Figure 2.13 the region where fracture aperture is zero has been changed to a contrasting magenta color. The aperture is zero along the edges of the fracture plane due to the invasion of the high viscosity epoxy. The side view of core C indicates that the fracture is mostly in one plane, about 30 to 35 mm from the bottom of the core, but the fracture plane does actually rise and fall with respect to the mean fracture height. The angular projection is useful for visualizing the magnitude of the higher aperture regions with respect to the average aperture. The x, y,

and z coordinates and the fracture aperture of each pixel containing the fracture have been stored in a sparse matrix, to be able to reconstruct it for numerical modeling of flow.

The second granite core (Core D) has multiple fractures. The core has a diameter of 81.9 mm. 240 scans were acquired, with a spacing of one millimeter. Figure 2.14 presents 9 slices at regular intervals of 25 mm. From these images, it is clear that the core is fractured in at least 5 pieces. The complete set of scans is available in Appendix B. The core is aligned such that there is a main horizontal fracture plane, and the other principal fractures are mostly perpendicular to the horizontal plane. The vertical fracture near the inlet thins out until it disappears on the right side at around 60 mm. At around 175 mm, a thin rock sliver appears between the two main rock surfaces. A fracture at an angle to the scanning plane appears at around 200 mm, and is seen on the scans as a broad fracture with rock and air intermixed. At around 225 mm, there is a thin vertical fracture, almost perpendicular to the horizontal fracture plane, and a wide fracture at an angle of about 60° with respect to the horizontal fracture plane. Fracture aperture is consistently greater at the intersection of two fracture planes, which is of significance in terms of flow through a fracture network. Due to this larger fracture aperture, channeling is more likely to occur at fracture intersections if it's perpendicular to the flow. In addition, when contaminants are transported in a single phase (e.g. aqueous) in a single fracture and another fracture intersects the first fracture plane, mixing among streamlines is more likely given the large fracture aperture at the intersection, and the abrupt change in direction.

The top view of the horizontal fracture plane is shown in Figure 2.15. The top image in this figure presents the entire fracture aperture distribution from inlet to outlet. Although the vertical fractures are not considered as fracture aperture (but rather as different fractures, seen on the side view), the large fracture apertures near the inlet and around 215-225 mm into the core are more than an order of magnitude greater than the mean fracture aperture in the midsection of the core. The lower image in Figure 2.15 presents just the middle section of the core, from 30 mm to 200 mm into the core, where the fracture aperture ranges from about 200 μm to 2.5 mm. Some preferential flow paths can

be deduced from this fracture aperture distribution, as well as points of contact between the upper and lower rock surfaces. The side view of the fracture plane, presented in Figure 2.16, shows a rising trend from inlet to outlet, as well as the location and width of the vertical fractures. Since the vertical fracture near the inlet of the core (3 to 25 mm into the core) is almost perpendicular to the fracture plane, it is seen as a very sharp feature, whereas the vertical fracture around the outlet (200 to 240 mm) is presented as a broad feature, since it is at an angle in this view. In addition, in the side view the middle section of the core is integrated such that it is also presented as a rather broad feature, since the fracture plane is not truly horizontal.

The third core is a red sandstone, with visual evidence of layering, appreciable also in the CAT-scans. Subsequent studies confirmed a small difference in porosity and possibly in absolute permeability among layers. The layering runs almost longitudinally, as seen in an unfractured sample in Figures 2.17 and 2.18. Although the fracture plane also runs along the longitudinal axis of the core, it does not coincide with the layering planes, as can be seen in the CAT-scan images in Figure 2.19 . These sample scans are taken at regular intervals; the entire set of scans is available in Appendix C. The 76 scans were taken at a 3 mm spacing, given the regularity of the fracture and matrix material. Although there is some variability in the fracture aperture and the fracture plane is not very flat, it is considerably simpler than the granite cores. On the edges of the fracture the high-viscosity epoxy can be noticed as the “white” material in the CAT-scans; it imbibes only slightly into the fracture and almost negligibly into the matrix before hardening, due to its very high viscosity.

The fracture aperture distribution can be appreciated in Figure 2.20 . The top view, shown in Figure 2.20a, confirms that the fracture aperture is relatively homogeneous, mostly in the range from 150 to 400 μm . At around 115 mm into the core, there is a relatively large gap (up to 2.5 mm) to one side of the fracture plane. In Figure 2.20b, the entire top view is presented but cutting off all apertures greater than one millimeter. This allows us to better discern the low apertures in most of the fracture plane. The side view

is presented in Figure 2.20c . The fracture plane is practically horizontal, with little oscillation about the mean fracture plane.

2.5 Characterization of the Fracture Aperture Distribution

The distribution of apertures in a fracture is bound by zero aperture as a minimum and tend to be skewed, suggesting either a lognormal or a gamma distribution. Although Tsang and Tsang (1987) used a gamma distribution to describe the results of a surface profiling study, the fracture aperture distributions in the studies by Gale (1987), Pyrak-Nolte *et al.* (1987) and Johns (1993) appeared lognormal. Figures 2.21, 2.22 and 2.23 present the histograms for the three cores studied, which suggest that a lognormal distribution is the most adequate model for characterizing the fracture aperture distribution in these cores. The contact points ($a = 0$) have been removed from the distribution. As Renshaw (1995) points out, if only a small percentage of the fracture apertures is zero, then those apertures can be reasonably ignored. This is valid for a statistical characterization, although of course those contact points are very significant in terms of the flow channels that may develop in a fracture plane.

The statistics of the fracture aperture distributions for the three cores are presented in Table 2.3. These distributions do not consider the contact points, which are few within the fracture plane, but make a significant contribution around the edges of the fractures. The arithmetic mean, a_m , sometimes referred to as the mechanical aperture is largest for core C, partially due to the large gaps and also since the aperture in the small aperture region is not so small. In core D, the large region of small apertures between the two vertical fractures is rather tight, with an average mechanical aperture of 244 μm , so that the average mechanical aperture for the entire core is smaller than core C. By contrast, the mechanical aperture of the first vertical fracture in core D is rather large. For the sandstone core F, the mechanical aperture is even tighter ($a_m = 204 \mu\text{m}$), and the small

standard deviation reflects the relatively uniform aperture distribution. The standard deviation of mechanical aperture for the granite cores is significantly larger, reflecting the large gaps.

Table 2.3 Fracture Aperture Distribution Statistics

SAMPLE	Mechanical Aperture a_m (mm)	Standard Deviation s_m (mm)	Hydraulic Aperture a_h (mm)	Standard Deviation s_h (mm)	Variance variogram s^2	Correlation Length l (mm)
Granite Core C						
Entire Core	0.825	0.683	0.586	0.864	0.42	6
Small Aperture Region	0.553	0.092	0.545	0.176	0.022	0.8
Granite Core D						
Entire Core (horizontal)	0.639	0.963	0.402	0.966	0.49	7
Small Aperture Region	0.459	0.265	0.414	0.442	0.018	2.5
First Vertical Fracture	1.35	1.69	0.509	1.66	2.9	12
Sandstone Core F						
Entire Core	0.204	0.282	0.135	0.846	0.20	1.5
Small Aperture Region	0.134	0.081	0.116	0.529	0.017	1.5

The geometric mean of the aperture distribution, also known as the hydraulic aperture, a_h ,

$$a_h = a_{gm} = \exp(E(\log(a_{ij}))) \quad (2.6)$$

is consistently lower than the mechanical aperture for all cores, as expected. This reflects the smaller effective average cross-section for flow due to the low aperture regions. The difference is greatest for the complex core D, with some very high aperture voids and a large region of very low aperture. For a perfect lognormal distribution (Vanmarcke, 1983),

$$\frac{a_h}{a_m} = \exp\left(-\frac{\mathbf{s}_h^2}{2}\right) \quad (2.7)$$

The actual ratio of apertures is presented in Table 2.4, as well as the ratio obtained using equation 2.7. This represents the deviation from lognormality of the aperture distribution. The vertical fracture in core D exhibits the greatest deviation. This may partially indicate that the fracture is not completely parallel to the scanning plane. For the horizontal fractures, core D represents the greatest deviation from lognormality. However, the small aperture region in core D follows a lognormal distribution (Figure 2.24).

Zimmerman et al. (1991) have suggested that the roughness (i.e. deviation from parallel plate geometry) of a fracture can be represented by the ratio between the standard deviation and the mean of the mechanical aperture:

$$\text{roughness factor} = \frac{\mathbf{s}_m}{a_m} \quad (2.8)$$

A perfectly parallel-plate geometry would have zero standard deviation, such that the roughness ratio would be zero for this definition of roughness. The small aperture region in core C is closest to parallel-plate geometry. In general, the small aperture regions have low standard deviation and thus are the smoothest regions. Figures 2.25, 2.26 and 2.27 provide close-ups of the small aperture regions for cores C, D, and F respectively. The non-ideality is brought in by the large gaps in all three cores.

As shown by Gelhar (1993), the correlation length of the fracture aperture distribution can be related to the dispersivity of a tracer through the fracture. Table 2.3 presents the correlation length, λ , and the variance of the exponential semivariogram, σ , fitted to the data using a kriging algorithm. The correlation lengths are all small relative to the overall dimensions of the cores. The smallest correlation length is that of the small aperture region for core C (0.8 mm), while the largest correlation length corresponding to a horizontal fracture plane is in core D (7 mm). The vertical fracture presents the longest range correlation, with 12 mm. It also has the largest variance, which corresponds to its

high roughness. The small correlation lengths in the horizontal planes suggest that the variability in fracture aperture has little long-range structure.

Table 2.4 Deviation from Lognormality and Roughness of the Fractures

SAMPLE	Actual Ratio of Apertures a_m / a_h	Theoretical Ratio of Apertures $exp(-s_h^2/2)$	Roughness s_m / a_m
Granite Core C			
Entire Core	0.710	0.688	0.828
Small Aperture Region	0.986	0.985	0.166
Granite Core D			
Entire Core (horizontal)	0.629	0.627	1.506
Small Aperture Region	0.910	0.907	0.577
First Vertical Fracture	0.378	0.250	1.258
Sandstone Core F			
Entire Core	0.662	0.699	1.383
Small Aperture Region	0.866	0.869	0.605

2.6 Discussion

High resolution images of the fracture aperture distribution in granite and sandstone rocks were obtained using a Picker 1200x CAT-scanner. Although the minimum pixel size is 0.27 x 0.27 mm, fractures as small as 35 μm can be accurately measured using a calibration standard for the variation in CT number due to the “missing rock mass” in a given pixel. A calibration standard for each rock type yields distinctly different calibration slopes, about 17% greater for the granite core, indicating that whenever possible, each rock type should be analyzed against its own calibration standard.

The best correlation between CT number and fracture aperture is the integration of the missing rock mass, by adding up the CT values of all those pixels that are below the minimum CT number for the rock. The coefficient of variation for the conversion factor between CT number of the fracture and fracture aperture is 0.9 % for the granite cores and 3.6 % for the sandstone cores, reflecting the larger number of samples for the granite cores. In fact, because the granite cores are more heterogeneous in composition than the sandstone cores, exhibiting more variability in CT numbers, it is more difficult to discern the smallest apertures ($< 35 \mu\text{m}$) in granite cores. Other methods studied for correlating CT number in the pixel(s) against fracture aperture were biased either towards smaller or larger apertures.

Even for relatively simple fractures (cores C and F), the fracture aperture distribution is rather heterogeneous. Some potential flow channels can be deduced from the reconstruction of the two-dimensional fracture aperture distribution. When several fracture planes intersect (core D), the aperture is consistently larger at the intersection. This may lead to flow channeling along a fracture intersection, deviating the flow from its main flow direction and spreading contaminants in less predictable directions. These fracture intersections may also result in greater mixing among streamlines.

The distribution of fracture apertures can best be described by a lognormal function. This was also corroborated by comparing the theoretical to actual ratio of hydraulic to mechanical apertures. The small aperture regions conformed best with the lognormal distribution. The mechanical roughness of the fractures ranged from 0.17 to 1.5; when large voids are included the overall roughness increases substantially. The variability in fracture aperture displayed only short range structure, with correlation lengths of 0.8 mm to 7 mm at maximum, which is at most one-tenth of the minimum dimension (width) of the fracture plane.

The high resolution images of the fracture aperture distribution are an important tool in studying the flow and transport of contaminants in single and multiphase flow through a fractured porous media. For single phase flow, the permeability and dispersivity

of a fracture can be deduced from the statistics of the aperture distribution. In addition, streamlines can be calculated for the fracture plane and thus channeling and breakthrough can be estimated. For multiphase flow, the streamlines can also be used to construct a “Buckley-Leverett” solution, and thus predict the preferential movement of the invading phase through the fracture plane, the possibility of trapping the resident phase as well as potential snap-off events.

2.7 References

- Atkinson, B. K., 1989: Fracture Mechanics of Rock, Academic Press, pp. 548
- Brown, A. R., R. L. Kranz and B. P. Bonner, 1986: Correlation between the surfaces of natural rock joints, *Geophysical Research Letters*, 13(13), 1430-1433
- Brown, A. R. and C. H. Scholz, 1985: Broad bandwidth study of the topography of natural rock surfaces, *Journal of Geophysical Research*, 90(B14), 12575-12582
- Chatzis, I., A. Kantzas and F. A. L. Dullien, 1988: On the investigation of gravity-assisted inert gas injection using micromodels, long Berea sandstone cores and Computer-Assisted Tomography, paper SPE 18284 presented at the 1988 SPE Annual Tech. Conference and Exhibition, Houston, TX, October 2-5
- Dagan, G., 1979: Models of groundwater flow in statistically homogeneous porous formations, *Water Resources Research*, 15(1), 47-63
- Dagan, G., 1989: *Flow and Transport in Porous Formations*, Springer-Verlag, New York
- Darilek, G. T., 1986: A color borehole television system for developing gas production from Devonian shales, paper SPE 15219 presented at the 1986 SPE Unconventional Gas Recovery Symposium, Louisville, KY, May 18-21
- Gale, J. E., 1987: Comparison of coupled fracture deformation and fluid flow models with direct measurement of fracture pore structure and stress-flow properties, *Proceedings of the 28th U. S. Symposium of Rock Mechanics*, 1213-1222
- Gelhar, L. W., 1993: *Stochastic Subsurface Hydrology*, Prentice-Hall, Englewood Cliffs, N. J.
- Gentier, S., D. Billaux and L. V. Vliet, Laboratory testing of the voids of a fracture, *Rock Mechanics*, 22, 149-157
- Hunt, P. K., P. Engler and C. Bajscrowicz, 1987: Computed tomography as a core analysis tool: applications and artifact reduction techniques, paper 16952 presented at the 1987 SPE Annual Technical Conference and Exhibition, Dallas, TX, September 27-30
- Hsieh, P. A., S. P. Neuman, G. K. Stiles and E. S. Simpson, 1985: Field determination of the three-dimensional hydraulic conductivity of anisotropic media: 2. Methodology and application to fracture rocks, *Water Resources Research*, 21(11), 1667-1676
- Hsieh, P. A., S. P. Neuman and E. S. Simpson, 1983: Pressure testing of fractured rocks- A methodology employing three-dimensional cross-hole tests, Report NUREG/CR-3213 RW, Dept. of Hydrology and Water Resources, University of Arizona, Tucson, AZ 85721
- Johns, R. A., 1991: Diffusion and dispersion of solute in a variable aperture fracture, Ph.D. Dissertation, Stanford University, Stanford, California
- Johns, R. A., J. D. Steude, L. M. Castanier and P. V. Roberts, 1993: Nondestructive measurements of fracture aperture in crystalline rock cores using X-ray computed tomography, *J. Geophysical Research*, 98, 1889-1900
- Keller, K. and B. P. Bonner, 1985: Automatic digital system for profiling rough surfaces, *Review Scientific Instruments*, 56, 330-331
- Lawn, B. R. and T. R. Wilshaw, 1975: Fracture of brittle soils, *Cambridge University Press*, Cambridge, Massachusetts
- Lenormand, R., F. Kalaydjian, M-T Bieber and J-M Lombard, 1990: Use of a multifractal approach for multiphase flow in heterogeneous porous media: comparison with CT-scanning experiments, paper SPE 20475 presented at the 1990 SPE Annual Technical Conference and Exhibition, New Orleans, LA, September 23-26

- National Research Council, 1996: Rock Fracture and Fracture Flow: Contemporary Understanding and Applications, Committee on Fracture Characterization and Fluid Flow, National Academy Press, Washington, D. C. (in press).
- Novakowski, K. S., and P. A. Lapcevic, 1994: Field measurement of radial solute transport in fractured rock, *Water Resources Research*, 30, 37-44
- Novakowski, K. S., G. V. Evans, D. A. Lever and K. G. Raven, 1985: A field example of measuring hydrodynamic dispersion in a single fracture, *Water Resources Research*, 21(8), 1165-1174
- Overbey, W. K., L. E. Yost and A. B. Yost, 1988: Analysis of natural fractures observed by borehole video camera in a horizontal well, paper SPE 17760 presented at the 1988 SPE Gas Technology Symposium, Dallas, June 13-15
- Paillet, F. L. and K. Kapucu, 1989: Fracture characterization and fracture permeability estimates from geophysical logs in the Mirror Lake watershed, New Hampshire, Water Resources Investigations Report 89-4058, U. S. Geological Survey, Lakewood, CO
- Palmer, I. D. and D. P. Sparks, 1991; Measurement of induced fractures by downhole TV camera in Black Warrior Basin coalbeds, *Journal of Petroleum Technology*, 43(3), 270
- Peters, E. J. and N. Afzal, 1992: Characterization of heterogeneities in permeable media with computed tomography imaging, *Journal of Petroleum Science and Engineering*, 7, 283-296
- Piggott, A. R., J. Xiang, and D. Elsworth, 1991: Inversion of hydraulic and electrical data for determination of fracture aperture, in *Rock Mechanics as a Multidisciplinary Science*, pp. 1135
- Pollard, D. D., 1993: Fundamentals of rock fracture mechanics, personal notes, Stanford University, Stanford, CA
- Pyrak-Nolte, L. J., L. R. Myer, N. G. W. Cook and P. A. Witherspoon, 1987: Hydraulic and mechanical properties of natural fractures in low permeability rock, *Proceedings of the 6th International Congress of Rock Mechanics*, 225-231
- Ramirez, A. L., F. J. Deadrick and R. J. Lytle, 1982: Cross-borehole fracture mapping using electromagnetic geotomography, Report UCRL-53255, Lawrence Livermore Laboratory, University of California, Livermore, CA 94550
- Renshaw, C. E., 1995: On the relationship between mechanical and hydraulic aperture in rough-walled fractures, *J. Geophysical Research*, 100(B12), 24629-24636
- Raven, K. G., K. S. Novakowski and P.A. Lapcevic, 1988: Interpretation of field tests of a single fracture using a transient solute storage model, *Water Resources Research*, 24(12), 2019-2032
- Silliman, S. and R. Robinson, 1989: Identifying fracture interconnections between boreholes using natural temperature profiling: I. Conceptual basis, *Groundwater*, 27(3), 393
- Tollner, E. W. and B. P. Verma, 1989: X-ray CT for quantifying water content at points within a soil body, *Transactions ASAE*, 32, 901-905
- Tsang, Y. W., 1992: Usage of "equivalent apertures" for rock fractures as derived from hydraulic and tracer tests, *Water Resources Research*, 28(5), 1451-1455
- Vanmarcke, E., 1983: *Random fields: Analysis and Synthesis*, MIT Press, Cambridge, MA
- Vinegar, H. J. and S. L. Wellington, 1991: Tomographic imaging of three-phase flow experiments, *Review of Scientific Instruments*, 58, 96-107
- Witherspoon, P. A., J. S. Y. Wang, K. Iwai and J. E. Gale, 1980: Validity of cubic law for fluid flow in a deformable rock fracture, *Water Resources Research*, 16(6), 1016-1024
- Withjack, E. M., 1988: Computed tomography for rock property determination and fluid flow visualization, *SPE Formation Evaluation*, December, 696-704
- Wellington, S. L. and H. J. Vinegar, 1987: X-ray Computerized Tomography, *Journal of Petroleum Technology*, 885-898
- Zimmerman, R. W., S. Kumar and G. S. Bodvarsson, 1991: Lubrication theory analysis of the permeability of rough-walled fractures, *Intl. J. Rock Mech. Min. Sci. Geomech. Abstr.*, 28, 325-331

Figure 2.1 Schematic of CAT-Scanner operation

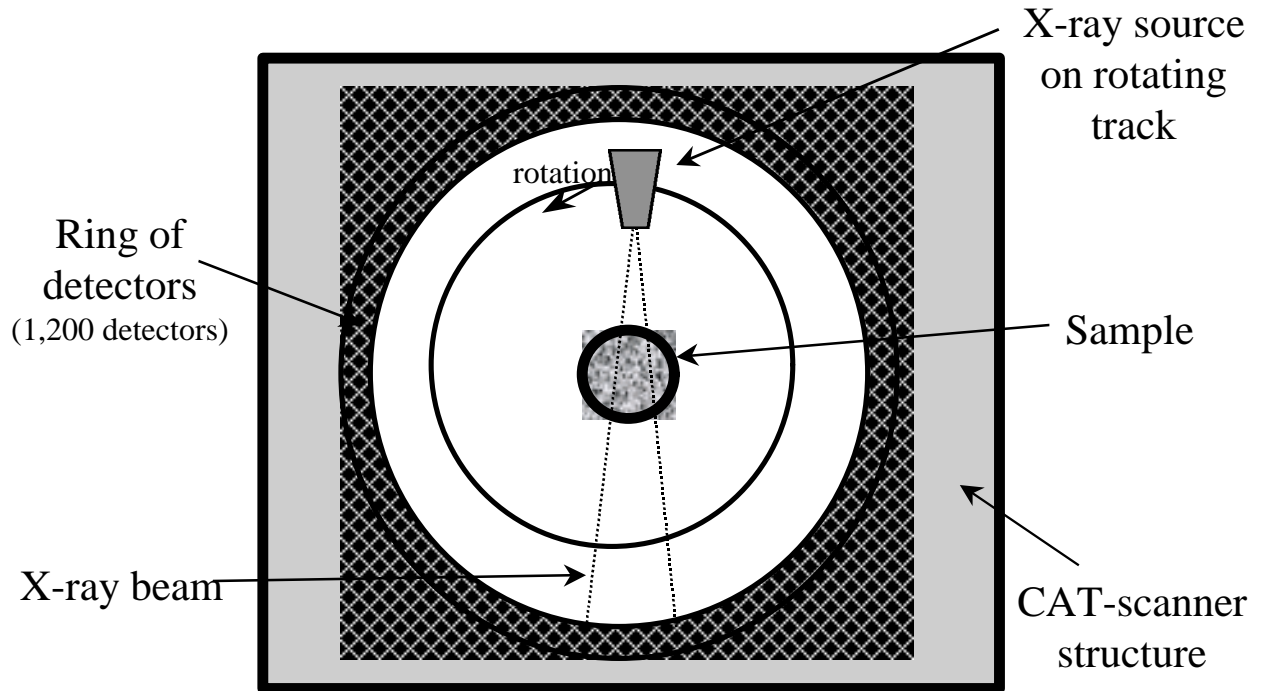


Figure 2.2 Greyscale representation of CT numbers

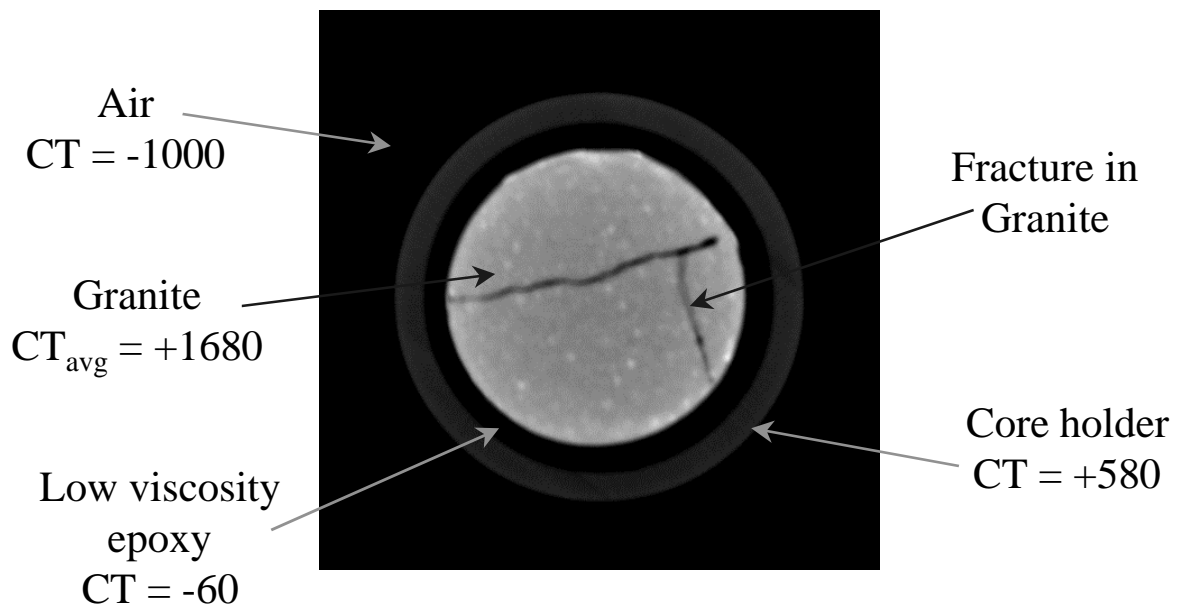


Figure 2.3 Construction of aperture calibration standard

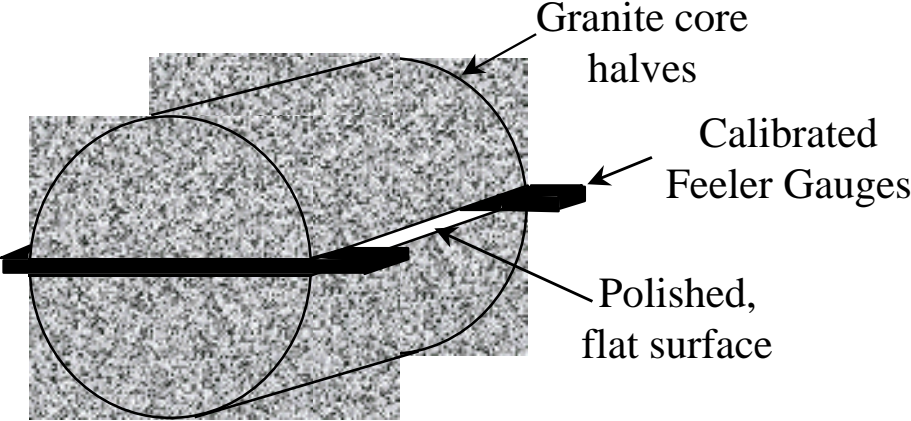


Figure 2.4 Typical section through fractured rock

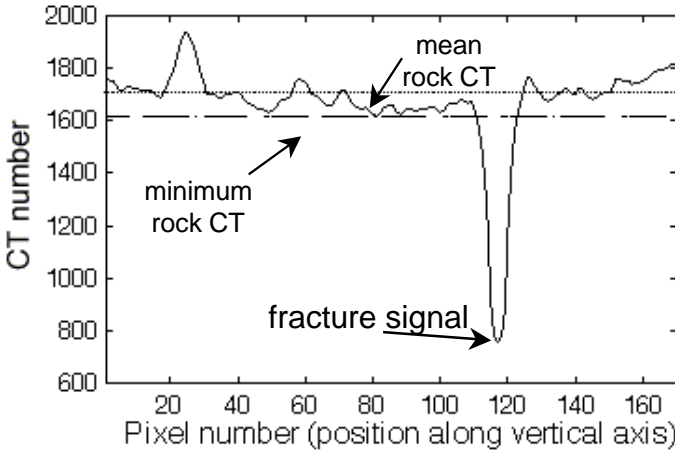


Figure 2.5 Integration of fracture aperture

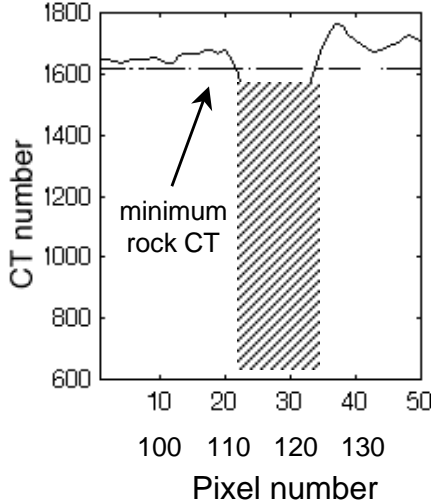


Figure 2.6 Calibration curve for fracture aperture in granite vs. integrated CT signal; (a) all apertures sampled; (b) small apertures only; and (c) logarithmic plot.

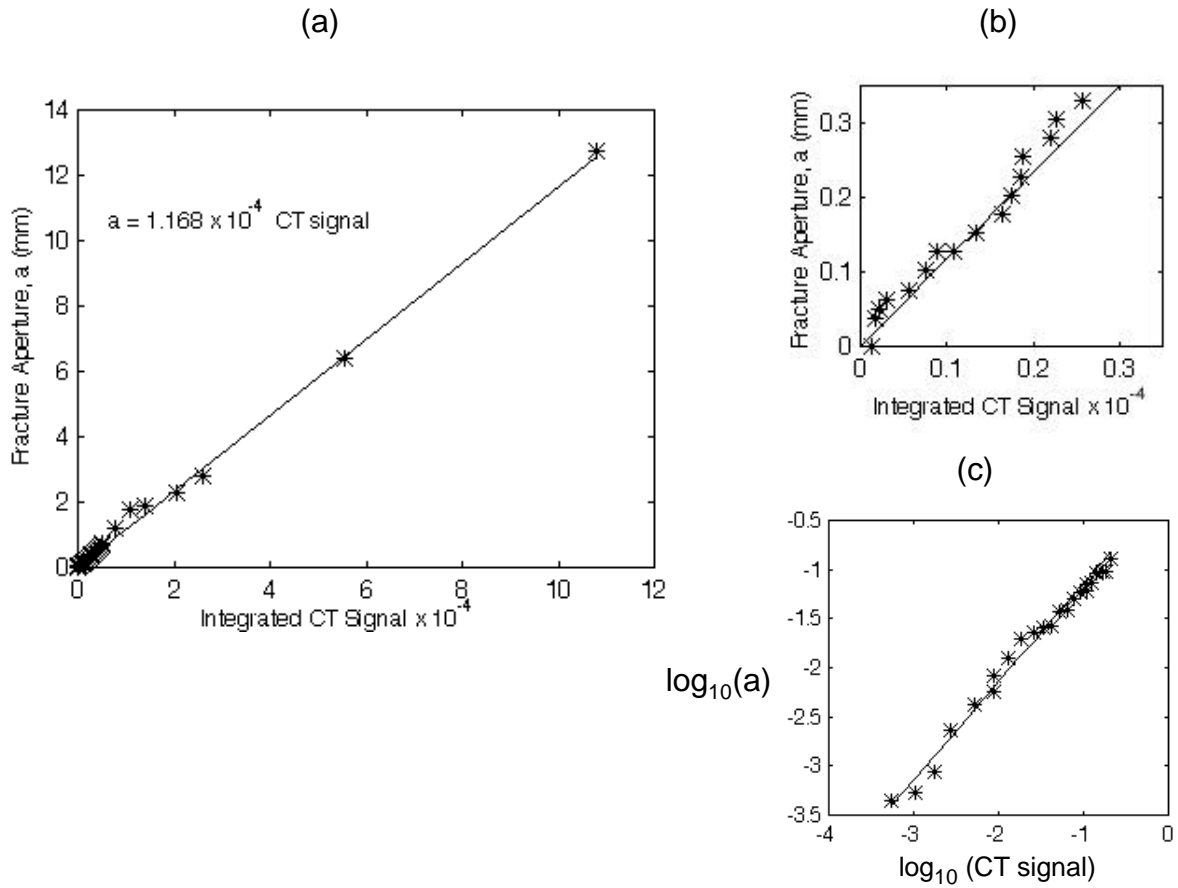


Figure 2.7 Calibration curve for fracture aperture in sandstone

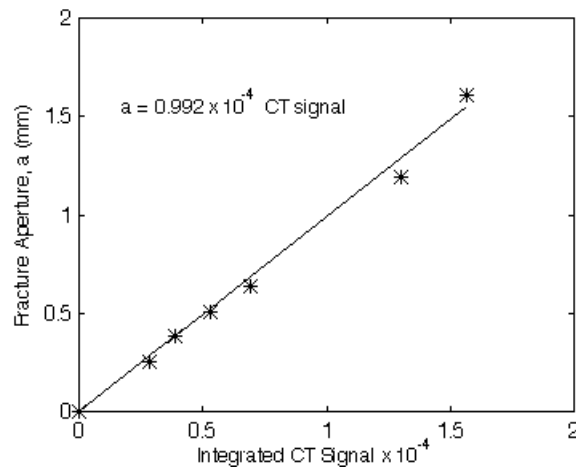


Figure 2.8 Image of granite core



Figure 2.9 Close-up of fracture in granite core



Figure 2.10 Image of fractured sandstone core

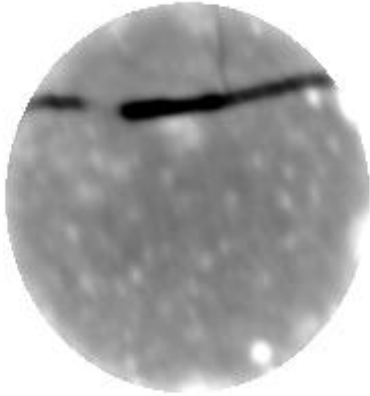


Figure 2.11 Close-up of fracture in sandstone core

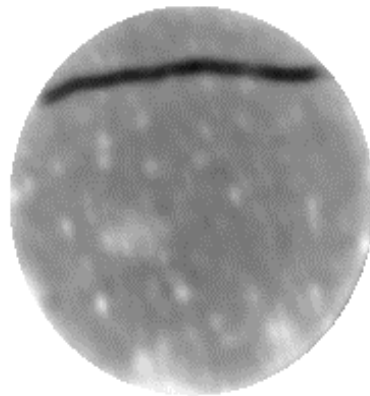


Figure 2.12 Representative scans of Core C
(position indicated above image)

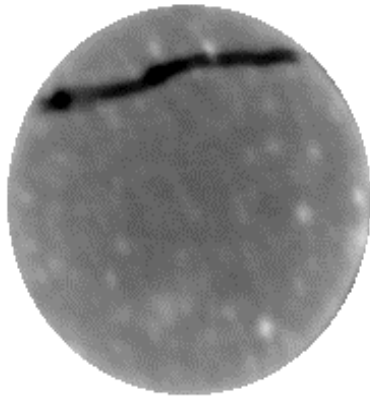
6 mm



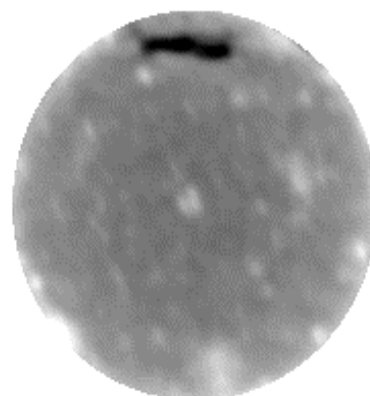
36 mm



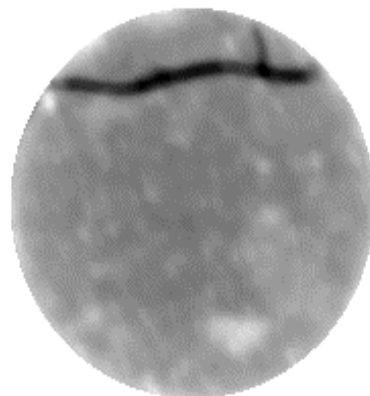
50 mm



108 mm



140 mm



161 mm

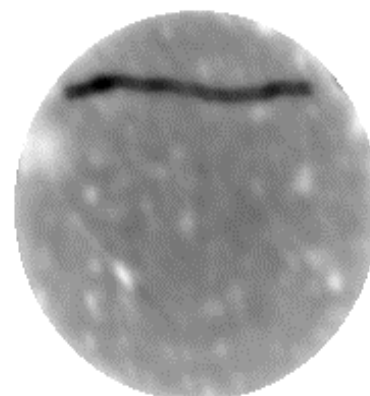
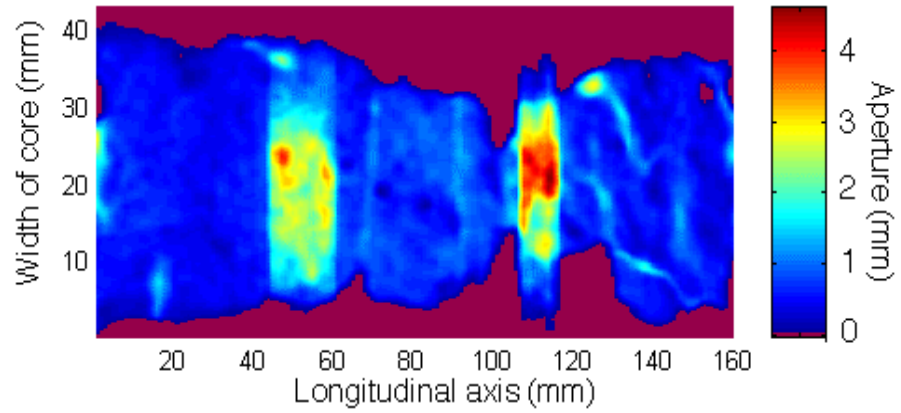
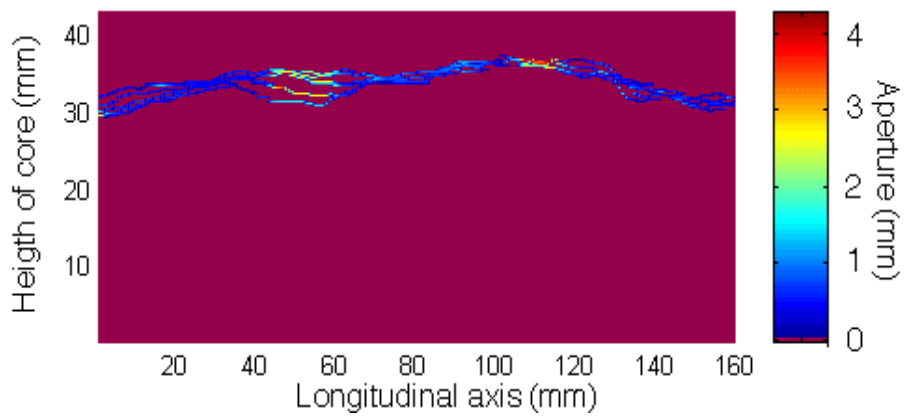


Figure 2.13 Fracture aperture distribution of core C:
(a) top view, (b) side view and (c) perspective

(a)



(b)



(c)

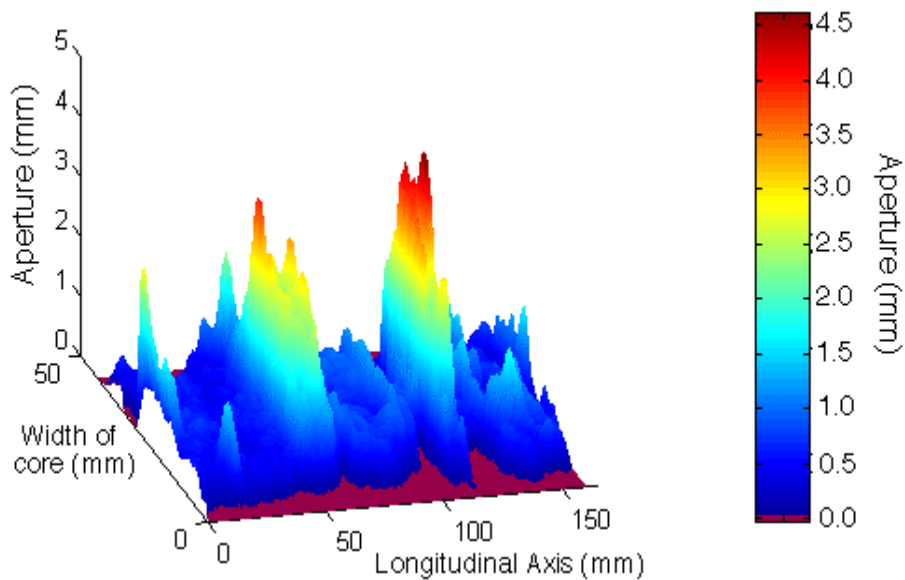


Figure 2.14 Selected CAT-scans of fracture aperture from core D

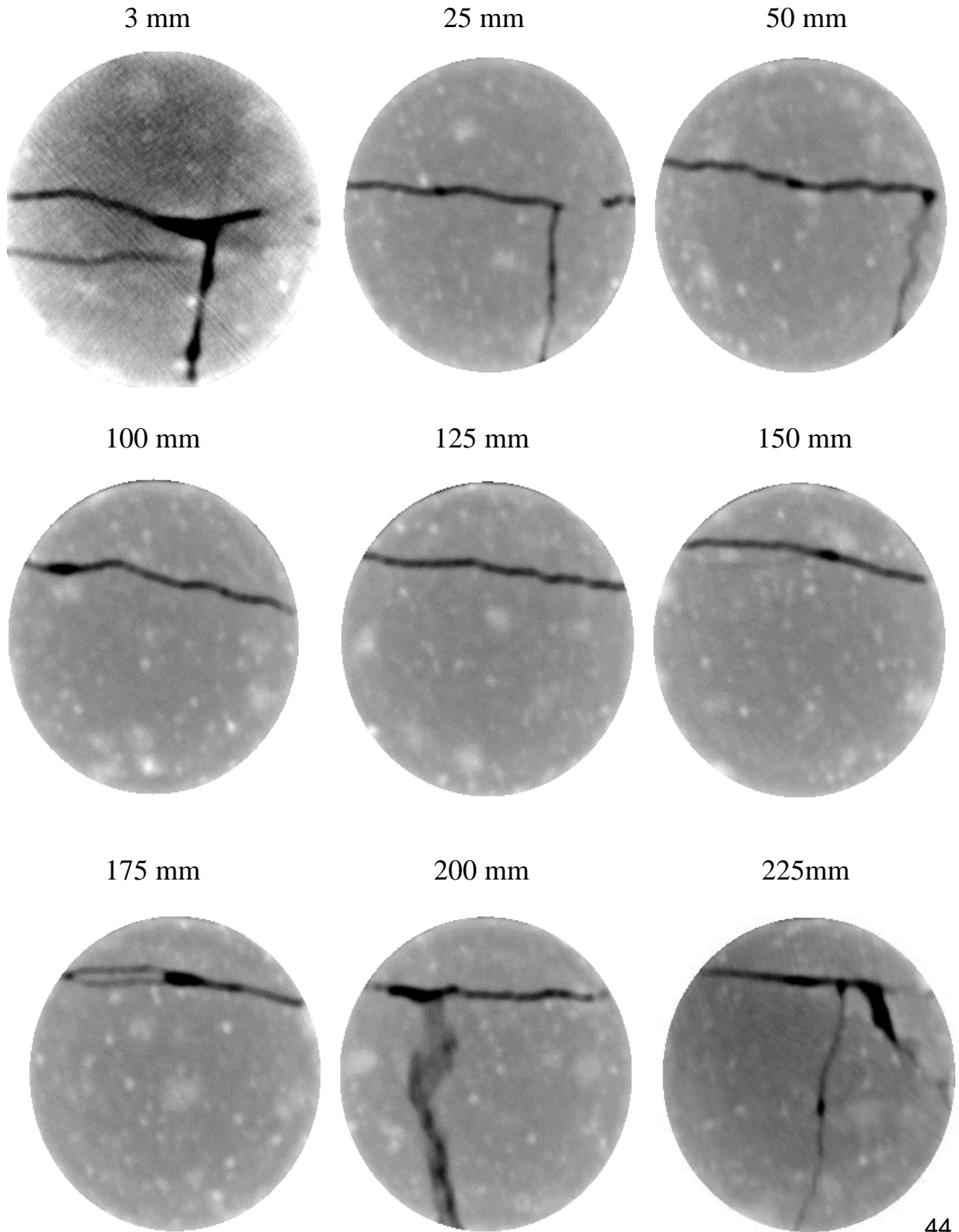


Figure 2.15 (a) Top view of fracture aperture distribution for core D; (b) Zoom-in of detail in middle section, from 30 to 200 mm.

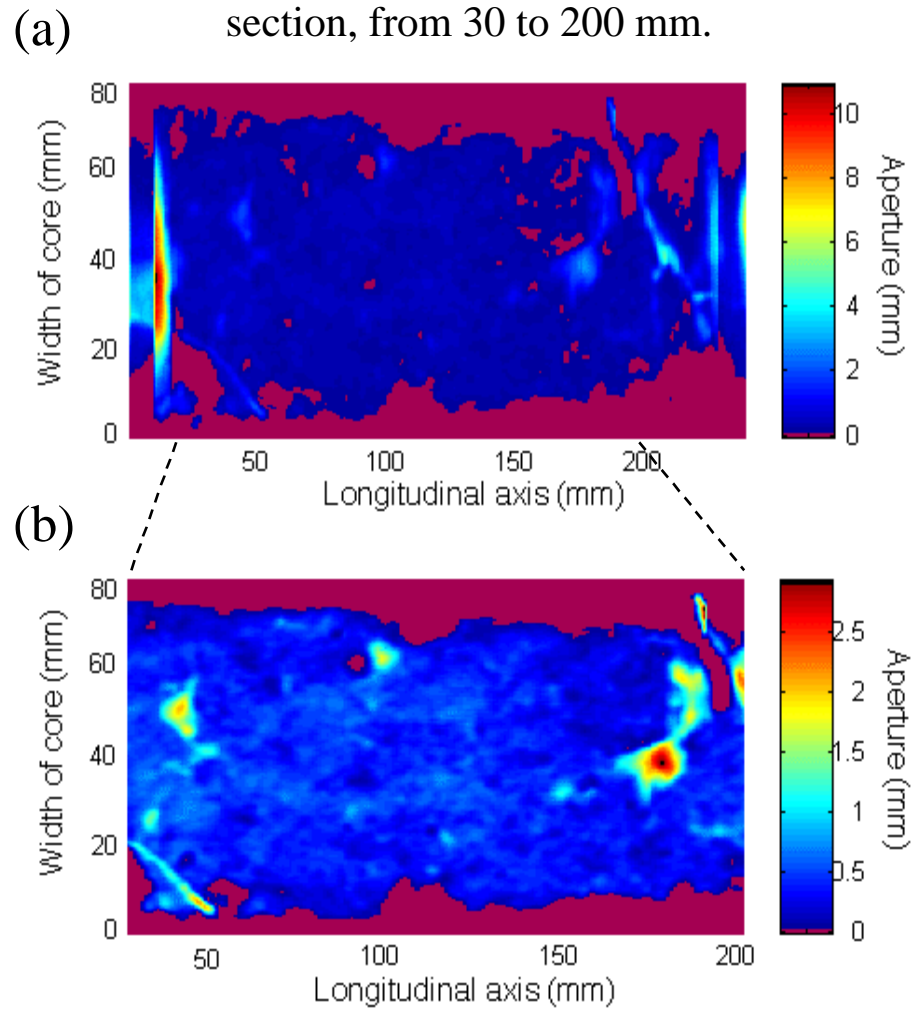


Figure 2.16 Side view of fracture aperture distribution for core D

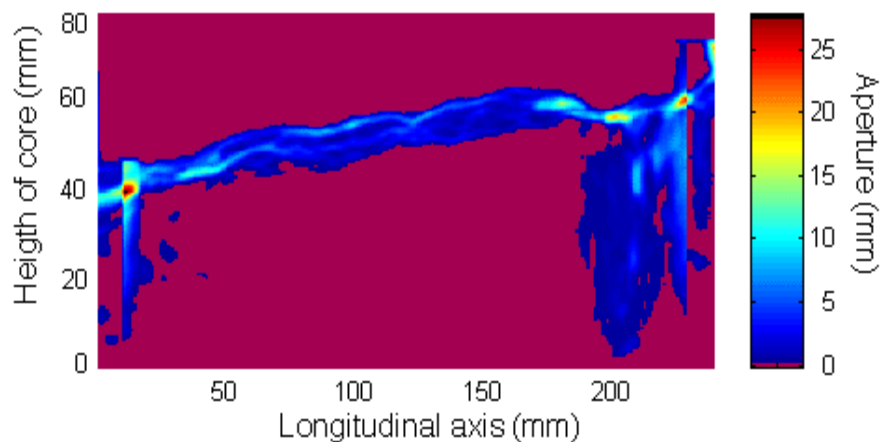


Figure 2.17 Side view of unfractured red sandstone, with longitudinal layers



Figure 2.18 Close-up of layers in red sandstone



Figure 2.14 Selected CAT-scans of fracture aperture from core D

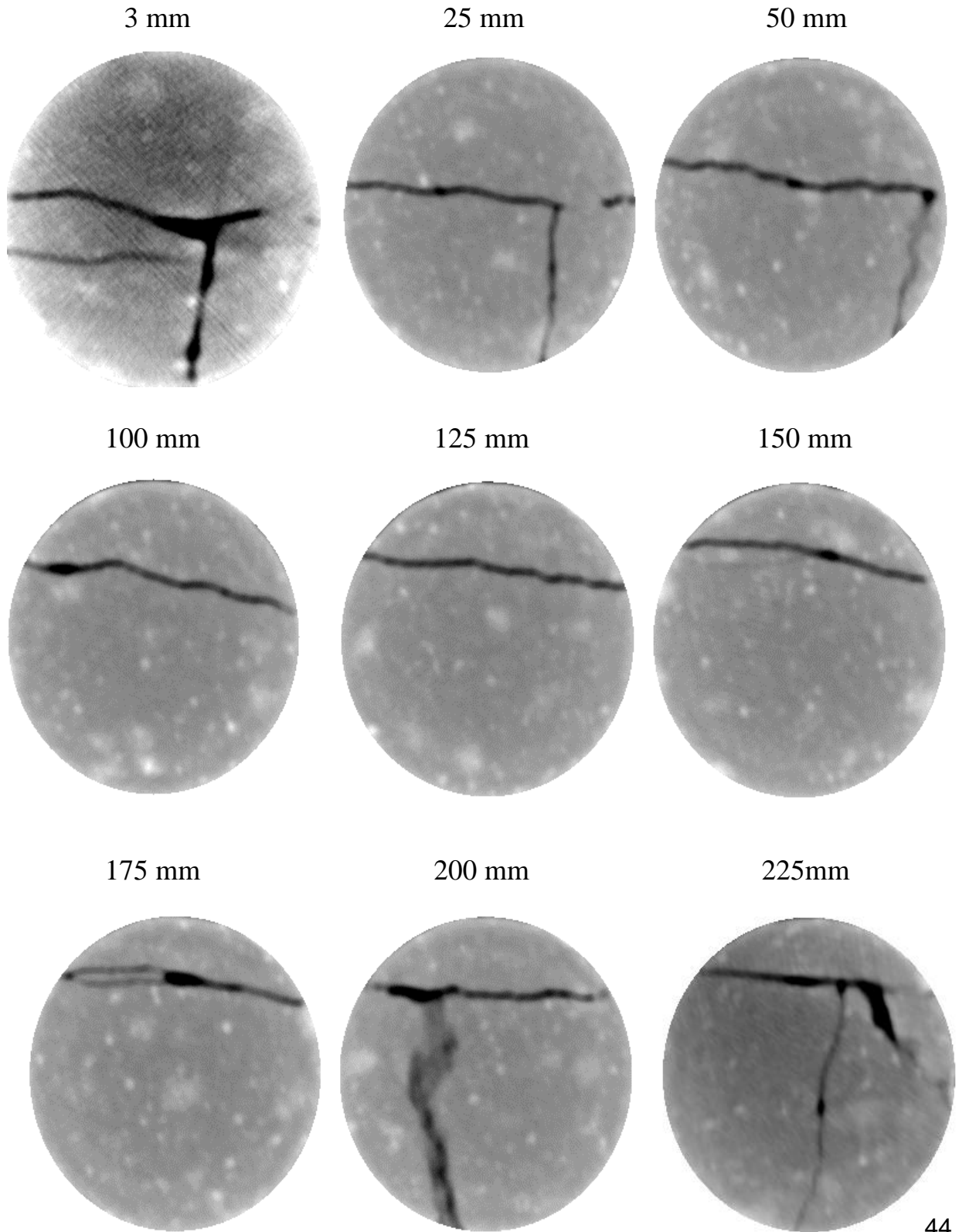


Figure 2.15 (a) Top view of fracture aperture distribution for core D; (b) Zoom-in of detail in middle section, from 30 to 200 mm.

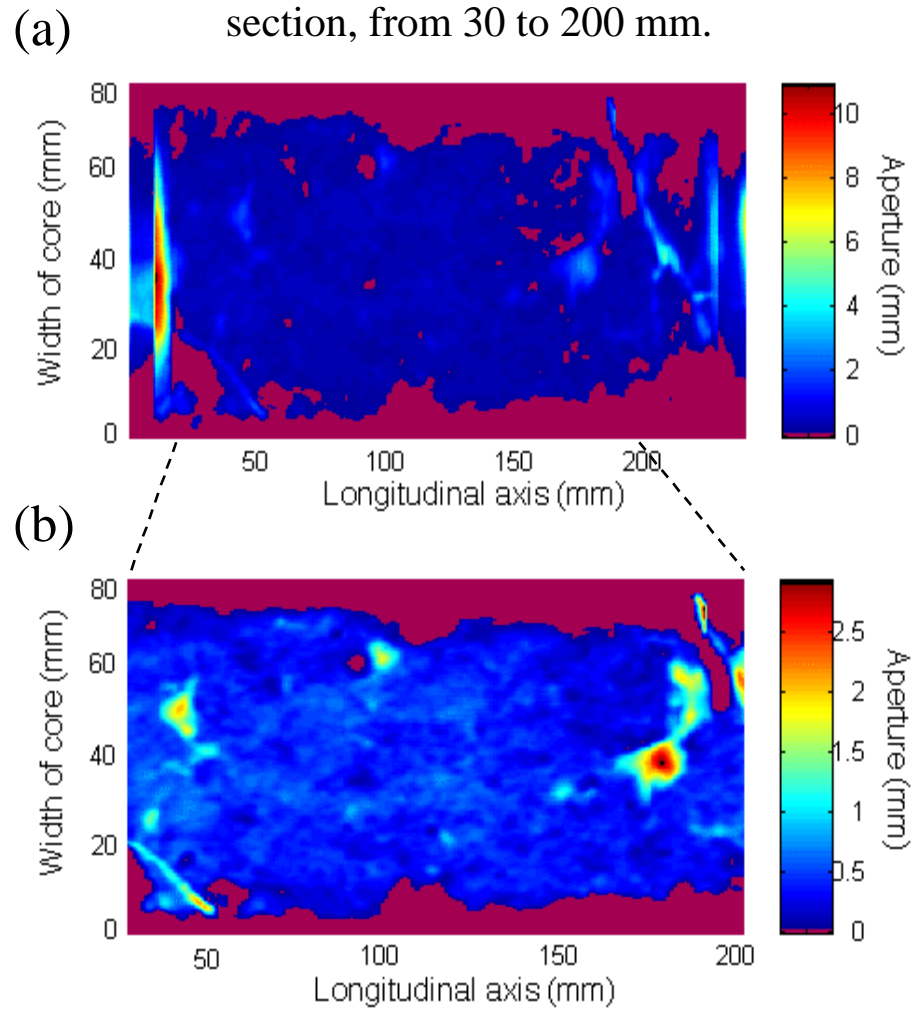


Figure 2.16 Side view of fracture aperture distribution for core D

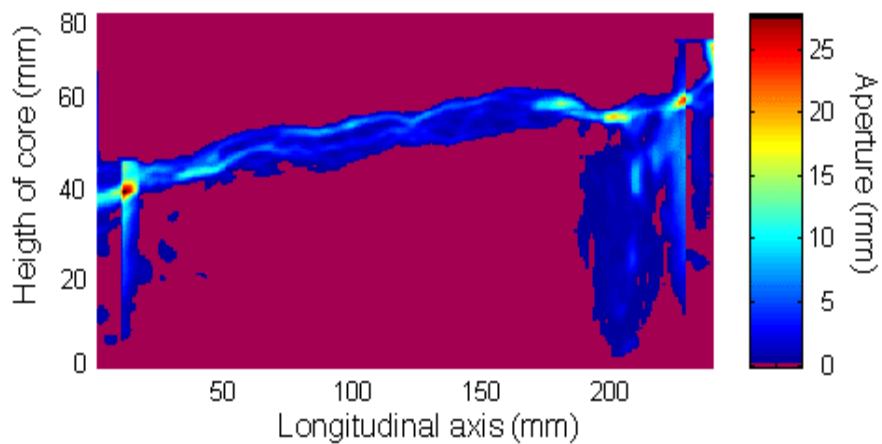


Figure 2.21 Histogram of the fracture aperture distribution for core C.

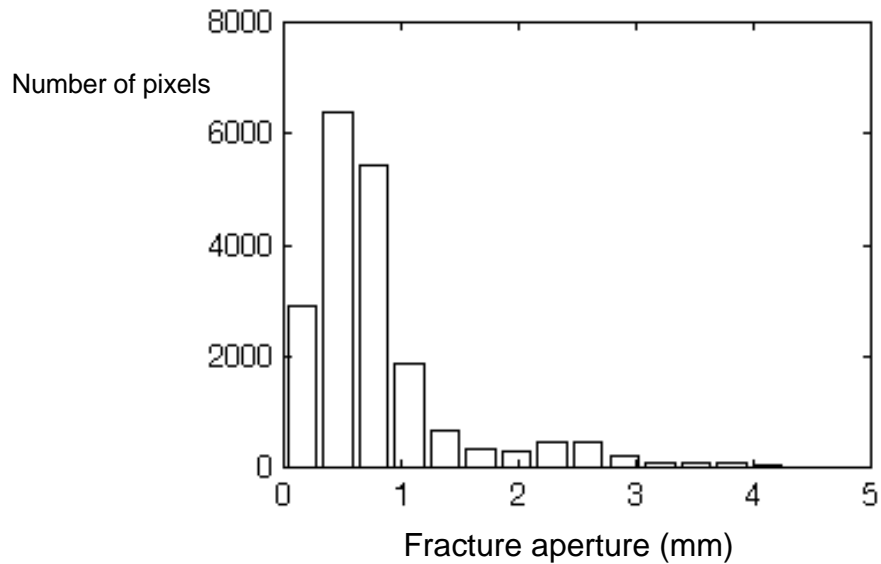


Figure 2.22 Histogram of the fracture aperture distribution for core D.

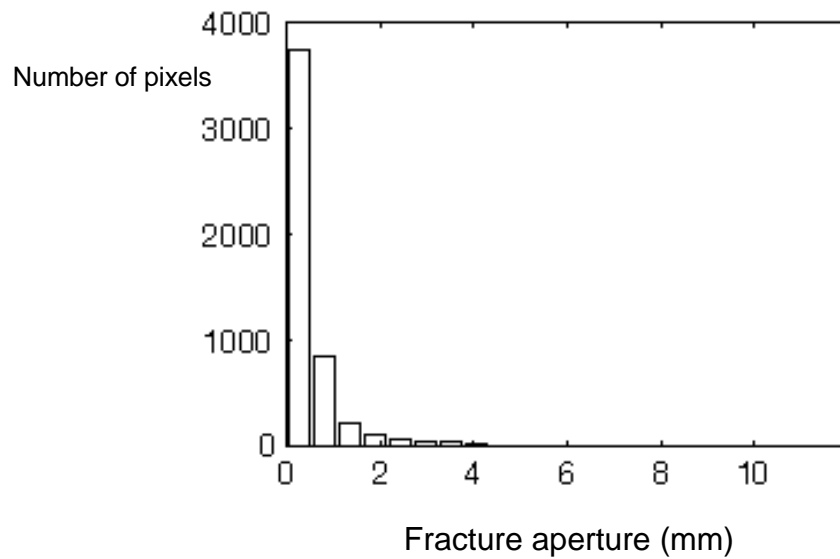


Figure 2.23 Histogram of the fracture aperture distribution for core F.

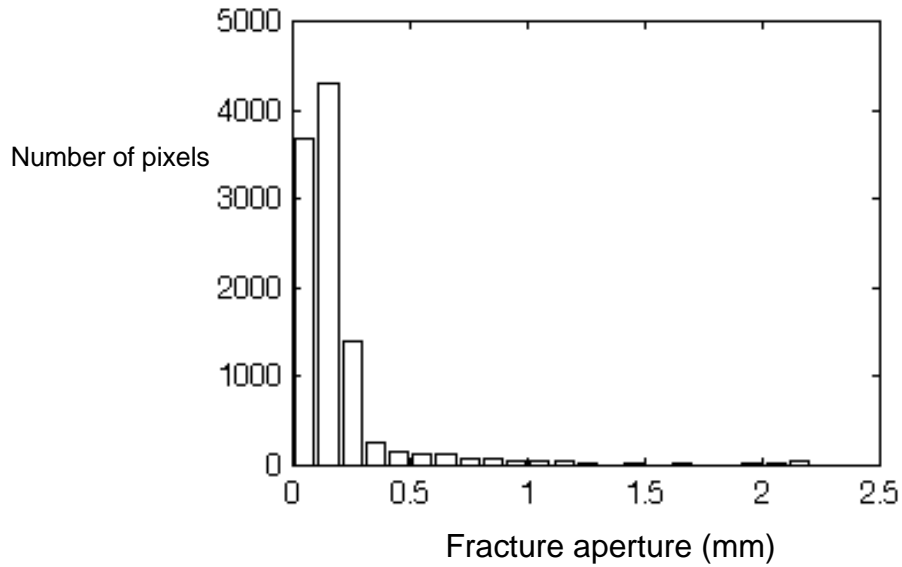


Figure 2.24 Histogram of the fracture aperture distribution for the small aperture region of core D.

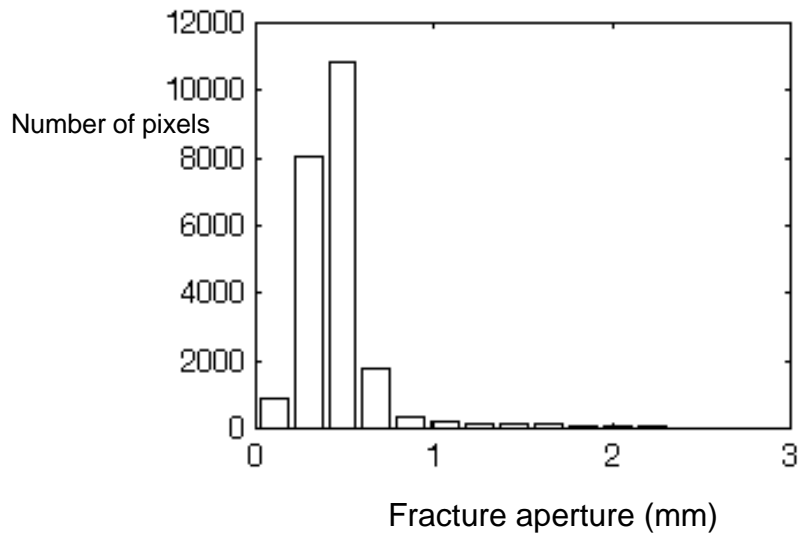


Figure 2.25 Close-up of the small aperture region of core C.

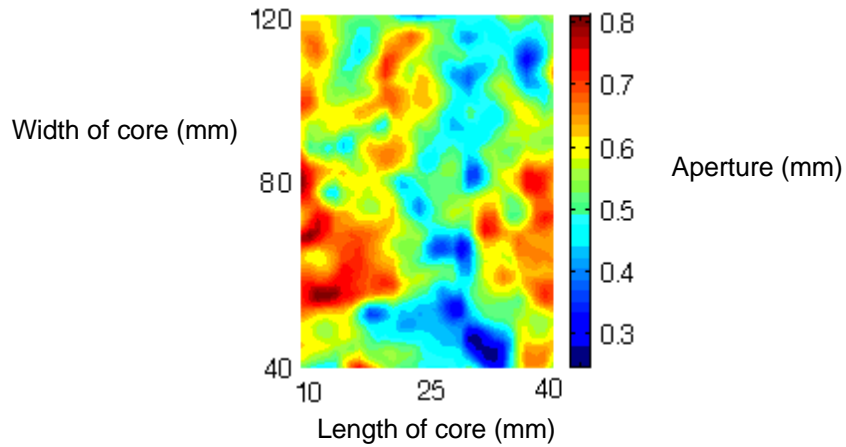


Figure 2.26 Close-up of the small aperture region of core D.

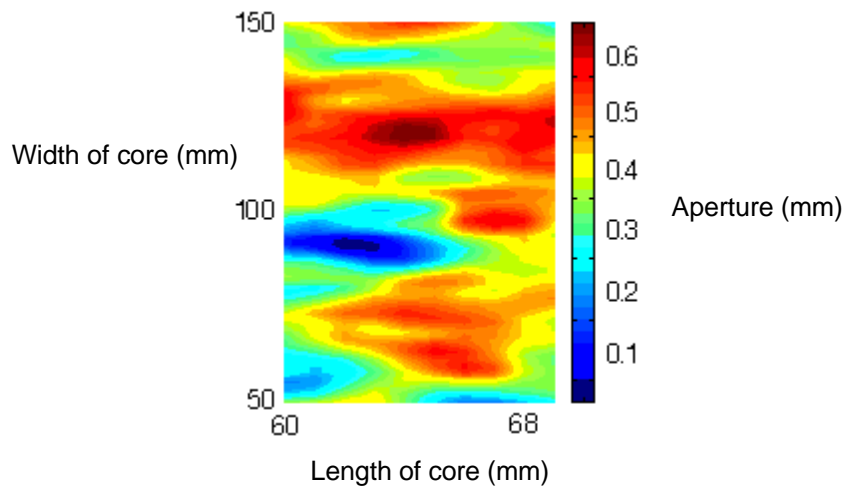
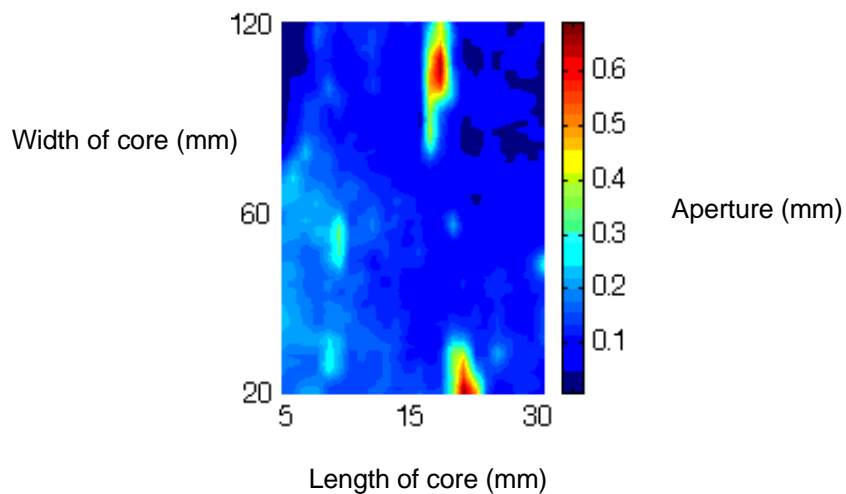


Figure 2.27 Close-up of the small aperture region of core F.



Chapter 3

Single Phase Flow and Transport in Fractured Media

3.1 Introduction

The transport of a contaminant dissolved in water is governed by advection, dispersion, sorption and biogeochemical transformation. To evaluate the risk of exposure to contaminated ground water or to model its remediation, it is important to understand the relative magnitude of these processes. For porous media it is common to consider dispersion as negligible, specially for longer times. However, in fractured media, dispersion may play a significant role due to channeling (Abelin, Birgersson *et al.*, 1994; Haldeman, Chuang *et al.*, 1991; Johns and Roberts, 1991; Moreno and Neretnieks, 1993; Tsang, Tsang *et al.*, 1991), which results in much earlier breakthrough of the contaminant at monitoring wells than would be expected considering a porous medium of "equivalent" hydraulic conductivity, where equivalent is a bulk averaged conductivity. Even in unfractured porous media, large heterogeneities (two or more orders of magnitude) in conductivity result in considerable flow channeling and earlier solute breakthrough (Moreno and Tsang, 1994) . For this study, we considered only non-sorbing, inert solutes, to isolate the effects of flow advection and dispersion in a natural fracture.

For heterogeneous porous media, fluid flow and solute transport has been modeled using stochastic analysis (Gutjahr *et al.*, 1978; Gelhar and Axness, 1983; Gelhar, 1987; Gelhar, 1993; Dagan, 1982, 1984 and 1986). A key element of these models is that the variations in hydraulic conductivity are relatively small, with a variance, σ^2 , less than two, such that the resulting equations may be linearized, neglecting higher order terms, and a solution may be obtained. Using this small perturbation analysis, and assuming the fracture aperture is lognormally distributed and correlated in space, the effective transmissivity and macrodispersivity of the porous medium can be estimated.

The results of the stochastic models have been used with some success to predict the breakthrough of solutes at field sites (Dykaar and Kitanidis, 1992; Gelhar, 1986, 1987; Graham and McLaughlin, 1991; LeBlanc *et al.*, 1991; Rehfeldt and Gelhar, 1992; Bellin, Salandin *et al.*, 1992; Kapoor and Gelhar, 1994) . This approach is applied here to the *a priori* estimation of the transport parameters for single phase transport in a single variable aperture fracture plane, assuming flow in fractures can be described by the Boussinesq relation or "cubic" law (Witherspoon *et al.*, 1980) and that the fracture aperture distribution can be obtained.

A naturally fractured granite core was scanned using a CT scanner, to generate an image of the aperture distribution in the single fracture plane (Chapter 3). Geostatistical analysis of this information yielded the power spectrum of the normalized log aperture and the covariance function for the single fracture plane. The experimental semivariogram was fitted to an exponential semivariogram using kriging, to obtain the variance and the correlation scale of the log aperture distribution. The geostatistical information is applied here to the small perturbation analysis results to predict the effective transmissivity and dispersivity.

Single phase tracer experiments were conducted to determine the effective transmissivity and dispersivity of the single variable aperture fracture, to compare against the estimated parameters. Transport of a solute in the fracture was imaged using CT-scanning. The results were also compared to the breakthrough curve generated from a numerical transport model based on the fracture aperture distribution.

3.2 Theory

The governing equation for flow across the single variable aperture fracture plane is:

$$\frac{\mathcal{I}Q_i}{\mathcal{I}x_i} = \frac{\mathcal{I}}{\mathcal{I}x_i} \left(T \frac{\mathcal{I}f}{\mathcal{I}x_i} \right) = 0, \quad i = 1,2 \quad (3.1)$$

where Q_i is the discharge in the i th direction; $T = T(x_1, x_2)$ is the transmissivity of the fracture, which is related to the fracture aperture by the cubic law, assuming laminar flow between parallel plates:

$$T = \frac{ga^3}{12\mathbf{n}} \quad (3.2)$$

$a = a(x_1, x_2)$ is the fracture aperture; x_1, x_2 are the coordinates of the fracture plane; f is the potentiometric head; g is the gravitational acceleration; and \mathbf{n} is the kinematic viscosity.

We assume that the fracture aperture distribution is lognormally distributed, which implies that the aperture must always be positive. Given the large variability in aperture, as measured by its coefficient of variation and since $a \geq 0$, it is more convenient and relevant to use $Y = \ln a$ for the analysis, following Gelhar (1987). For the small perturbation analysis (variance less than two), we use a first-order approximation to describe the variability in the fracture aperture, discharge and head potential:

$$Y = \bar{Y} + \hat{Y}, \quad E[Y] = \bar{Y} = \ln a_g, \quad E[\hat{Y}] = 0 \quad (3.3)$$

$$f = \bar{f} + \hat{f}, \quad E[f] = \bar{f}, \quad E[\hat{f}] = 0 \quad (3.4)$$

$$Q_i = \bar{Q}_i + \hat{Q}_i, \quad E[Q_i] = \bar{Q}_i, \quad E[\hat{Q}_i] = 0 \quad (3.5)$$

where the overbar denotes mean value and the hatted variables are the random fluctuations about the means, which have an expected value of zero in all cases. By definition, the mean of Y is the logarithm of the geometric mean of the aperture, a_g .

Assuming constant flow rate, the stochastic differential equation is solved (Gutjahr *et al.*, 1978) considering these small perturbations in the log aperture which translate into small perturbations of the transmissivity. The equation for the head perturbation is

$$\frac{\overline{\hat{f}}}{\overline{x_i^2}} = 3J_i \frac{\overline{\hat{Y}}}{\overline{x_i}}; \quad J_i = -\frac{\overline{\hat{f}}}{\overline{x_i}} \quad (3.6)$$

where the factor of three results from the cubic law assumption. J_i is the mean hydraulic gradient in the i th direction. The solution to equation 3.1, assuming an isotropic fracture aperture distribution, is given by

$$\overline{Q}_i = T_g J_i \quad (3.7)$$

The larger apertures are important in defining the large channels through the fracture plane (given that $T \propto a^3$), but since the geometric mean is always less than or equal to the arithmetic mean, the smaller fracture apertures play an important role in reducing the effective transmissivity of the fracture.

To obtain the effective macrodispersivity, the governing equation for transport of a conservative tracer by a constant density liquid in a two-dimensional variable aperture fracture, is (Gelhar, 1987):

$$a \frac{\overline{c}}{\overline{t}} + Q_i \frac{\overline{c}}{\overline{x_i}} - D_{ij} \frac{\overline{c^2}}{\overline{x_i} \overline{x_j}} = 0; \quad i = 1, 2 \quad (3.8)$$

where D_{ij} is the local fracture dispersion coefficient, assumed constant. The random aperture variations will result in flow variations which in turn result in a randomly perturbed concentration field, described by:

$$c = \bar{c} + \hat{c}, \quad E[c] = \bar{c}, \quad E[\hat{c}] = 0 \quad (3.9)$$

An approximate solution of the macroscopic longitudinal dispersivity in the fracture has been obtained by assuming that the local dispersivity is small compared to the correlation length of the fracture aperture variations, λ_Y (Gelhar and Axness, 1983). In addition, if the covariance model used to describe the variation in transmissivity is isotropic and exponential, then the longitudinal macrodispersivity is given by (Gelhar, 1987)

$$A_{ll} = [3 + G(\mathbf{s}_Y^2)] \mathbf{s}_Y^2 \mathbf{I}_Y \quad (3.10)$$

where A_{ll} is the longitudinal macrodispersivity, \mathbf{s}_Y^2 is the variance in the fracture aperture variations and G is a polynomial fit to the numerical evaluation of the integral of the Fourier transform of the autocovariance function of the log aperture, given by (Gelhar, 1987):

$$G(\mathbf{s}_Y^2) \approx 1 + 0.205\mathbf{s}_Y^2 + 0.16\mathbf{s}_Y^4 + 0.045\mathbf{s}_Y^6 + 0.115\mathbf{s}_Y^8, \quad \text{for } 0 < \mathbf{s}_Y^2 < 5 \quad (3.11)$$

Equation 3.10 is derived considering that a sufficient distance has been traversed (more than 10 correlation lengths), such that the dispersivity is fully developed for the scale of interest. At earlier times, when the dispersion is still developing, the macrodispersivity is expected to be smaller (Gelhar and Axness, 1983) and increasing towards the asymptotic solution given by equation 3.10.

These results can then be applied to obtaining the effective transport parameters, transmissivity and dispersivity, for a variable aperture fracture, if the geostatistics of the aperture distribution can be calculated. Gelhar (1993) presents an extension of this work to fracture networks. Alternatively, the geometric mean of the fracture aperture distribution, a_g , can be obtained from field hydraulic tests, and the arithmetic mean from conservative tracer tests. The two are related by:

$$\frac{\bar{a}}{a_g} = \exp(\mathbf{s}_Y^2 / 2) \quad (3.12)$$

providing information on all the relevant geostatistics to calculate the effective transmissivity and macrodispersivity . These results can then be applied in other sites where aperture distributions are determined from outcrops or borehole imaging by a variety of geophysical techniques. To evaluate the applicability of the theory, tracer tests were conducted on a fractured core whose aperture distribution was obtained via CT scanning.

3.3 Experimental Determination of Flow and Transport Parameters

3.3.1 Analysis of Breakthrough Curves

Single phase tracer experiments were conducted to determine the pressure drop across a fractured granite core (Core C, characterized in Chapter 3) and the breakthrough curve of a non-sorbing iodide tracer in artificial ground water. Figure 3.1 presents the fracture aperture and Figure 3.2 the logarithm of the corresponding permeability, k , using :

$$k = \frac{a^2}{12} \quad (3.13)$$

to estimate the permeability field. The variations in aperture are significantly magnified, producing some clear flow channels in the permeability field. The statistics of the fracture aperture distribution are given in Table 3.1. The fracture aperture distribution is nearly log-normal, but with a slight skew toward smaller apertures, as seen in Figure 3.3.

Table 3.1 Fracture Aperture Distribution Statistics

SAMPLE	Mechanical Aperture a_m (mm)	Standard Deviation s_m (mm)	Hydraulic Aperture a_h (mm)	Standard Deviation s_h (mm)
Granite Core C	0.825	0.683	0.586	0.864

The naturally fractured granite core was placed in a cylindrical plastic holder, attempting to preserve the original fracture aperture and location of the two fracture planes. To avoid flow short-circuiting the fracture, the outside of the core was sealed using an epoxy sealant, except for the inlet and outlet faces. Separate pumps were used for the tracer and the groundwater flush, with a valve arrangement such that both pumps would be operating continuously when switching from one solution to the other, to maintain essentially constant flow. Dead volume outside of the core, the core holder end plates and the tubing leading into and out of the core was minimized. The external dead volume is 0.69 mL, out of a total flow volume of 4.07 mL. The fracture flow volume, integrated from the fracture aperture distribution, is 2.44 mL, including the feeder into and out of the core. Within the core, the fracture flow volume is only 1.15 mL. The average cross-sectional area within the core is 26.7 mm², with local values ranging from a minimum of 7.42 mm² to a maximum of 78.4 mm².

A 10% by weight solution of potassium iodide was used for the tracer analysis. This solution provides a distinct CT signal (compared to pure water), for imaging the flow of the tracer within the core. To measure the breakthrough curve, a Wescan Conductivity Detector was used continuously, acquiring the information into a PC using LabView 3.0. The breakthrough curves were then analyzed by plotting $1 - t_d / \sqrt{t_d}$ against $\text{erf}^{-1}(1 - 2c)$, where t_d is dimensionless time (in pore volumes) and c is the normalized concentration. The slope is $2\sqrt{Pe}$, where Pe is the Peclet number, defined as $Pe = VL^2/D_e$, where D_e is the effective dispersion coefficient, V is the flow rate and L is the length of the core (0.166 m). Five different flow rates were used, from 1.53×10^{-5} m/s to 4.74×10^{-4} m/s, with three repetitions at each flow rate. The dispersion coefficients at several flow rates yielded the experimental dispersivity.

A typical breakthrough curve is shown in Figure 3.4. The breakthrough time is consistent from run to run, for the same flow rate, with small variations in the main breakthrough curves. Tailing was consistently long, both when the step input of tracer was applied, and during the groundwater flushing of the core, during which the inverse of the breakthrough curve was measured. The tails varied among runs, resulting in some uncertainty associated with the calculation of the dispersion coefficient. This was more pronounced for the larger flow rates. A possible explanation is that the flow may take different smaller channels during the various runs, storing variable amounts of solute in the immobile regions, which are contributing most to the tailing end of the breakthrough curve. This is analogous to modeling stochastic flow, where each realization of the aperture varies; in this case, the small differences in initial and boundary conditions may create a small instability that directs the flow through different small channels. Figure 3.5 presents a typical fit to obtain the Peclet number and the dispersion coefficient from the

breakthrough curve. The fit to a straight line is good in the central region, with some deviations at the leading and trailing ends of the breakthrough curve, perhaps due to the deviation from the assumed log normal distribution of aperture.

The dispersivity for the granite core with a natural fracture was then determined by plotting the flow rate against dispersion (Figure 3.6), assuming a linear relation. The correlation is quite good, considering the mean values of the dispersion coefficient. The dispersivity is estimated to be 0.238 m, with 95% confidence intervals of ± 0.020 m. In Figure 3.7 we evaluate the validity of the linear relation between dispersion and flow velocity. From the logarithmic plot, dispersion varies proportionally to velocity to a power of 1.04 (± 0.06), which does not differ significantly from the expected linear relation. The effective dispersion coefficient at the lowest flow rate (1.53×10^{-5} m/s) is 3.6×10^{-6} m²/s, which is still several orders of magnitude larger than the molecular diffusion coefficient of potassium iodide (which is on the order of 10^{-9} m²/s). Thus, molecular diffusivity is probably not very significant in the flow direction.

The pressure drop across the core was measured using calibrated 1 psi (6893 Pa) pressure transducers (Celesco), as well as the actual flow rate. The effective transmissivity was calculated, using Equation 3.7, to be 2.07×10^{-4} ($\pm 0.31 \times 10^{-4}$) m²s⁻¹ with 95% confidence interval.

3.3.2 Imaging of Tracer Flow in Fractured Media

At sufficiently low flow rates, the transport of the non-sorbing iodide tracer through the fracture can be imaged using CT scanning. Each scan requires approximately 50 sec of cooling time for the CT scanner. Although the fracture aperture distribution was imaged with 166 scans for Core C, it would not be possible to do the same for the moving

tracer. At an equivalent flow rate of about 0.25 pore volumes per hour, 16 scans spaced 10 mm apart were acquired every hour, during approximately 15 minutes. Nine such studies were conducted, each comprising 16 scans. The first study was done with no tracer in the core, serving as the reference for the other studies.

To determine the concentration of tracer, the reference study is subtracted from the subsequent studies, and then it is normalized by considering that the tracer had essentially reached all the pore space after 7.5 pore volumes (PV), when the outlet concentration reached its maximum value, based on the breakthrough curve and reference calibration. The individual scans were then reconstructed to provide a two dimensional representation of the tracer movement on the fracture plane, as shown in Figure 3.8. As explained in Chapter 2, flow is excluded from the large channels along the edges of the fracture, since these were sealed with a low viscosity epoxy. Thus, the longitudinal boundaries of the fracture plane are quite irregular.

After 0.22 PV have been injected the tracer front is already exhibiting preference for some channels. This becomes more noticeable at 0.49 PV, at which time breakthrough is occurring at the outlet. By 0.80 PV, most of the major flow channels have been contaminated by the tracer, with very high concentrations. However, it takes many more pore volumes to reach complete tracer saturation in the very low aperture regions. Although there appears to be some small longitudinal dispersion along the streamtubes, especially at low pore volumes, there is very little evidence of transverse dispersion.

3.4 Modeling of Single Phase Flow and Transport in Fractures

3.4.1 Stochastic analysis

The CT imaged fracture aperture field was transformed using the cubic law relation to a transmissivity field. For the analysis, the log transmissivity was normalized by removing the mean. An exponential function was used to fit a theoretical semivariogram to the experimental semivariogram:

$$\mathbf{g} = \sigma_Y^2 \left(1 - \exp\left(-\frac{h}{\lambda_Y}\right)\right) \quad (3.13)$$

The parameters σ_Y and λ_Y were optimized by using kriging to calculate the orthonormal residuals and then minimizing the residuals. The resulting variance is 2.4 and the correlation length scale around 6 mm. The variability in Y is thus about 20% larger than the suggested upper bound for the small perturbation analysis. The condition that the flow travel at least ten correlations lengths (considered in Equation 3.10) is met in the longitudinal direction. Figure 3.9 presents the experimental and the theoretical variograms calculated using the optimized parameters, plotted as the distance between a pair of points, h , and the semivariogram, \mathbf{g} . The match at small distances is quite good. The correlation length scale is essentially the same as for the fracture aperture distribution, as expected. The variance of the log permeability field is much larger than the variance of the aperture field (0.42). The theoretical transmissivity is $1.64 \times 10^{-4} \text{ m}^2\text{s}^{-1}$, calculated using the geometric mean in equation 3.2. The theoretical dispersivity is 0.142 m, calculated using equations 3.10 and 3.11. The experimental values are 26% larger than the

predicted transmissivity, and 68% larger than the dispersivity predicted by the stochastic analysis.

The larger experimental dispersivity may be explained by several factors. First, perturbation theory is limited, and the variance in Y is larger than the upper limit of the theory (variance less than two). Also, we observe considerable channeling rather than dispersion, which is not predicted by perturbation theory. Second, even though considerable effort was placed in reducing the dead volume in the end plate zones and tubing into and out of the core, it still represents a significant fraction of the total volume, and mixing of the streamlines in this region is very likely. Finally, because of the limitation in measuring very low apertures in the fractured core, it is possible that very small channels may exist which we are unable to predict. Also, we scan the core every millimeter, but some features may actually be smaller (e.g. closure of the fracture) and are thus not sampled.

3.4.2 Numerical Modeling

To model single-phase flow in a fracture, we can use the fracture aperture distribution obtained from CT imaging to generate the streamlines in the fracture plane. The streamlines can then be used to map a solution of the advection-dispersion differential equation onto each streamline, as developed by Thiele *et al.* (1996). Although this method does not account for mixing across streamlines (transverse dispersion), it is a rather fast and accurate method for predicting breakthrough. The assumption that transverse dispersion is negligible is corroborated by the CT scans during tracer breakthrough.

Figure 3.10 shows the streamlines for the permeability field obtained from the fracture aperture distribution of Core C, evaluated by determining the pressure distribution under steady state conditions (i.e. solving the Laplace equation) on a grid with 160 x 130 blocks. The streamline information is useful in graphically viewing where most of the flow will take place, and may also be used in two and three phase flow simulations, as a first approximation to the position of a miscible or immiscible front, by mapping one-dimensional solutions. A channel carrying a significant fraction of the flow develops at a position along the length of the core of about 15 mm, and another channel carries most of the flow from a 50 mm into the core almost directly to the outlet of the core. Flow in both the tracer experiments and numerical simulations is presented from left to right.

The numerical simulation was accomplished by mapping to the streamlines a one-dimensional solution of the advection-dispersion equation, using a Peclet number of 1000, i.e. with very little dispersion in the advancing front. The results are presented in Figure 3.11. A main flow channel is observed in the middle region of the fracture plane, with some side channels developing parallel to the main flow. Some tracer has broken through even after only 0.5 pore volumes (PV) are injected, indicating that, early breakthrough will be significant in a fracture with variable aperture. On the other hand, even after 2.5 PV the concentration in the core is still not uniform, because the regions of relatively immobile water continue to provide fresh water, which is observed in the breakthrough curves as very long tailing. Because the Laplace solver requires finite permeabilities even in regions where the CT scans indicate there is no aperture, the numerical simulation predicts a complete sweep of the core. No flow boundaries are specified along the length of the core.

The numerical simulation does not capture all of the features seen in Figure 3.8 (the CT scan of a tracer experiment), particularly the constriction observed at approximately 100-120 mm. In addition, the current version of the streamline simulation does not consider the change in pixel volume (or what in porous media would be considered variations in porosity), which has a significant effect on simulation outcome. The current simulations only consider variations in permeability. We expect that the current simulation can be improved to match the experimental curve by considering the variation in pixel volume.

Figure 3.12 compares the breakthrough curve for a typical experimental run, the numerically simulated breakthrough curve and the prediction of perturbation theory. Breakthrough at the outlet is earlier in the simulation, since the model predicts that flow is rapidly channeled through the fastest streamlines, but it takes a longer time to saturate the entire core with the tracer (or contaminant). This numerical prediction of even longer tailing is due to the very slow flow through the wide streamtubes along the boundaries of the core (Figures 4.10 and 4.11), which are eventually swept by the tracer at 7.5 PV. Although the two breakthrough curves appear to correspond, there is room for improvement in the simulation. Perturbation theory under estimates dispersion since it ignores macroscopic channeling. Direct streamline simulation over estimates dispersion since it does not allow transverse dispersion to invade slow flowing regions, and we have not accounted for the change in pixel volume.

3.5 Summary and Conclusions

A method for predicting *a priori* the effective transmissivity and dispersivity has been applied to a fracture plane, given information of the fracture aperture distribution. Although information on the fracture aperture distribution is seldom available in field settings, this method can be used to study naturally fractured cores of different materials, fractured under different modes, to generate a set of guidelines for estimating transport parameters with the knowledge of the mean fracture aperture, fracture mode and type of material. Also, field hydraulic and tracer tests at one location can be used to determine the necessary geostatistical parameters to estimate the transport parameters for related fractured sites.

The measured transmissivity is 26% larger than the predicted transmissivity of a fractured granite core using stochastic analysis and the fracture aperture distribution measured by CT scanning. The measured effective dispersivity is 68% larger than the predicted dispersivity (0.238 m vs. 0.142 m). The greater dispersion observed in the core can be attributed to: (1) errors associated with the first order approximations made by perturbation theory, and the fact that this theory ignores channeling; (2) mixing in the end plate zones; (3) additional mixing in the tubing into and out of the core holder; (4) additional heterogeneities in the fracture aperture distribution not captured with the CT scanning.

Direct numerical simulation using the streamline method over estimated dispersion. Possible explanations are: (1) we do not allow for transverse dispersion, which may actually allow transport of solute into the slow flowing regions; (2) we have not accounted for the variation in pixel volume, which has an effect on flow and transport, since the transmissivity scales as the cube of the aperture and the porosity scales directly with

aperture, so that the tracer velocity would scale as the square of the aperture, and not as we have assumed in the streamline simulations as the cube of the aperture; (3) we may not have a fine enough representation of the permeability field. The first two issues can be addressed by modifying the simulator, while the third requires even higher resolution scanning, which may be achieved by future generations of CT-scanners.

The method can be improved with higher resolution CT scanning, and larger cores to reduce end effects. The systematic application of the method to study different media and different known fracture modes may yield a useful prediction tool for field work.

3.6 References

- Abelin, H., L. Birgersson, H. Widen, T. Agren, L. Moreno, I. Neretnieks, 1994: Channeling experiments in crystalline fractured rocks. *J. Cont. Hydrology* **15**: 129-158.
- Bellin, A., P. Salandin, A. Rinaldo, 1992: Simulation of Dispersion in Heterogeneous Porous Formations: Statistics, First Order Theories, Convergence of Computations. *Water Resources Res.* **28**(9): 2211-2227.
- Dagan, G., 1982: Stochastic modeling of groundwater flow by unconditional and conditional probabilities. 1. Conditional simulation and the direct problem. *Water Resources Res.*, **18**(4), 813-833.
- Dagan, G., 1984: Solute transport in heterogeneous porous formations. *J. of Fluid Mechanics* **145**, 151-177.
- Dagan, G., 1986: Statistical Theory of Groundwater Flow and Transport: Pore to Laboratory, Laboratory to Formation, and Formation to Regional Scale. *Water Resources Res.*, **22**(9), 120S-134S.
- Dykaar, B. B. and P. K. Kitanidis, 1992: Determination of effective hydraulic conductivity in heterogeneous porous media using a numerical spectral approach. 2. Results. *Water Resources Res.*, **28**(4), 1167-1178.
- Haldeman, W. R., Y. Chuang, T. C. Rasmussen, D. D. Evans, 1991: Laboratory analysis of fluid flow and solute transport through a fracture embedded in porous tuff. *Water Resources Res.* **27**(1): 53-65.
- Gelhar, L. W. and C. L. Axness, 1986: Three-dimensional stochastic analysis of macrodispersion. *Water Resources Res.*, **19**(1), 161-180.
- Gelhar, L. W., 1986: Stochastic subsurface hydrology from theory to applications., *Water Resources Res.*, **22**(9), 1355-1455.
- Gelhar, L. W., 1987: Applications of stochastic models to solute transport in fractured rocks. Swedish Nuclear Fuel and Waste Management Company, *SKB Tech. Report 87-05*, Stockholm, Sweden.
- Graham, W. D. and D. B. McLaughlin, 1991: A stochastic model of solute transport in groundwater: Application to the Borden, Ontario, tracer test. *Water Resources Res.*, **27**(6), 1345-1359.
- Gutjahr, A. L., L. W. Gelhar, A. L. Bakr and J. R. MacMillan, 1978: Stochastic analysis of spatial variability of subsurface flow, 2. Evaluation and applications. *Water Resources Res.*, **14**(5), 953-959.
- Johns, R. A., J. S. Steude, L. M. Castanier and P. V. Roberts, 1993: Nondestructive measurements of fracture aperture in crystalline rock cores using X-ray computed tomography. *J. of Geophysical Res.*, **98**, 1889-1990.
- Johns, R. A. and P. V. Roberts, 1991: A solute transport model for channelized flow in a fracture. *Water Resources Res.* **27**(8): 1797-1808.

- Kapoor, V. and L. W. Gelhar, 1994: Transport in three-dimensionally heterogeneous aquifers, 1. Dynamics of concentration fluctuations. *Water Resources Res.* **30**(6): 1775-1788.
- LeBlanc, D. R., S. P. Garabedian, K. M. Hess, L. W. Gelhar, R. D. Quadri, K. G. Stollenwerk and W. W. Wood, 1991: Large-scale natural gradient test in sand and gravel, Cape Cod, Massachusetts, 1. Experimental design and observed tracer movement, *Water Resources Res.*, **27**(5), 895-910.
- Moreno, L. and I. Neretnieks, 1993: Fluid flow and solute transport in a network of channels. *J. Cont. Hydrology* **14**: 163-192.
- Moreno, L. and C. Tsang, 1994: Flow channeling in strongly heterogeneous porous media: A numerical study. *Water Resources Res.* **30**(5): 1421-1430.
- Rehfeldt, K. R. and L. W. Gelhar, 1992: Stochastic Analysis of Dispersion in Unsteady Flow in Heterogeneous Aquifers. *Water Resources Res.* **28**(8): 2085-2099.
- Thiele, M. R., R. P. Batycky, M. J. Blunt and F. M. Orr Jr., 1996: Simulating flow in heterogeneous systems using streamtubes and streamlines. SPE Reservoir Engineering, February 1996, 5-12.
- Tsang, C. F., Y. W. Tsang, F. V. Hale, 1991: Tracer transport in fractures: Analysis of field data based on a variable-aperture channel model. *Water Resources Res.* **27**(12): 3095-3106.
- Witherspoon, P. A., J. S. Y. Wang, K. Iwai and J. E. Gale, 1980: Validity of cubic law for fluid flow in a deformable rock fracture, *Water Resources Research*, 16(6), 1016-1024

Figure 3.1 Aperture distribution of Core C.

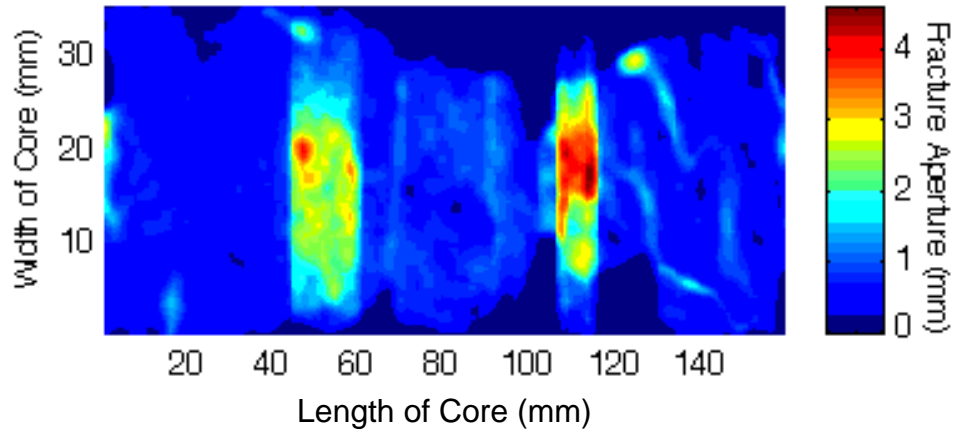


Figure 3.2 Permeability field for Core C.

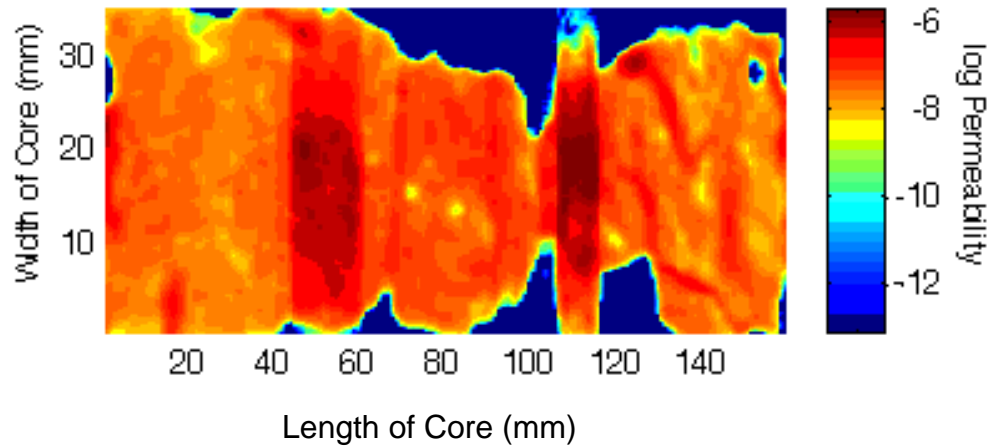


Figure 3.3 Histogram of logarithm of aperture field for Core C.

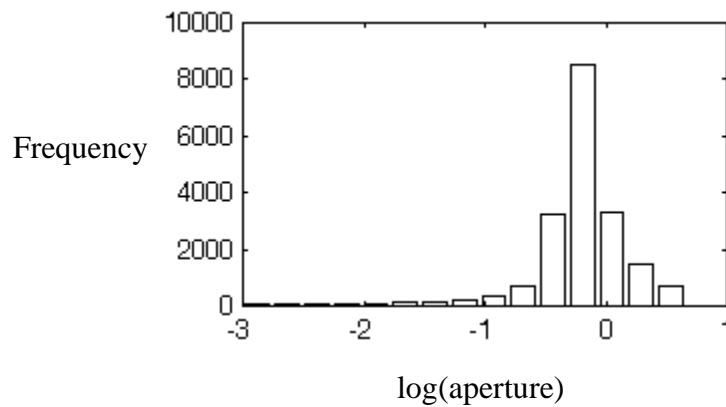


Figure 3.4 Typical breakthrough curve for Core C. This run is at a flow rate of 0.050 mL/min, or 3.06×10^{-5} m/s .

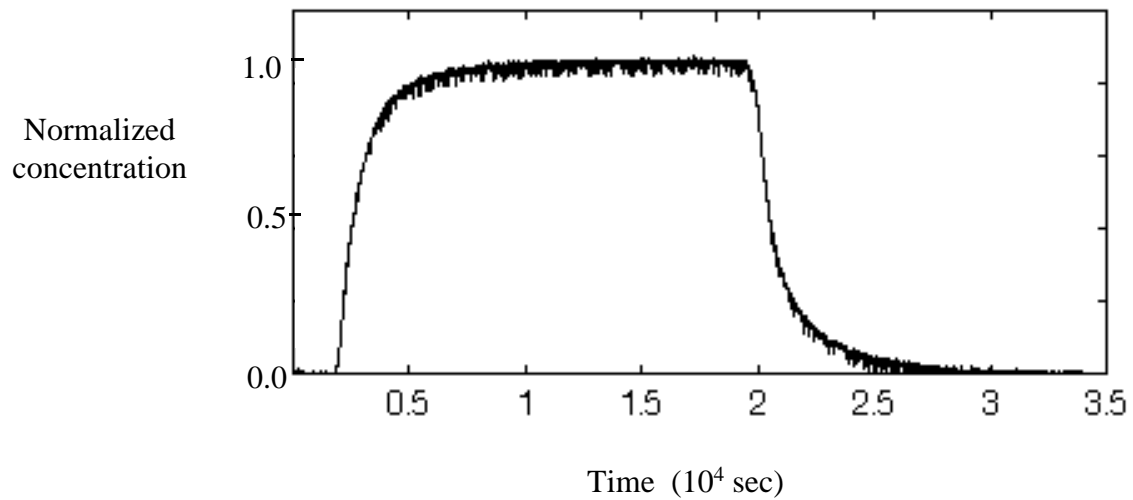


Figure 3.5 Non-dimensional analysis of the breakthrough curve to estimate the Peclet number and the dispersion coefficient.

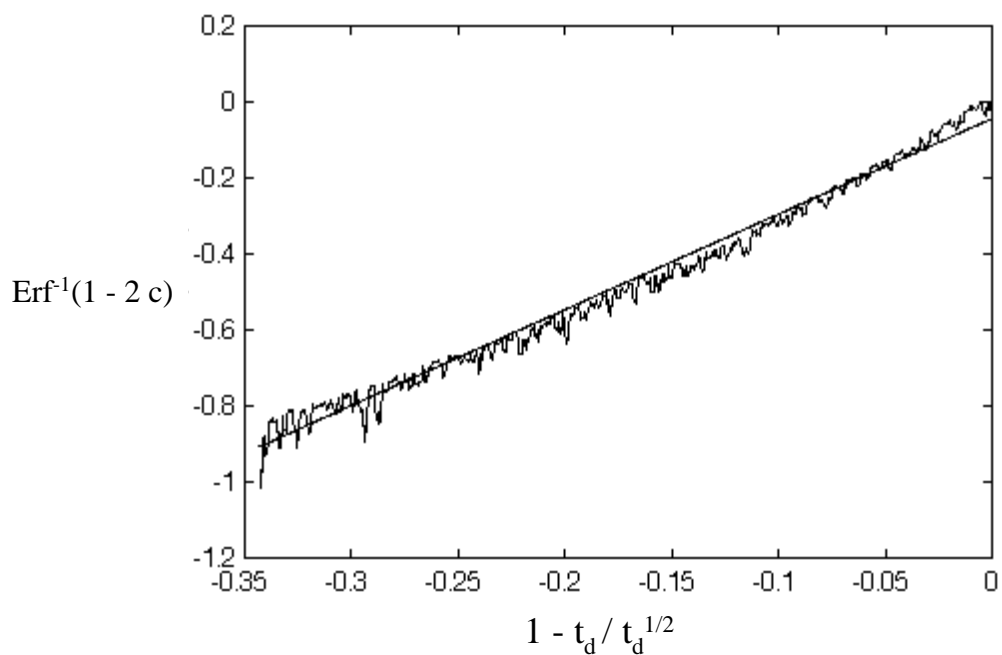


Figure 3.6 Dispersivity of Core C from the analysis of the breakthrough curves.

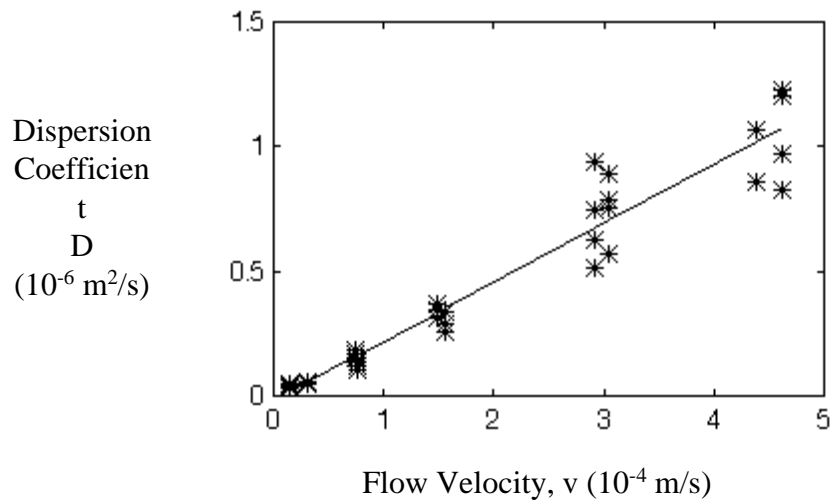


Figure 3.7 Analysis of the linear relation between dispersivity and flow velocity.

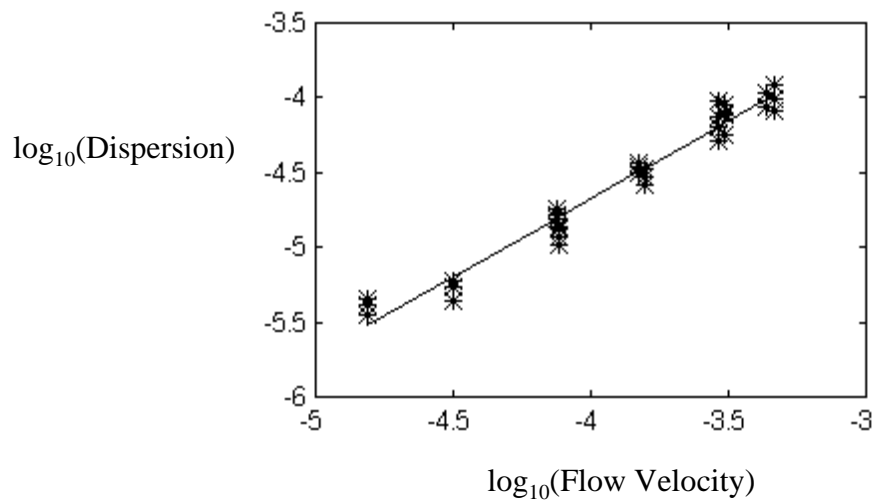


Figure 3.8 Experimental tracer breakthrough imaged using CT scanning, for a 10% KI tracer in Core C. Pore volumes injected shown at left of each image. Concentration is normalized from 0 to 1000 (right-hand bar).

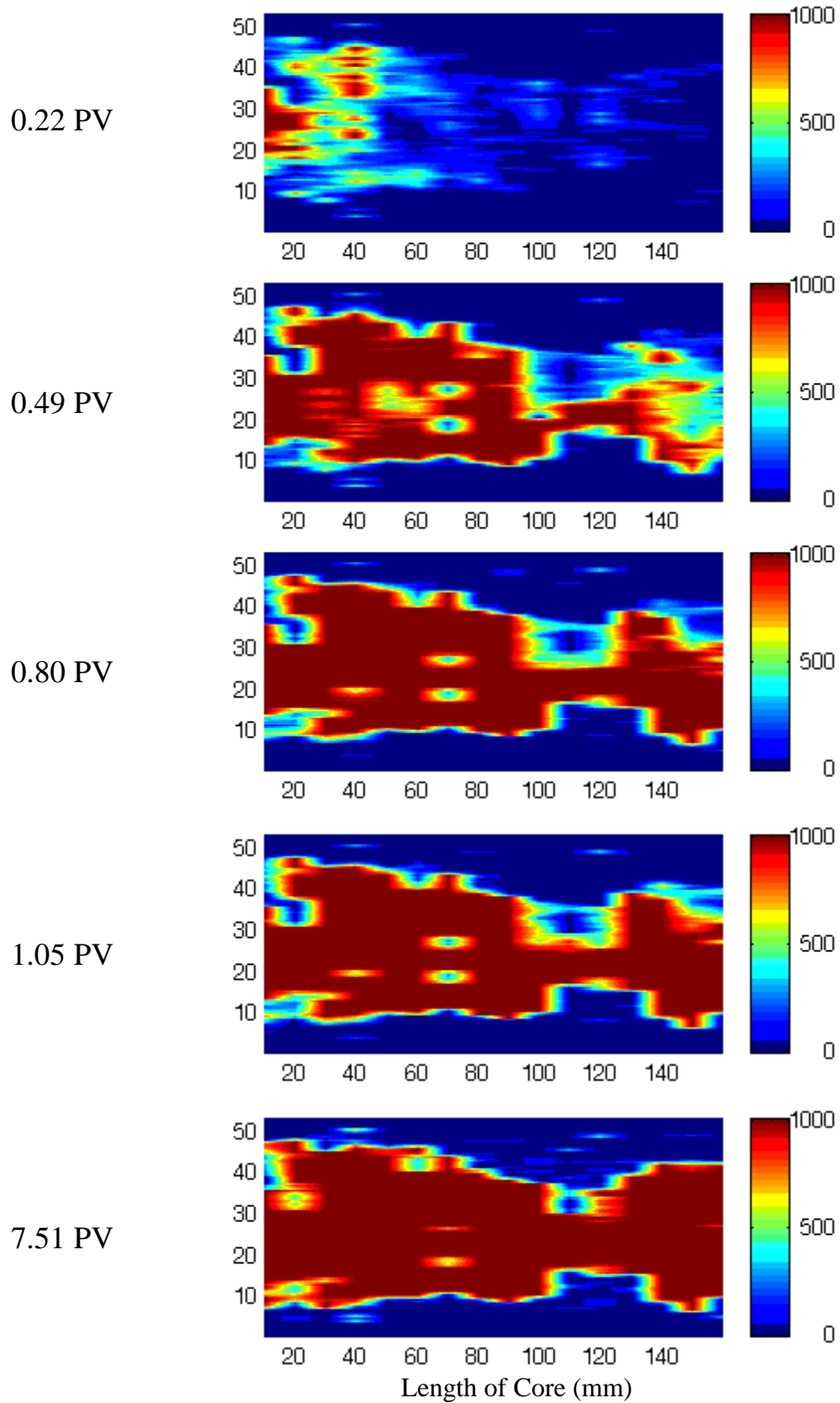


Figure 3.9 Experimental and theoretical variogram for the logarithm of the permeability field.

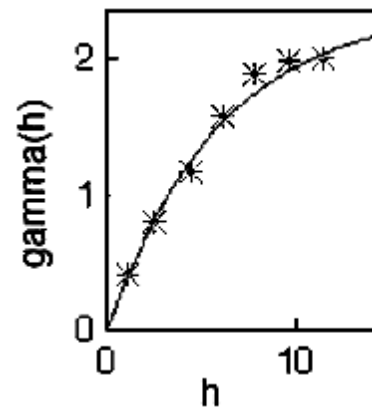


Figure 3.10 Predicted streamlines for core C.

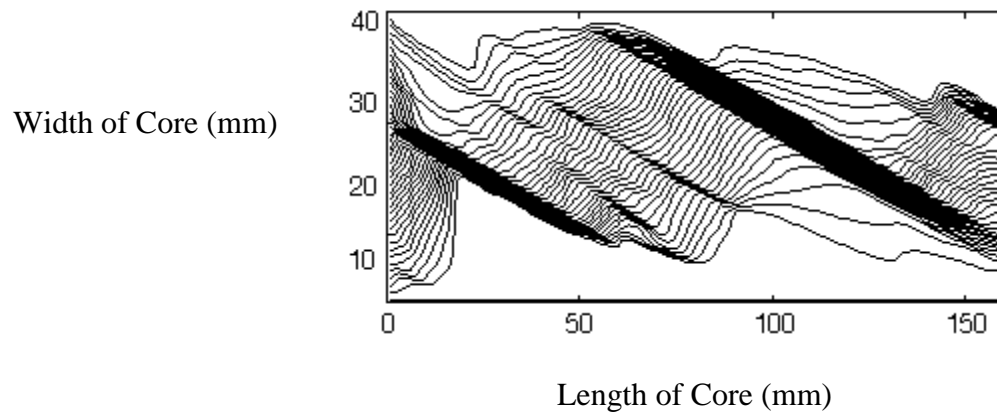


Figure 3.11 Numerical simulation of tracer breakthrough using the streamline method with the permeability field of Core C. Pore volumes (PV) injected shown at left of each image. Concentration is normalized from 0 to 1.

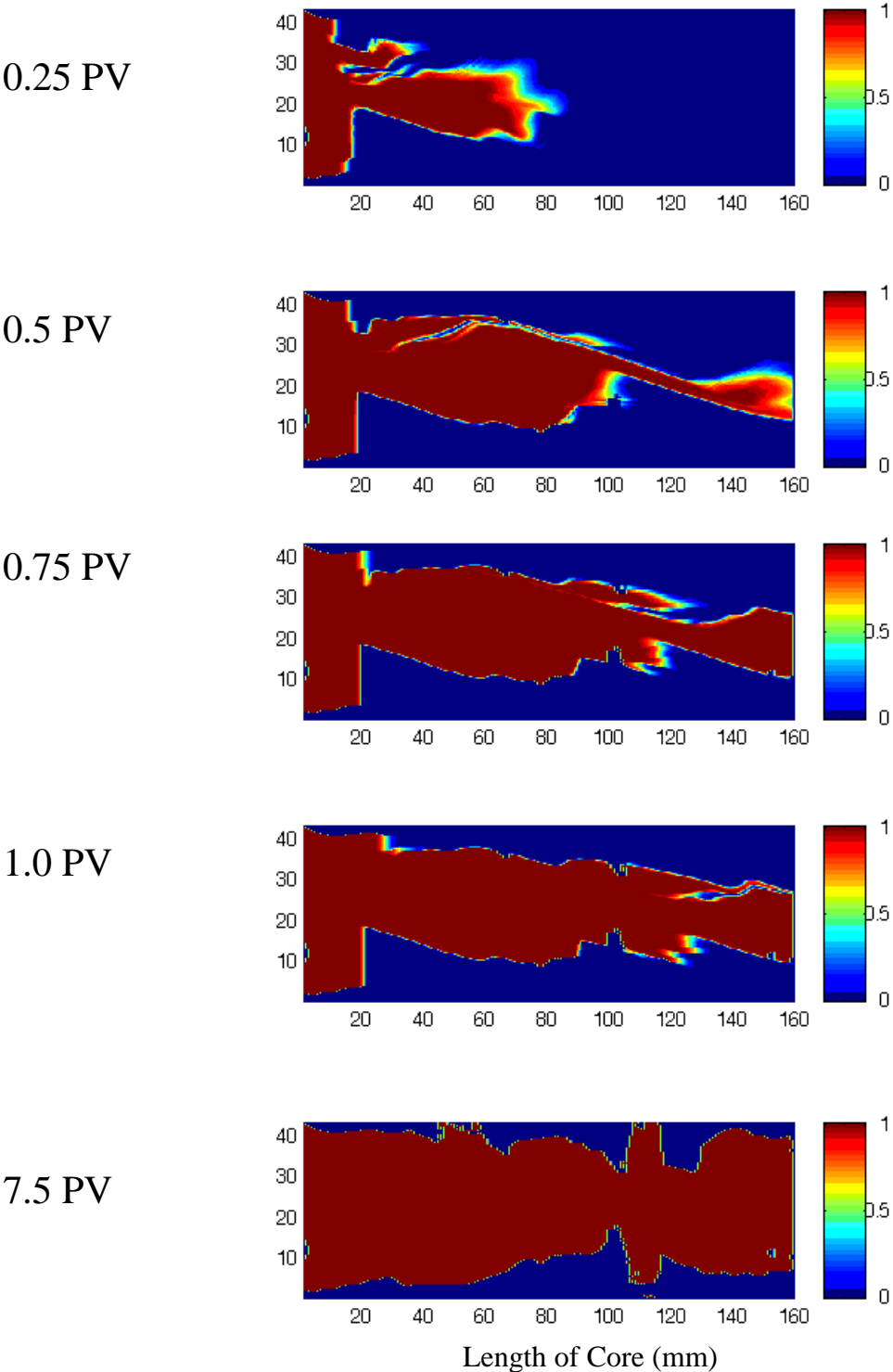
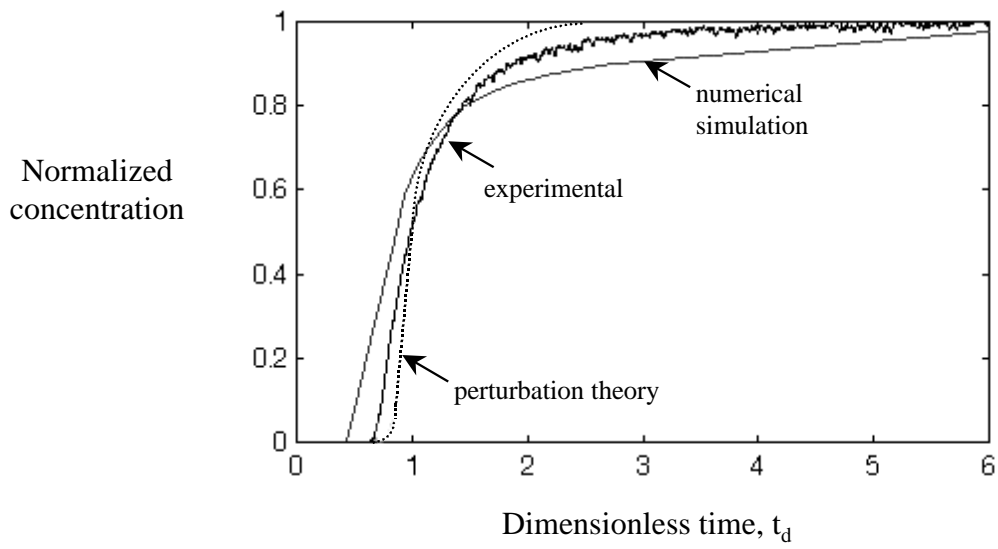


Figure 3.12 Comparison between experimental (black) , numerically simulated (gray) and perturbation theory (dashed) breakthrough curves.



Chapter 4

Two- and Three-Phase Flow at the Pore Scale

4.1 Introduction

Understanding two and three phase flow in porous media is important in many engineering fields, for example in environmental modeling of flow of a non-aqueous phase liquid (NAPL) in the subsurface, the recovery of oil from underground reservoirs in the presence of gas and water phases, and chemical engineering applications. Two phase flow is reasonably well understood and can be adequately modeled at the macroscopic level using the concepts of relative permeabilities and capillary pressures as a function of saturation. Two phase studies at the pore scale level, both experimental (e.g. Mohanty *et al.*, 1994; Vizika *et al.*, 1994; Billiote *et al.*, 1993; Lenormand and Zarcone, 1988; Lenormand *et al.*, 1983) and with network models (e.g. Berkowitz and Balberg, 1993; Sahimi 1993; Blunt *et al.*, 1992; Blunt and King, 1991; Lenormand and Zarcone, 1987; Touboul *et al.*, 1987; Dias and Payatakes, 1986) provide a physical framework for the functional relationships between relative permeability or capillary pressure and saturation. The effect of heterogeneities (Ferrand and Celia, 1992; Jerauld and Salter, 1990), flow in fractured media with a porous matrix, surfactants, miscible fluids and wetting properties of porous media (McDougall and Sorbie, 1995) are some of the remaining challenges in two phase flow.

The multiphase flow behavior is complicated by the introduction of a third fluid phase into the porous medium. This may occur as a result of the natural movement of the water table, when oil is either trapped in ganglia above or below the water table or floating as a pool on top of the water table. In addition, active injection of a gaseous or aqueous phase to remove NAPL, for example water flooding, steam injection and gas injection in oil reservoirs or dewatering for soil vapor extraction, all result in three-phase flow conditions. Much of the early work on three phase flow has been concentrated on developing empirical correlations for three phase relative permeabilities and capillary pressure curves as a function of phase saturation(s) (Parker and Lenhard, 1990; Fayers, 1989; Baker, 1988; van Genuchten, 1980; Stone, 1973, 1970), based on numerical matching of limited experimental and field data. These empirical three phase relative permeabilities do not adequately represent the physics of NAPL flow at low NAPL saturation, which is of importance for predicting NAPL saturations for environmental remediation schemes or to evaluate the efficiency of a tertiary oil recovery project.

More recently, researchers have attempted to incorporate a physical explanation for the functional form of the relative permeability and capillary pressure relationships at the pore scale level using network models (Fenwick and Blunt, 1996; Oren *et al.*, 1994; Soll and Celia, 1993) and micromodel studies (Dong *et al.*, 1995; Oren and Pinczewski, 1995; Soll *et al.*, 1993; Oren *et al.*, 1992; Chatzis *et al.*, 1988). The micromodel studies by Oren and Pinczewski (1995), Soll *et al.* (1993) and Oren *et al.* (1992) were conducted on regular networks with pore spaces at least ten times larger than those seen in most consolidated or unconsolidated porous media, which leads to relatively large

capillary numbers. Our study involves irregular networks with pores ranging in size from 3 to 30 μm across, and flow at low capillary numbers. These conditions are representative of those observed for natural displacements.

We consider water to be the most-wetting phase on the clean solid surface. The gas phase is the most non-wetting phase. The NAPL phase is usually of intermediate wettability. Depending on the interfacial tensions of the three phases, NAPL may spread between water and gas, or may form a droplet. Over a flat water surface, a spreading NAPL will eventually form a thin film of molecular thickness, a few nanometers across at most. In a porous medium, a spreading NAPL will coat all water/gas interfaces with a molecular film, but the flow rates through these films are negligible and cannot account for any appreciable movement of NAPL (Blunt *et al.*, 1995). To be of significance for flow, NAPL must form a layer between water and gas in the crevices or roughness in the pore space. These layers may be on the order of one or more micrometers (Blunt *et al.*, 1995). Three-phase flow experiments in sand columns (Blunt *et al.*, 1995) indicate that very low residual NAPL saturations can be achieved (on the order of 1%) even for systems with negative spreading coefficients, which indicates that after the main NAPL front passes, additional flow must be through layers in the crevices. We distinguish between molecular films, through which there is negligible flow, and layers which may account for significant NAPL migration.

Although it was initially considered that only spreading oils could form layers in a porous medium, Dong *et al.* (1995) have theoretically predicted and experimentally

verified that non-spreading oils can form thick layers in the crevices of the pore space, depending not only on the spreading coefficient and capillary pressures but also on the geometry of the crevice. Thick NAPL layers may provide additional channels for NAPL flow at low NAPL saturations, resulting in very low residual NAPL saturations. Because many NAPLs of environmental significance are non-spreading, the role of NAPL layers is important in modeling the flow of three phases in the subsurface. Blunt *et al.* (1995) observed rapid NAPL (iso-octane) layer flow in the corners using capillary tubes with square cross-section, in a time-frame that is environmentally significant. In micromodel studies, NAPL layers have been observed for Soltrol, which is spreading (Oren and Pinczewski, 1995). For non-spreading oils, Oren and Pinczewski (1995) and Oren *et al.* (1992) did not observe NAPL layers.

In addition to piston-like displacement of the residing phase by the invading phase, and the trapping mechanisms observed in two phase flow (Lenormand, 1988), six additional displacement mechanisms can occur when the three phases are present in the same pore space, as discussed below. Oren and Pinczewski (1995) observed double drainage, where gas displaces NAPL that displaces water.

In this study, we extend our investigation of the role of NAPL layers in three phase flow by observing the various displacement mechanisms in a micromodel, which contains corners that allow for NAPL flow in layers. Our motivation is to find if oils with negative spreading coefficients can form layers, and the significance of these layers for reaching very low NAPL saturations. The observations are directed to understand displacement mechanisms at the pore scale, but not to study overall displacement

efficiency, which is better understood from three-dimensional laboratory experiments. The results of this study can be used in network models to study physically based relative permeabilities and capillary pressure relationships. We briefly review the theoretical background for the existence of NAPL layers, followed by a description of the experimental setup, and then we present our observations.

4.2 Theory

4.2.1 Spreading Coefficient

The spreading coefficient, C_S is defined as:

$$C_S = \gamma_{gw} - (\gamma_{ow} + \gamma_{go}) \quad (4.1)$$

using the subscripts w for water, o for NAPL and g for gas. Typically, $\gamma_{gw} > \gamma_{ow} > \gamma_{go}$, but the magnitude of the sum of interfacial tensions $\gamma_{go} + \gamma_{ow}$ can be larger than γ_{gw} , resulting in a negative spreading coefficient, as is the case for many hydrocarbons (e.g. decane and higher hydrocarbons) and chlorinated solvents (e.g. carbon tetrachloride, trichloroethylene, tetrachloroethylene) as well as for some NAPL mixtures. This means that on a flat surface, NAPL will form droplets and will not spread. If $C_S > 0$, the NAPL will spread between water and gas, as occurs for the lighter hydrocarbons.

The interfacial tensions can change as the interfaces age, i.e. they become contaminated with molecules from the other fluids. Even for fairly immiscible fluids, the dissolution of NAPL in water, the volatilization of NAPL and water to the gas phase, and

the formation of molecular NAPL films over the gas/water interface (if $C_s > 0$), result in a decrease in γ_{gw} that is usually larger than the changes in γ_{go} and γ_{ow} , resulting in a change in the spreading coefficient. The aged spreading coefficient is considered here as the equilibrium spreading coefficient, C_s^e . When thermodynamic equilibrium is reached, $C_s^e \leq 0$ (Adamson, 1990).

4.2.2 NAPL Layers

Free-energy calculations and experimental work by Dong *et al.* (1995) have shown that NAPL layers may exist in a porous matrix for $C_s^e \leq 0$, and that the NAPL phase will imbibe into crevices in the porous medium. Fenwick and Blunt (1996) have shown theoretically that layers of NAPL may be present in a crevice, provided that the geometry and ratio of capillary pressures are within certain ranges. Figure 4.1 presents the situation for (a) a circular cross-section, (b) a square cross-section and (c) a more realistic pore space configuration. In the case of the circular cross-section, only a film will exist if $C_s > 0$, and will be very thin, of molecular thickness. Flow through these thin films is very slow, and may result in drainage of NAPL phase from the porous media only over very long time frames. On the other hand, these very thin films present a large surface area for volatilization of the NAPL to the gas phase. For the configurations in Figures 4.1b and 4.1c thick NAPL layers may be present.

For the geometry of a crevice shown in Figure 4.2, an NAPL layer will be present as long as the ratio of the NAPL-water interfacial radius, r_{ow} , to the gas-NAPL radius, r_{go} ,

is below a critical ratio, R_c . Fenwick and Blunt (1996) assumed that the NAPL layer would disappear when the NAPL/water and gas/NAPL contacts with the solid surface coincided, i.e. when points A and B in Figure 4.2 meet. Thus:

$$R_c = (r_{ow} / r_{go})_c = (\gamma_{ow} P_{c_{go}} / \gamma_{go} P_{c_{ow}})_c = \cos(\theta_{go} + \beta) / \cos(\theta_{ow} + \beta) \quad (4.2)$$

where β is the half-angle of the crevice, θ_{go} is the gas/NAPL contact angle and θ_{ow} is the NAPL/water contact angle, and assuming that $\theta_{go} \geq \theta_{ow}$. Having three phases in equilibrium imposes a constraint on the contact angles and interfacial tensions (Zhou and Blunt, 1996):

$$\gamma_{gw} \cos \theta_{gw} = \gamma_{go} \cos \theta_{go} + \gamma_{ow} \cos \theta_{ow} \quad (4.3)$$

where θ_{gw} is the gas/water contact angle measured at thermodynamic equilibrium.

For a completely water-wet surface, $\theta_{gw} = \theta_{ow} = 0$, and from Equations 4.1 and 4.2 we find (Kalaydjian, 1992):

$$\cos \theta_{go} = 1 + C_s^e / \gamma_{go} \quad (4.4)$$

In Figure 4.3 we explore the relationship between the half-angle and the critical ratio, for several non-aqueous phase liquids of environmental significance, with $C_s^e < 0$. We assume a completely water-wet medium, with $\theta_{ow} = 0$. The ratio of interfacial radii, $R = r_{ow} / r_{go}$, goes to zero as the crevice becomes wider. At $R = 0$, only NAPL and a water layer or gas and a water layer can occupy the crevice, but not the three phases. As R increases, all three phases can coexist in a crevice. When R_c is reached the NAPL layer becomes unstable and disappears. In the limit, for $\beta = 90^\circ$, we have the

configuration of a circular capillary tube, and only for a spreading NAPL with $C_s^e = 0$ can NAPL layers exist. In fact, if $C_s^e = 0$, then $R_c = 1$ for all values of β , if $\theta_{ow} = 0$. As C_s^e becomes more negative, the range of radii and crevice angles where NAPL layers can occur decreases.

The micromodel experiments of Oren *et al.* (1992) were been performed in strongly water-wet media ($\theta_{ow} \approx 0$) with “eye” shaped crevices for either ‘spreading’ systems with $C_s^e = 0$ or for NAPL with a large and negative spreading coefficient ($C_s^e = -8 \text{ mN m}^{-1}$). Figure 4.3 indicates why NAPL layers were observed for the spreading fluids, but were absent for the non-spreading oils. However, many oils have a spreading coefficient that is only slightly negative ($C_s^e > -5 \text{ mN m}^{-1}$), and the porous medium may not be completely NAPL-wet ($\theta_{ow} \neq 0$). For instance, in the work of Soll *et al.* (1993), $\theta_{ow} = 55^\circ$. In this case, while the presence of NAPL layers does depend on the interfacial tensions, and thus indirectly on the spreading coefficient, it is evident that the assertion that spreading systems result in NAPL layers while non-spreading systems do not is simplistic. The point to emphasize here is that the existence of molecular films (governed by the initial value of C_s) is of negligible importance in analyzing flow in porous media: far more significant is the presence of macroscopic NAPL layers, whose existence depends on the interfacial tensions, the contact angles, C_s^e and the capillary pressures.

In our experiments with decane in pores with a rectangular cross-section, Figure 4.2 implies that $R_c \approx 0.28$, which means that NAPL layers will only be observed if the NAPL/water capillary pressure is much greater than the gas/NAPL capillary pressure. As we will show later, the ratio of curvatures in our experiments is actually much larger than R_c . However, in our micromodels, $\theta_{ow} \neq 0$. Increasing θ_{ow} aids the formation of NAPL layers (Equation 4.2) and allows them to be stable over a much larger range of capillary pressures than for a completely water-wet medium.

4.2.3 Double Displacement Mechanisms

When the three phases are present in a region of the pore space, six possible double displacements can occur (Fenwick and Blunt, 1995), where one phase displaces another which displaces the third. The six possible double displacement combinations are shown in Figure 4.4 for the case where no NAPL layers form and the case where NAPL layers are stable. These displacements are valid for LNAPLs and DNAPLs, since at the pore scale the behavior is dominated by capillary forces and surface wettability, not by gravity or viscous forces. Double drainage (DD) and double imbibition (II) are mechanisms that may mobilize trapped NAPL. In addition we may observe direct two-phase displacements. These may be drainage events - gas into NAPL, NAPL into water or gas into water; or imbibition by piston-like advance or snap-off - NAPL into gas, water into NAPL and water into gas.

If NAPL forms a layer between gas and water, direct displacements of gas by water or vice versa are unlikely to be seen. In terms of the three phase mechanisms shown in Figure 4.4, this implies that only DD and II will be observed, since the other double displacements involve gas-water contacts during an intermediate stage. As we show later, DD and II are indeed the most common double displacements. We only observe the other events when NAPL layers are not present, and direct gas/water displacements are possible.

This study will use a two dimensional physical model, at low capillary numbers, to confirm (1) whether or not NAPL layers exist for a system with negative spreading coefficient, and (2) to observe double displacement mechanisms at the pore scale.

4.3 Experimental Setup

A thin slice of Berea sandstone was imaged through an optical microscope and then digitized by Hornbrook *et al.* (1991). To improve the connectivity in the two-dimensional micromodel, the digitized image was modified slightly. The pattern was then repeated 100 x 100 times. The digital image of the pore space was then transferred to a chrome plated glass mask, at no magnification from the original sandstone thin slice. Using technology similar to the manufacture of microchips, the image was photochemically etched on a silicon wafer, at a constant etching thickness of 15 μm . The final etched repeat pattern is shown on Figure 4.5. Pore diameters are in the range from 3 to 30 μm . Figure 4.6 is a scanning electron micrograph of a section of the repeat pattern,

which shows the shape of the grain walls (square corners) and the regularity of the etching depth. Notice the crevices in the grain geometry. The porosity of the micromodel has been experimentally determined to be 35%. We are able to make identical micromodels, for different studies.

The silicon wafer was then placed between two glass plates. The top glass plate was attached to the silicon wafer using anodic bonding. Four ports were constructed on the top plate to allow independent injection of three phases and an outlet port. The bottom plate was attached with epoxy, and is mainly to provide support for the micromodel. In some micromodels, a linear channel approximately 100 μm wide was etched between two ports, to have better control over the entry of an invading phase into the porous region.

Although a two-dimensional network cannot have the same connectivity as a three-dimensional network of pores, the continuity of the wetting water layer and the NAPL layers can still be preserved by the rectangular flow cross-section.

The silicon surface is oxidized by oxygen after etching, leaving a water-wet silica surface, approximately 10 nm deep. To ensure that the model remains water-wet, carbon dioxide is introduced to displace the air, and then water is injected, which eventually dissolves the carbon dioxide, allowing the wetting fluid to saturate the model completely. This was followed by injection of a 10% acetic acid solution into the micromodel for at least 50 pore volumes. The acetic acid was flushed out with distilled water for at least 100 pore volumes, before drainage or three phase experiments were conducted. In all

cases the model is strongly water-wet ($\theta_{gw} \approx 0$) in the presence of air. Examination of NAPL/water interfaces indicate the model is only weakly water-wet in the presence of NAPL, although it is difficult to judge this accurately, since we cannot measure the vertical interfacial curvature. Water is seen to flow through crevices in NAPL filled pores, which implies $\theta_{ow} < 45^\circ$. However, some NAPL/water interfaces appear almost perpendicular to the grain surface, indicating a contact angle significantly larger than 0° .

The experimental setup is shown in Figure 4.7. The light from the microscope is reflected on the micromodel and the image is then captured with a video camera and transferred either directly to a computer for digitizing or saved on videotape for later viewing. The fluids are injected either at constant rate using syringe pumps, or at constant pressure from pressurized reservoirs. The injection pressure is captured with pressure transducers and recorded in the computer.

4.4 Experimental Results

4.4.1 Two-Phase Flow

When distilled, de-ionized water is first allowed to imbibe very slowly into a completely dry micromodel filled with air, a layer of water flows ahead of the main front through the crevices and corners, similar to observations by Dong and Chatzis (1995) for flow of a wetting liquid in a capillary tube. The approximately rectangular cross-section of the flow channels in the micromodel allows water to displace air from the corners. In

Figure 4.8, a sequence of images captures the growth of the water layer in the crevices, until the water front displaces air from the pore space. The presence of the water layer can first be observed in Figure 4.8b, and is also confirmed by the succession of gas snap-off events in the narrow pore throats is shown in Figures 4.8c-f, which leaves trapped gas in the pore space.

For drainage of the water saturated micromodel by air (Figure 4.9), the movement of the air front under even a small pressure drop across the micromodel of 10.4×10^3 Pa (1.5 psi) results in entrapment of water, due to by-passing. This corresponds to a pressure gradient of approximately 2×10^5 Pa m^{-1} , or around 10 Pa across a pore of length 50 μm . This compares with a capillary pressure of approximately 9.6×10^3 Pa in a pore of the same size. The wetting layer facilitates the flow of water out of these pockets (Figures 4.9b-d). However, as the layer of water thins, flow out of large pockets of by-passed water can be extremely slow, on the order of weeks or more. Very small pore bodies will not drain out because capillary forces hold the wetting fluid in place at thin pore throats.

In two phase flow, we have observed gas invading water and water invading gas, both by snap-off and by piston-like advance, as well as flow in wetting layers.

4.4.2 Three-Phase Flow

4.4.2.1 Equilibrium Spreading Coefficient

For three phase flow, we studied the water-decane-air system, where according to literature values, $\gamma_{go} = 23.5 \times 10^{-3}$ N/m and $\gamma_{ow} = 52.0 \times 10^{-3}$ N/m at 24.5 °C (Johnson and Dettre, 1966), with $C_s^e = -3.9 \times 10^{-3}$ N/m at equilibrium (Hirasaki, 1993). To verify the literature values of interfacial tensions (IFT) we measured them using the Drop-Weight Method (Adamson, 1990). We used certified grade decane (Fischer, 99.8% pure) and distilled and de-ionized water. We evaluated the IFT for pure fluids and for the three phases in contact for 24 hr. The results are presented in Table 4.1. All measurements were made at 23.0 °C. The experimental $C_s^e = -4.1$ is very close to the literature value. However, in a natural setting, all the IFTs would probably be lower, and further studies of IFTs of contaminated fluids are needed to determine experimental C_s^e for environmental conditions.

Table 4.1 Experimental Spreading Coefficient

Interfacial Tensions	Initial	In contact 24 hr
Air-water, γ_{gw}	71.6 ± 0.2 mN m ⁻¹	69.5 ± 0.2 mN m ⁻¹
Air-Decane, γ_{go}	23.6 ± 0.1 mN m ⁻¹	23.4 ± 0.1 mN m ⁻¹
Water-Decane, γ_{ow}	51.4 ± 0.2 mN m ⁻¹	50.2 ± 0.2 mN m ⁻¹
Spreading Coefficient, C_s^e	-3.4 ± 0.2 mN m ⁻¹	-4.1 ± 0.2 mN m ⁻¹

4.4.2.2 Micromodel Observations

The micromodel was first fully saturated with water. Then decane was introduced at a slow flow rate to displace water from the larger pore bodies. Only a small amount of

decane was introduced, since we wanted to observe the displacement of NAPL at low saturation. As with air drainage, some water was bypassed as decane invaded the micromodel. Decane injection was stopped and then air was introduced at a very low pressure through the decane injection port.

The capillary entry pressure must be exceeded before air enters the micromodel. For air drainage of the water wet micromodel, the capillary entry pressure into a pore much wider than it is deep, is given by

$$P_{C_{gw}} = \gamma_{gw} \cos \theta_{gw} / r \quad (4.5)$$

with the radius, $r = 7.5 \mu\text{m}$, determined by the etching depth of $15 \mu\text{m}$, $\gamma_{gw} = 72 \times 10^{-3} \text{ N/m}$ and $\cos \theta_{gw} = 1$, assuming a zero contact angle, resulting in a minimum injection pressure of $9.7 \times 10^3 \text{ Pa}$ (1.4 psi). However, when air enters through the decane port, the required capillary entry pressure is given by:

$$P_{C_{go}} = \gamma_{go} \cos \theta_{go} / r \quad (4.6)$$

The capillary entry pressure is then at most only $3.1 \times 10^3 \text{ Pa}$ (0.45 psi), since air displaces decane rather than water. The measured entry pressures are $10.4 \times 10^3 \text{ Pa}$ (1.5 psi) for air into a water saturated model and $3.5 \times 10^3 \text{ Pa}$ (0.51 psi) for air through the decane port.

The volumetric flow rate, Q , was measured as $2.8 \times 10^{-11} \text{ m}^3/\text{s}$ (0.10 cm^3/hr). Considering an average cross-sectional area, A , of $5 \times 10^{-2} \text{ m}$ by $15 \times 10^{-6} \text{ m}$, and the definition for the capillary number:

$$N_{\text{cap}} = \mu q / \gamma \quad (4.7)$$

where μ is the viscosity of water, $q = Q/A$ and $\gamma = \gamma_{\text{gw}}$, then $N_{\text{cap}} \approx 5 \times 10^{-7}$. This flow rate was typical of most runs.

For stable NAPL layers in the water-decane-air system, Equation 4.2 constrains R to the range $0 < R < 0.26$, considering $\beta = 45^\circ$ for the square crevice in the micromodel and $\theta_{\text{ow}} = 0$. At $R_c = 0.26$, the theoretical ratio of capillary pressures, $P_{\text{c}_{\text{go}}} / P_{\text{c}_{\text{ow}}}$, is 0.13. In our experiments, the pressure drop across the model is comparable with typical capillary pressures, which means that it is difficult to measure capillary pressures locally with any accuracy. However, the imposed pressure differences in the model implied $P_{\text{c}_{\text{go}}} / P_{\text{c}_{\text{ow}}} \approx 0.3$, and yet NAPL layers are still observed. Since the actual value θ_{ow} is greater than zero, R_c is in fact larger than 0.26. This analysis is thus consistent with the presence of NAPL layers in our experiments.

The sequence in Figure 4.10 presents the entry of air into the porous matrix, which contains decane and water. The air phase enters at a large pore throat. It is not initially apparent that air is surrounded by a layer of decane, but this becomes clear as the air phase first stops at the water/decane interface and the decane layer bulges out, displacing the surrounding water in the matrix (Figure 4.10c). This sequence demonstrates that NAPL layers of a non-spreading NAPL exist in the micromodel. A thin layer of water is between the two decane interfaces, slowly draining out in a few minutes, until finally (Figure 4.10d) the water is displaced, the decane interfaces coalesce and the air phase breaks into the rest of the porous matrix, displacing both decane and water. The

sequence of images captures a DDI displacement (where air displaces water which displaces NAPL). This occurs since initially air contacts water directly before decane layers are formed. The water phase escapes through the crevices, and displaces NAPL at some other pore region not captured in these images. Due to the low injection pressures, the air front travels slowly into the matrix, as it must exceed the capillary pressure at each pore throat. The injection pressure is slowly increased to observe the displacements.

Double-drainage, where air displaces NAPL that displaces water, is observed in Figure 4.11. The advancing air phase is actually covered by a thin layer of decane, not apparent in the first images. As air advances under increasing injection pressure, it displaces decane (Figures 4.11b and 4.11c) which displaces water in the porous matrix. Snap-off of air within the decane layer occurs at pinched pore throats, resulting in disconnected air bubbles ahead of the main air front (Figure 4.11d). In Figures 4.11e-g, it becomes clear that the air phase is surrounded by a decane layer, as the disconnected air bubble leaves behind a continuous decane “channel”.

The two images in Figure 4.12 present a double imbibition sequence. In this case, water is injected into the model containing decane and air. Air is continuous to the outlet and is surrounded by decane. Decane is being displaced by water. Figure 4.12a shows the air phase just before it is displaced. Water displaces decane that in turn displaces air. The whole process occurs in about one-tenth of a second. Double imbibition processes are extremely fast, especially when the initial water saturation in the matrix is very low. Although the overall process is double imbibition, in most of the micromodel the local

displacements observed are two-phase imbibitions, and double imbibition is seldom observed.

IDI, where NAPL displaces water that displaces air, is captured in Figure 4.13. A large bubble of air is trapped, surrounded by water in the matrix. Decane is injected at an injection pressure of 41.6×10^3 Pa (6 psi). The decane front advances (Figures 4.13 b and c) displacing water but with little movement in the air/water interface. Figure 4.13c shows when the water becomes surrounded by decane and air, and water displacement must be through the crevices (Figure 4.13d). Eventually, the pressure is sufficient to force decane to displace water that then displaces air (Figure 13e). In this sequence, there is direct contact of air by water, since decane has not yet contacted air. After decane contacts air, NAPL layers are observed and we do not see further IDI events. Decane can then continue direct displacement of air (Figure 4.13f).

4.5 Discussion and Conclusions

Stable NAPL layers have been observed in a porous medium for the air-decane-water system which has a negative spreading coefficient. Four of the six possible double displacements have been observed, namely double drainage (DD), double imbibition (II), and drainage-imbibition with overall imbibition (IDI) and drainage-imbibition with overall drainage (DDI). Double-drainage is the most commonly observed double displacement. Although double displacements occur, most of the displacements observed in a realistic pore space configuration involve only two phases in motion, with the third

phase usually trapped by capillary forces. However, under three phase conditions, water and NAPL layers play a significant role in drainage, by allowing both NAPL and water to flow at low saturation.

In the presence of decane, direct gas/water displacements are not observed, except near the inlet, since a layer of NAPL surrounds the gas, which then does not contact the water directly. This explains why double drainage and double imbibition are readily observed, but the corresponding two phase displacements do not occur, since gas and water do not directly contact each other. These observations are consistent with the work of Oren and Pinczewski (1992) and Soll *et al.* (1993). Moreover, the presence of NAPL layers between gas and water is the reason why the other double processes are much rarer, since they all involve a gas/water displacement as an intermediate step. In the IDI and DDI events we observed there were direct gas/water contacts, because gas had yet to contact decane.

During water drainage, wetting layers allow the outflow of the water, even for bypassed pockets of water. Thus, wetting layers result in a finite relative permeability of the wetting phase even at low wetting phase saturations.

The observed displacement mechanisms and the existence of water and NAPL layers can be used as input into a pore level numerical network model that can compute three phase relative permeabilities and capillary pressures as a function of saturation, in a three-dimensional system (Fenwick and Blunt, 1996). From this, a physically based characterization of three phase flow should be possible.

4.6 References

- Adamson, A. W.: 1990, *Physical Chemistry of Surfaces*, 5th ed., John Wiley & Sons, New York
- Baker, L. E.: 1988, Three-phase relative permeability correlations, *Proceedings of the SPE/DOE Enhanced Oil Recovery Symposium*, Tulsa, Oklahoma
- Berkowitz, B. and I. Balberg: 1993, Percolation theory and its application to groundwater hydrology, *Water Resources Research* **29**:4, 775-794
- Billiotte, J. A., De Moegen, H., Oren, P. E.: 1993, Experimental Micromodeling and Numerical Simulation of Gas/Water Injection/Withdrawal Cycles as Applied to Underground Gas Storage, *SPE Advanced Tech. Series 1*, **1**, 133-139
- Blunt, M. J., D. Zhou and D. H. Fenwick: 1995, Three Phase Flow and Gravity Drainage in Porous Media, *Transport in Porous Media*, **20**, 77-103
- Blunt, M. J., M. J. King and H. Scher: 1992, Simulation and Theory of Two phase Flow in Porous Media, *Physical Review A*, **46**:12, 7680-7699
- Blunt, M. J. and M. J. King: 1991, Relative Permeabilities from Two- and Three-Dimensional Pore-Scale Network Modeling, *Transport in Porous Media*, **6**:12, 407-433
- Chatzis, I., A. Kantzas and F. A. L. Dullien: 1988, On the investigation of gravity-assisted inert gas injection using micromodels, long Berea sandstone cores and computer-assisted Tomography, SPE 18284, in *Proceedings of the 63rd Annual Technical Conference and Exhibition of the SPE*, Society of Petroleum Engineers, Houston, Texas, Oct. 2-5, 1988
- Dias, M. M. and A. C. Payatakes: 1986, Network Models for Two phase Flow in Porous Media. Part 1: Immiscible Microdisplacements of Non-wetting fluids, *J. Fluid Mech.*, **164**, 305-336
- Dong, M., F. A. L. Dullien and I. Chatzis: 1995, Imbibition of oil in film form over water present in edges of capillaries with an angular cross section, *J. Colloid Interface Sci.*, **172**, 21-36
- Dong, M. and I. Chatzis: 1995, The Imbibition and Flow of a Wetting Liquid along Corners of a Square Capillary Tube, *J. Colloid Interface Sci.*, **172**, 278-288
- Fayers, F. J.: 1989, Extension of Stone's Method 1 and conditions for real characteristics in three phase flow, *Society of Petroleum Engineers Reservoir Engineering* **4**, 437-445
- Fenwick, D. H. and M. J. Blunt: 1996, Three Dimensional Modeling of Three Phase Imbibition and Drainage, *Advances in Water Resources*, (in press)
- Fenwick, D. H. and M. J. Blunt: 1995, Pore Level Modeling of Three Phase Flow in Porous Media, 8th European Symposium on Improved Oil Recovery, Vienna, May 1995
- Ferrand, L. A. and M. A. Celia: 1992, The effect of heterogeneity on the drainage capillary pressure-saturation relation, *Water Resources Research* **28**:3, 859-870
- Hirasaki, G. J.: 1993, Structural interactions in the wetting and spreading of van der Waals fluids, *J. Adhesion Sci. Technology*, **7**:3, 285-322
- Jerauld, G. R. and S. J. Salter: 1990, Effect of pore-structure on hysteresis in relative permeability and capillary pressure: pore-level modeling, *Transport. Porous Media* **5**, 103
- Johnson, R. E. and R. H. Dettre: 1966, *J. Colloid Interface Sci.*, **21**, 610-622
- Kalaydjian, F. J. M.: 1992, Performance and analysis of three phase capillary pressure curves for drainage and imbibition in porous media, SPE 24878, presented at the *67th Annual Technical Conference and Exhibition of the SPE*, Washington D. C.
- Lenormand, R. and C. Zarcone: 1988, Physics of Blob Displacement in a two-dimensional Porous Medium, *SPE Formation Evaluation*, 271-275
- Lenormand, R. and C. Zarcone: 1983, Mechanisms of the Displacement of One Fluid by Another in a Network of Capillary Ducts, *J. Fluid Mech.*, **135**, 337-353
- McDougall, S. R. and K. S. Sorbie: 1995, The impact of wettability on waterflooding: pore-scale simulation, *SPE Reservoir Engineering* **10**, 208-213
- Mohanty, K. K., A. Gupta and R. A. DeRuiter: 1994, Pore-Level Mechanisms of Residual Oil Formation during Miscible Displacement, *J. Colloid Interface Sci.*, **163**, 199-216
- Oren, P. E. and W. V. Pinczewski: 1995, Fluid distribution and pore-scale displacement mechanisms in drainage dominated three phase flow, *Transport in Porous Media*, **20**, 105-133
- Oren, P. E. and W. V. Pinczewski: 1992, The effect of wettability and spreading coefficients on the recovery of waterflood residual oil by miscible gas flooding, SPE 24881, *Proceedings of the 67th Annual Technical Conference and Exhibition of the SPE*, Washington, D. C.
- Oren, P. E. and W. V. Pinczewski: 1991, The effect of film flow on the mobilization of waterflood residual oil by immiscible gas flooding, *Proceedings of the 6th European IOR symposium*, Stavanger, Norway
- Oren, P. E., J. Billiotte and W. V. Pinczewski: 1994, Pore-scale network modeling of residual oil recovery by immiscible gas flooding, SPE/DOE 27814, presented at the *9th Symposium on EOR*, Tulsa, OK, April 17-20, 1994
- Oren, P. E., J. Billiotte and W. V. Pinczewski: 1992, Mobilization of waterflood residual oil by gas injection for water-wet conditions, *SPE Formation Evaluation*, **7**:1, 70-78

- Parker, J. C. and R. J. Lenhard: 1990, Determining Three-Phase Permeability-Saturation-Pressure Relations from Two phase System Measurements, *J. Pet. Sci. Eng.*, **4**, 57-65
- Ransohoff, T. C. and C. J. Radke: 1988, Laminar Flow of a Wetting Liquid along the Corners of a Predominantly Gas-Occupied Noncircular Pore, *J. Colloid Interface Sci.*, **121**, 392-401
- Sahimi, M.: 1993, Flow phenomena in rocks: from continuum models to fractals, percolation, cellular automata, and simulated annealing, *Reviews of Modern Physics* **65**, 1393-1534
- Soll, W. E., M. A. Celia and J. L. Wilson: 1993, Micromodel studies of three-fluid porous media systems: pore-scale processes relating to capillary pressure-saturation relationships, *Water Resources Research* **29**:9, 2963-2974
- Soll, W. E. and M. A. Celia: 1993, A modified percolation approach to simulating three-fluid capillary pressure-saturation relationships, *Advances in Water Resources* **16**, 107-126
- Stone, H. L.: 1973, Estimation of Three-Phase Relative Permeability and Residual Oil Data, *J. Can. Pet. Tech.*, **22**, 214-218
- Stone, H. L.: 1970, Probability Model for Estimating Three-Phase Relative Permeability, *J. Pet. Tech.*, **12**:4, 53-61
- Touboul, E., R. Lenormand and C. Zarcone: 1987, Immiscible Displacements in Porous Media: Testing Network Simulators by Micromodel Experiments, SPE 16954, presented at *62nd Annual Technical Conference and Exhibition SPE*, Dallas TX, Sept. 27-30, 1987
- van Genuchten, M. T.: 1980, A closed-form equation predicting the hydraulic conductivity of unsaturated soils, *Soil Science Society of America Journal* **44**, 892-898
- Vizika, O., D. G. Avraam and A. C. Payatakes: 1994, On the role of the Viscosity Ratio during Low-Capillary-Number Forced Imbibition in Porous Media, *J. Colloid Interface Sci.*, **165**, 386-401

Figure 4.1. Three phases in a single pore space, for (a) a circular cross-section, (b) a rectangular cross-section and (c) a realistic pore space configuration. The outer boundary is the pore wall in black; the wetting film (light gray) coats the pore wall and in between the non-wetting phase (white) and the wetting phase lies the intermediate wettability layer (dark gray).

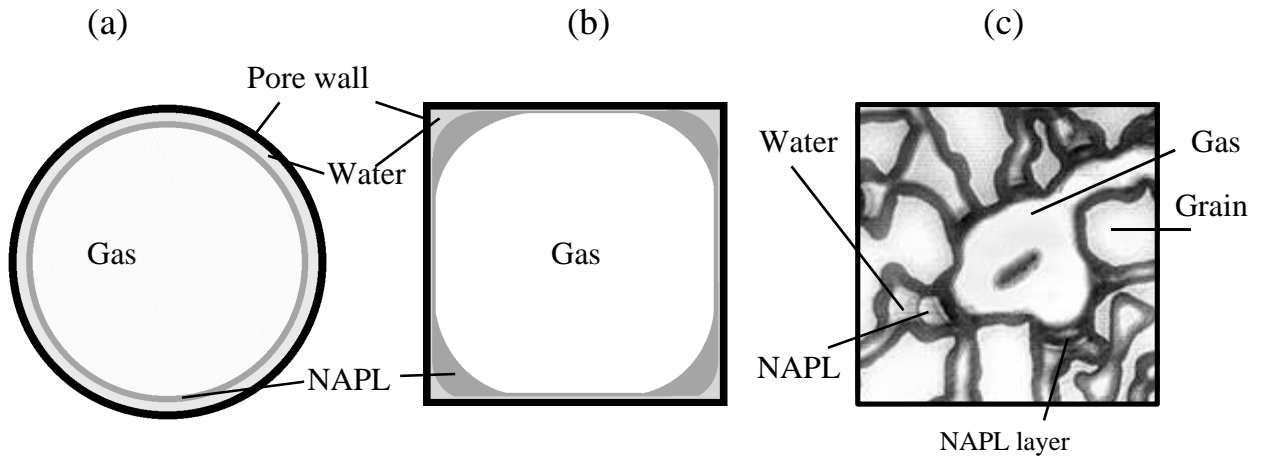


Figure 4.2. Geometry of a crevice with a stable NAPL layer between the air and water phases. The NAPL layer is no longer stable when the contact points A and B coincide.

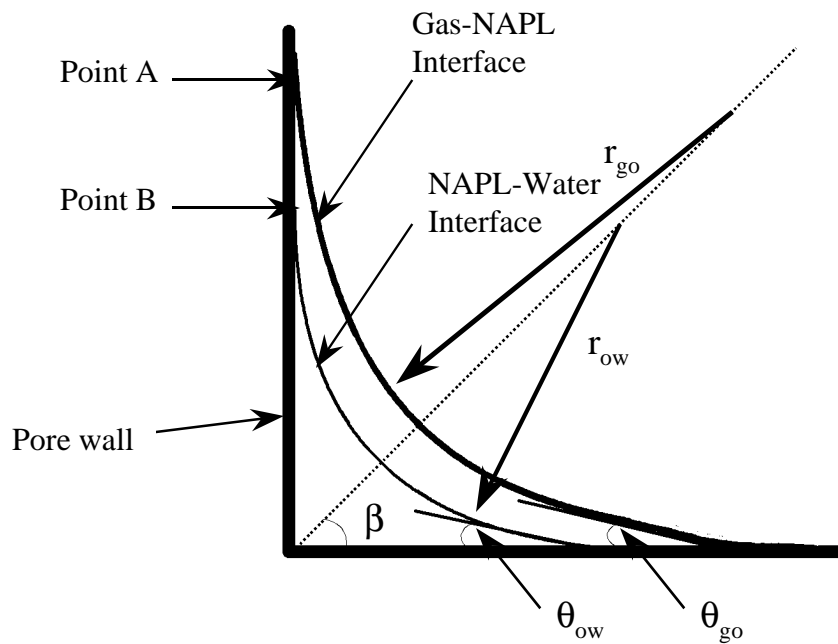


Figure 4.3. Dependence of critical radius, R_c , on the half angle β of the crevice and the equilibrium spreading coefficient. Equilibrium spreading coefficients obtained from Hirasaki (1993).

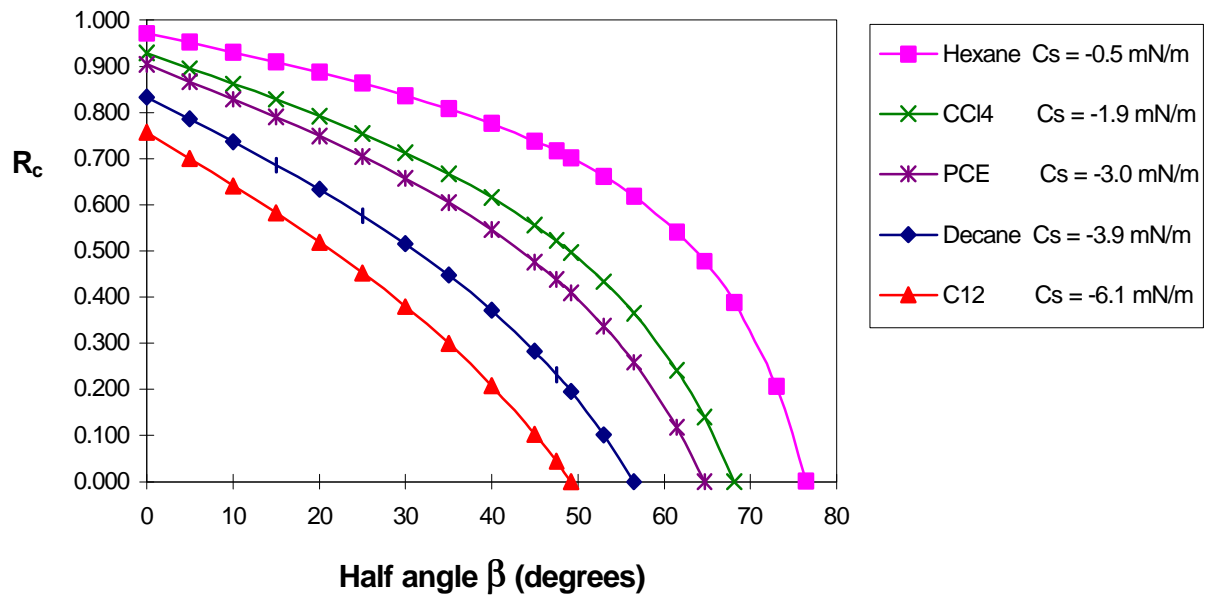


Figure 4.4. Possible three phase displacements in a pore cavity: (a) DD, double drainage, where gas displaces oil that displaces water, (b) DD with an oil layer, (c) II, double imbibition, where water displaces oil that displaces gas, (d) II with an oil layer, (e) DID, imbibition-drainage with overall drainage, where oil displaces gas that displaces water, (f) DID with an oil layer, (g) IID, imbibition-drainage with overall imbibition, where water displaces gas that displaces oil, (h) IID with an oil layer, (i) IDI, drainage-imbibition with overall imbibition, where oil displaces water that displaces gas, (j) IDI with an oil layer, (k) DDI, drainage-imbibition with overall drainage, where gas displaces water that displaces oil, (l) DDI with an oil layer.

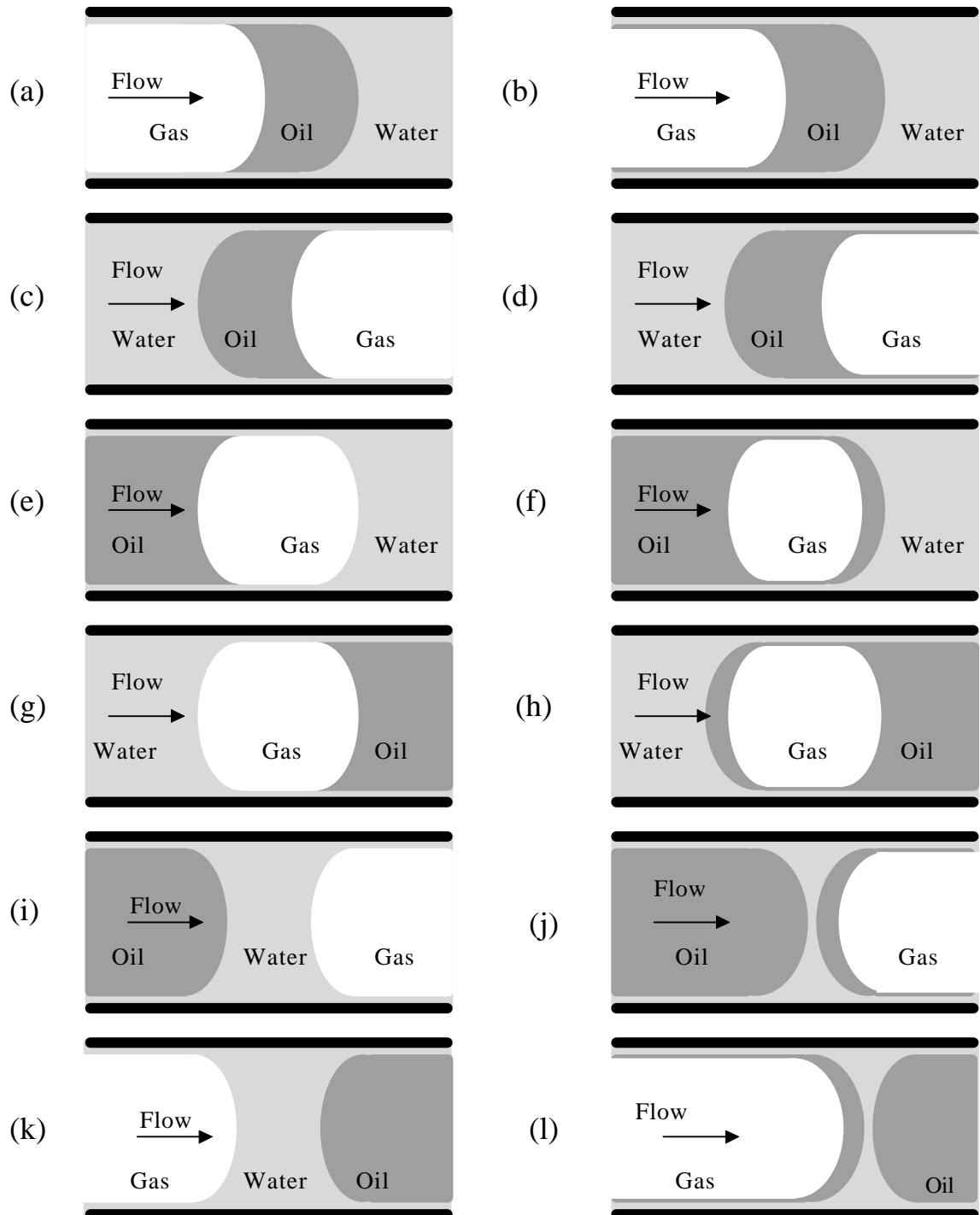


Figure 4.5 Composite image of the etched repeat pattern in the micromodel, which is approximately $509 \times 509 \mu\text{m}$, and etched to a depth of about $15 \mu\text{m}$. Pore throats are on the order of 3 to $20 \mu\text{m}$ in diameter and the pores may be up to $50 \mu\text{m}$ across. The pattern is repeated 100×100 times in the micromodel, forming a square domain, with the inlet and outlet ports on each of the corners. A scale is shown at the bottom for reference.

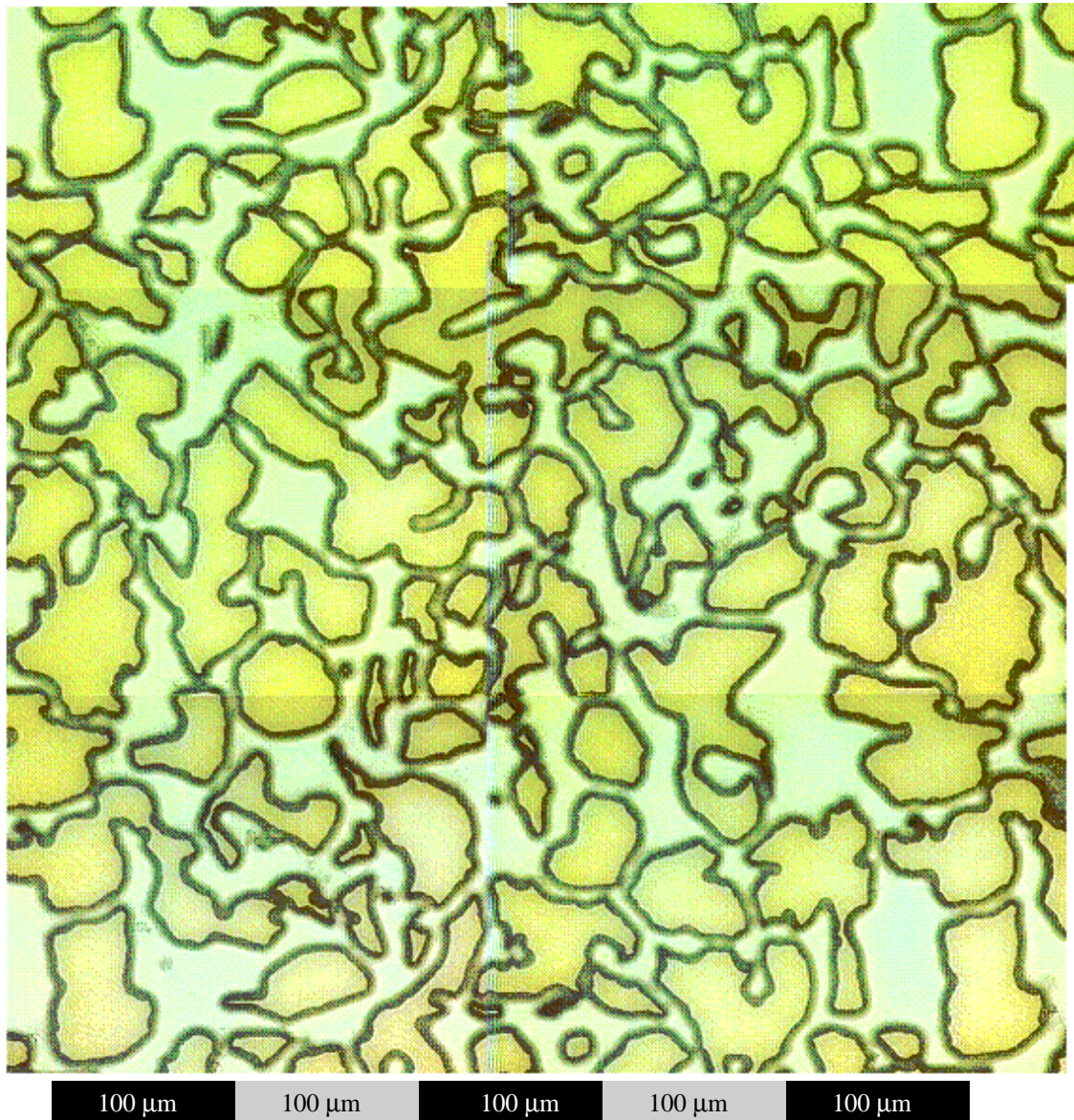


Figure 4.6. Scanning Electron Microscope image of the repeat pattern in the silicon wafer, without the top glass plate. The sharp edges of the “grain” walls produce practically a rectangular cross-section. Oil layers may form in the square corners of the micromodel.

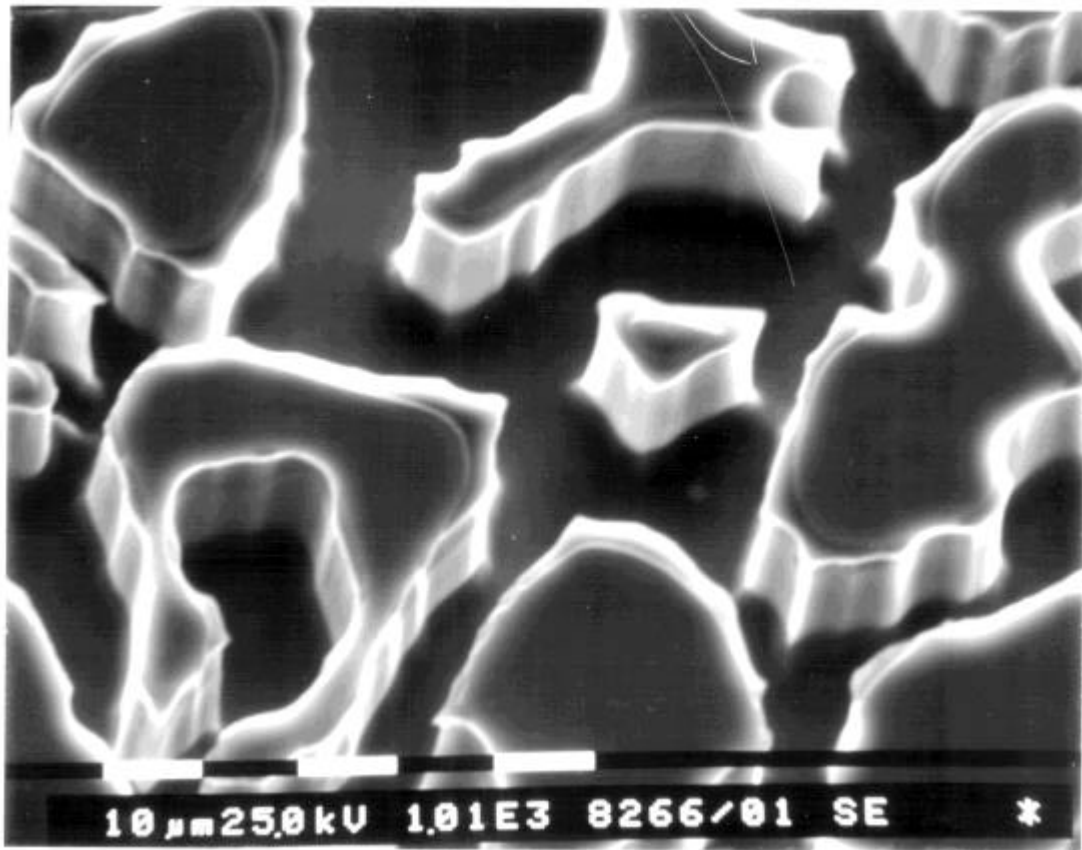


Figure 4.7. Experimental setup.

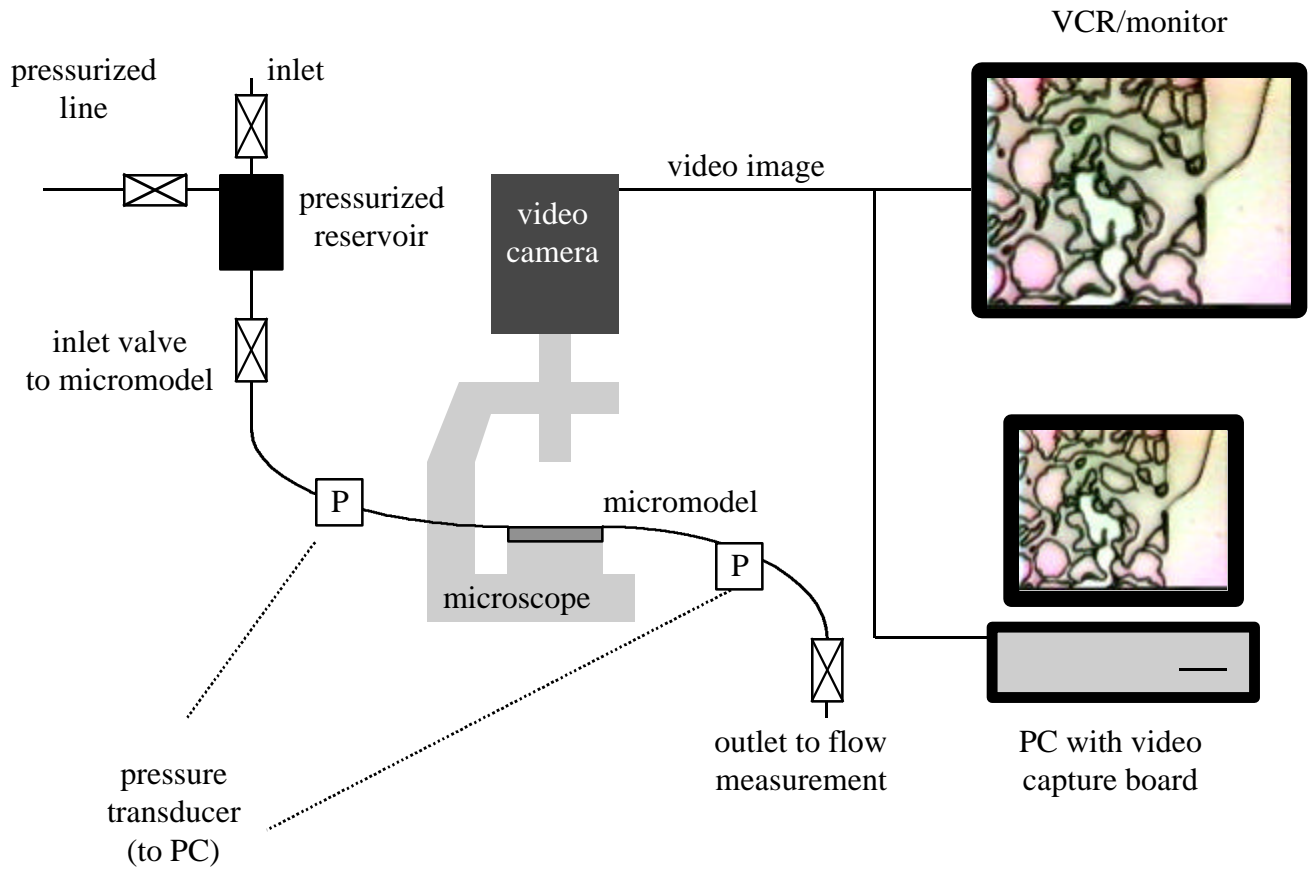


Figure 4.8. Imbibition of water into a dry micromodel: (a) the pore space is almost 100% air saturated, with water imbibing from the lower left corner; (b) as water imbibes first into the crevices of the square corners through layers, it displaces the air towards the center of the pore space; (c) at the thinner pore throats, snap-off of the air phase occurs as the water layers on both sides join; (d) even before the gas phase is completely displaced, water imbibes into the thinner pores, flowing through the layers in the crevices; (e-f) at the end of the imbibition, many snap-off events occur in rapid succession, leaving some trapped air bubbles.

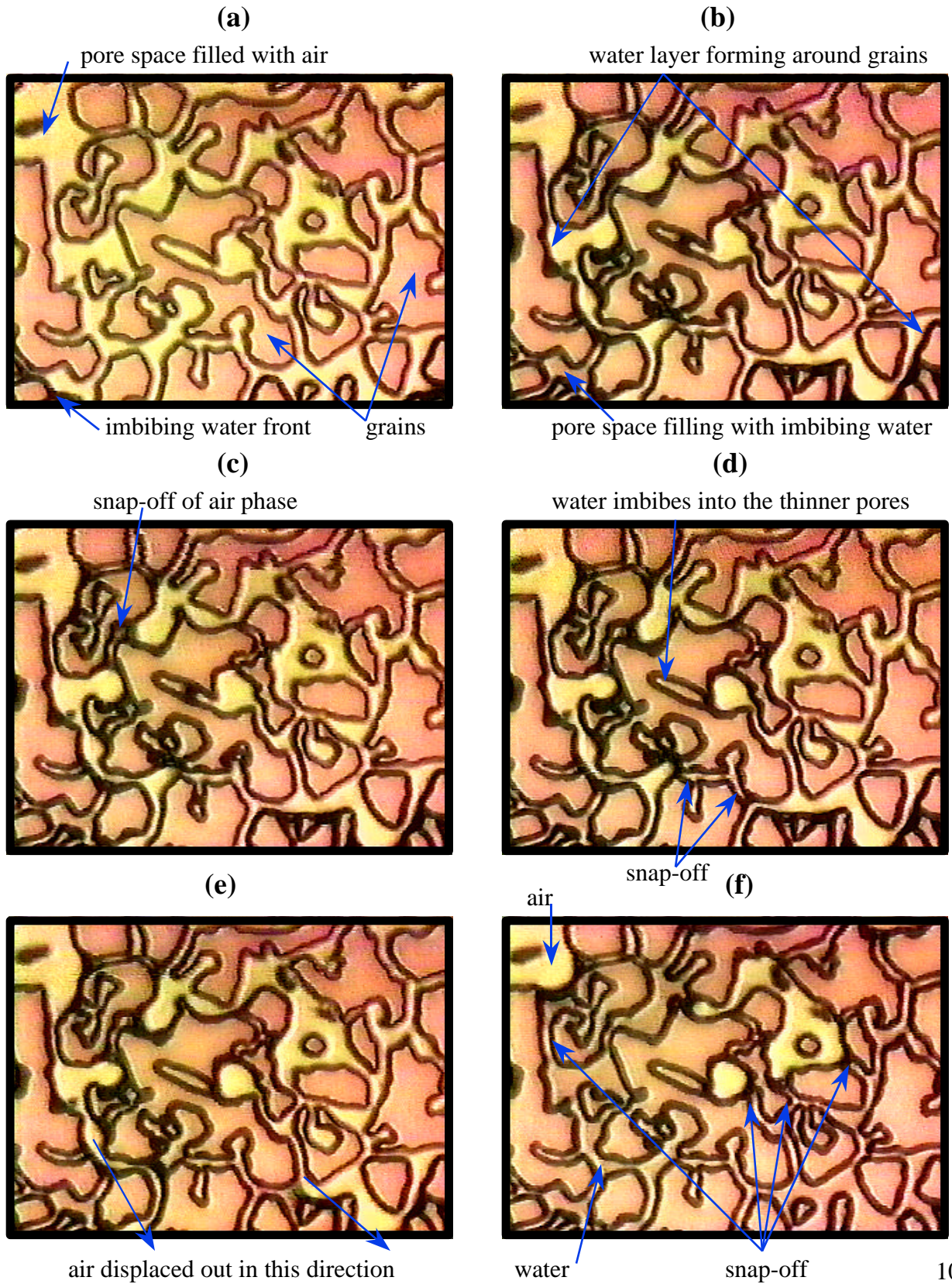


Figure 4.9. Water layers during air drainage of 100% water saturated micromodel: (a) when the capillary entry pressure is exceeded, air enters the porous matrix; (b) as soon as the capillary pressure is exceeded for the next narrow pore throat, air quickly fills in the main pore bodies, by-passing water in the smaller pores; (c) water begins to drain from a small pore through the water layer; (d) drainage of the small pore is complete in only a few minutes, but water remains in smaller throats; (e) in an irregular pore space, the air front moves in less predictable modes, by-passing water either from above or below; (f) larger areas of by-passed water take a long time to drain, especially when the drainage is only through long, thin layers.

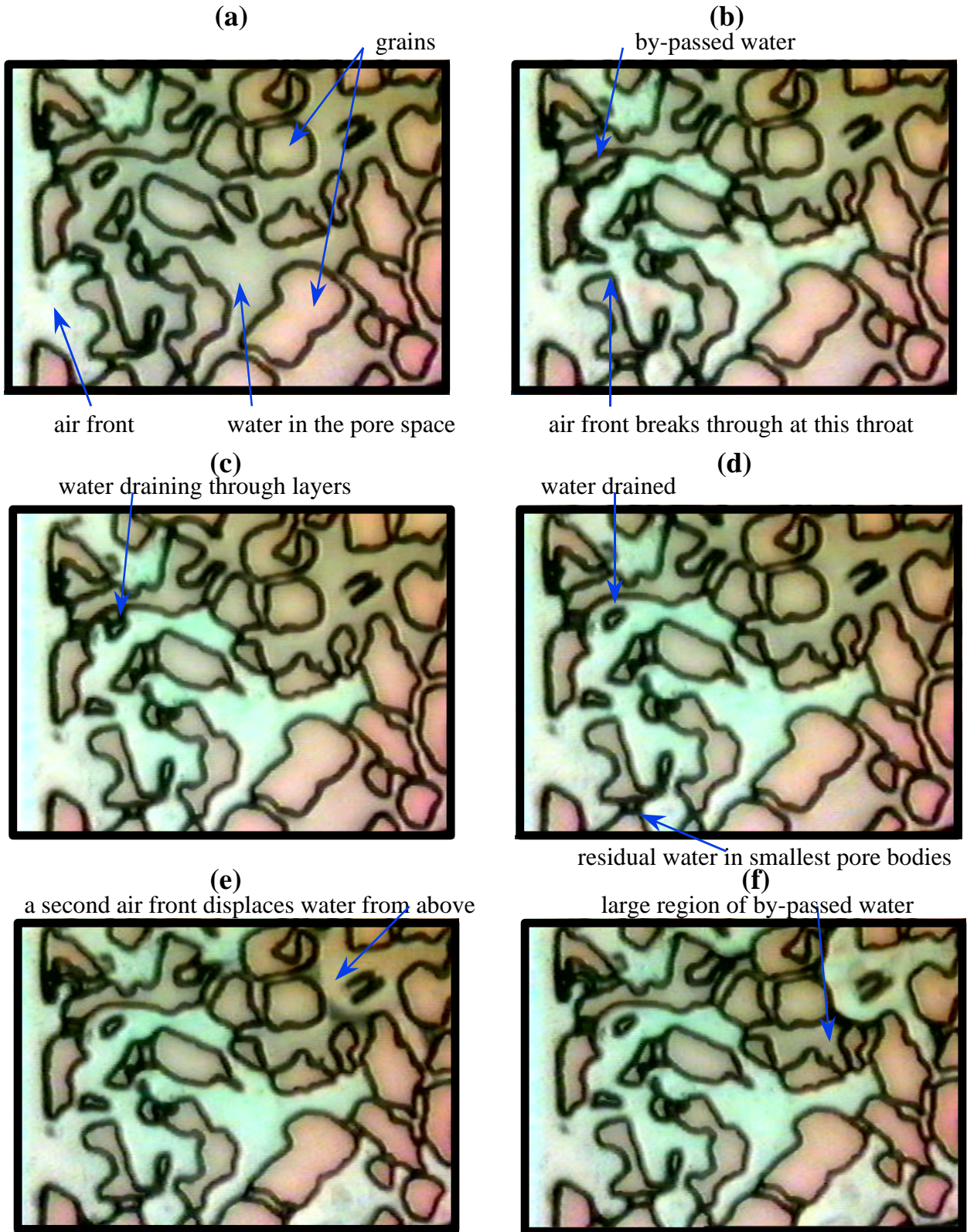


Figure 4.10. Water-decane-air system in the micromodel, showing oil layers: (a) air enters into the porous matrix which contains water and decane; (b) as the air pressure is slowly increased, the air front advances until it meets the water/decane interface; (c) the decane layer surrounding the air bubble bulges out into the water saturated pore space, corroborating the existence of a decane layer; (d) when the thin water layer between the decane interfaces finally drains out, the decane interfaces coalesce; (e-f) once the decane-decane interface coalesces, the air front can move rapidly into the decane filled pore space. A possible DDI displacement, air displacing water that displaces decane, is seen in Figure 10b.

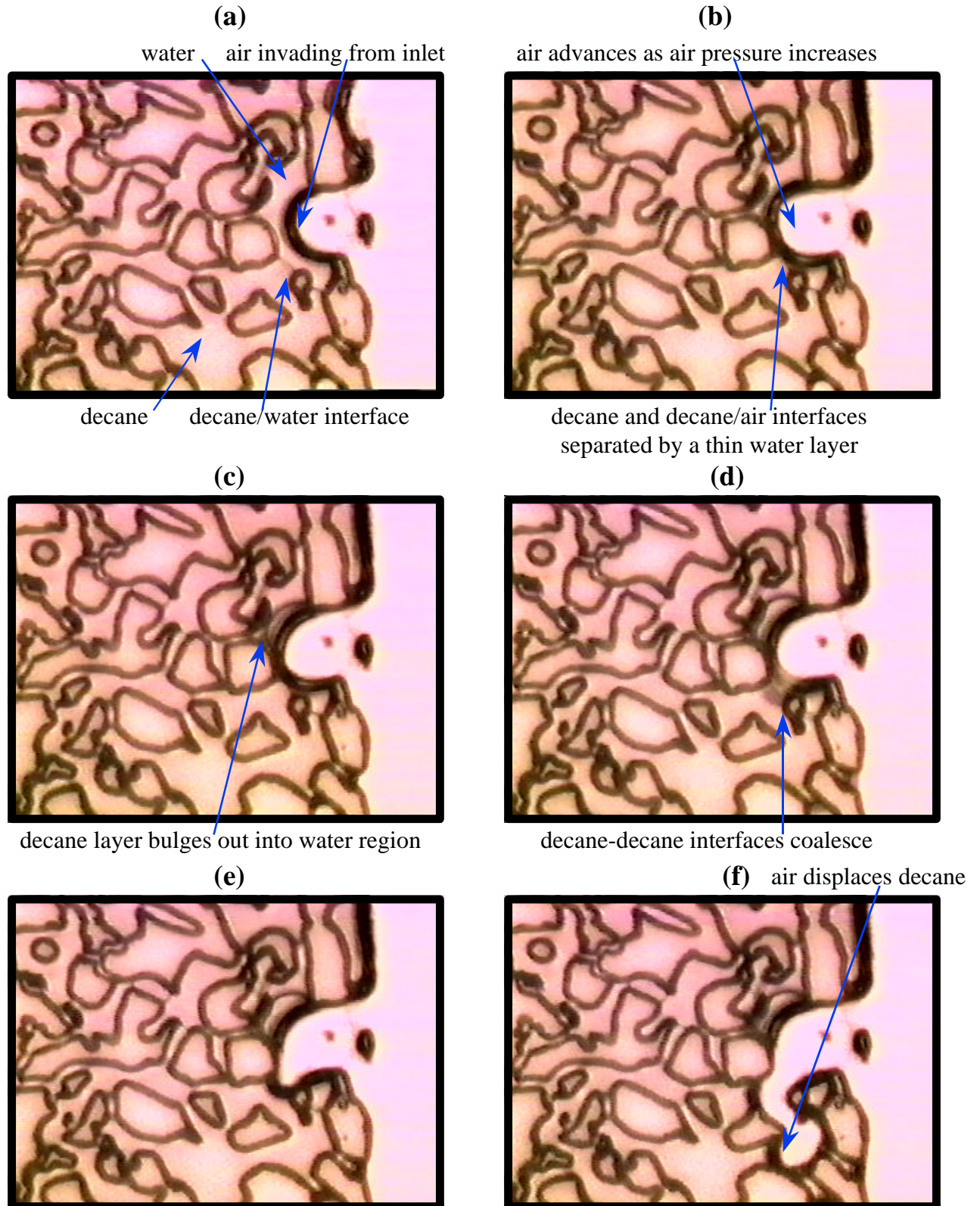


Figure 4.11. Double drainage sequence, with air displacing decane that displaces water, at the advancing water/decane interface: (a) air surrounded by decane; (b) as the air advances, decane is also forced into the surrounding water - this is double drainage; (c) air displaces decane; (d) momentary snap-off of air front, leaving a disconnected bubble; (e-f) disconnected air bubble adopts a lower energy configuration; (g) main air front continues to advance, displacing more decane; (h) recoalescence of air front with disconnected air bubble.

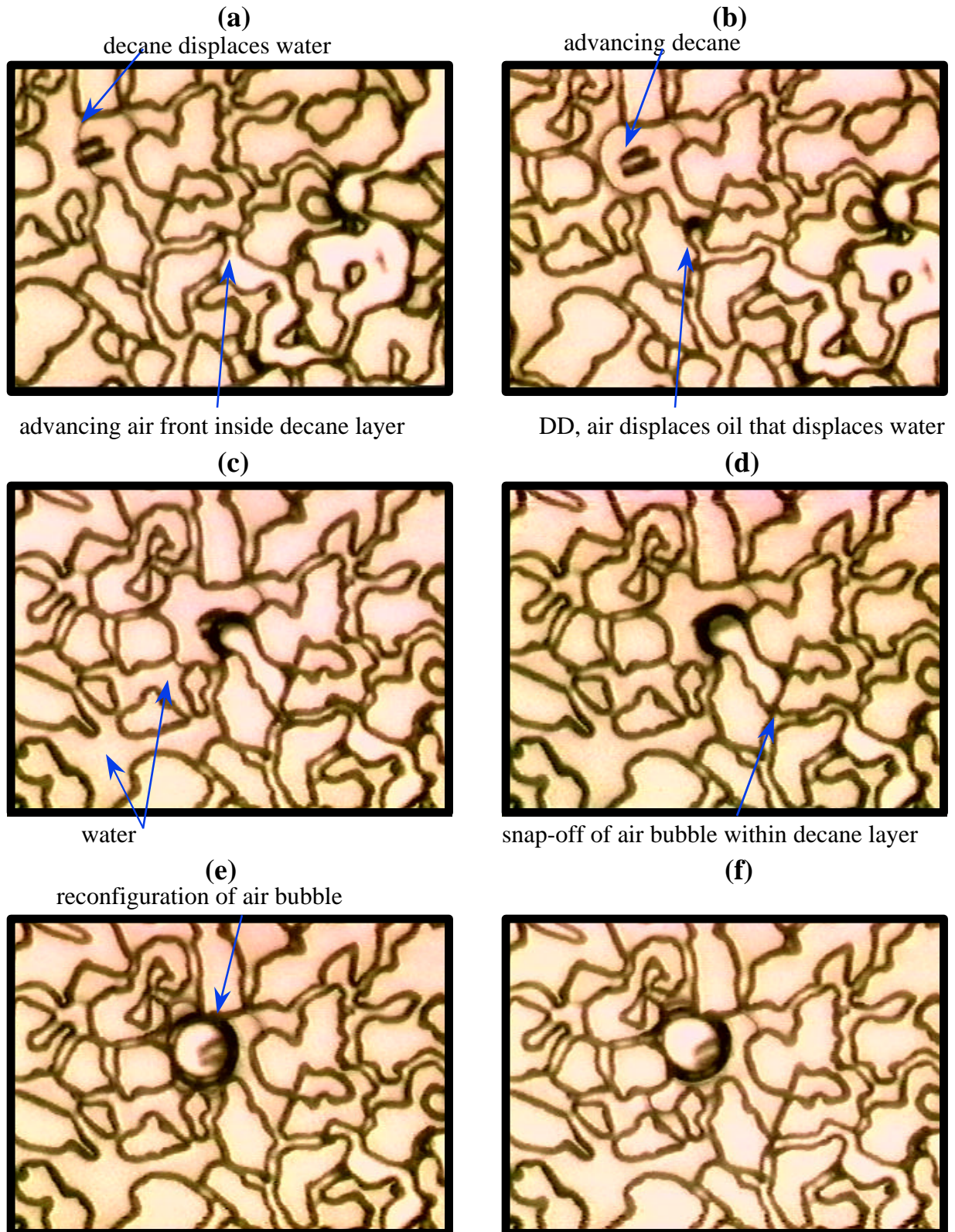


Figure 4.11.

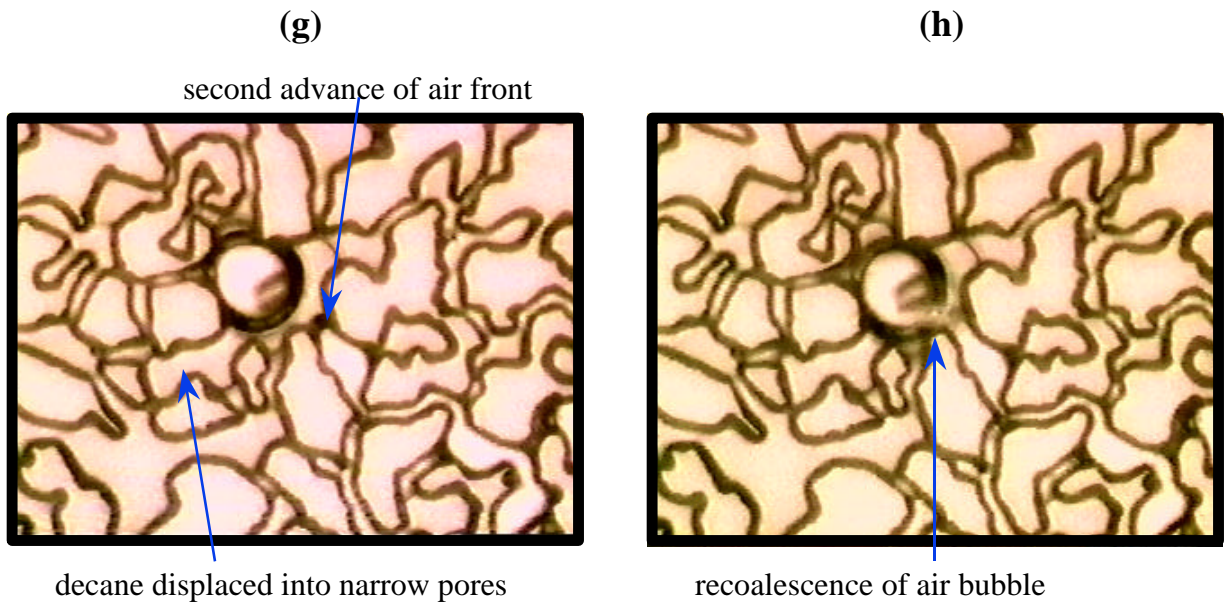


Figure 4.12. Double imbibition in the pore space: (a) air connected to the outlet port remaining after decane imbibition has either displaced most of the air or left it as trapped air bubbles. Water imbibition has also displaced most of the decane in the rest of the micromodel. (b) In one frame, water jumps across the pore space, displacing decane that displaces air.

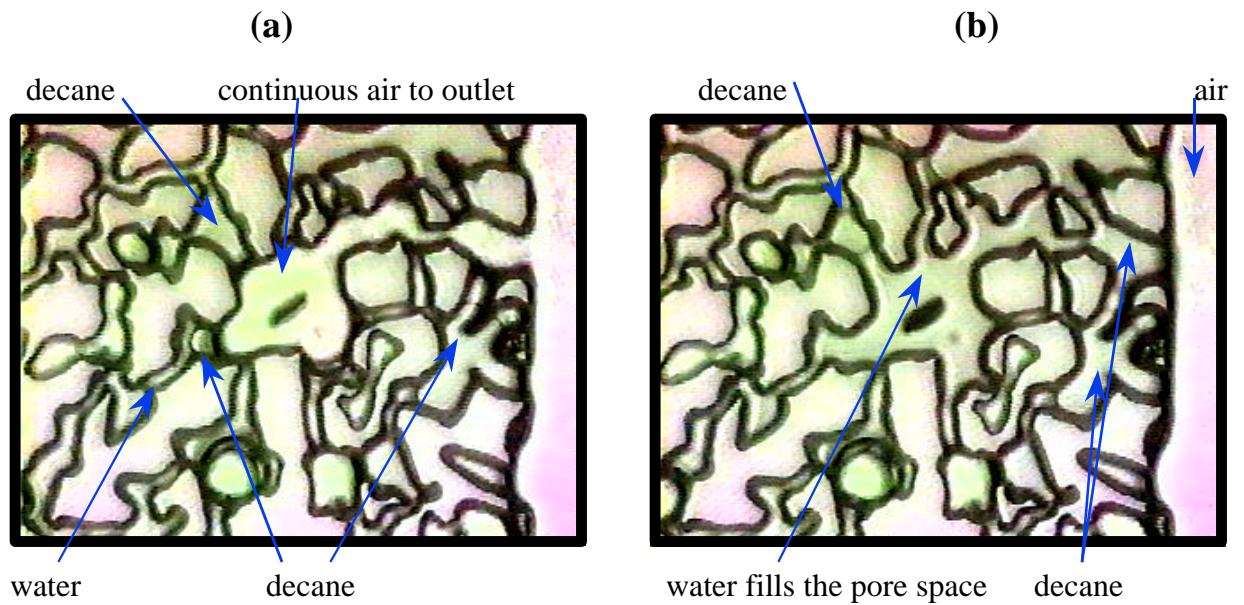
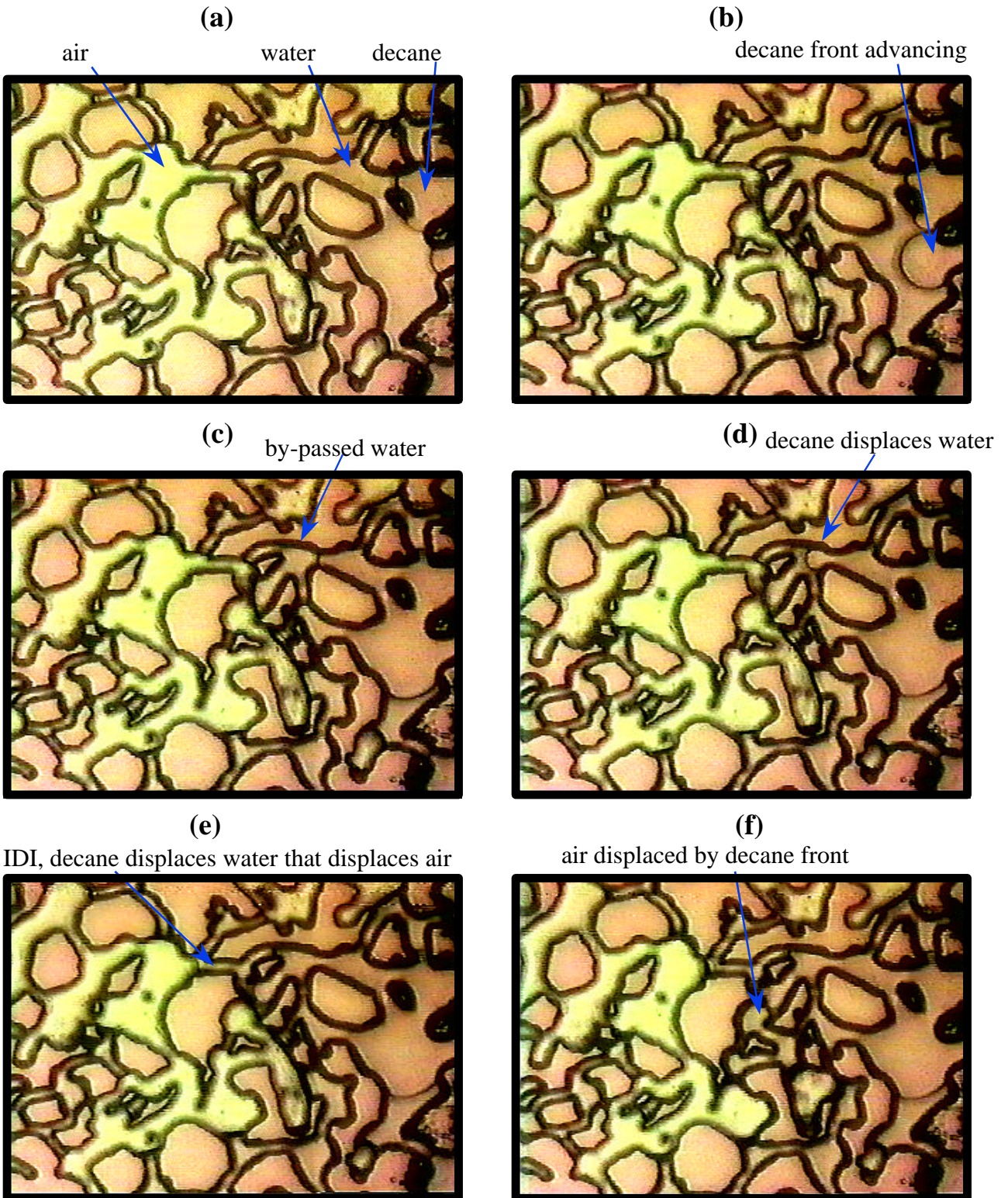


Figure 4.13. An IDI displacement, where oil displaces water that displaces air: (a) the air is receding due to water imbibition, but the decane front has advanced to by-pass water; (b) as the decane front advances, water flows out towards the bottom of the image, around the air; (c) finally the decane completely surrounds water, which must now flow out either through the crevices or by displacing air; (d) as decane continues to advance, the air/water interface stress increases; (e) finally the water displaces air, flowing out through the top of the image; (f) the decane front advances until it begins to displace directly the air phase.



Chapter 5

Two-Phase Flow in Fractured Porous Media

5.1 Introduction

Our focus is the flow of Dense Non-Aqueous Phase Liquids (DNAPLs) into water-saturated fractured bedrock and clay layers, where the displacement of water is a two-phase immiscible process into the fracture network. However, understanding two-phase flow in fractured porous media is a subject of active research in many other fields: flow in fractured oil and gas reservoirs (Kazemi and Gilman, 1989; Thomas *et al.*, 1983; Warren and Root, 1963) and the resulting impact on oil recovery, and water or gas breakthrough to the producing well, which may reduce the economic feasibility of a reservoir; the production of steam from geothermal reservoirs, which are usually dominated by flow through fractures (Pruess *et al.*, 1984); and more recently the potential long-term storage of nuclear waste at deep underground repositories which will most likely contain fractures, such that any release of liquid waste would result in two-phase flow through the fracture network (Long *et al.*, 1990).

Until recently, very little experimental work had been done on two-phase flow in real fractures. In single phase flow (Chapter 3), we determined that the intrinsic permeability for flow can be derived from the geometric mean of the fracture aperture distribution, obtained either via CT-scanning or via pumping tests. When there are two phases in the fracture, flow of either phase is affected by the presence of the other phase, whether it be static or dynamic. The full cross-section for flow is not available to both phases, and capillary forces may be significant in further increasing the interference between phases. This interference is usually modeled using a correction factor to the intrinsic permeability, denoted the relative permeability of phase p , k_{rp} (Peaceman, 1977).

Experimental work by Romm (1966) using parallel plates led to the generalization that relative permeability in a fracture was a linear function of phase saturation, S_p , such that $k_{rp} = S_p$. By definition, the sum of the phase saturations is always unity, so Romm's model implies that the sum of the two relative permeabilities is also unity. This result may be valid for the case of two-phase flow of a single component, for example water and its own vapor (steam), where Verma (1986, 1990) has shown using thermodynamic analysis that vapor bubbles cannot be trapped by the resident liquid, and thus there is little or no interference between phases. This relative permeability model has commonly been used in petroleum engineering reservoir simulation, when fractures are modeled explicitly.

However, recent experiments by Fourar *et al.* (1993) and Persoff and Pruess (1995) on flow in artificial fractures indicate that the linear model is not valid for two-component, two-phase flow. Fourar *et al.* found that for concurrent two-phase flow in fractures, the concept of relative permeability was probably not the best model for expressing the relationship between saturation and flow interference, and proposed using a homogenous pipe flow model that treats two-phase flow as a single phase, determining a friction factor as a function of a modified Reynolds number. Unfortunately, fitting the model to their experimental results indicates that the friction factor is a strong function of surface roughness. In their experiments, Fourar *et al.* encountered five different flow regimes depending on the average saturation of the gas phase, S_g , in the fracture, namely: (1) at low gas saturation, $S_g < 20\text{-}30\%$, the gas phase snaps-off at the entry point into numerous small bubbles, which travel through the fracture without coalescing into larger bubbles; (2) for S_g from approximately 20% to 45%, the gas bubbles coalesce within the fracture and form larger "fingering" bubbles; (3) for S_g from 40% to 65%, flow is very complex, with very large bubbles of gas forming and breaking up throughout the flow path; (4) for S_g from 60% to approximately 80%, water flows in layers or in "rivulets", from inlet to outlet; and (5) for $S_g > 75\%$, water flows as discontinuous droplets. These five flow regimes are also observed in pipe and capillary tube flow, which in many ways resembles the flow in a fracture, and were observed by Fourar *et al.* for both smooth and

rough fracture walls. Avraam and Payatakes (1995) also observed similar flow regimes even at low capillary numbers in a two-dimensional matrix with very uniform pore throats and bodies (i.e. with less likelihood of trapping the discontinuous phase). When fitting a relative permeability model to the data, Fourar *et al.* found that the relationship was almost linear on a semi-logarithmic plot, but that the relative permeability of the liquid phase was a strong function of liquid velocity. The relative permeability of the gas or non-wetting phase was almost independent of liquid velocity. The sum of relative permeabilities was less than unity at intermediate saturations. Although Fourar *et al.* did not study counter-current flow, it is very likely that the same flow regimes will exist. Merrill (1975) also observed several flow regimes in fracture flow.

Persoff and Pruess (1995) used an experimental setup to visualize and measure two-phase flow in natural rough-walled rock fractures. Although they were unable to measure saturation, they did correlate relative permeability to the gas-to-liquid mass flow rate ratio. Their results indicate that relative permeability of either phase is essentially linear with the mass flow rate ratio on a logarithmic plot. A Corey (1954) power law model, where $k_{rp} = S_p^4$, does not fit the data. They do not report on the visual observation of different flow regimes.

Theoretical work and numerical simulations by Pruess and Tsang (1990) indicate that if one considers the flow through the fracture to be capillary dominated (i.e. capillary forces are about equal or greater than the sum of viscous and gravity forces), then the relative permeability of the wetting phase will be non-linear with respect to saturation. Assuming a lognormal aperture distribution, Pruess and Tsang showed that the permeability-saturation relationship generally follows a power law model, with the relative permeability equal to unity when the fracture is completely water saturated and dropping off rapidly to a zero value at some “irreducible” water saturation, in contrast to the linear behavior that Romm (1966) found. The predicted relative permeability of the wetting phase is not a strong function of fracture aperture distribution (i.e. surface roughness). However, the predicted relative permeability of the non-wetting phase, k_{rnw} , is much more complex. From an analysis of two different numerically generated fracture

aperture distributions, Pruess and Tsang found that at relatively low wetting phase saturation, from 16 to 48% depending strongly on the fracture aperture distribution, the non-wetting phase becomes trapped and thus k_{rnw} drops immediately to zero. The sum of the relative permeabilities is less than unity at intermediate saturations. Numerical work by Rossen and Kumar (1992), Pyrak-Nolte *et al.* (1992) and Karasaki *et al.*(1994) to determine the relative permeabilities of measured or numerically generated fracture aperture fields also indicate that the relative permeabilities are non-linear and the sum of the relative permeabilities is less than unity at intermediate saturations.

For steady, unsaturated two-phase flow (i.e. air-water) in fractured porous media, Martinez *et al.* (1992) proposed using Richards' equation (Bear, 1972). This model assumes that the gas phase is displaced with no resistance out of the medium, due to its low viscosity and density relative to the wetting phase. The unsaturated hydraulic conductivity is modeled with an exponential relationship to soil moisture (i.e. water saturation). However, their results indicate that since the fracture has a much larger "pore" size than the surrounding matrix, steady unsaturated flow will be preferentially in the porous matrix, due to capillary forces. Most of the fracture will be dry, except for a thin water film on the fracture walls and in those low aperture regions where capillary forces are comparable to those of the matrix. Similar conclusions have been reached by Wang and Narasimhan (1985) and Dykhuisen (1987).

Demond and Roberts (1993) have shown experimentally that the two-phase relative permeability relationships for organic liquid contaminants in porous media are significantly non-linear, for both light and dense NAPLs. The sum of the relative permeabilities is significantly less than unity, and in fact the NAPL relative permeability is typically below 0.4 even at the lowest water saturation attained, which ranged from 8.6% to 25%. Only when the flow rate was increased significantly was the NAPL relative permeability up to 0.7, with a residual water saturation of only 2.1%. We can see that there is significant interference to flow due to the higher capillary forces in a porous media. The water relative permeability-saturation relationship was adequately modeled using a power law model, such as those of Corey (1954) or Wyllie (1962). The NAPL

relative permeability was also fitted using a power law model, but the different NAPL-water pairs resulted in very different exponents for the power law, and there was noticeable hysteresis among drainage and imbibition paths.

Our objective with this study is to use our knowledge of the fracture aperture distribution of fractured granite and sandstone cores (Chapter 2) and the observations of two-phase flow mechanisms at the pore scale (Chapter 4) to analyze the behavior of two phases in fractured porous media. Using this information, we construct capillary pressure and relative permeability relationships as a function of saturation, to use as predictive tools. We use the CT-scanner to visualize two-phase displacements, including the imbibition of water into a completely unsaturated fracture, the drainage of water from the fracture by invading NAPL and the re-imbibition of water into the fracture during water flooding to remove the NAPL. The CT-scanner allows us to measure *in-situ* air, water or NAPL saturations at various stages during the displacements. We then compare the resulting final distribution of fluids after each displacement to numerical simulations of the displacements.

5.2 Theory

There are several alternatives for modeling multi-phase flow in a fractured porous medium. Here we will discuss two of these methods. The first is the continuum model, based on a conventional approach, using approximations of governing equations and constitutive relationships to build a numerical model. The second method is a discrete fracture network model, which assumes that capillary forces are dominant with respect to viscous and gravity forces, and evaluates the flow paths of an invading phase based on the capillary-driven distribution of the phases. The theory behind the discrete fracture network model is similar to that presented by Pruess and Tsang (1990) and Rossen and Kumar (1992).

5.2.1 Continuum model

The governing equation for the flow of two phases in porous media, independent of the presence of fractures, is conservation of mass. In its most general form, we consider the accumulation over time of any component, i , in any of the fluid phases, p , as well as accumulation of any component on the medium itself, due to sorption. In addition, the components are transported due to advection and diffusion or dispersion in each phase. At any one point, we can have source or sink terms for any of the components in a given phase, for example mass coming in from a spill or being removed at an extraction well. For this analysis, we consider sorption to be negligible in terms of the mass transferred, in comparison to the total mass of a sorbing component available in its own phase. Even at residual NAPL saturation, the mass in the NAPL phase is typically three or more orders of magnitude larger than the mass sorbed. If we were considering only a sorbing solute in the aqueous phase, then the sorption term would not be negligible. We can then write the general conservation of mass equation (Abriola and Pinder, 1985; Baehr and Corapcioglu, 1987):

$$\frac{\partial}{\partial t} \left[\sum_p \mathbf{f} x_{ip} \mathbf{r}_p S_p \right] + \sum_p [\nabla \cdot x_{ip} \mathbf{r}_p \mathbf{u}_p] - \sum_p [\nabla \cdot \mathbf{f} \mathbf{r}_p D_{ip} \nabla x_{ip}] = \sum_p x_{ip} \mathbf{r}_p q_p \quad (5.1)$$

where:

S_p is the saturation of phase p

\mathbf{r}_p is the density of phase p

x_{ip} is the mass fraction of component i in phase p

\mathbf{f} is the porosity of the medium

\mathbf{u}_p is the velocity of phase p

D_{ip} is the dispersion/diffusion coefficient for component i in phase p

q_p is the source or sink term for phase p , per unit of bulk volume

For the time scale of the experiments we are considering, in a single core, the mass transferred from any phase to another, for example organic contaminant to the water phase via dissolution, water transfer to the organic phase, or even volatilization of either organic contaminant or water to the gaseous phase, is relatively small at the time scale of advection and will be neglected. We can then simplify Equation 5.1 by assuming that the

mass fraction of any component in its own phase is equal to unity. This assumption may not hold for larger travel times, in particular for volatilization or dissolution of the organic contaminant, where the amount of mass transferred from the organic phase to the other phase may be significant. By making this assumption, we are also considering that the density of each phase remains constant over time and space, so that it can be divided out of Equation 5.1.

From our study of single phase advection and dispersion in a fracture (Chapter 3), we concluded that although dispersion due to channeling is significant in a macroscopic sense, there is little longitudinal or transverse dispersion in any particular streamline, compared to the relatively fast advection process. Furthermore, by neglecting mass transfer between phases we are also assuming that diffusion and dispersion are not significant in this time scale. Finally, we assume that the medium is incompressible, so that there is no change in porosity with time. Equation 5.1 can then be simplified to:

$$\mathbf{f} \frac{\mathcal{I}S_w}{\mathcal{I}t} + \nabla \cdot \bar{\mathbf{u}}_w = q_w \quad (5.2a)$$

$$\mathbf{f} \frac{\mathcal{I}S_{nw}}{\mathcal{I}t} + \nabla \cdot \bar{\mathbf{u}}_{nw} = q_{nw} \quad (5.2b)$$

where the subscripts w and nw refer to the wetting and non-wetting phases.

Although the flow channels in a fracture are considerably larger than in most porous media, flow is still in the laminar regime, so we assume that the relationship between flow velocity and pressure gradient is governed by a modified Darcy's law (Aziz and Settari, 1979):

$$\bar{\mathbf{u}}_p = \frac{kk_{r,p}}{\mathbf{m}} \nabla (P_p - \mathbf{r}_p g z) \quad (5.3)$$

where:

k is the absolute permeability of the medium

k_{rp} is the relative permeability of phase p
 m_p is the viscosity of phase p
 P_p is the pressure in phase p
 g is the gravitational constant
 z is the position along the vertical axis

The capillary pressure between the wetting and non-wetting phases, P_c , is the difference in pressure between the two phases at the interface, and can be modeled using the Young-Laplace equation (Adamson, 1982):

$$P_c = P_{nw} - P_w = 2g \cos \mathbf{q} \left(\frac{1}{r_1} + \frac{1}{r_2} \right) \quad (5.4)$$

where:

g is the interfacial tension
 \mathbf{q} is the contact angle between the fluid phases on a solid
 r_1, r_2 are the principal radii of curvature of the interface.

In a fracture, $r_1 \ll r_2$, considering that r_2 is along the fracture width, such that $P_c \approx 2g \cos \mathbf{q} / r_1$. We can also write the saturation constraint:

$$S_w + S_{nw} = 1 \quad (5.5)$$

Substituting Equations 5.3, 5.4 and 5.5 in Equations 5.2 and rearranging, we obtain two equations with two unknowns, S_w and P_w , assuming that the source or sink terms are known, as well as the values of absolute and relative permeabilities and phase viscosities:

$$\mathbf{f} \frac{\mathbf{q} S_w}{\mathbf{q} t} + \nabla \cdot \left(\frac{k k_{r,w}}{m_w} \nabla (P_w + gz) \right) = q_w \quad (5.6a)$$

$$-\mathbf{f} \frac{\mathbf{q} S_w}{\mathbf{q} t} + \nabla \cdot \left(\frac{k k_{r,nw}}{m_{nw}} \nabla (P_w + P_c + gz) \right) = q_{nw} \quad (5.6b)$$

If we neglect capillary forces, by assuming that they are small with respect to viscous forces, then Equations 5.6 can be solved using analytical methods, in one

dimension, such as the method of characteristics, as was done by Buckley and Leverett (1942). However, for this analysis we want to consider the effect of capillary forces in a fracture, and examine the shape of the functional relationship between capillary pressure and saturation in a fracture, compared to porous media. We also seek to examine the functional relationship between relative permeability and saturation.

Since capillary pressures and relative permeabilities are a strong function of saturation, we have a highly non-linear solution to Equations 5.6. Numerical solution is usually CPU-intensive, in particular for large problems. There are several examples of numerical models, or simulators, that can solve multiphase flow in porous media under a variety of conditions, from models evaluating the movement of immiscible phases (e.g. Pinder and Abriola, 1986; Kueper and Frind, 1991), to models that consider both flow and interphase mass transfer (e.g. Guarnaccia and Pinder, 1992; Reeves and Abriola, 1988), to multiphase flow conditions (e.g. White, Oostrom and Lenhard, 1995; Kaluarachchi and Parker, 1990). The major issue in all these conventional simulators is the constitutive equations, i.e. the capillary pressure-saturation-relative permeability (also termed K-S-P) relationships. This is even more important in multiphase flow in fractures, where little experimental basis exists for describing the K-S-P functions.

These conventional simulators are best for modeling flow in a porous, permeable medium, with or without a fracture, to study the effect of capillary imbibition into the matrix. They are ill-suited for studying flow in a single fracture in a non-permeable matrix (e.g. granite) at high resolution, since it is practically impossible to define a capillary pressure-saturation (S-P) relationship for each grid point (pixel), based on its aperture. Thus, they tend to predict a uniform final saturation of the invading phase in the fracture, based on the estimated residual saturation of the initially-residing phase in the K-S-P functions, without regard for the physical processes involved in non-wetting phase trapping.

5.2.2 Discrete Fracture Network Model

In the discrete fracture network model, the movement of the invading phase front is controlled by capillary pressure. For the case of drainage, the non-wetting fluid can displace the wetting fluid from the surrounding pixels (or grid points) based on two rules: (1) the non-wetting phase must be continuous to the inlet, and (2) the injection pressure of the non-wetting phase must exceed the capillary pressure of the pixel to be invaded. The capillary pressure of each pixel can be calculated using Equation 5.4, using the fracture aperture determined by CT-scanning for each pixel. For the case of imbibition, the wetting fluid advances first through the smallest apertures displacing non-wetting fluid ahead. As the imbibition proceeds, wetting fluid may by-pass non-wetting fluid, resulting in trapped non-wetting phase fluid.

In the model presented here, we assume that the inlet face is fully saturated with the invading fluid. For drainage, the injection pressure is increased step-wise. At each step, the model searches for all the pixels saturated with wetting fluid which are contiguous to the non-wetting front. The model then determines the next pixel(s) to be invaded based on the balance between capillary and injection pressures. Invasion can occur in all directions, i.e. along the flow direction, perpendicular to the flow direction, and in a connected pixel which is on either diagonal direction (Figure 5.1). We assume that water can drain through thin layers on the fracture face, and thus it may be displaced even though it may appear disconnected (as observed in Chapter 4).

For the case of imbibition, at each step the smallest accessible pore is located and then water flows into it. At every step the connected and disconnected (trapped) non-wetting phases are discriminated. Trapped wetting phase is identified so that additional imbibition will not continue to displace it. In this case, we may err in assuming that capillary forces are strong enough to keep the non-wetting phase in place, since it may be that with a high enough injection pressure the trapped non-wetting phase bubbles or drops may be displaced from the fracture, and at a much lower injection pressure than in porous media.

The simulation proceeds until a limiting pressure is reached for drainage or the remaining non-wetting phase is trapped during imbibition. The model generates the

saturation distribution at each step, from which the average saturation can be determined. A capillary pressure curve can then be constructed. At this “pore scale” level, we can not adequately define a relative permeability. However, we can determine if the network conducts the wetting and non-wetting phases from inlet to outlet, and the limiting cross-sectional area through which it flows, relative to the single-phase cross-sectional area.

The discrete fracture network model is most suitable for studying the flow in a single fracture in an impermeable matrix and thus constructing the K-S-P relationships for the fracture. It may be extended to flow in a permeable matrix, by using a three-dimensional version. However, it may become impractical to describe the porous matrix at the same level of resolution as the fracture. Furthermore, the pore and throat size distributions of the porous matrix have to be estimated either from capillary pressure measurements or by making certain assumptions about the statistics of the distributions. We thus apply the network model to develop the K-S-P functions for each fracture and then model flow in fractured porous media, applying the K-S-P relationships developed in the network model in a continuum model.

5.3 Modeling Results of Two-Phase Flow in Fractured Porous Media

5.3.1 Capillary pressure

From Equation 5.4, capillary pressure depends on the radius of curvature of the interface, the contact angle and the interfacial tension. In a porous medium, the radius of curvature is determined by the dimensions of the pore bodies and pore throats, which vary widely depending on the particle size distribution and the arrangement of the particles, which is a function of both deposition history and resettling, as well as cementation. In a fracture, the local radius of curvature can be obtained from the fracture aperture distribution, measured for example using CT-scanning.

The effective contact angle within a porous medium or a fracture depends on at least two factors: surface wetting properties and the angle between the surfaces. For example, in Figure 5.2 a pore with a sinusoidal shape can be seen to have a continuously varying angle between the two grain surfaces, α . We can modify Equation 5.4 to accommodate the effect of the angle between surfaces, separating the contact angle into its surface wetting component, q , and α :

$$P_c = \frac{2g \cos(q + \alpha)}{r} \quad (5.7)$$

For the pore space in Figure 5.2, we can plot the capillary pressure as a function of position within the pore (Figure 5.3), considering for example $q = 10^\circ$. It is due to these variations in the local capillary pressure that we observe the non-wetting phase advance rapidly from pore throat to pore throat during drainage, since the advance occurs at a decreasing capillary pressure until a narrower pore throat is encountered. It is also a major factor in the hysteresis observed in the S-P relationship for drainage and imbibition (Jerauld and Salter, 1990; Parker and Lenhard, 1987). In a fracture, we can assume that locally we have practically parallel plates, such that $\alpha = 0^\circ$.

Understanding the wetting properties of a given medium is considerably more complicated. We assume that the static air-water contact angle is zero, i.e. the surface is perfectly water wetting (Myshkis *et al.*, 1987). Demond (1988) found that NAPL-water contact angles on typical mineral surfaces (albite and calcite) are around 20 to 30° for six compounds, ranging from n-alkanes, to aromatics and to chlorinated organic solvents. Natural surfaces are likely to have significant heterogeneity in terms of composition and surface films, resulting in patches of weak water wettability or even strongly NAPL-wetting regions. Even under ideal laboratory conditions, the surfaces have to be treated and conserved under special conditions (Dong and Chatzis, 1995; Ichikawa and Satoda, 1994) to achieve and maintain strongly water-wetting conditions. Future research into characterizing the heterogeneities of surface wetting properties is needed, to understand their effect on both capillary pressure and relative permeability. At present, we are

unable to deal with these heterogeneities and for simplicity we assume that the wetting contact angle is constant.

If we know the pore size distribution, then we can construct an S-P relationship, using an analogous bundle of capillary tubes which are filled sequentially. The smallest pores, which connect larger pore spaces denominated pore bodies, will have the smallest interfacial radius, i.e. the highest capillary pressure. In fact, once the wetting phase imbibes into these pores, it will be extremely difficult to displace it using viscous or gravity forces; typically, oven-drying is required to remove the strongly bound wetting phase. As pore size increases, the capillary force decreases. Using only the distribution of fracture apertures for the granite and sandstone cores measured in Chapter 2 (Core C, Core D and Core F), we can construct macroscopic S-P curves for the fractures in these cores (Figures 5.4a, b, and c). We plot a scaled capillary pressure, obtained by dividing the capillary pressure by the interfacial tension and cosine of the contact angle. This scaled S-P curve is in principle general, and valid for any two fluid pairs, whether gas-liquid or liquid-liquid. The macroscopic S-P curves are qualitatively similar to those measured experimentally by Reitsma and Kueper (1994) for fractured rocks or derived using macroscopic percolation theory (Kueper and McWhorter, 1992) on a small, theoretical aperture distribution. An alternative method, proposed by Pruess and Tsang (1990), is based on a lognormal distribution of apertures, using the geometric mean of the aperture, also denoted as the hydraulic aperture, a_h , and the variance of the logarithm of fracture aperture, \mathbf{s}^2 , to construct the S-P relationship from:

$$S_w = \frac{1}{2} \operatorname{erfc} \left(\frac{\log(a_h / a_c) + \mathbf{s}^2 \ln 10}{(2\mathbf{s}^2)^{1/2}} \right) \quad (5.8)$$

where a_c is the aperture corresponding to the increasing capillary pressure, P_c .

These macroscopic S-P curves are significantly different for the three rocks. Core C has very few low aperture pixels, compared to the other two cores, so it has only a small amount of water (which translates into saturation) tightly bound at very high

capillary pressures. In contrast, core F has a large number of very small aperture pixels, which collectively hold a significant amount of water at high capillary pressures. Core D is intermediate, but the smallest apertures are larger in average than those of cores C and F, so that the highest capillary pressure attainable is 50 to 100% lower than in the other cores. Since the detection of fracture apertures below 0.035 mm is questionable, there may be regions in the fracture plane with smaller apertures that we are not able to resolve.

The “residual” water saturation, S_{wr} , in a fracture is a function of the injection pressure and interfacial tension. For example, if air invades the fracture in core C at a pressure of 0.05 psi (0.34 kPa), and considering $g_{air-water} = 72 \text{ mN m}^{-1}$ and $q_{air-water} = 0^\circ$, then S_{wr} is less than 0.025 from Figure 5.4a. For tetrachloroethylene (PCE) invading a water-saturated core C at 0.05 psi, with $g_{PCE-water} = 44 \text{ mN m}^{-1}$ (Dawson, 1992) and $q_{PCE-water} = 30^\circ$ (Demond, 1988), results in S_{wr} less than 0.01. Note that a pressure of 0.05 psi implies a PCE hydraulic head of only 0.02 m, which practically would drain the fracture. For core F, air invading the fracture at 0.1 psi (0.69 kPa) would result in $S_{wr} = 0.19$, and increasing the air pressure to 0.2 psi (1.38 kPa) would decrease S_{wr} to less than 0.05. These calculations assume that the non-wetting phase has access to all the invadable pores. Our observations at the pore scale using a two-dimensional micromodel (Chapter 4) indicate that since the wetting phase can flow through the layers in the crevices, it is in fact displaced from most or all of the invadable pores, although some might take considerably more time to be displaced, relative to displacement from the larger pores, since flow in layers is slow. Water is left only in the smallest pores and in thin wetting layers.

We can also calculate the capillary entry pressure (Kueper and McWhorter, 1991) for air or NAPL drainage of a water saturated fracture, by determining the largest aperture along the fracture inlet, and using Equation 5.7. For core C, the capillary entry pressure is 360 m^{-1} , which corresponds to 51 Pa (0.007 psi) for air entry, or 27 Pa (0.004 psi) for PCE entry. The pressure needed to continue the invasion increases to 1260 m^{-1}

just 10 mm into the core, which corresponds to 179 Pa (0.026 psi) for air entry, or 96 Pa (0.014 psi) for PCE entry. Clearly this fracture is rapidly invaded and drained. For core F, considering the matrix is fully water saturated, the capillary entry pressure is 2440 m^{-1} , which corresponds to 346 Pa (0.05 psi) for air entry, or 186 Pa (0.027 psi) for PCE entry.

The capillary pressure in a fracture will typically be much lower than that in the porous matrix, based on the pore sizes. In a typical sandstone matrix, pore throats and bodies may range from 1 to $100 \text{ }\mu\text{m}$, resulting in a scaled capillary pressure for the water trapped in these regions of 10^4 to 10^6 m^{-1} . In the fracture, capillary pressures are typically one to two orders of magnitude smaller. For example, assuming an average pore throat of $10 \text{ }\mu\text{m}$, entry into the porous matrix requires a capillary entry pressure of 10^5 m^{-1} , or 14000 Pa (2 psi) for air entry and 7600 Pa (1.1 psi) for PCE entry. This also explains the observation that water or NAPL traveling through a fracture in a dry, porous medium will readily imbibe into the matrix, and full liquid saturation in the fracture will not be achieved until a significant fraction of the matrix is water saturated.

The S-P functions obtained using the discrete fracture network model contain more information than the macroscopic S-P functions obtained simply from the aperture size distribution. In Figure 5.5 we present the drainage process in core C at different steps in injection pressure, P_{inj} . At low pressure ($P_{inj} = 220 \text{ m}^{-1}$), the non-wetting phase can only penetrate a small fraction of the core. The injection pressure must be increased to 284 m^{-1} (which corresponds to 41 Pa for air-water or 21 Pa for PCE-water) before the non-wetting phase pressure is sufficient to break through to the rest of the fracture. At that point, water saturation in the fracture drops in one step from 89.2 % to 14.6 % (Figures 5.5 c and d). This phenomenon is not captured when constructing the macroscopic S-P function from the aperture size distribution. Further increasing P_{inj} to 1380 m^{-1} (105 Pa or 0.2 psi) can reduce S_w to 1.2%, which is a rather low water saturation compared to what can be achieved in a typical porous medium, for such a relatively small pressure drop. The capillary forces in a porous medium are typically much greater, due to the very small pore throats, which traps a larger fraction of the water.

For imbibition, the invasion process occurs in a series of discrete jumps (Figure 5.6), as water invades first the immediate lowest apertures, which in general are decreasing as the imbibition proceeds, but along the imbibition path some very small aperture pixels are encountered. Since we have assumed that the non-wetting phase is trapped once it becomes disconnected, a significant fraction (56.9%) of non-wetting phase remains in the fracture. In fact, if the imbibition is forced and the injection pressure is increased to overcome the capillary forces holding the non-wetting phase in place, the fracture may become fully water-saturated.

The corresponding microscopic S-P curves based on the discrete network model for the three cores are presented in Figure 5.7. The large decrease in saturation at a given point in the drainage process occurs in all three cores. Imbibing one pixel at a time results in an S-P curve which decreases almost monotonically with saturation, but presents sharp spikes in pressure, when a very small aperture pixel is encountered. We also present representative saturations of the drainage and imbibition processes for core D (Figures 5.8 and 5.9) and core F (Figures 5.10 and 5.11). We have assumed as before that flow occurs only in the horizontal fracture plane, and that the matrix is impermeable (even for the sandstone core F). Once the potential for phase trapping is built into the model, the S-P curves from the network model differ distinctly from those obtained using the fracture aperture distribution, exhibiting significant hysteresis and the sharp jumps in saturation at relatively constant pressure. During imbibition, typically more than 50% of the non-wetting phase remains trapped for capillary dominated flow.

5.3.2. Relative Permeabilities

To construct a set of relative permeability curves, we use the discrete fracture network model, combined with the observation of two-phase displacements at the pore scale (Chapter 4). Our first approach was to assume that the K-S curve could be constructed by determining the cross-sectional area available for flow for each phase, as long as the phase was connected to the inlet or outlet. We present these first results, but

later qualify them. For drainage, with the assumption that the water phase cannot be trapped, the relative permeability functions generated by the network model indicate an almost linear relationship between k_{rp} and S_w (Figures 5.12a, b and c), even for the regions where saturation varies slowly with pressure, except for core D. In the case of core D, k_{rw} remains quite high because the initial drainage occurs as a sharp front, so that most of the flow paths to the outlet are available, and only when the non-wetting fluid's injection pressure rises above 50 m^{-1} , when the injection front begins to finger, does k_{rw} drop quite fast, with k_{rp} rising sharply. The linear relationship between k_{rp} and S_w is a direct result of the assumption that the wetting phase cannot be trapped, which is true at capillary equilibrium, but may not necessarily occur instantaneously as the micromodel work indicates. In a dynamic situation, the observed k_{rp} may actually be lower than for the linear case, since there is interference among phases.

For the case of imbibition, where the wetting fluid readily moves into the medium, we observed in the micromodels that a film or layer of wetting fluid travels ahead of the main wetting front along the crevices of the pore space (see Figure 4.8) displacing the non-wetting phase. This indicates that flow will occur even at very low water saturations. This observation is confirmed by Dong and Chatzis (1995) for flow in a square capillary tube. As the wetting fluid displaces continuous non-wetting fluid, the thickness of the layers in the crevices grows, until suddenly there is a rapid displacement of the remaining non-wetting fluid out of the pore. Snap-off in the pore throats (Figure 5.13) and bypassing (Figure 5.14) of the non-wetting fluid by the wetting fluid results in some residual saturation of non-wetting fluid in the matrix.

The relative permeability curves for imbibition of the wetting phase are close to linear for all three cores. However, k_m in all cores is broken into a series of steps, every time a large region of non-wetting phase is trapped, which sharply reduces the available flow path to the outlet. This situation is extreme in the case of core D, where a large amount of non-wetting phase is trapped, such that the maximum water saturation is only 14%. If the flow rate is low enough such that non-wetting phase is trapped, for example

in the case of natural imbibition, then we can scale the K-S functions using an effective saturation (Parker and Lenhard, 1987):

$$S_w^e = \frac{S_w - S_{nw,r}}{1 - S_{nw,r}} \quad (5.9)$$

The issue is how to determine the residual saturation of non-wetting fluid, $S_{nw,r}$. Depending on the path (or in the network model, depending on the rules used to search for the next invadable pore), different $S_{nw,r}$ result.

If we consider that relative permeabilities are a macroscopic property, then the above analysis is incorrect, since there is actually no flow of the invading phase until breakthrough, so its macroscopic relative permeability is zero before breakthrough. The displaced phase flows out with a relative permeability close to unity (if we consider capillary-dominated flow). This can actually be inferred from the shape of the displacing/displaced fronts in Figures 5.5, 5.6, 5.8, 5.9, 5.10 and 5.11, which indicate that these are rather sharp fronts, as Buckley-Leverett theory assumes for immiscible displacement.

In the fracture, it is possible that non-wetting fluid will not remain trapped as easily, since there are few “narrow throats” to overcome. In addition, the various flow regimes observed by Fourar *et al.* (1993) indicate that even if the non-wetting phase becomes disconnected, it may travel as bubbles or droplets, at higher flow rates. Thus, k_{rw} in the fracture may be a function of flow rate.

To mobilize the trapped non-wetting phase, we need to overcome the capillary pressure in the narrow throats ahead of the trapped phase. If we assume that the average small fracture aperture is on the order of 10 to 50 μm , then the pressure drop needed to mobilize a trapped air bubble is on the order of 2.8 to 14 kPa (0.4 to 2 psi) across the bubble, considering air which has the largest surface tension with respect to water. If these flow conditions prevail, then we may use the results of Fourar *et al.* for a rough fracture, fitting the following models for k_r :

$$k_{r,w} = \exp((-3 - 3 * V_L) + 3.6S_w) \quad \text{for } S_w > 0.1 \quad (5.10)$$

$$k_{r,nw} = \exp(-1 - 6.8S_w) \quad \text{for } S_w > 0.1 \quad (5.11)$$

where V_L is the velocity of the liquid phase (m s^{-1}), to account for the effect of flow rate on the wetting phase permeability. The non-wetting phase relative permeability appeared not to be significantly modified by increasing flow rate in Fourar *et al.*'s experiments. These relative permeabilities would result in significant lower flow, or alternatively higher pressures for the same flow rate, than the linear K-S model. Figure 5.15 presents the comparison between the linear model for k_{rp} , and the functions (Equations 5.10 and 5.11) fitted to Fourar *et al.*'s experiments. The wetting phase k_{rw} is reduced somewhat from the linear model, especially at higher liquid velocities, but the deviation is not very large, relative to the large effect of high flow rate and concurrent flow on k_{rn} . This is more evident in the semi-logarithmic plot of the K-S functions in Figure 5.15b.

5.3.3 Fracture Flow in a Porous Matrix

Using the discrete fracture network model we studied the flow in a fracture, neglecting the matrix-fracture interactions, to generate K-S-P relationships. Modeling fracture flow with an impermeable matrix in a continuum model results in an almost uniform saturation front, with some movement ahead of the front due to capillary effects. In Figure 5.16 we present as an example a simulation with the continuum model of the displacement of water by a DNAPL front in core C, at different pore volumes. These simulations produce results that differ substantially from the network model and the experimentally observed saturation profiles, because they do not account for the variations in capillary pressure within the fracture plane due to the variable aperture distribution.

The continuum models are best for evaluating the effect of the fracture-matrix interactions in a fractured porous medium. For this study we used the ECLIPSE

simulator (Intera, 1994). The properties of the medium and fluids are given in Table 5.1, which correspond to a fractured sandstone with most of the values determined experimentally, and water and PCE as the fluids with values from Demond (1988). We define two regions in the domain: (1) for the fracture, with very high permeability relative to the surrounding matrix, small volume, a low capillary pressure even at low S_w , and linear relative permeabilities; and (2) for the porous matrix, with low permeability and porosity (as measured for the sandstone core E), large volume relative to the fracture, high capillary pressure and the relative permeability functions fitted by Demond and Roberts (1993). The grid is 60 x 1 x 51 blocks (length x width x height), with a horizontal fracture in the middle of the domain. The dimensions of the hypothetical core are 180 x 50 x 50 mm, with a 0.5 mm fracture aperture. The injected phase is exposed to the whole inlet face of the core, and the displaced phase can flow out of the entire outlet face. No flow is considered out of the other boundaries.

We first analyze the injection of NAPL into a water saturated core (Figure 5.17). Due to the high capillary pressure in the matrix and the low resistance path through the fracture, NAPL travels exclusively through the fracture, breaking through in just 0.055 pore volumes (PV). The simulator actually predicts that after some time, water will begin to be slowly displaced out of the matrix, as can be seen in Figure 5.17e, around the fracture at the core inlet after 1 PV.

Table 5.1 Input Parameters for Continuum Simulator

Rock Parameters	Matrix	Fracture
Porosity	0.18	1.0
Absolute Permeability (D)	0.2	1500
Water Relative Permeability	Power law (n = 3)	Linear
NAPL Relative Permeability	Modified Mualem*	Linear

Maximum Capillary Pressure (Pa)	7,600	1,380
Initial Pressure (atm)	1.001	1.001
Fluid Parameters	Water	PCE
Density (kg/m ³)	1000	1623
Viscosity (kg/m s)	0.0010	0.0093
Compressibility factor (%/atm)	0%	1%

* based on Demond and Roberts (1993), with $c = 0.4$, $d = 1.0$ $e = 0.5$.

The next simulation considers water imbibition into a permeable matrix with a fracture (Figure 5.18). The core is considered to be fully saturated with NAPL. Due to the homogeneous properties of the simulated matrix, water imbibes mostly as a uniform front, but since it can travel faster through the fracture, this creates a “shock wave” pattern ahead of the main wetting front. For comparison, in Figure 5.18d we present a similar situation but with no capillary pressure either in the matrix or the fracture. In this case, water travels extremely fast through the fracture (since there is no suction into the matrix), and the wetting front is uniform. We have not assumed any non-wetting phase trapping in these simulations (i.e. the relative permeabilities range from $S_w = 0$ to 1).

The third simulation compares water flooding to displace NAPL from two different cores, one with a fracture and one unfractured, with all other conditions the same. The initial water saturation is 25%, which is more realistic. Due to the higher initial water saturation, displacement of NAPL is easier (since the initial k_{rw} is larger than for a core 100% saturated with NAPL). After 0.25 PV, the wetting front is already breaking through at the outlet for the fractured core. For the unfractured core, the main wetting front has traveled less than half the core length after 0.25 PV. However, a comparison of the difference in water saturation between the fractured and unfractured cores after 0.50 PV (Figure 5.19e) indicates that NAPL removal is actually proceeding faster in the unfractured core, for the same volume of water injected. The explanation is that a

significant amount of water travels through the fracture to the outlet and thus does not contribute to cleaning the core. The implications for contaminant removal using water flooding in a fractured medium are clear.

5.4 Experimental Observation of Two-Phase Flow

5.4.1 Experimental Method

In addition to the three fractured cores characterized in chapter 3 (Core C, Core D and Core F), a non-fractured sandstone core (labeled Core E) of the same material as Core F was used to evaluate the differences between two-phase flow in porous media with or without fractures. The four cores were coated on the outside with a high viscosity, high temperature epoxy to eliminate the possibility of flow short-circuiting along the perimeter of the core, and prevent significant imbibition of the epoxy into the core or fracture. They were then placed inside a polycarbonate tube which served as the core holder. The annular space between the cores and the core holder was filled with a low viscosity, high temperature epoxy, which can easily fill in all the gaps and traps very little air. The end plates were constructed of the same polycarbonate material. To seal the end plates, a Viton O-ring was placed between the core and the end plate. In addition, outside the O-ring, a high-temperature silicon rubber (Dow Corning DAP) was applied. The construction of the core holder is shown in Figure 5.20 and the overall setup is shown in Figures 5.21 and 5.22.

Four different variables were measured during the displacements:

- (1) Phase saturation, using the CT scanner, typically by acquiring scans every 9 mm along the core. Even though the flow rates were generally low, in most cases the displacement was stopped during the CT-scanning, to obtain a static saturation profile along the core. At the beginning and end of a given displacement, a more intense scanning pattern was used, typically every 3 mm along the core, to obtain the final saturation.

- (2) Pressure, both at the inlet and the outlet, using pressure transducers (Celesco DP-31 with demodulators model CD10B). For the fractured cores, the transducers had a range of up to 1 psi ($6.9 \times 10^3 \text{ kg m}^{-1}\text{s}^{-2}$); for the unfractured sandstone, transducers with a range of 25 psi ($172 \times 10^3 \text{ kg m}^{-1}\text{s}^{-2}$) were used, given the much larger pressure drop for the same flow rate.
- (3) Flow rate, measured as the volumetric flow rate of the two liquid phases in the core's outlet, and also by maintaining a measured constant pumping rate from the two HPLC pumps (Model 48-00, Rainin Instruments), one for each liquid phase. Only one fluid was injected into the core at any one time. A four-way valve arrangement at the core entrance allowed us to almost instantaneously switch from one fluid to another, with both pumps already pumping at a constant flow rate.
- (4) Temperature, measured using five thermocouples placed at equal distances along the perimeter of the core and anchored in the high viscosity epoxy, as well as the outside temperature. The outside temperature was controlled at $22 \pm 1 \text{ }^\circ\text{C}$.

The displacements were performed in the following sequence:

- 1) Each dry core was first flushed with CO_2 for at least 30 minutes. The objective was to obtain complete water saturation of the core after imbibition, by dissolving the CO_2 . CO_2 dissolves slowly enough that we can measure the trapped gas saturation with the CT-scanner, but fast enough that we can achieve complete water saturation in less than 48 hr. This was also used to measure the permeability of the cores to gas, by measuring the flow rate of CO_2 using a Wet Test Flow Meter (Precision Scientific Co.).
- 2) Water was then allowed to imbibe at a low flow rate. Typical flow rates were 0.5 to 1.0 mL/min. Water was pumped through the cores for at least 48 hr before considering that complete saturation was achieved and that all the dissolved CO_2 had been pumped out of the core. After steady-state conditions

were achieved, the permeability of the cores to water was measured considering the flow rate and the pressure drop across the core.

- 3) NAPL was injected to displace water. Tetrachloroethylene (Baker) and n-decane (Fischer Chemical) were used for these displacements, in separate experiments. Flow rates were typically 0.75 to 1.25 mL/min. NAPL injection proceeded until the output from the core was consistently only NAPL. The sandstone cores were contaminated only with PCE, since it was not known *a priori* if we could clean them completely for another set of experiments.
- 4) Water flooding followed NAPL injection, to evaluate the effectiveness of NAPL removal using only water. Water injection proceeded until the output was consistently only water.
- 5) To ensure complete cleanup of the cores, water flooding was followed by steam injection. The details are explained in Chapter 6. Typically, additional NAPL was produced during the steam injection, and steam injection was continued until the condensate was essentially pure water. Samples of the final condensate were analyzed using liquid chromatography (Perkin-Elmer Series 400 Liquid Chromatograph, with Hewlett-Packard Series 1050 detector), to verify that the contaminant concentration was below detection limits.
- 6) The cores were then flushed with air for at least 24 hr before a new set of experiments.

5.4.2 Absolute permeability measurements

The absolute permeability of each core was measured both with gas (CO₂) and with water. In principle, absolute permeability is only a function of the material properties. The permeability to water was calculated assuming linear flow of an incompressible fluid (Dake, 1978):

$$k = \frac{QLm}{A\Delta P} \quad (5.12)$$

where Q is the volumetric flow rate (m^3/s)
 L is the length of the core (m)
 m is the viscosity of the fluid ($\text{kg m}^{-1} \text{s}^{-1}$)
 A is the cross-sectional area available for flow (m^2)
 DP is the pressure drop across the core ($\text{kg m}^{-1} \text{s}^{-2}$)

For the permeability to gas, Equation 5.12 is modified to account for the compressibility of the fluid (Scheidegger, 1974):

$$k = \frac{2QLm_g P_o}{A(P_i^2 - P_o^2)} \quad (5.13)$$

where m_g is the viscosity of the gas ($\text{kg m}^{-1} \text{s}^{-1}$)
 P_i is the inlet pressure ($\text{kg m}^{-1} \text{s}^{-2}$)
 P_o is the outlet pressure ($\text{kg m}^{-1} \text{s}^{-2}$)

For the sandstone cores, the whole core cross-section is available for flow, but for the granite cores, only the fracture's cross-section is actually available for flow, given the extremely low permeability of the granite matrix. The resulting permeabilities are shown in Table 5.2 .

Table 5.2 Absolute permeabilities

Type of core	Core C	Core D	Core E	Core F
	Single fracture in granite	Complex fractures in granite	Unfractured, layered sandstone	Fractured, layered sandstone
Theoretical permeability from fracture aperture (m^2)	29×10^{-9}	14×10^{-9}	Not applicable	1.5×10^{-9}
Gas permeability* (m^2)	$36 \pm 4 \times 10^{-9}$	$19 \pm 6 \times 10^{-9}$	$0.26 \pm 0.05 \times 10^{-12}$	$7.6 \pm 0.7 \times 10^{-12}$
Water permeability* (m^2)	$39 \pm 7 \times 10^{-9}$	$28 \pm 3 \times 10^{-9}$	$0.21 \pm 0.03 \times 10^{-12}$	$6.5 \pm 1.2 \times 10^{-12}$

*mean \pm standard deviation

There is a small discrepancy between the permeability to gas and the permeability to water; typically the water permeability is higher, in particular in the fractured cores. The theoretical permeability is calculated using the square of the hydraulic aperture (geometric mean) according to Equation 3.13, and in general is a good predictor of the actual permeability. The error is greater for Core D given the complexity of the fracture network in that core. For Core F, the permeability of the fracture is considerably larger than the permeability of the matrix, and even a fracture with a hydraulic aperture of 0.135 mm is sufficient to increase the overall permeability of the core by more than an order of magnitude. Note that for the fracture we consider the mean cross-sectional area of the fracture, whereas for the whole core we consider the total cross-sectional area.

5.4.3 Saturation profiles

To obtain the two-phase saturation information, three CT-scans are needed at each position: (a) a scan of the initial resident phase (e.g. air or water); (b) a scan of the fully saturated core with the invading phase (e.g. water or NAPL); and (c) a scan of the core during the displacement of the resident phase by the invading phase, at various saturations. Saturation can then be calculated using:

$$S_w = \frac{(CT_{aw} - CT_{ar})}{(CT_{wr} - CT_{ar})} \quad (5.14)$$

where CT_{aw} is the scan with intermediate air-water saturation
 CT_{wr} is the scan with the rock fully saturated with water
 CT_{ar} is the scan with the rock fully saturated with air.

For NAPL saturations, the same equation is used, substituting NAPL for air. To obtain nearly 100% NAPL saturation, at the end of the displacements experiments, the core was steam-cleaned, dried overnight in an oven at 110 °C, then filled with dry CO₂, which was then displaced with NAPL for at least 48 hr. After scanning, the core was again water-flooded, steam-cleaned and oven-dried.

From the individual CT images (or slices), a two- or three-dimensional reconstruction of the saturation profile was realized using MATLAB. For the fractured granite cores, the saturation is presented as a top and side view of the fracture plane. For the sandstone cores, the saturation is presented in a set of horizontal and vertical “reconstructed slices” along the length of the core, which best present the advancing front. The difference between the PCE and decane saturations after the displacements is generally not very large, so unless it is otherwise noted, we only present the PCE saturations.

5.4.3.1 Water imbibition into dry cores

Figure 5.23 presents the imbibition of Core C at four different stages. In the top image, after 0.28 pore volumes (PV) have been injected into the core, the water front has moved along more than half of the fracture plane, but apart from a rather sharp front carrying high saturation (at around 70 mm along the length of the core), the saturations behind the front are low. This may be explained by the fact that this first region is generally of low aperture, with flow mostly through layers along the fracture walls. There is also some evidence that flow through layers is occurring ahead of the main front.

After 0.56 PV, the front has smeared to a large wet region with an average water saturation of about 0.4, and a few highly saturated regions which probably are large drops of water in the larger aperture regions. The water imbibing through layers has moved well ahead and is beginning to collect at the outlet (although there is still no flow in the outlet tubing). By 1.1 PV, the average water saturation in the core is higher, with many more regions already at full saturation. A few highly conducting channels appear to have evolved. The last image in Figure 5.23 presents the situation after 2.3 PV have flowed. While some regions exhibit quite high (or full) water saturation, some regions with quite low water saturation remain.

After more than 24 hours of continuous water flow through the core, approximately 180 PV, the core was scanned at 3 mm spacing between scans. At this point, the fracture plane was assumed to be essentially water saturated. The top and side views of the water

saturated fracture plane are shown in Figure 5.24. Fairly uniform complete water saturation in the fracture is achieved. Comparing Figure 5.24 to Figure 2.13 (which presents the reconstruction of the fracture aperture for Core C), there is a very good correlation between the available flow region from the aperture distribution and the actual flow based on water saturation. Features such as regions of extremely low aperture in Figure 2.13 appear as dry spots in Figure 5.24, indicating that these are probably contact points between the upper and lower fracture faces. These results also correlate reasonably well with the discrete fracture network model simulations, which indicate that initially flow is around the sides of the fracture, in the low aperture region, leaving large gas bubbles trapped. Only after dissolution of CO₂ does the water saturation rise in these regions.

In Figures 5.25 and 5.26 we present the imbibition of water into Core D as seen on the top and side views respectively, from 0.19 PV to 37 PV injected. Although the main front is always connected to the inlet, at early times only a few pathways have high water saturation. At later times, the whole fracture plane becomes almost completely saturated with water. Although the plane has a mean aperture of 0.6 mm, it appears much wider in the side view (Figure 5.26) since the plane is oriented at an angle with respect to the view. By 1.3 PV water is already being produced at the outlet, but the image indicates that the vertical fracture still contains trapped gas bubbles. After 37 PV, the vertical fracture is also water saturated. The higher resolution of the image at 37 PV is due to a more intense scanning spacing of 3 mm. The fully water saturated images of the top and side view correlate very well with the images from the fracture aperture reconstruction, Figures 2.15 and 2.16. As noted for Core C, there are several points that have zero water saturation, corresponding to contact points between the upper and lower fracture faces. The only anomaly is the absence of water saturation in the vertical fracture near the inlet of Core D, which according to the aperture reconstruction should be a region where water could imbibe.

Due to the much higher capillary pressures in a dry sandstone matrix, imbibition into the unfractured, layered sandstone Core E occurs very readily, as seen in Figure 5.27.

Ahead of the main wetting front, imbibing water at low saturation coats the grain surfaces, seen as a “halo” in the 0.1 PV and 0.36 PV images. These images are reconstructed longitudinal, horizontal slices through the middle of the core and are representative of the movement of the wetting front through the core. Although care was taken to avoid low-viscosity epoxy in the end faces, apparently a thin coating of epoxy affected the periphery of the inlet face. However, the wetting front stabilizes as it travels further into the core, so this end effect is not very severe. At 0.83 PV, water begins to flow in the outlet, although the core is not yet fully saturated. After 7.8 PV of water have been pumped, the saturation profile is almost stable, with only a few residual gas bubbles still dissolving. The core was pumped an additional 24 hr before the next set of displacements. The average porosity of the core was calculated using both a mass balance and the information from the CT scans to be 17.6 ± 2.2 %. There is an apparent variation in porosity between the lighter and darker layers in the sandstone. This variation in properties for the two layers was also evident in the channeling of the water front, seen in the image at 0.36 PV. Associated with the variation in porosity may be a difference in wetting properties and/or capillary pressure.

Imbibition into the dry, fractured, layered sandstone Core F proceeds in a very similar manner (Figure 5.28). The images present a reconstructed longitudinal, vertical slice through the middle of the core, with the fracture shown above a height of 20 mm as a linear feature, since the horizontal fracture plane is almost perpendicular to this view. While the wetting front is advancing in the porous media, capillary forces pull practically all of the moisture from the fracture into the matrix. Water is also moving into the matrix through advection, but not inside the fracture. Only a thin wetting layer partially coats the fracture walls ahead of the wetting front. After 20 PV have been pumped, the water saturation in the matrix is comparable to the unfractured Core E, and the fracture is 100% water saturated. On this side view it is also possible to observe the preferential wetting of certain layers first, and that even at very high saturation, there is some variability in the

water saturation in the layers, and possibly some variation in the x-ray signal due to differences in chemical composition of the various sandstone layers.

In comparing the images between the simulated saturation profiles (Figures 5.8 to 5.19) and the experimentally observed profiles (Figures 5.23 to 5.35), there are some common points and some notable differences. First, comparing the granite fractures with respect to the result of the network model simulations, we observe that at early time there are preferential flow paths for the imbibing water, which in both cases tend to be towards the edges of the fracture, where some of the smallest apertures are found. Since the wetting phase can travel quickly through these paths, it tends to bypass the non-wetting phase, leaving behind a significant “residual” gas saturation. This is common to both the simulation results and the experimental observations. However, it is likely that during the experiments the flow was not only dominated by capillary forces, but there was also a non-negligible advective component, which displaces more of the trapped gas phase, resulting in lower gas residual. Since we used a very soluble gas, eventually most or all of the trapped gas was displaced.

In the case of the sandstone cores, we observe the significant role that capillary forces have during imbibition, both in the numerical simulation (Figures 5.18 and 5.19) and in the experimental observations (Figures 5.27 and 5.28). Although the fracture is a very low resistance flow path, capillary forces drive the water into the matrix, and only when the matrix is fairly water saturated does water flow in the fracture become significant. The main difference between the simulation and the experimental observations is the rather square front observed experimentally, as opposed to the conical front predicted by the simulator. This may be due to differences in the assumed P-S curve for the matrix in the simulator with respect to the actual P-S curve of the sandstone cores.

5.4.3.2 Primary Drainage: NAPL displacing water

The drainage of the water-saturated granite cores using either decane or PCE results in only partial displacement of water. The decane and PCE images are qualitatively similar, so we present only the PCE displacements unless otherwise noted in the text. In Figure 5.29, the displacement of water from Core D using PCE is presented, from 0.21 PV to 1.45 PV. The figure presents both the top views and the side view of the displacement, to observe the flow of PCE into the vertical fractures of Core D. As the PCE front progresses through the core, it fills the vertical fracture near the inlet, which appears as a region of very high saturation. In the low aperture region of the core (from 50 to 200 mm along the length of the core), some PCE channels form, by-passing water, which remains in place due to capillary forces. PCE begins to fill the large vertical fracture near the core outlet after 0.65 PV have been injected. The image at 1.45 PV is at a higher resolution (3 mm between scans), but essentially confirms that the vertical fractures are PCE filled and that the low-aperture region contains a mixed water-PCE saturation.

For comparison, the drainage of the water-saturated Core D by decane is presented in Figure 5.30. In this case, decane is less dense than water and so it does not invade the vertical fracture, and travels basically only through the horizontal fracture plane. The final NAPL saturations for PCE and decane injection are similar, with some differences in the total amount of water displaced.

Drainage of the water-saturated sandstone Core E also results in incomplete water displacement (Figure 5.31). In this particular instance, flow occurs from right to left. At 0.19 PV, the PCE front exhibits some fingering, as seen on a horizontal slice through the middle of the core. The fingering appears to be well correlated with the layers in the core. One type of layer is a preferential pathway for PCE, with higher average PCE saturations. In addition (not shown), the front advances faster through the lower part of the core than through the upper part, due to gravity segregation of the flow. Breakthrough of PCE occurs quite fast, since it is only filling a small percentage of the void space. The saturation profile of PCE that is established along the core after

breakthrough (0.46 PV) varies little as more and more PCE flows through the core (e.g. image at 1.1 PV).

The situation is quite different for the water-saturated, fractured sandstone Core F. In this case, the NAPL (either decane or PCE) does not overcome the capillary entry pressure to displace water out of the pore space. As seen in Figure 5.32, PCE travels only through the fracture. Breakthrough at the core outlet is extremely fast, within 0.07 pore volumes, since the only pore space that the PCE can access due to capillary pressure is in the fracture. Even then, not all of the fracture plane is saturated with PCE, as seen in the last image in Figure 5.32. A main PCE channel forms on one side of the core, with a secondary channel along the other side of the core. Although the flow rate through the core was subsequently increased by a factor of ten, to 12.5 mL/min, there was still no displacement of water from the sandstone matrix, since the additional pressure is relieved through the fracture. The fractured sandstone matrix thus behaves like the impermeable granite matrix when it is fully water saturated and there is a fracture to allow the flow of NAPL.

Direct correspondence between the simulations and the experimental observations was not expected, but the common results are encouraging. The network simulations (Figures 5.5, 5.8 and 5.10) predict a very low residual for water in the fracture, held only in the lowest aperture regions, since the pressure required to displace water from the rest of the fracture is very low. Experimentally we observe (Figures 5.29, 5.30, 5.31 and 5.32) that the water saturation at the end of these displacements is very low, but there are clearly some regions where water is held tighter. In the case of the fractured sandstone core, the simulation accurately predicted that there would be practically no displacement of water from the matrix, since NAPL would flow preferentially through the fracture. In fact, since the pressure is easily relieved through the fracture, it is likely that little NAPL will enter the matrix even after several pore volumes of NAPL are injected, or in a natural setting, even with a pool of several centimeters of NAPL.

5.4.3.3 Secondary Imbibition (water flooding): water displacing NAPL

In a horizontal fracture in granite, for example in Core C, water flooding to displace NAPL can be an effective means of removing a large fraction of NAPL. For example, in Figure 5.33 we see the removal of PCE from Core C by pumping with water. The first image at 0 PV presents PCE saturation after it has been injected to displace water. A high NAPL saturation has been achieved in most of the core, although the low aperture region at left still has very low PCE saturation. Capillary forces holding the water in this low aperture region are probably larger than the viscous forces. As water is injected (from outlet to inlet, or right to left) PCE is displaced. After around 1 PV of injection, the PCE saturations have been reduced significantly. However, even after 2.44 PV, there is still a residual PCE saturation. For these small cores, injecting sufficient water may be enough to remove NAPL from the granite surface. However, in practical field settings, injecting several pore volumes may be impractical as a remediation scheme.

For Core D, with its more complex set of horizontal and vertical fractures, cleaning a fracture network via water flooding will leave behind a significant fraction of NAPL. In Figure 5.34, the NAPL saturation in the vertical fracture is still relatively unchanged after 1.2 PV have been pumped. The top image shows the saturation on the horizontal fracture plane, where remaining NAPL has decreased significantly, except where there are vertical fractures, i.e. near the inlet and outlet. The bottom image is the side view of the core. Because of the way the image is generated (projecting the three-dimensional NAPL saturation to a two-dimensional representation, rather than as a thin slice), it appears that the horizontal fracture plane still carries significant NAPL, while in fact the NAPL saturation is relatively low in this plane.

The situation is worse for NAPL in a porous matrix, exemplified by sandstone Core E. Figure 5.35 presents the results of a water flood after PCE has contaminated the matrix. The first image presents the NAPL saturation as seen in a vertical slice through the core. Layers with higher NAPL saturation are intermixed with layers of low NAPL saturation. The core was subjected to water flooding overnight. After 3.9 PV have been

injected, NAPL saturations have decreased near the inlet (the water was injected from inlet to outlet, or left to right in the images), but are still rather high near the outlet. There is a preferential removal of PCE based on the layering, but this may also reflect the higher relative permeability through the uncontaminated layers. Overall, NAPL removal via water flooding is probably quite slow, and depends on dissolution of the remaining NAPL as the principal mechanism for cleanup.

Since the network model assumes that flow is capillary dominated, it is inadequate for modeling water flooding in the granite cores. In fact, we observe that water flooding in these cores displaces most of the NAPL in the horizontal plane after several pore volumes have been injected, but it may leave a small (but environmentally significant) residual contamination, and especially in the case of a complex fracture, such as is the case with Core D. Numerical simulation of water flooding in the sandstone cores suggest that it takes a significant amount of time to remove all of the NAPL, and the experimental observation in Core E corresponds with this prediction. In the case of Core F, water flooding was very effective because only the fracture had been contaminated.

5.5 Discussion

Our experimental observation of imbibition into fractured and unfractured porous media, in this case sandstone cores, is in good agreement with the observations of Martinez et al. (1992), Wang and Narasimhan (1985) and Dykhuizen (1987). Water imbibes first into the matrix, displacing air or NAPL, and only fills the wider fracture apertures when the matrix achieves high water saturation. As the macroscopic P-S curves generated from the fracture aperture distribution indicate, the capillary pressures in the fractures are significantly smaller than those in the matrix, confirming the previous work by Pruess and Tsang (1990) and Kueper and McWhorter (1991). The shape of the P-S curves derived from the fracture aperture distribution is similar to the P-S curves presented by Kueper and McWhorter (1991).

Our initial analysis with the network model indicated a linear relationship between relative permeability and saturation, in agreement with the experimental work by Romm (1966) on fractures. However, as explained above, the calculation of the relative permeabilities from the available (and connected) cross-sectional area is incorrect. In fact, the displacing/displaced fronts move as sharp fronts, as assumed by Buckley-Leverett theory, with a relative permeability close to unity until the other phase is trapped. Further experimental work is needed in this area to confirm the actual shape of the relative permeabilities. It is clear that for a one-time imbibition or drainage (rather than co-current two-phase flow as done by Demond and Roberts, 1993), the macroscopic relative permeability is zero for the invading phase and close to one for the displaced phase until breakthrough, unless there are some dynamic flow patterns as observed by Fourar et al. (1993).

5.6 Summary and Conclusions

In this chapter the fracture aperture distribution information and the pore scale observation of two-phase flow behavior are employed to construct a discrete fracture network model, which can then be used to simulate two-phase displacements in a single fracture. We predict the saturation changes as a function of monotonically-increasing invading fluid pressure, and calculate the average saturation in the fracture at a given capillary pressure and the relative permeabilities of both phases as a function of saturation.

The capillary pressure-saturation curves from the network model predict hysteresis between the drainage and imbibition paths, because the flow path of the invading phase is significantly different for each case. Wetting fluid imbibes through the smaller fracture apertures first, and can by-pass non-wetting fluid, which is then trapped and immobilized unless the injection pressure is large enough to result in concurrent flow of both fluids.

In the case of drainage, the non-wetting fluid invades through the larger pores, and even if the wetting phase appears trapped, it can actually flow through thin layers along the walls of the fracture, although at a slow rate. The P-S curves from the network model exhibit sharp changes in saturation at particular points in the displacement, when the pressure has built up and is suddenly sufficient to breach a small aperture, at which point a large portion of the fracture can be invaded. This differs from the macroscopic P-S curves generated strictly from the known fracture aperture distribution or its statistical representation as a log-normal distribution, which predict a continuous change in saturation with increasing or decreasing pressure. The network model represents the microscopic or pore-scale behavior, whereas at the macroscopic scale the abrupt changes in saturation are averaged together. In general, the capillary pressures in a fracture are quite small relative to those in a porous matrix, resulting in preferential invasion through the fracture rather than displacement from the matrix, except for the case of imbibition.

The network model predicts a linear relationship between saturation and relative permeability of either phase. In the case of drainage, almost the full range of saturations is available, except for very low water saturations which require very high non-wetting fluid pressure to displace water from the smallest apertures. For imbibition, the trapping of non-wetting phase is strongly path dependent, resulting in a reduced range of saturations. The relative permeabilities are still linear with saturation within this reduced range. Since the pressure required to mobilize trapped non-wetting phase in a fracture is relatively small (compared to mobilization of trapped non-wetting phase in the porous matrix), it is possible that co-current flow of wetting and non-wetting phase will occur, which then results in significant flow interference and reduced relative permeabilities. The relative permeabilities in a fracture are thus dependent on flow rate.

The discrete fracture network model is adequate to simulate the changes in phase saturation during the displacements in a single fracture in an impermeable matrix, as the comparison between simulated and measured saturation fields indicates. A possible future extension of the model can include the flow behavior at fracture intersections and in a network of fractures, such as those in core D, with gravity forces playing a role in

driving the flow. Since the model requires a very high resolution description of the fracture geometry, it is more applicable as an analytical tool to study the effect of the fracture aperture variations (also called the fracture roughness) on capillary pressure and relative permeabilities.

The continuum model is a large-scale tool, that is inadequate for modeling multiphase flow at high pore geometry resolution. It is more suitable for studying the capillary driven flow interactions between fracture and matrix. It requires as inputs the K-S-P relationships, which can be generated by the discrete fracture network model. The comparison between simulated two-phase flow behavior in a fractured sandstone and the measured changes in saturation agree well.

Both the simulations and the experimental observations point to some common processes in two-phase flow in fractured media. Imbibition in an impermeable matrix occurs through preferential flow paths along the smallest apertures, and results in significant non-wetting phase trapping at low flow rates, where capillary forces dominate. At higher flow rates, the trapped non-wetting phase may be displaced by advective forces. In a permeable matrix, water imbibition is mostly through the matrix, until the matrix water saturation is high, allowing the fracture to fill.

Drainage proceeds through the largest apertures, but in a fracture the residual water saturation can be very small even at very low displacement pressures. When the matrix is permeable and water saturated, non-wetting phase travels practically only through the fracture and does not invade the matrix. It may of course dissolve with time, in which case the matrix is contaminated by diffusion through the aqueous phase.

The simulations also predict that water flooding will take even longer to remediate a NAPL-contaminated fractured permeable medium, since a significant volume of injected water travels through the fracture rather than displace NAPL from the matrix. Even in an impermeable matrix, water flooding to remove NAPLs from a fracture medium will most likely leave a significant amount of NAPL trapped in dead-end and complex fractures.

5.7 References

- Abriola, L. M. and G. F. Pinder, 1985: A multiphase approach to the modeling of porous media contamination by organic compounds, 1, Equation development, *Water Resources Research*, **21**:1, 11-18
- Adamson, A. W., 1982: *Physical Chemistry of Surfaces*, 4th ed., Wiley, New York
- Avraam, D. G. and A. C. Payatakes, 1995: Generalized relative permeability coefficients during steady-state two-phase flow in porous media, and correlation with the flow mechanisms, *Transport in Porous Media*, **20**, 135-168
- Aziz, K. and A. Settari, 1979: *Petroleum Reservoir Simulation*, Applied Science, London
- Baehr, A. L. and M. Y. Corapcioglu, 1987: A compositional multiphase model for groundwater contamination by petroleum products, 2, Numerical solution, *Water Resources Research*, **23**:1, 201-213
- Bear, J., 1972: *Dynamics of fluids in porous media*, American Elsevier, New York
- Buckley, S. E. and M. C. Leverett, 1942: Mechanism of fluid displacement in sands, *Trans. Am. Inst. Min. Metall. Pet. Eng.*, 107-116
- Corey, A. T., 1954: The interrelationship between gas and oil relative permeabilities, *Prod. Mon.*, **19**, 38-41
- Dake, L. P., 1978: *Fundamentals of reservoir engineering*, Elsevier, Amsterdam
- Dawson, H. E., 1992: *Entrapment and mobilization of residual halogenated organic liquids in saturated aquifer material*, Ph.D. dissertation, Stanford University, Stanford, California
- Demond, A. H. and P. V. Roberts, 1993: Estimation of two-phase relative permeability relationships for organic liquid contaminants, *Water Resources Research*, **29**:4, 1081-1090
- Demond, A. H., 1988: *Capillarity in two-phase liquid flow of organic contaminants in groundwater*, Ph.D. dissertation, Stanford University, Stanford, California
- Dong, M. and I. Chatzis, 1995: The imbibition and flow of a wetting liquid along the corners of a square capillary tube, *J. Colloid and Interface Science*, **172**, 278-288
- Dykhuizen, R. C., 1987: Transport of solutes through unsaturated fractured media, *Water Resources Research*, **23**:12, 1531-1539
- Fourar, M., S. Bories, R. Lenormand and P. Persoff, 1993: Two-phase flow in smooth and rough fractures: measurement and correlation by porous-medium and pipe flow models, *Water Resources Research*, **29**:11, 3699-3708
- Guarnaccia, J. F. and G. F. Pinder, 1992: A new two-phase flow and transport model with interphase mass exchange, in *Computational methods in water resources IX, vol. 2: Mathematical modeling in water resources*, Computational Mechanics Publications, Boston, Massachusetts
- Ichikawa, N. and Y. Satoda, 1994: Interface dynamics of capillary flow in a tube under negligible gravity condition, *J. Colloid and Interface Science*, **162**, 350-355
- Intera Information Technologies Limited, 1994: Eclipse 100 Reference Manual -- 95A Release, Intera Information Technologies Limited, Henly--on--Thames, Oxfordshire RG9 4PS, England}}
- Jerauld, G. R. and S. J. Salter, 1990: The effect of pore-structure on hysteresis in relative permeability and capillary pressure: Pore level modeling, *Transport in Porous Media*, **5**, 103-151
- Kaluarachchi, J. J. and J. C. Parker, 1990: Modeling multicomponent organic chemical transport in three-fluid phase porous media, *J. of Contaminant hydrology*, **5**, 349-374
- Karasaki, K., S. Segan, K. Pruess and S. Vomvoris, 1994: A study of two-phase flow in fracture networks, Lawrence Berkeley Lab. Rep., LBL-34706
- Kazemi, H. and J. R. Gilman, 1989, Multiphase flow in fractured petroleum reservoirs, paper presented at the Advanced Workshop on Heat and Mass Transport in Fractured Rocks, LNEC, Lisbon
- Kueper, B. H. and E. O. Frind, 1991: Two-phase flow in heterogeneous porous media: 1. Model development, *Water Resources Research*, **27**:6, 1049-1057
- Kueper, B. H. and D. B. McWhorter, 1992: Use of macroscopic percolation theory to construct large-scale capillary pressure curves, *Water Resources Research*, **28**:9, 3699-3708
- Kueper, B. H. and D. B. McWhorter, 1991: The behavior of dense, nonaqueous phase liquids in fractured clay and rock, *Ground Water*, **29**:5, 716-728
- Long, J. C. S., E. L. Majer, S. J. Martel, K. Karasaki, J. E. Peterson Jr., A. Davey and K. Hestir, 1990: Hydrologic characterization of fractured rocks - An interdisciplinary methodology, *Rep. LBL-27863*, Lawrence Berkeley Lab., Berkeley, California

- Martinez, M. J., R. C. Dykhuizen and R. R. Eaton, 1992: The apparent conductivity for steady unsaturated flow in periodically fractured porous media, *Water Resources Research*, **28**:11, 2879-2887
- Merrill, L. S., 1975: *Two-phase flow in fractures*, Ph.D. dissertation, Univ. of Denver, Denver, Colorado
- Myshkis, A. D., V. G. Babskii, N. D. Kopachevskii, L. A. Slobozhanin and A. D. Tyuptsov, 1987: *Low-gravity fluid mechanics*, Springer-Verlag, New York
- Parker, J. C. and R. J. Lenhard, 1987: A model for hysteretic constitutive relations governing multiphase flow, 1. Saturation-Pressure relations, *Water Resources Research*, **23**:12, 2187-2196
- Peaceman, D. W., 1977: *Fundamentals of numerical reservoir simulation*, Elsevier, Science, New York
- Persoff, P. and K. Pruess, 1995: Two-phase flow visualization and relative permeability measurement in natural rough-walled rock fractures, *Water Resources Research*, **31**:5, 1175-1186
- Pinder, G. F. and L. M. Abriola, 1986: On the simulation of non-aqueous phase organic compounds in the subsurface, *Water Resources Research*, **22**:9, 109s-119s
- Pruess, K. and Y. W. Tsang, 1990: On two-phase relative permeability and capillary pressure of rough-walled rock fractures, *Water Resources Research*, **26**:9, 1915-1926
- Pruess, K., G. S. Bodvarsson, V. Stefansson and E. T. Eliasson, 1984: The Krafla geothermal field, Iceland, 4, History match and prediction of individual well performance, *Water Resources Research*, **20**:11, 1561-1584
- Pyrak-Nolte, L. J., D. Helgeson, G. M. Haley and J. W. Morris, 1992: Immiscible fluid flow in a fracture, in Proceedings of the 33rd U. S. Rock Mechanics Symposium, edited by J. R. Tillerson and W. R. Wawersik, pp. 671-578, Balkema, Rotterdam, Netherlands
- Reeves, H. W. and L. M. Abriola, 1988: A decoupled approach to simulation of flow and transport of non-aqueous organic phase contaminants through porous media, in Celia, M. A. et al. (eds.), *Computational Methods in Water Resources, Vol. 1 Modeling surface and subsurface flows*, Elsevier, New York
- Reitsma, S. and B. H. Kueper, 1994: Laboratory measurement of capillary pressure-saturation relationships in a rock fracture, *Water Resources Research*, **30**:4, 865-878
- Romm, E. S., 1966: *Fluid flow in fractured rocks*, Nedra, Moscow
- Rossen, W. R. and A. T. A. Kumar, 1992: Single- and two-phase flow in natural fractures, paper SPE-24195 presented at the 67th Annual Technical Conference of the Society of Petroleum Engineers, Washington, D. C.
- Scheidegger, A. E., 1974: *The physics of flow through porous media*, 3rd ed., University of Toronto Press, Toronto
- Thiele, M. R., R. P. Batycky, M. J. Blunt and F. M. Orr Jr., 1996: Simulating flow in heterogeneous systems using streamtubes and streamlines. SPE Reservoir Engineering, February 1996, 5-12.
- Thomas, L. K., T. N. Dixon and R. G. Pierson, 1983: Fractured reservoir simulation, *Soc. Pet. Eng. J.*, **23**:1, 42-54
- Verma, A. K., 1990: *Effects of phase transformation on steam-water relative permeabilities*, Ph.D. Dissertation, Univ. of Calif., Berkeley, California
- Verma, A. K., 1986: Effects of phase transformation on steam-water relative permeabilities, *Rep. LBL-20594*, Lawrence Berkeley Laboratory, Berkeley, California
- Wang, J. S. Y. and T. N. Narasimhan, 1985: Hydrologic mechanisms governing fluid flow in a partially saturated, fractured, porous medium, *Water Resources Research*, **21**:12, 1861-1874
- Warren, J. E. and P. J. Root, 1963: The behavior of naturally fractured reservoirs, *Soc. Pet. Eng. J.*, **3**:5, 245-255
- White, M. D., M. Oostrom and R. J. Lenhard, 1995: Modeling fluid flow and transport in variably saturated porous media with the STOMP simulator. 1. Nonvolatile three-phase model description, *Advances in Water Resources*, **18**:6, 353-364
- Wyllie, M. R. J., 1962: Relative permeability, in Petroleum Production Handbook, vol. II, Reservoir Engineering, edited by T. C. Frick and R. W. Taylor, McGraw-Hill, New York

Figure 5.1 At every pressure step, the neighboring cells are evaluated to determine if the injection pressure is sufficient for invasion. 1 = non-wetting, 0 = water.

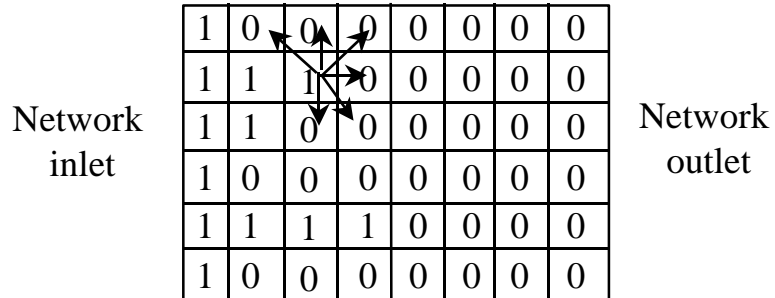


Figure 5.2 Idealized pore space to illustrate the concepts of contact angle, θ , and the angle between surfaces, α .

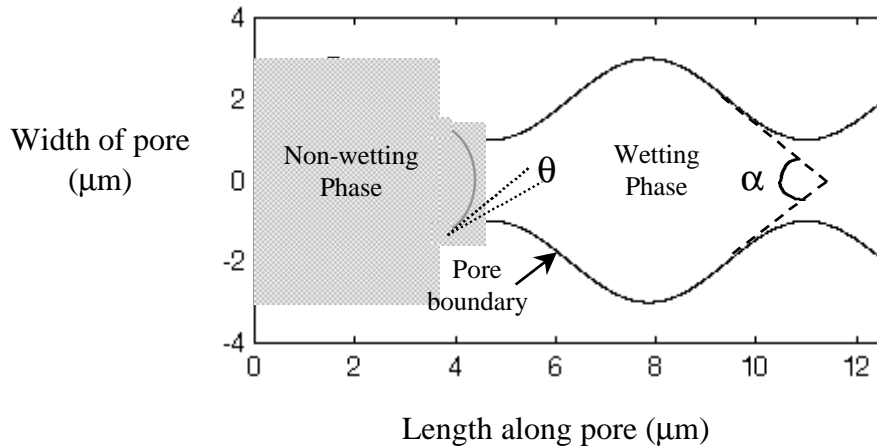


Figure 5.3 Normalized Capillary Pressure within a single pore, considering $\theta = 10^\circ$.

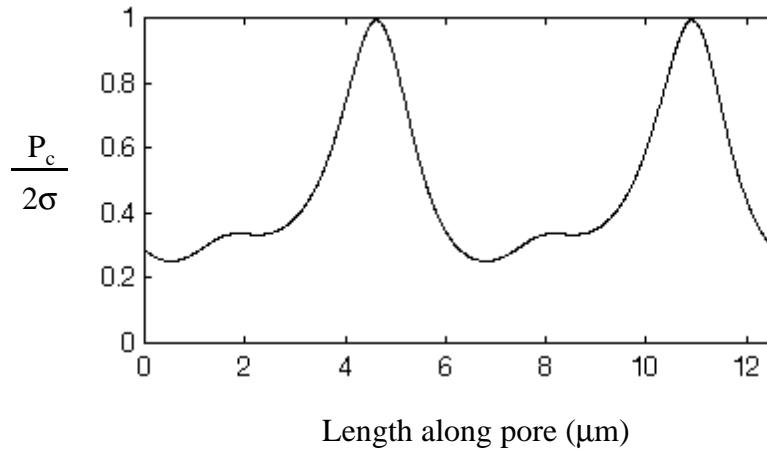


Figure 5.4 Scaled Capillary Pressure vs. Saturation relationship, based on the fracture aperture distribution for: (a) core C, (b) core D, horizontal plane, and (c) core F.

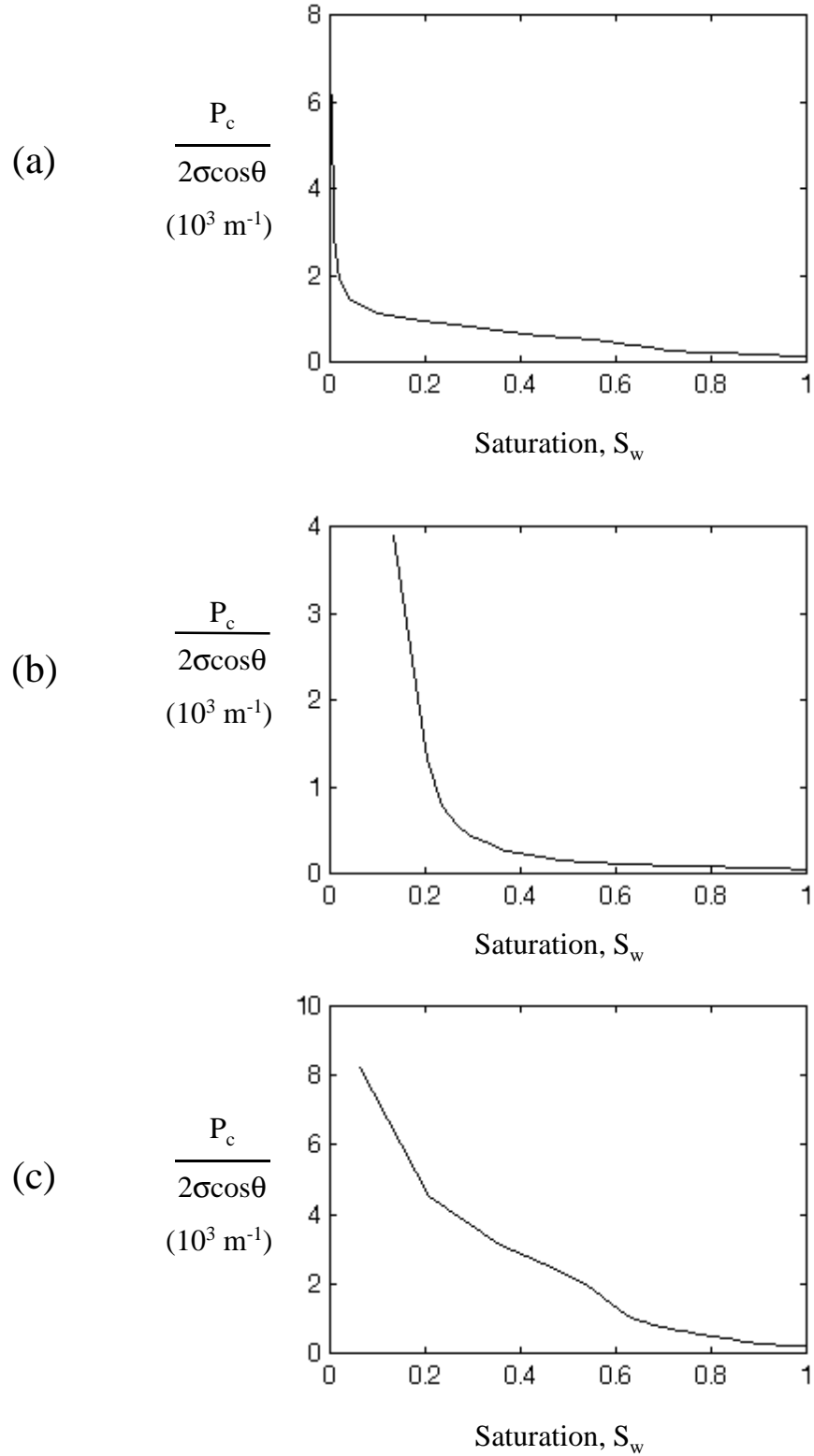


Figure 5.5 Simulated drainage sequence for core C, based on the discrete fracture network model. Water is in red, non-wetting phase in yellow and the impermeable matrix in blue. Injection pressure is increased as noted above the figures. Pressure is scaled to units of (m^{-1}). All displacements are in a horizontal plane from left to right.

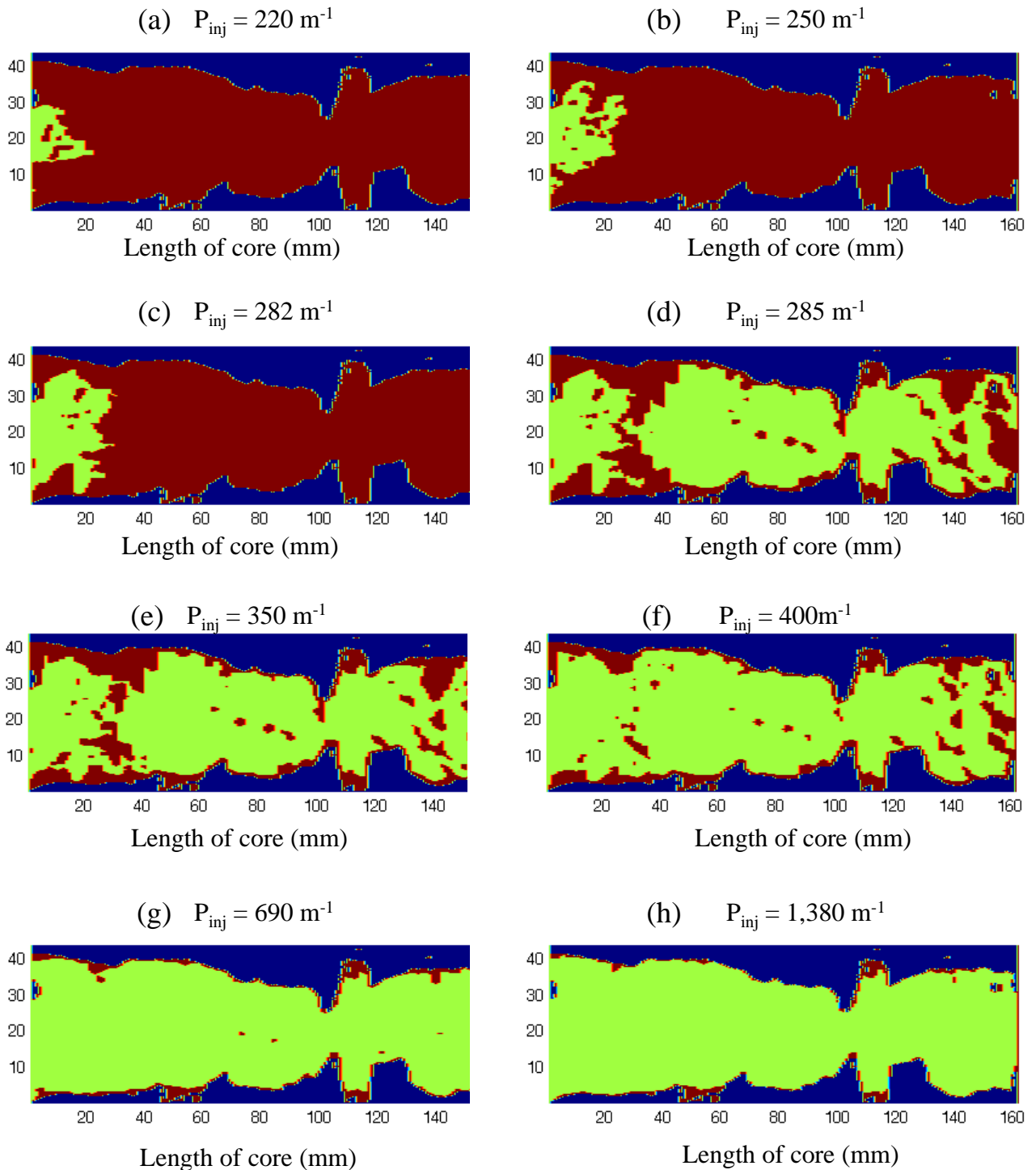


Figure 5.6 Simulated imbibition sequence for core C, based on the discrete fracture network model. Water is in red, trapped non-wetting phase in yellow-green, flowing non-wetting phase in light blue and the impermeable matrix in blue. Capillary pressure decreases as noted above the figures. Pressure is scaled to units of (m^{-1}). All displacements are in a horizontal plane from left to right.

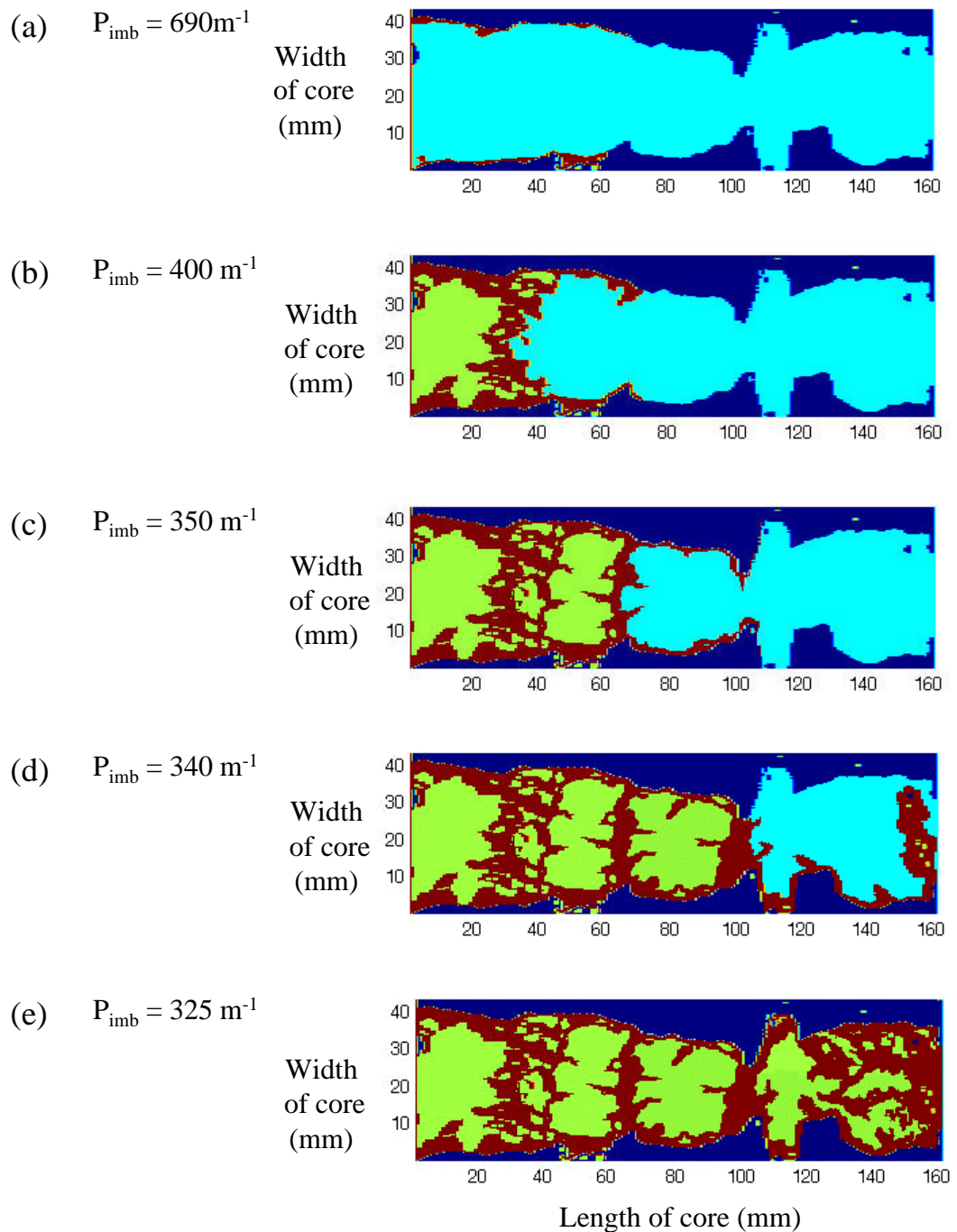


Figure 5.7 Scaled Capillary Pressure vs. Saturation relationship, based on discrete fracture network model for: (a) core C, (b) core D, horizontal plane, and (c) core F.

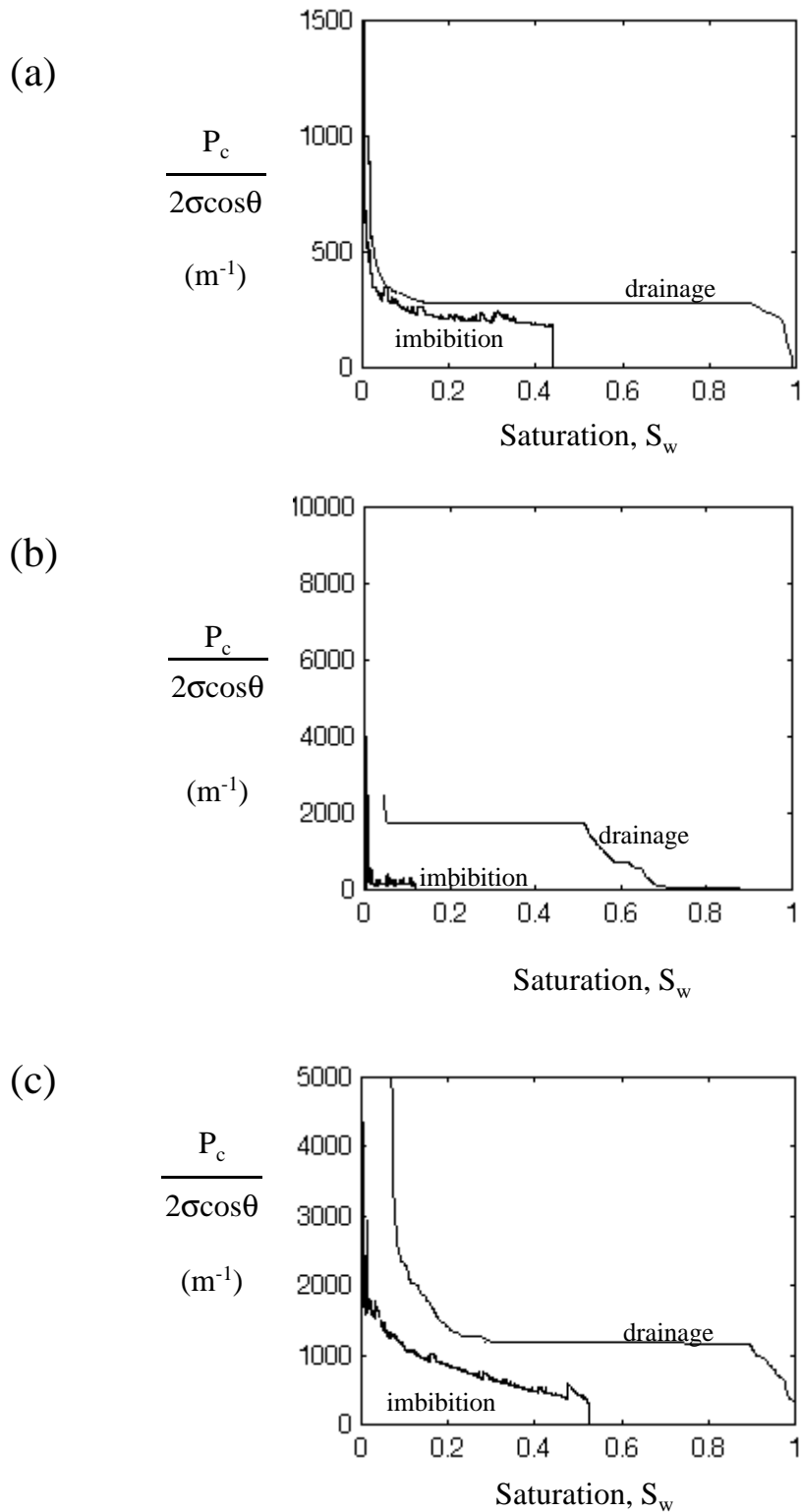


Figure 5.8 Simulated drainage sequence for core D, based on the discrete fracture network model. Water is in red, non-wetting phase in yellow-green and the impermeable matrix in blue. Capillary pressure increases as noted above the figures. Pressure is scaled to units of (m^{-1}). All displacements are in a horizontal plane from left to right.

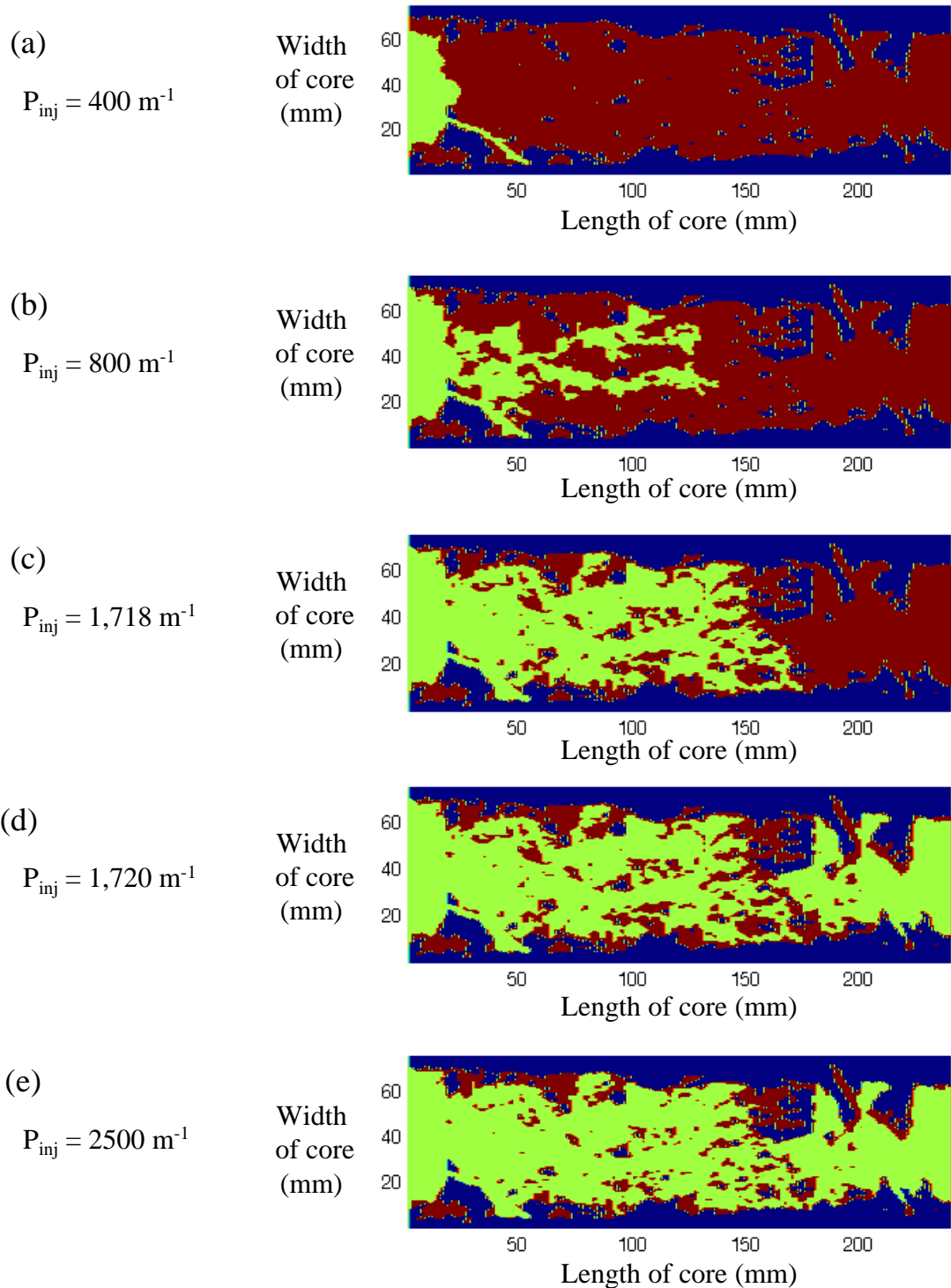


Figure 5.9 Simulated imbibition sequence for core D, based on the discrete fracture network model. Water is in red, trapped non-wetting phase in yellow-green, flowing non-wetting phase in light blue and the impermeable matrix in blue. Capillary pressure decreases as noted above the figures. Pressure is scaled to units of (m^{-1}). All displacements are in a horizontal plane from left to right.

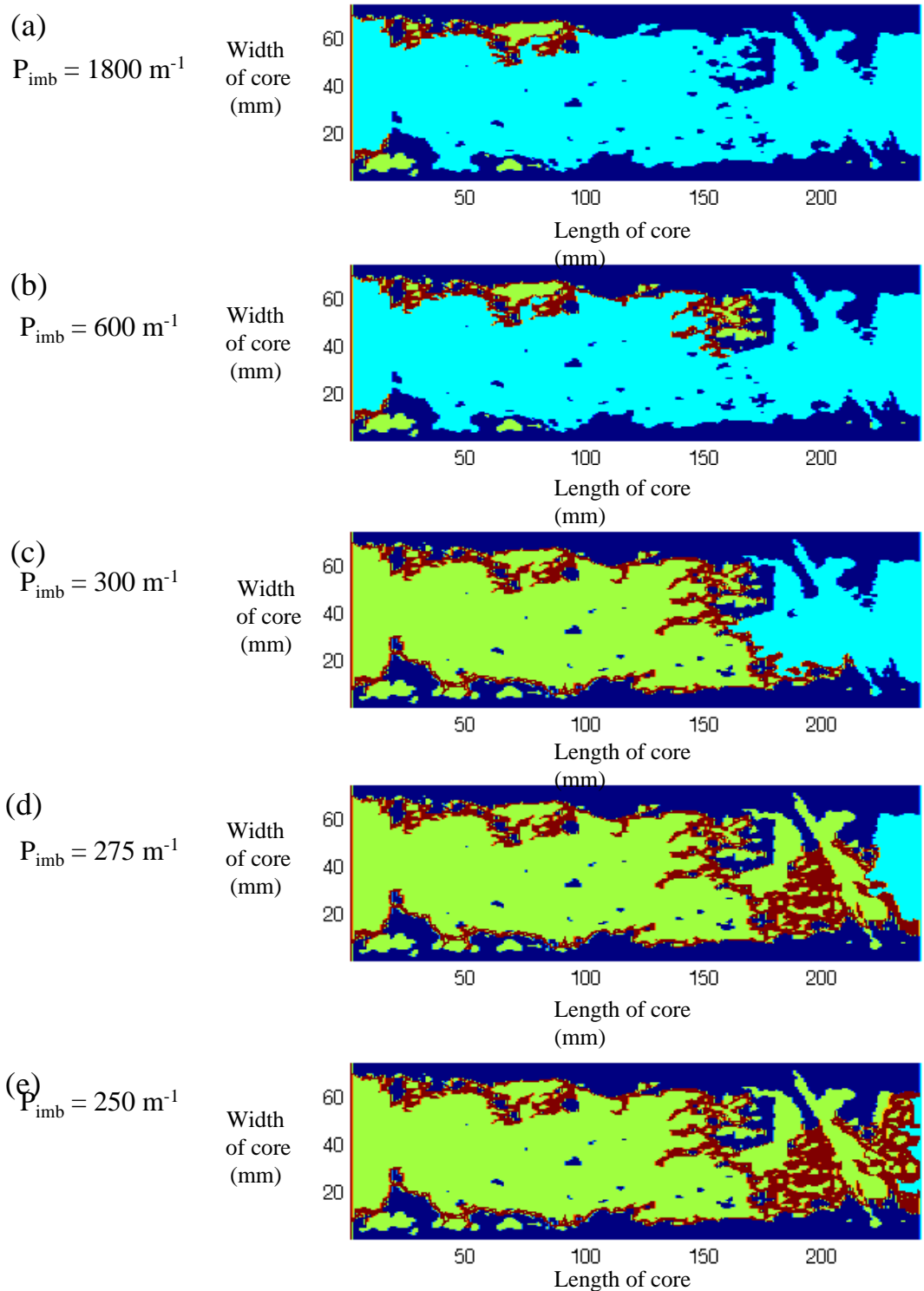


Figure 5.10 Simulated drainage sequence for core F, based on the discrete fracture network model. Water is in red, non-wetting phase in yellow-green and the impermeable matrix in blue. Capillary pressure increases as noted above the figures. Pressure is scaled to units of (m^{-1}). All displacements are in a horizontal plane from left to right.

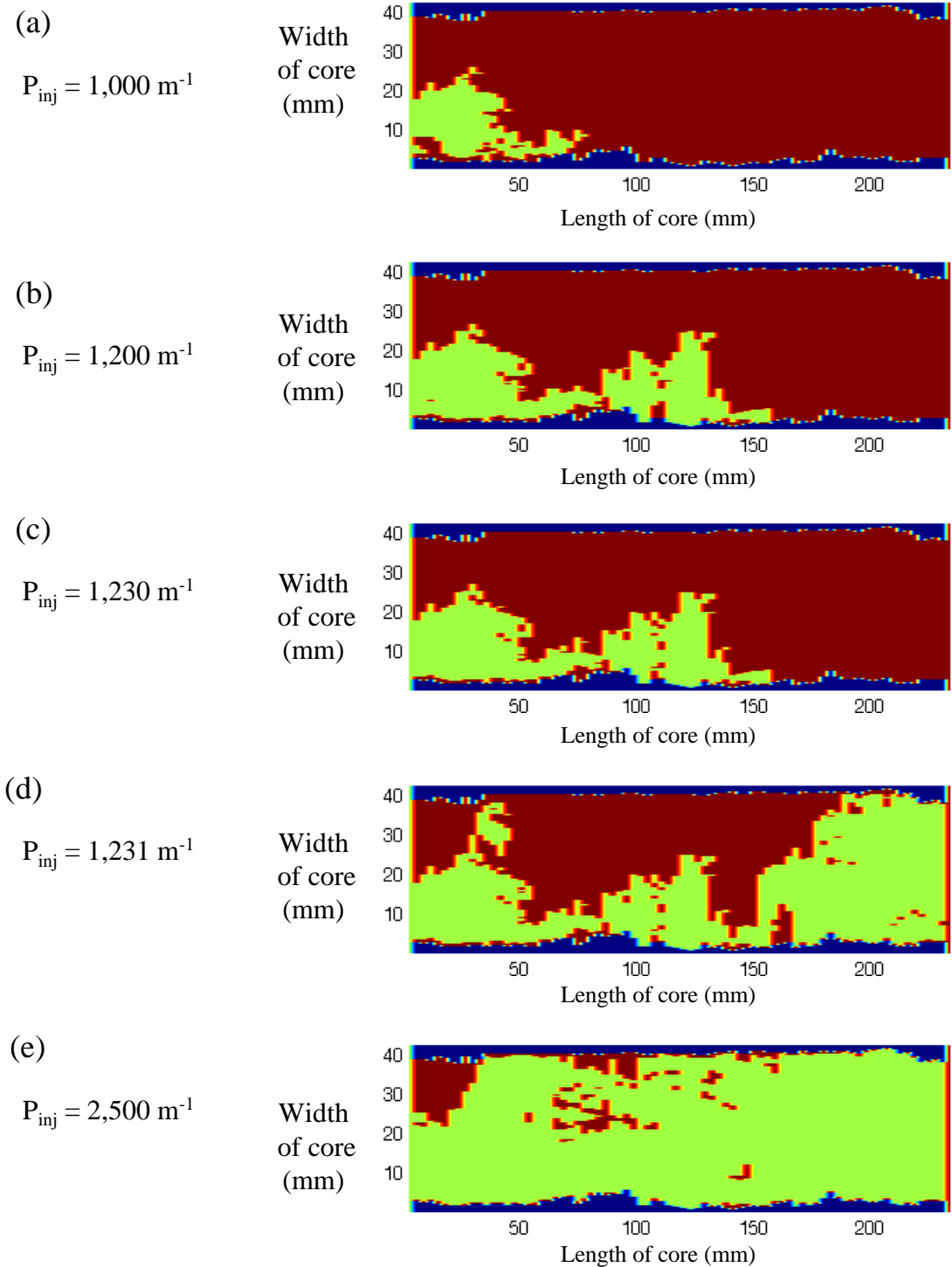


Figure 5.11 Simulated imbibition sequence for core F, based on the discrete fracture network model. Water is in red, trapped non-wetting phase in yellow-green, flowing non-wetting phase in light blue and the impermeable matrix in blue. Capillary pressure decreases as noted above the figures. Pressure is scaled to units of (m^{-1}). All displacements are in a horizontal plane from left to right.

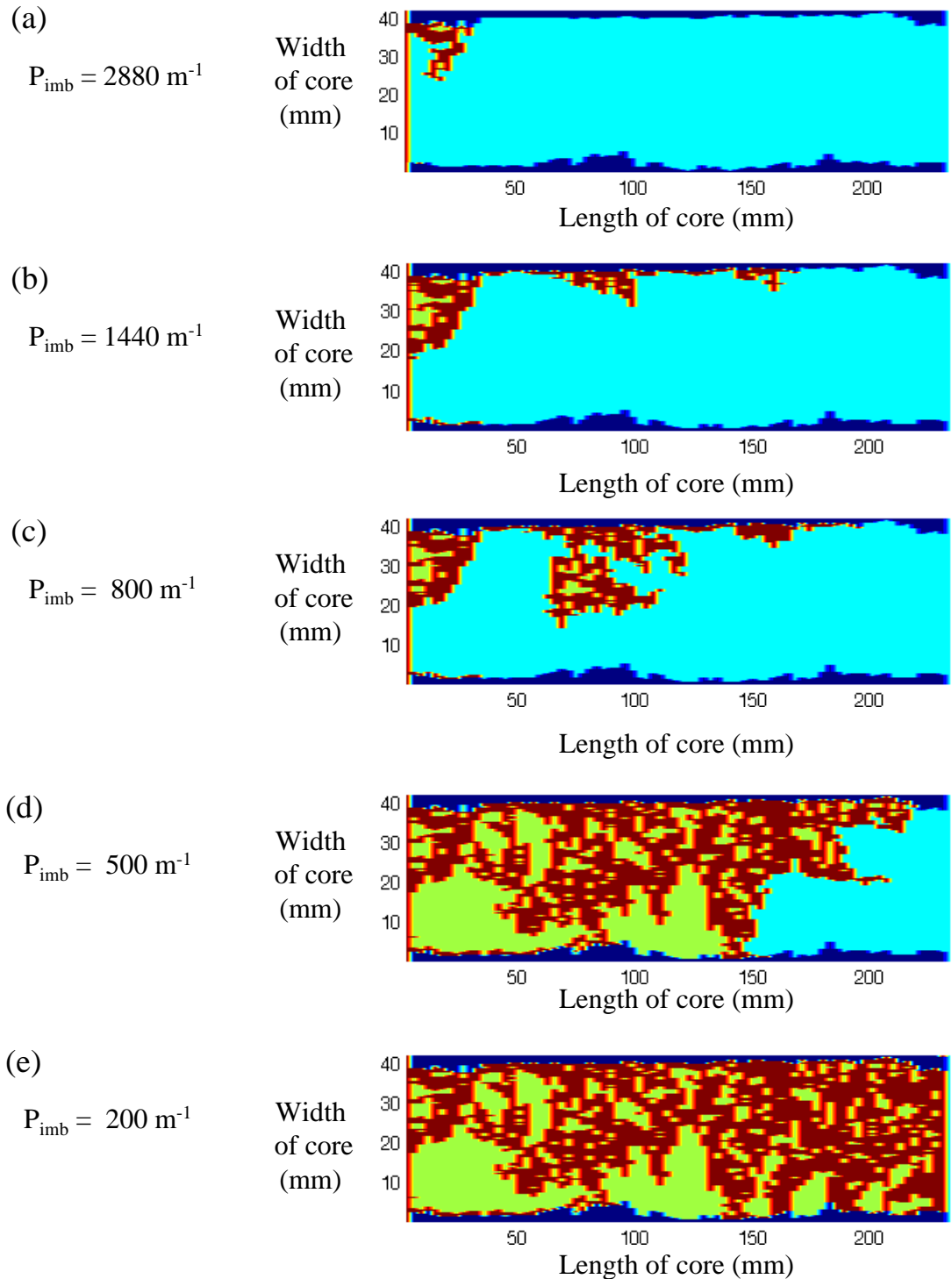


Figure 5.12 Relative Permeability-Saturation relationships for (a) core C; (b) core D, horizontal plane; and (c) core F. The drainage curves are shown in black and the imbibition curves in gray.

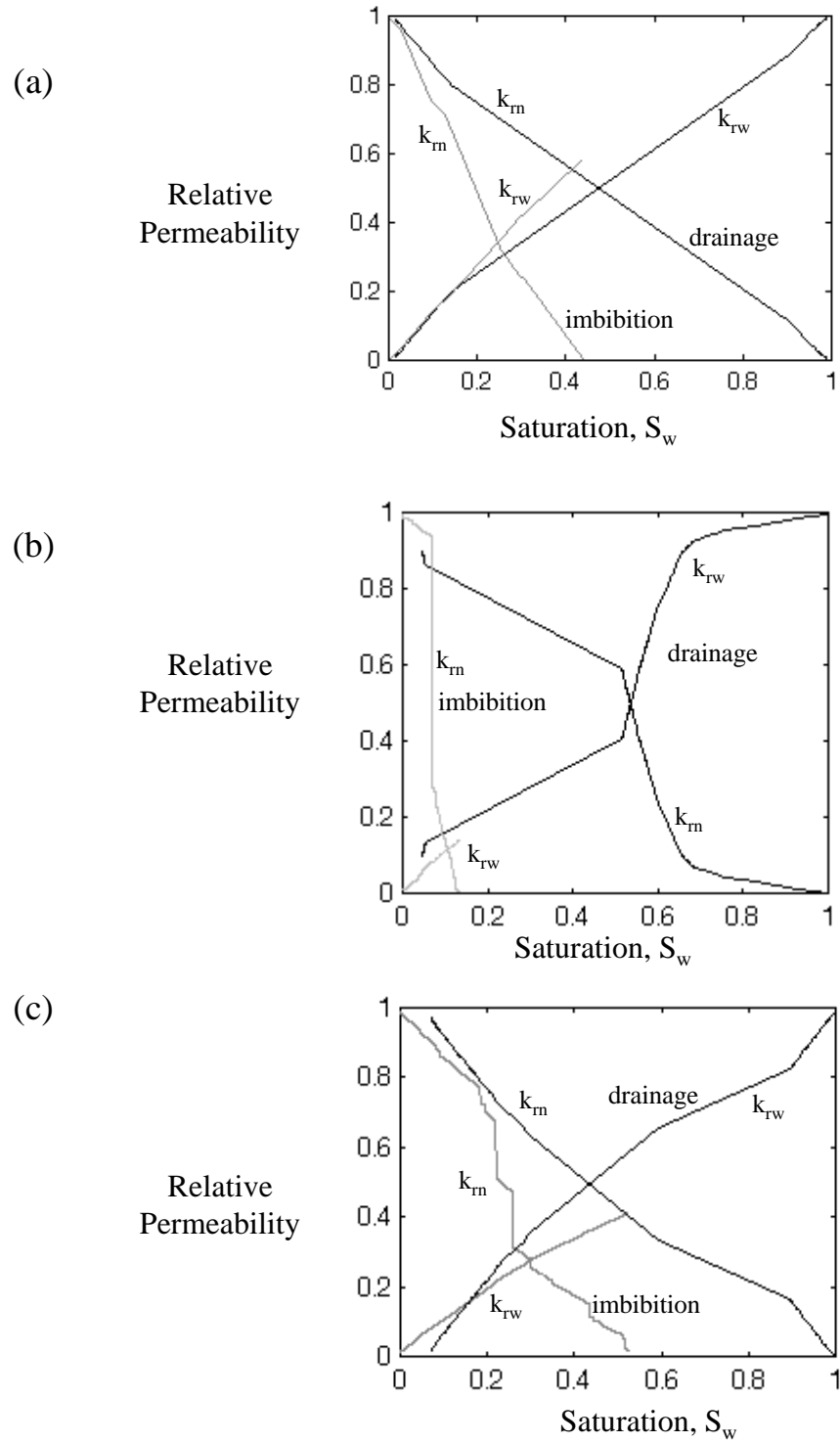


Figure 5.13 Snap-off process: (a) a thin layer of water imbibes ahead of the main wetting front and coats the grain surface; (b) the water layer bulges out at crevices; (c) snap-off breaks the non-wetting phase into two bubbles or blobs.

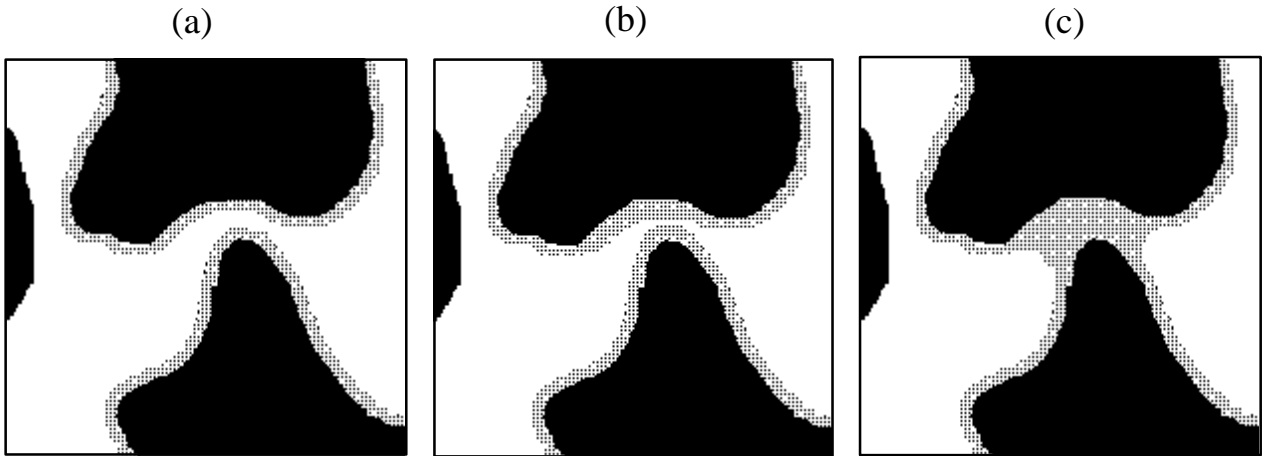


Figure 5.14 By-passing mechanism: (a) a pore body with narrow throats surrounding it; (b) water imbibes through layers, displacing non-wetting fluid, and snap-off begins to isolate the non-wetting fluid in the pore body; (c) water moves faster around the surrounding pores and after a sequence of snap-off events in the narrow throats, the wetting fluid is entrapped.

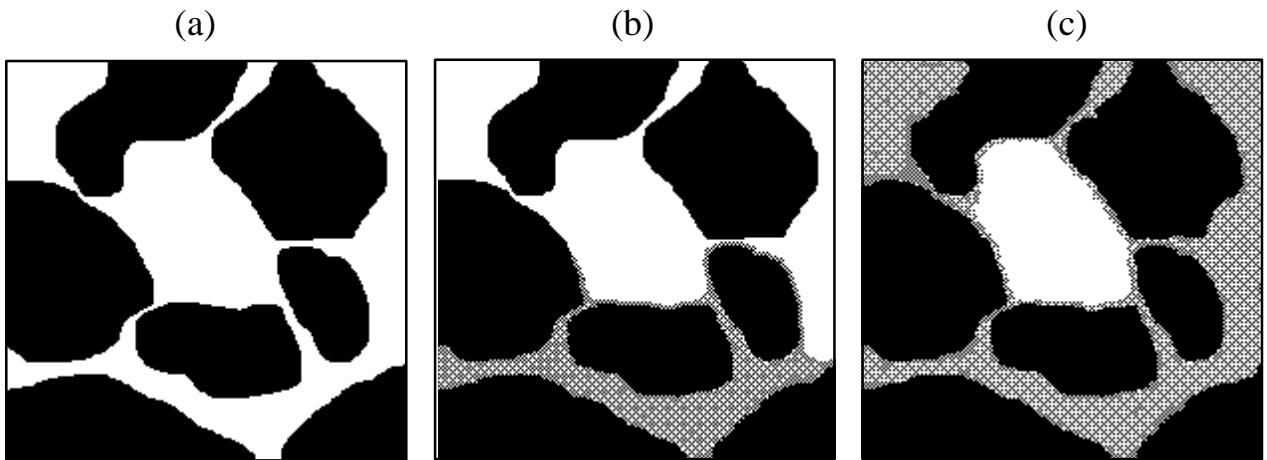


Figure 5.15 Comparison between the linear relative permeability model and the models used to fit Fourar's experimental observations. The water relative permeability is a function of liquid velocity, V_L (m s^{-1}).

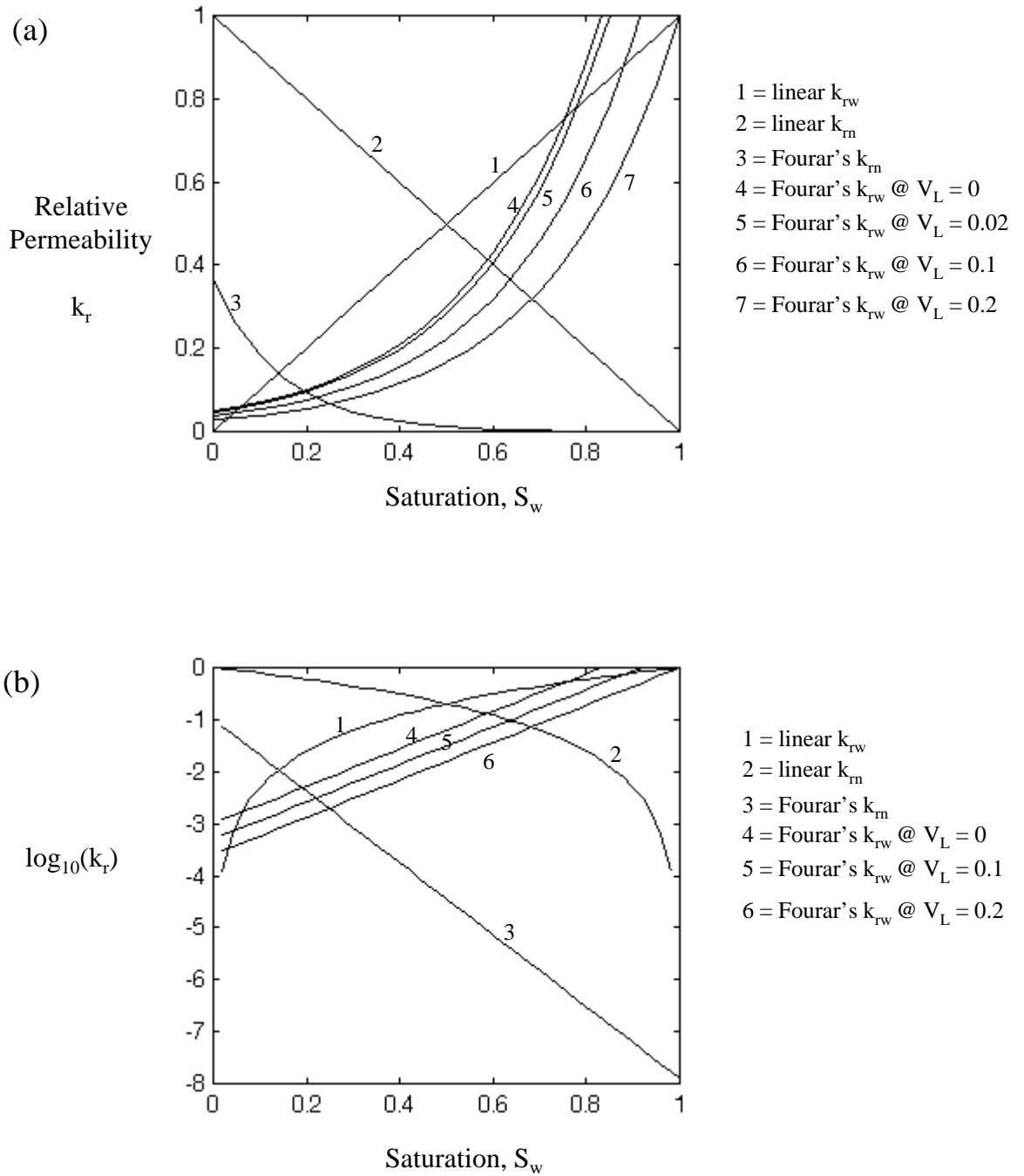


Figure 5.16 Simulation of NAPL displacing water in core C using the continuum model. Pore volumes injected shown at the left of each image. Flow is from left to right, on a horizontal plane.

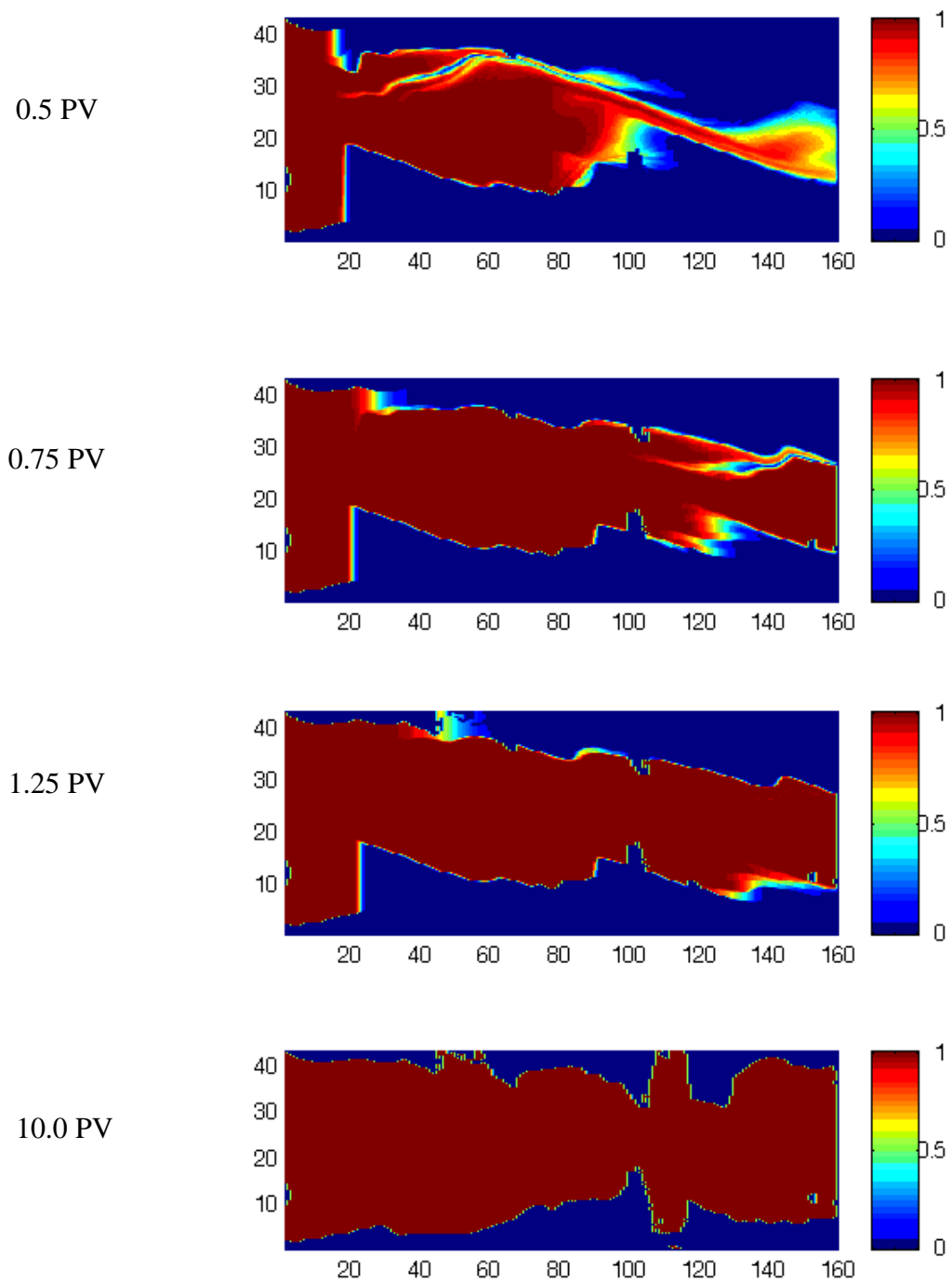


Figure 5.17 Numerical simulation of NAPL invading a water-saturated porous medium with a thin fracture. The color scale at right represents water saturation. Pore volumes injected are shown to the left of each image.

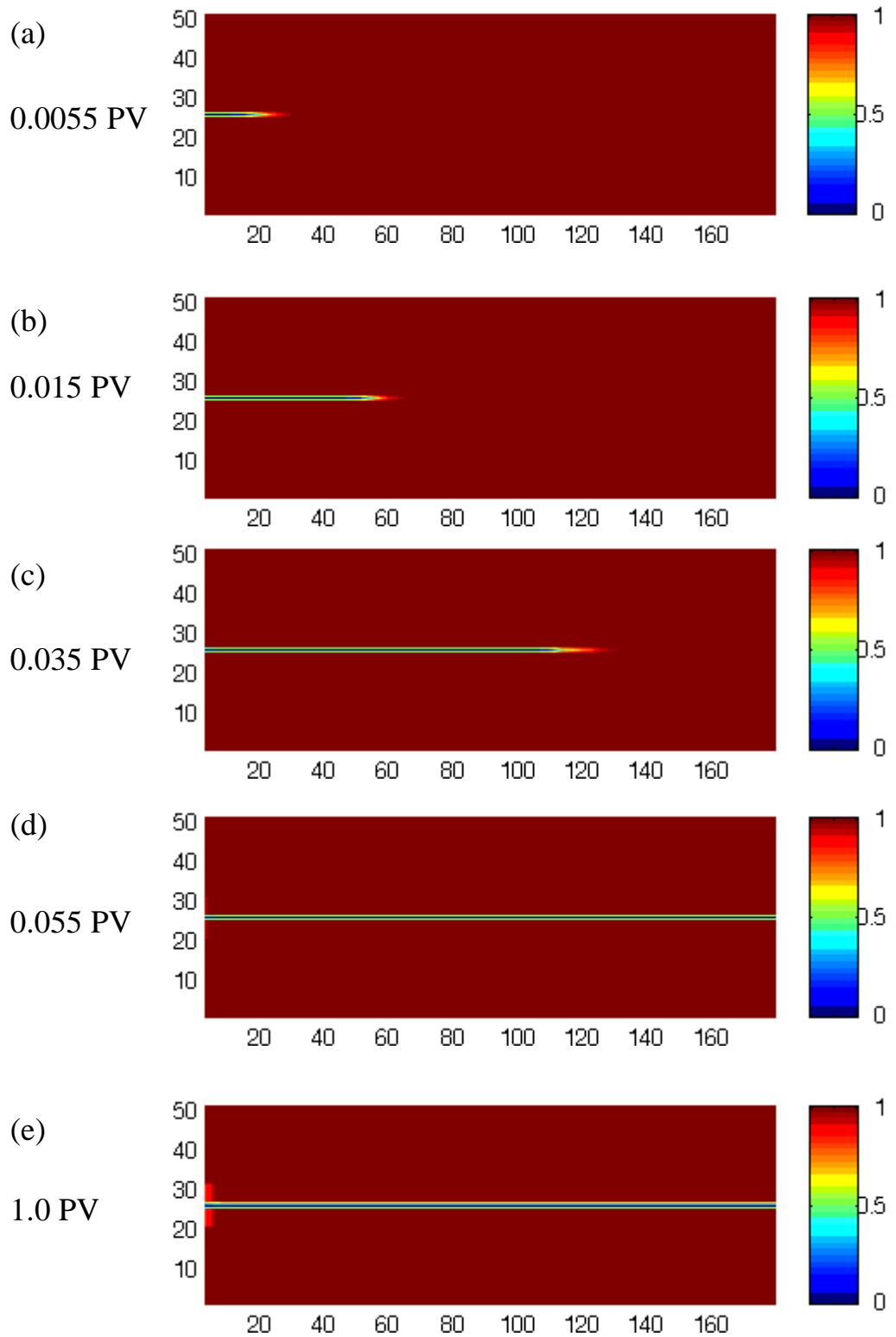


Figure 5.18 Numerical simulation of water displacing NAPL, with a 0.5 mm fracture in the sandstone core. In images a, b and c, capillary pressure is considered, whereas in image d, no capillary pressure is considered for either matrix or fracture. The color scale represents water saturation, and pore volumes injected are shown left of the images.

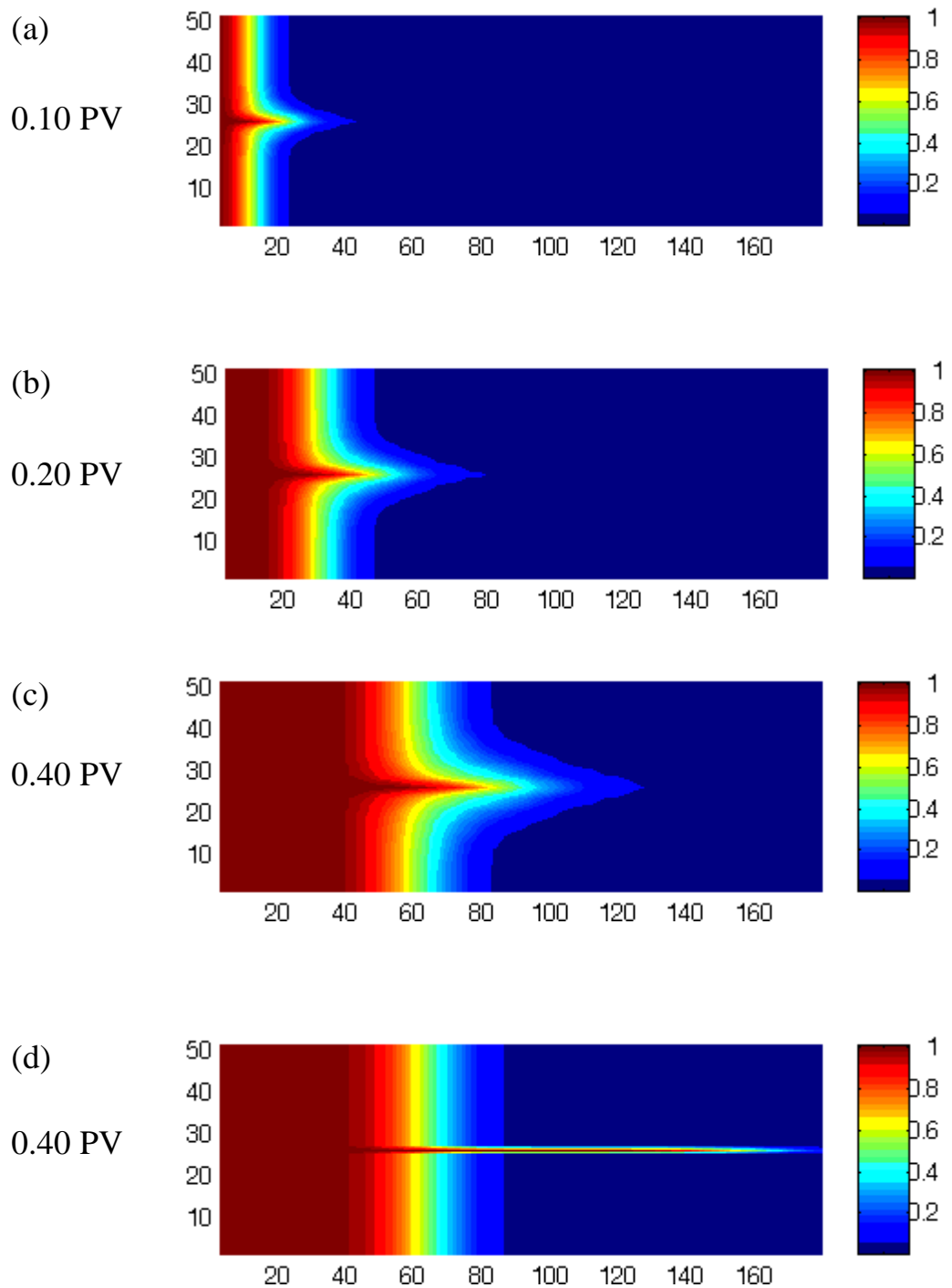


Figure 5.19 Numerical simulation of water flooding into a NAPL contaminated porous core, with (a and c) or without (b and d) a fracture, after the same pore volumes have been injected. Image e is the difference between d and c. The color scale represents water saturation, and pore volumes injected are shown left of the images.

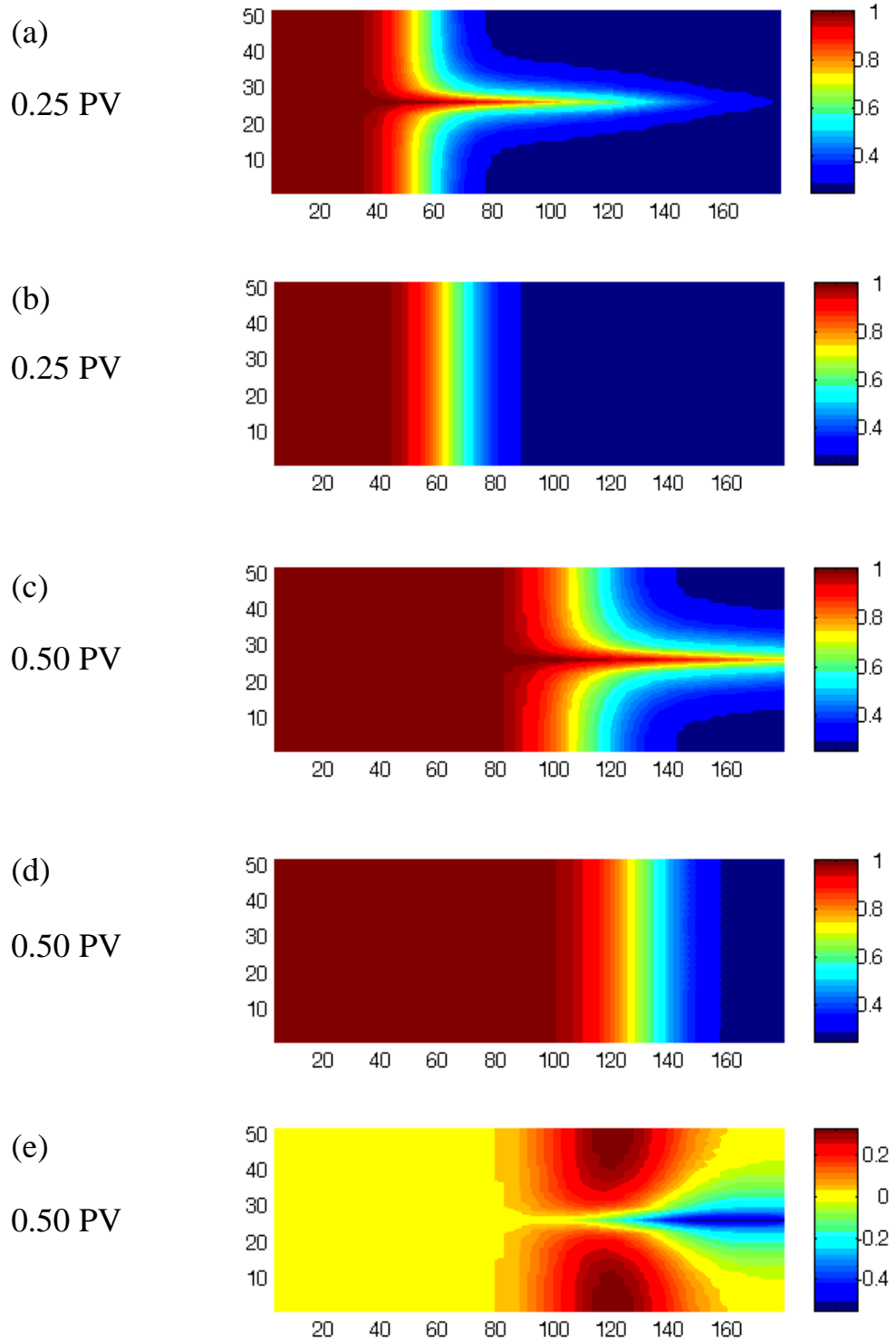


Figure 5.20 Construction of the Core Holder

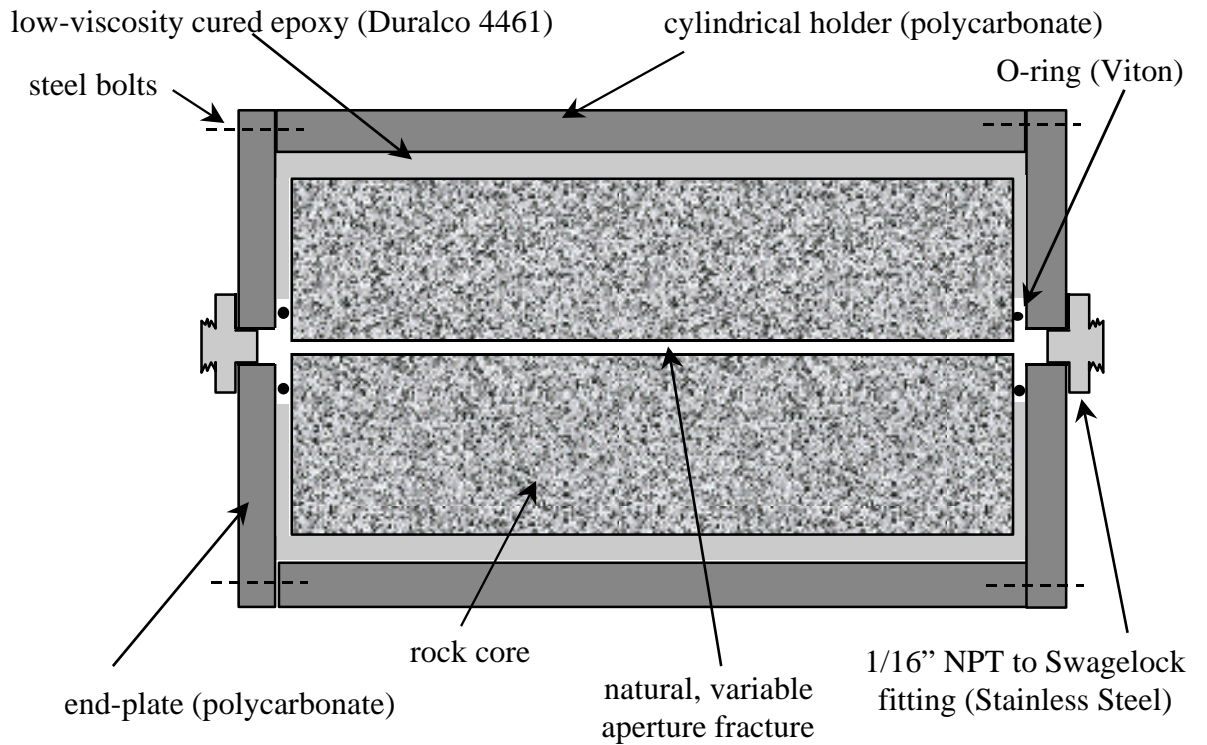


Figure 5.21 Schematic of laboratory set-up

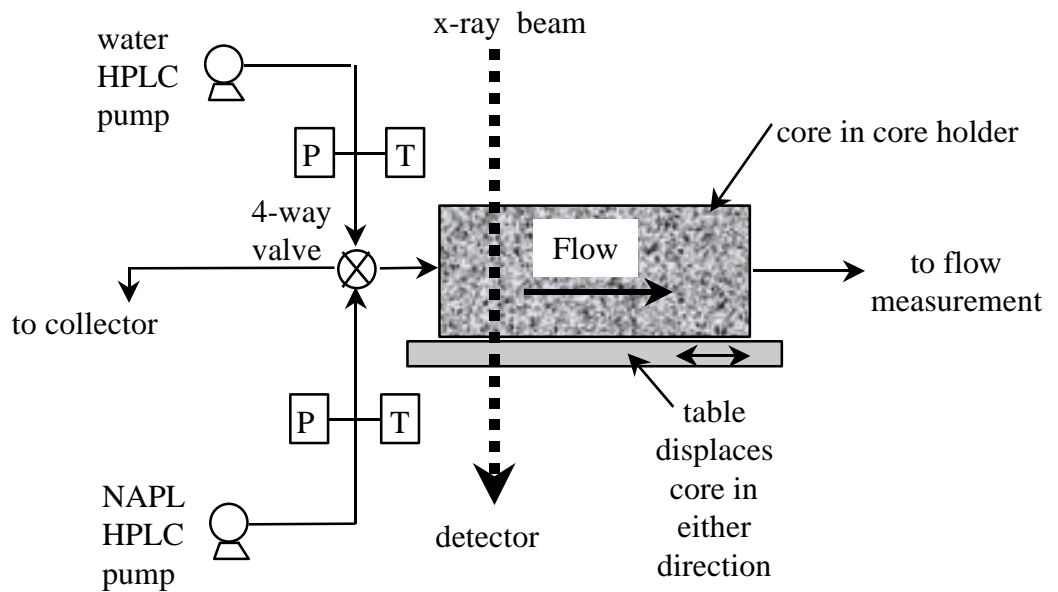


Figure 5.22 Images of laboratory set-up: (a) Core and core holder on CT-scanner table; (b) Instrumentation for pressure and temperature measurements; (c) CT-scanner control panel.



Figure 5.23 Imbibition of water into a completely dry granite core C. Pore volumes injected are indicated to the left of each image. The bar at the right indicates saturation of water, on a scale from 0 to 1000, where 1000 is fully saturated.

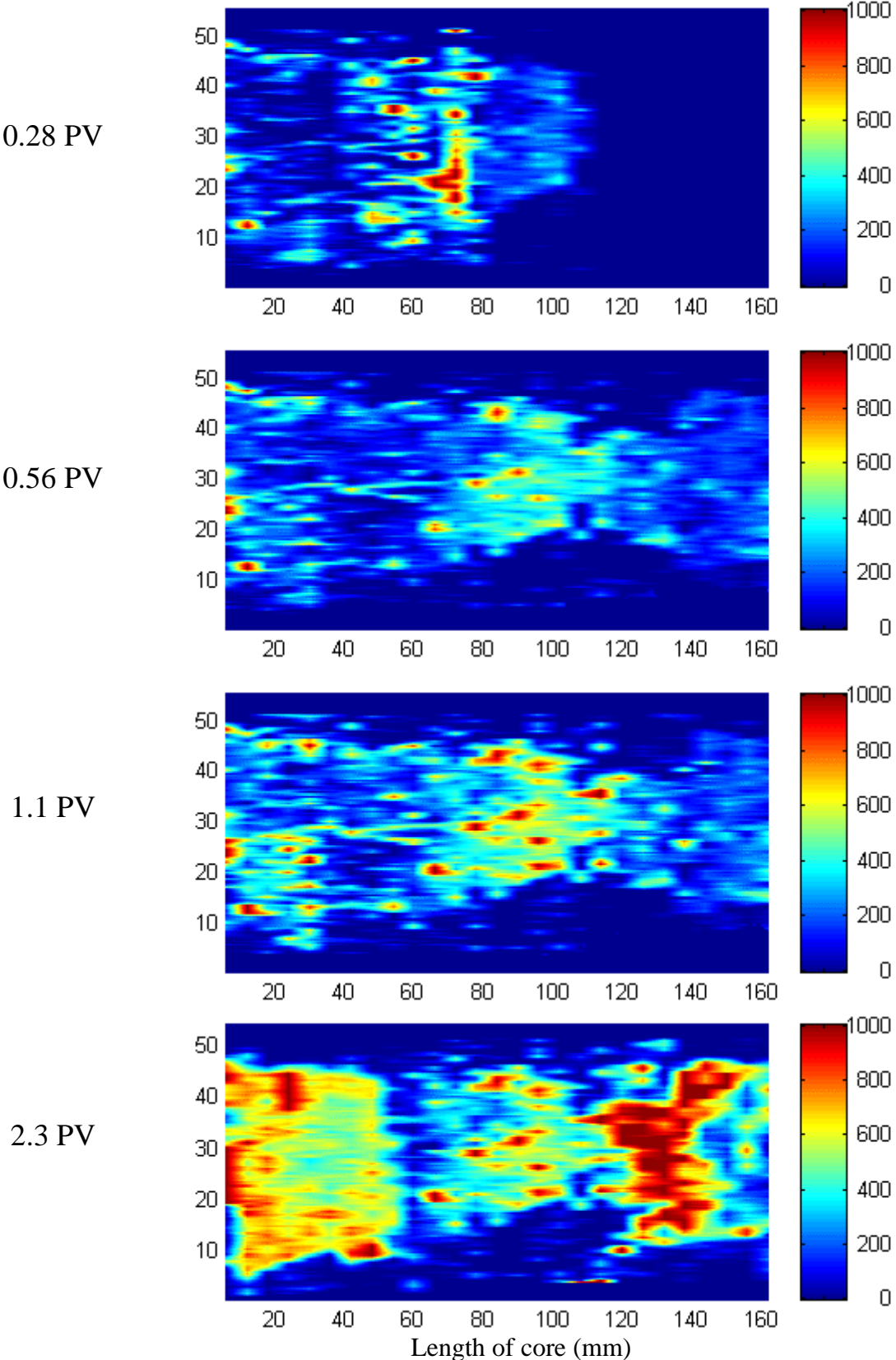


Figure 5.24 Core C after full saturation with water:
(a) Top view of fracture plane;
(b) Side view of fracture plane.

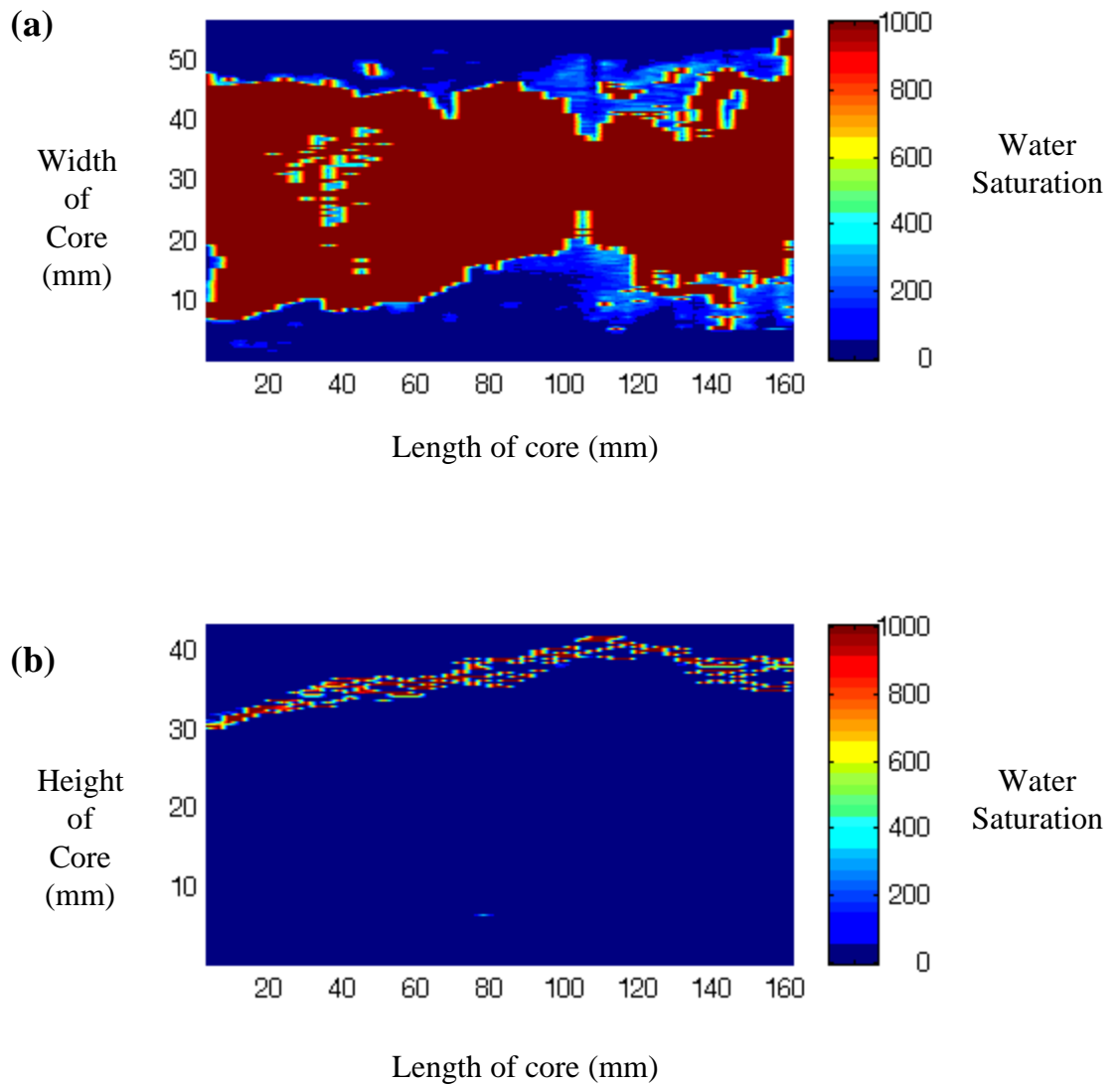


Figure 5.25 Water imbibition into core D, showing the progression of the water front on the top view of the fracture plane. Pore volumes injected are indicated to the left of each image. The bar at the right indicates the water saturation on a scale from 0 to 1000.

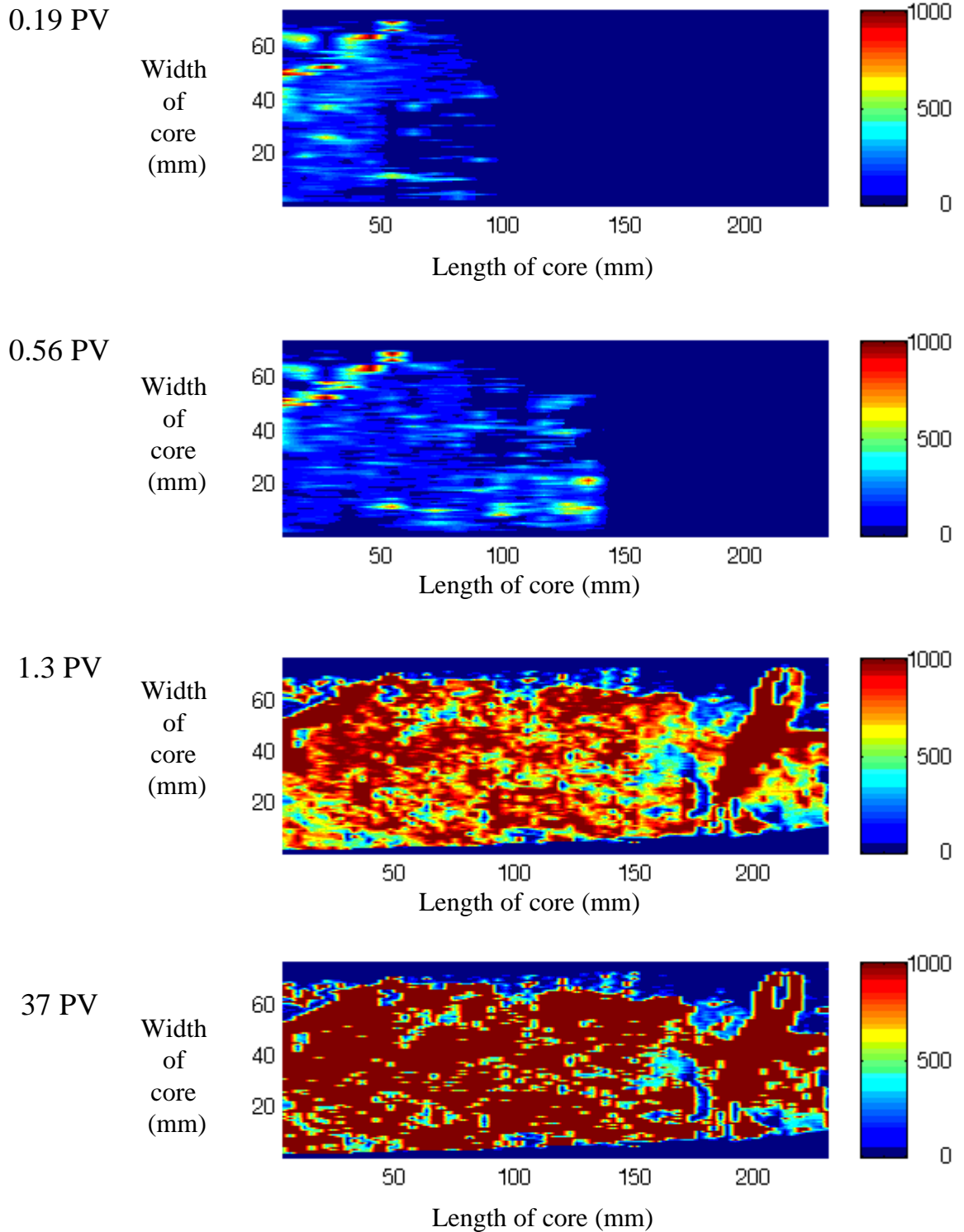


Figure 5.26 Water imbibition into core D, showing the progression of the water front on the side view of the fracture plane. Pore volumes injected are indicated to the left of each image. The bar at the right indicates the water saturation on a scale from 0 to 1000.

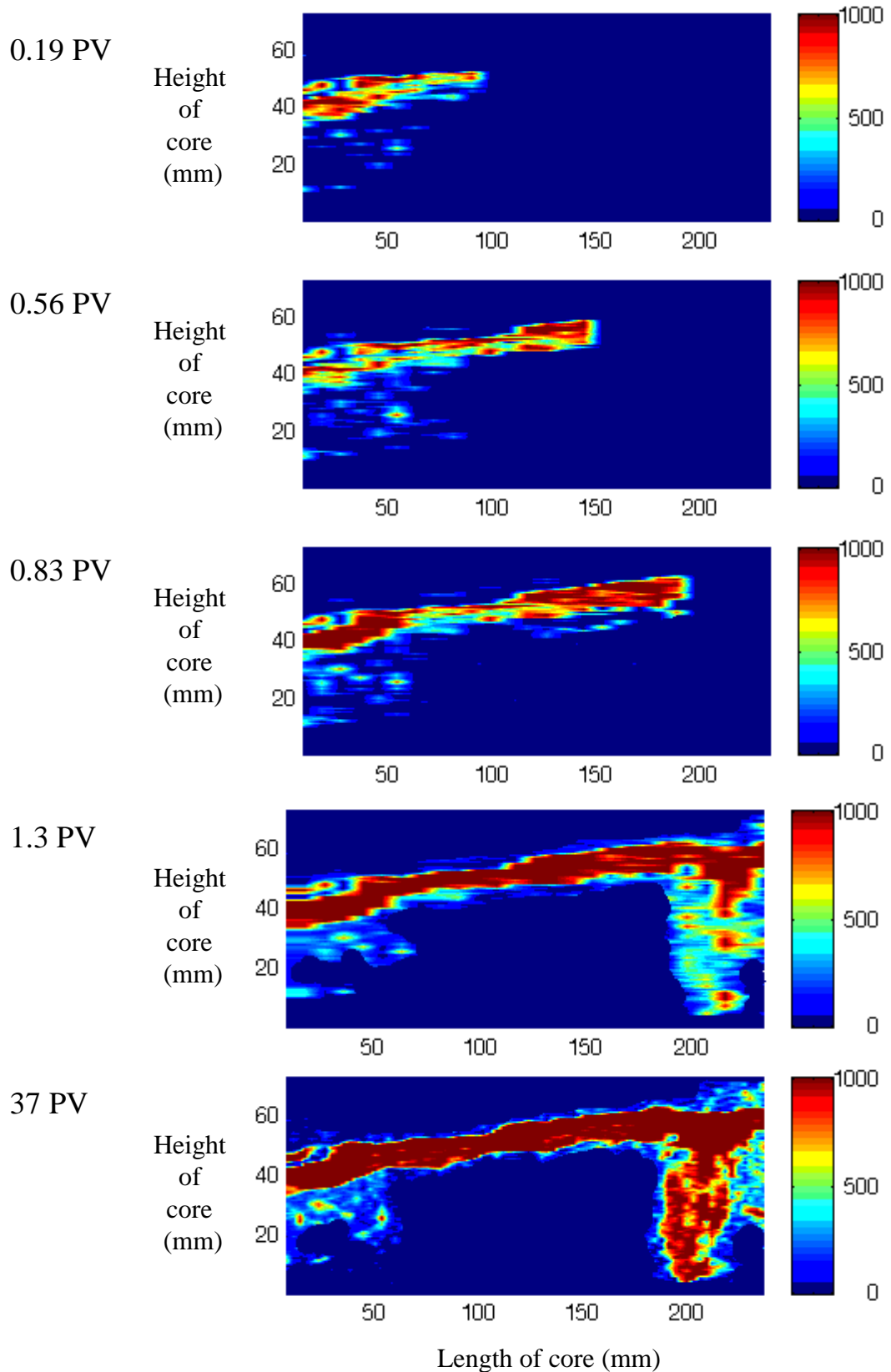


Figure 5.27 Water imbibition into an unfractured sandstone, Core E. Pore volumes are indicated to the left of each image. The right hand bar indicates water saturation on a scale from 0 to 1.

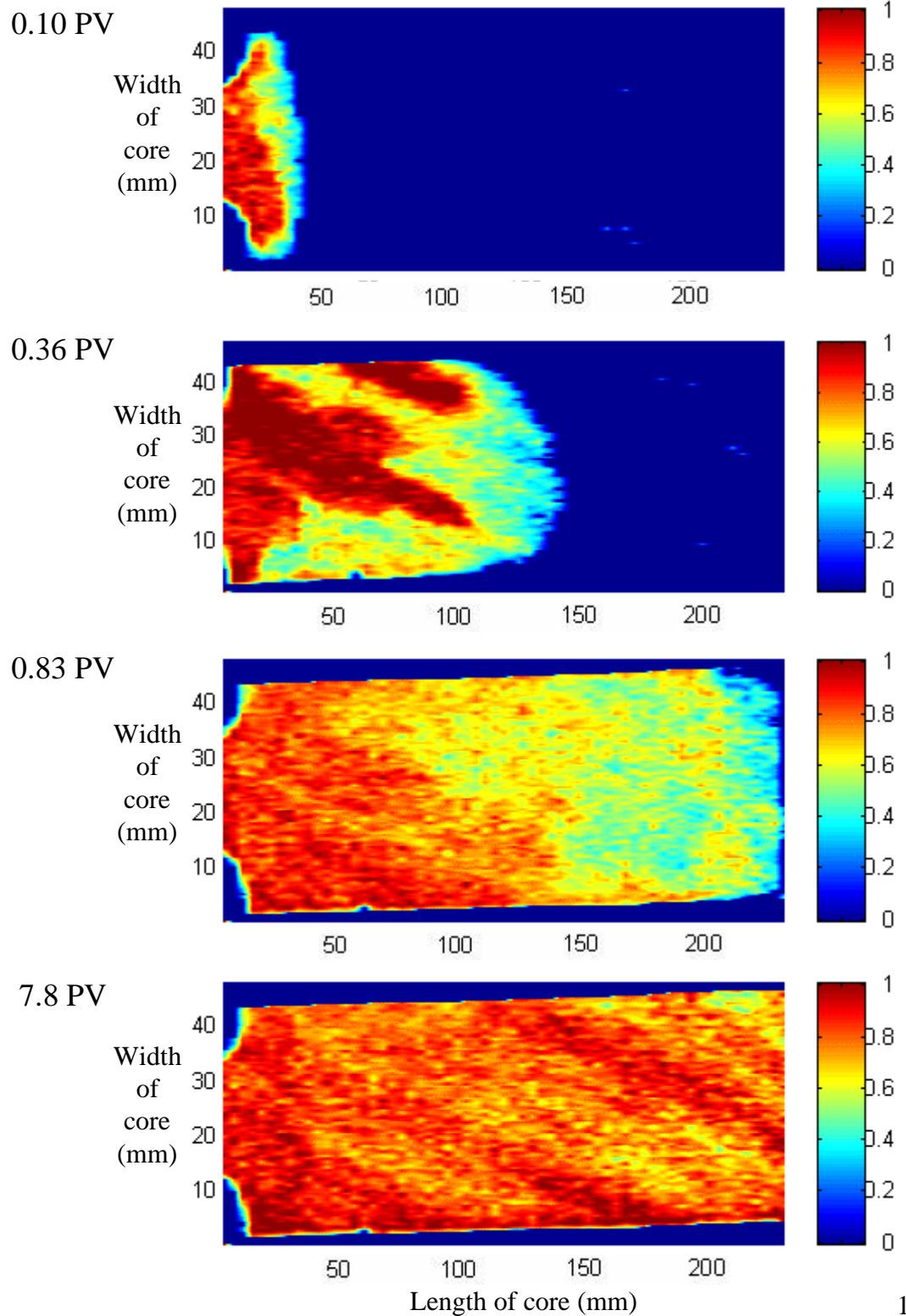


Figure 5.28 Water imbibition into a dry, fractured sandstone, Core F. Pore volumes injected shown to the left of the images, and water saturation is indicated by the right bar, on a scale from 0 to 1.

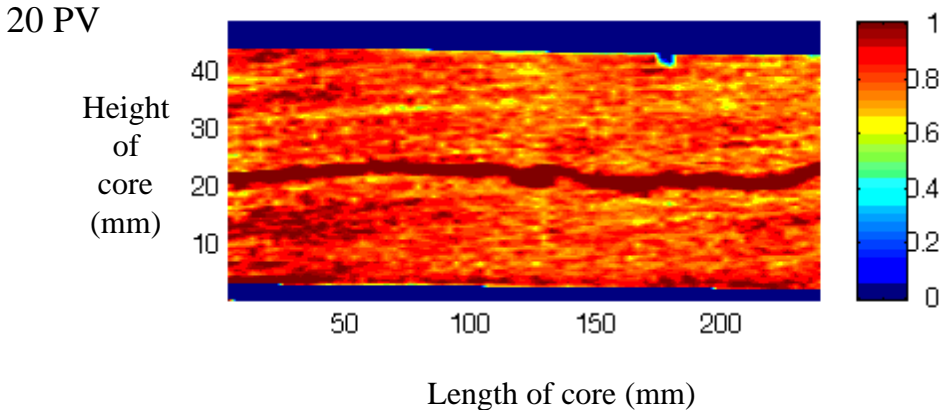
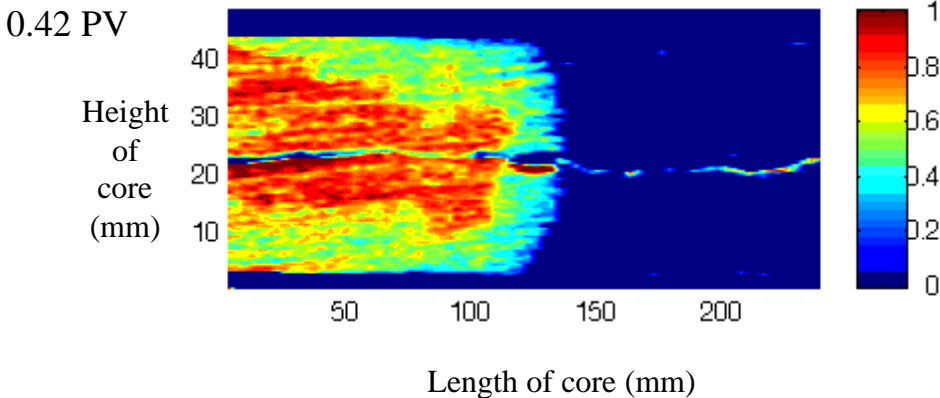
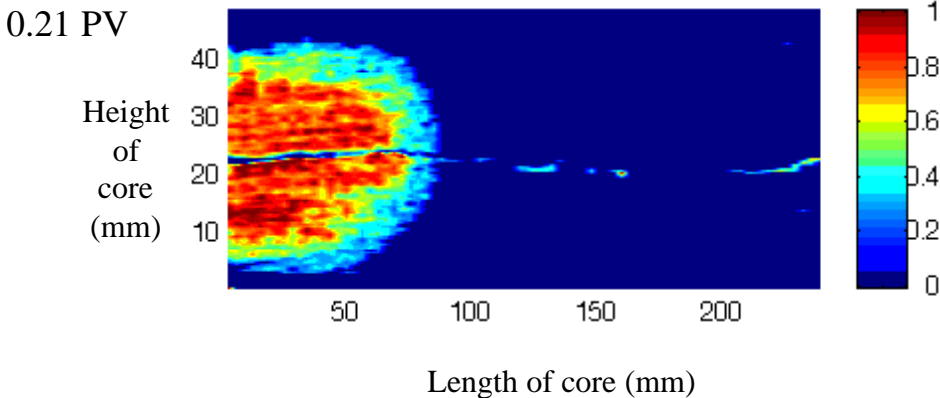


Figure 5.29 Primary Drainage: PCE displacing water in Core D. The images on the left side are the top view; those on the right are the side view. Pore volumes pumped are shown to the left of the images. The bar on the right side indicates NAPL saturation, on a scale from 0 to 1000.

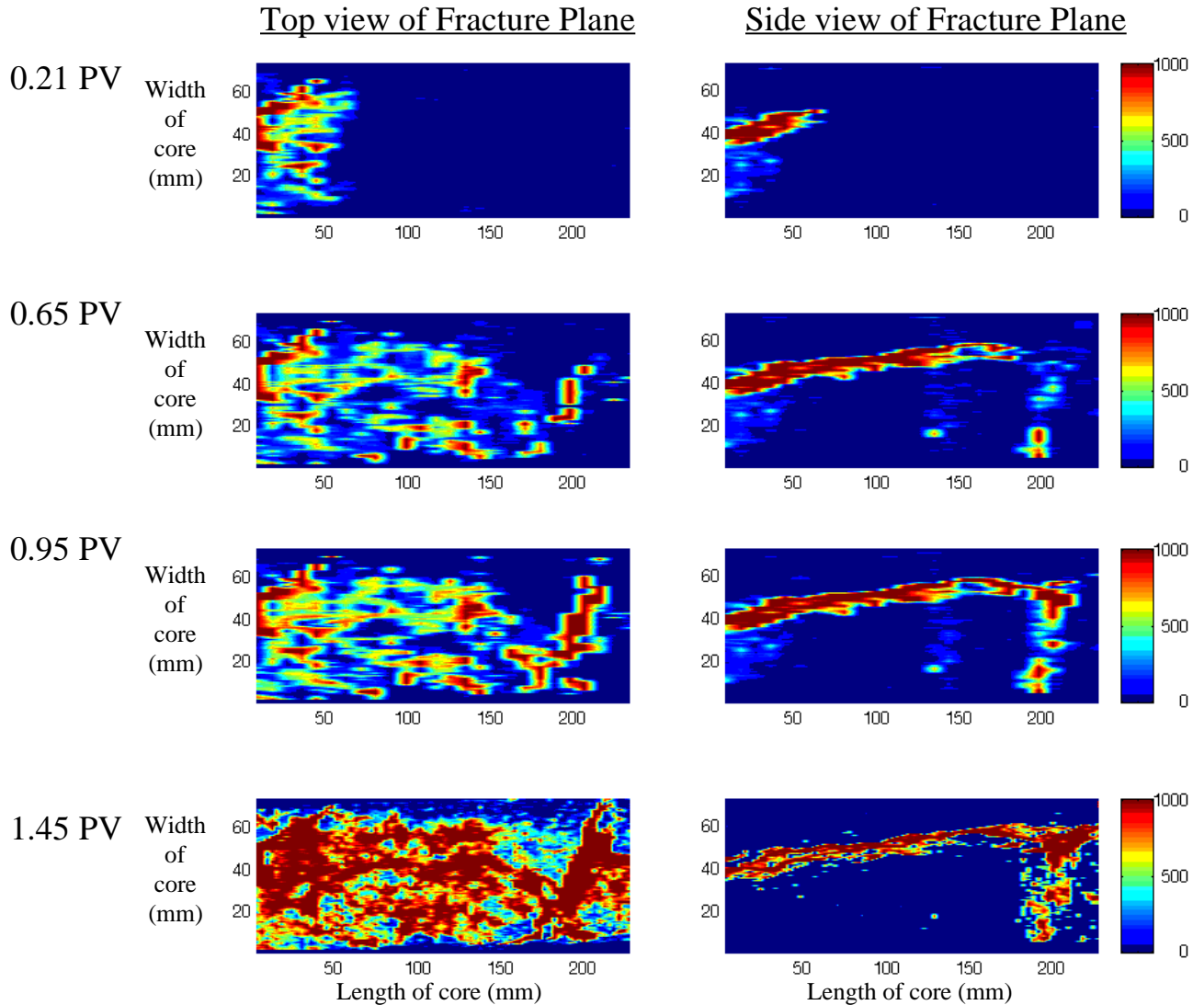


Figure 5.30 Primary Drainage: Decane displacing water in Core D.

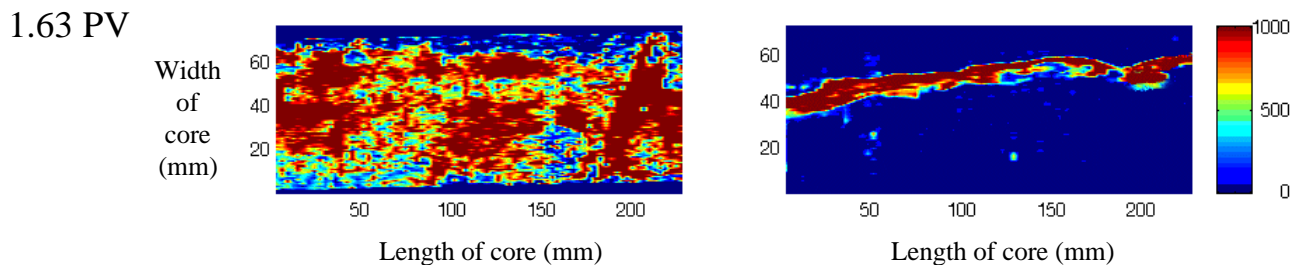


Figure 5.31 PCE displacing water in the unfractured sandstone Core E. Flow was reversed in these displacements (from right to left in the images). Pore volumes injected indicated at the left of the images, and saturation of NAPL on the right bar, on a scale from 0 to 1.

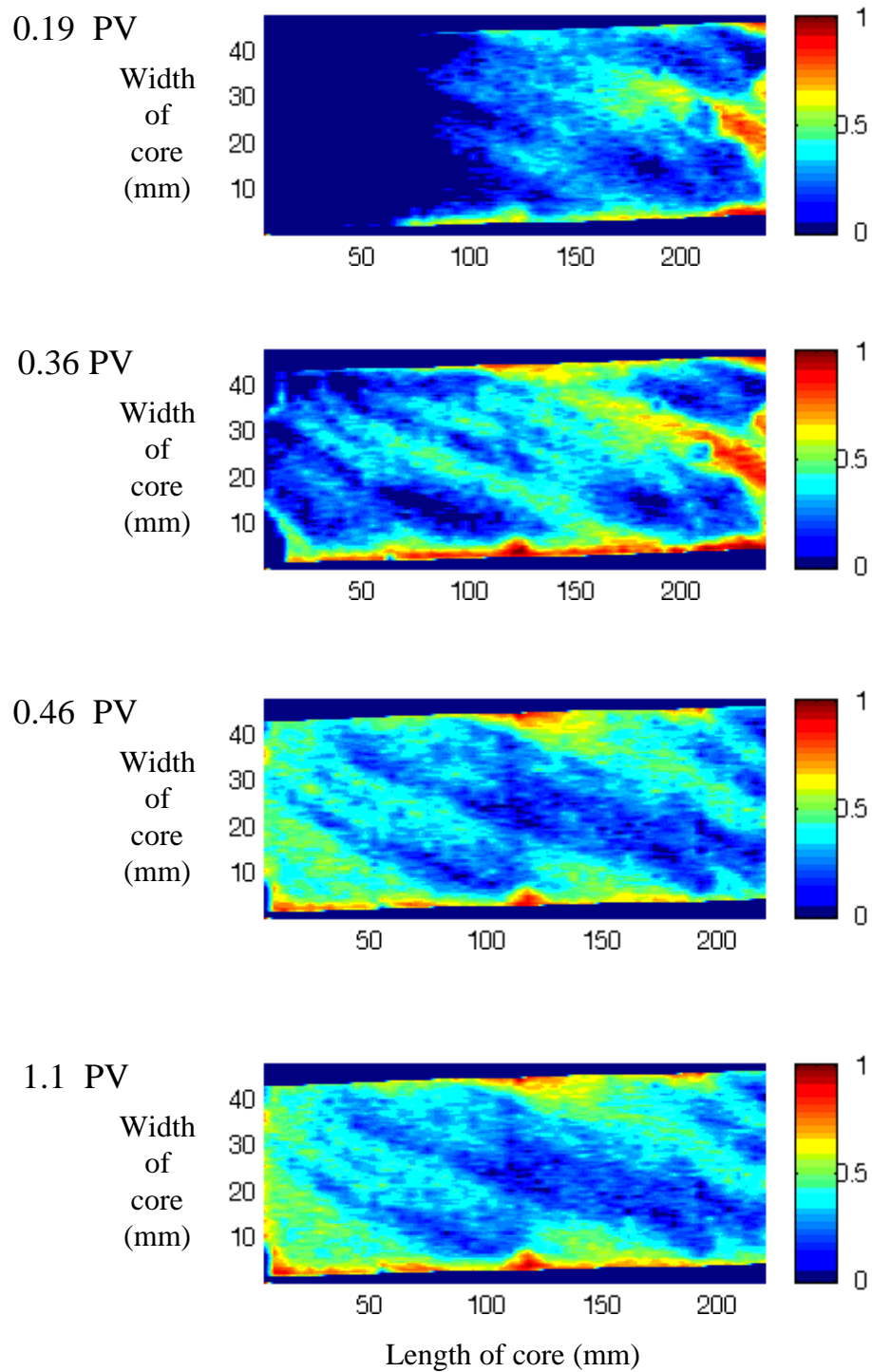


Figure 5.32 PCE displacing water in the fractured sandstone Core F. The top two images present vertical slices through the middle of the core at the pore volumes indicated left of the images. The third image is a reconstruction of the PCE saturation in the fracture plane as seen from a top view. The bars at right represent NAPL saturation on a scale from 0 to 1.

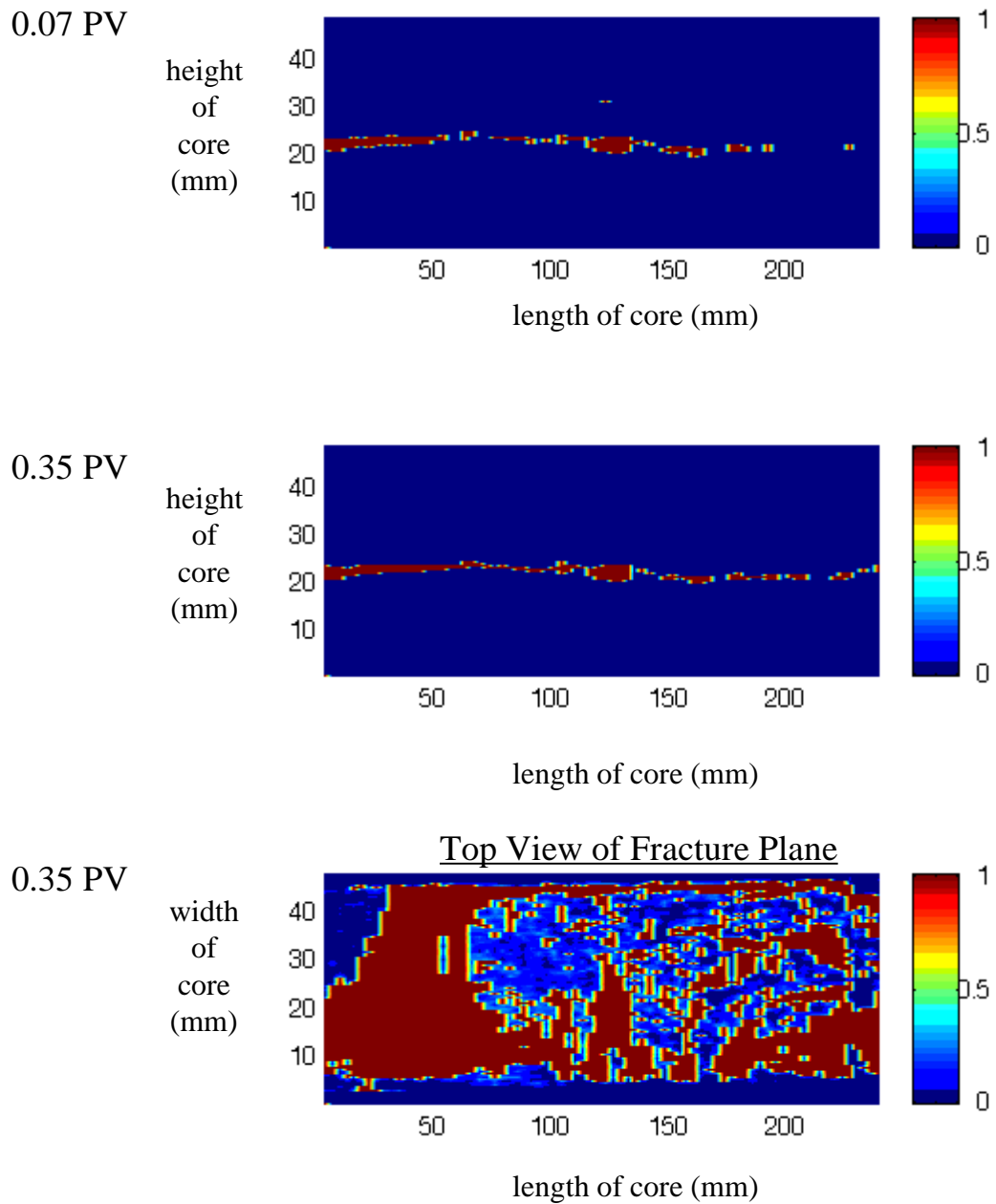


Figure 5.33 Water flooding of Core C to remove PCE. Water flow is from right to left in this set of displacements. The first image is the final PCE configuration after contamination (PCE \rightarrow water). Pore volumes of water injected are shown at the left of each image. The bars at right represent NAPL saturation on a scale from 0 to 1.

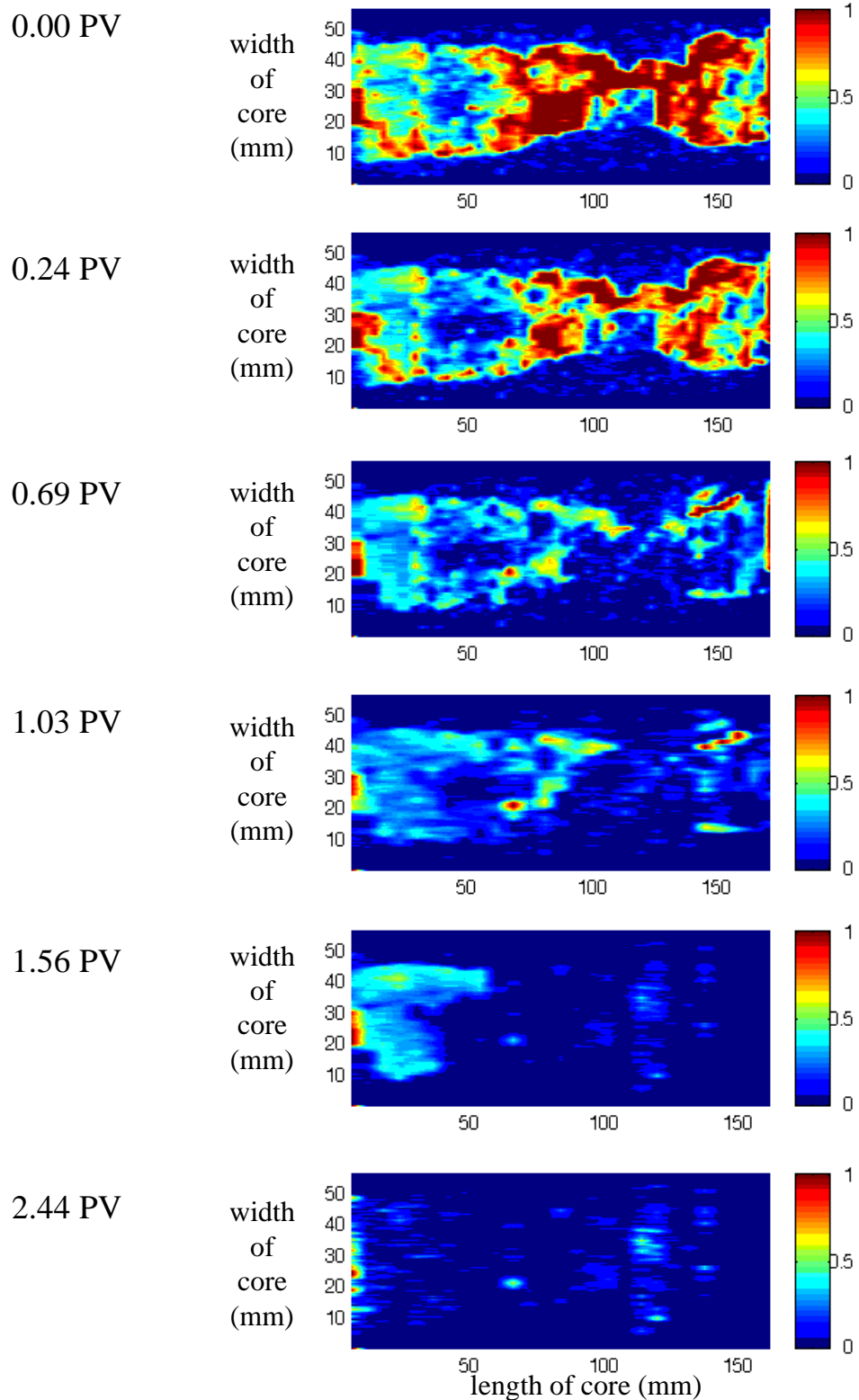


Figure 5.34 Water flooding of Core D to remove PCE. The top image is the top view of the fracture plane after 1.2 pore volumes injected and the bottom image is the side view. NAPL saturation is shown on the right bar, on a scale from 0 to 1.

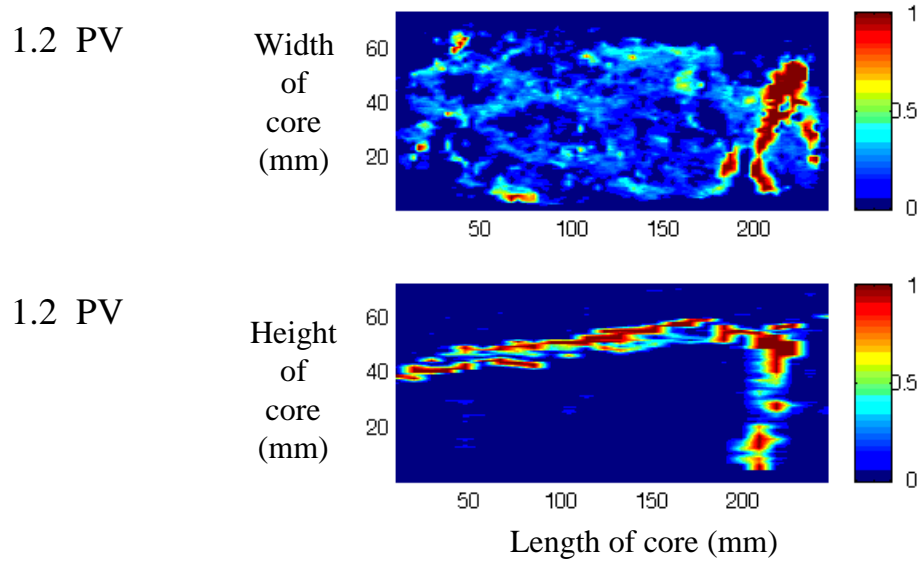
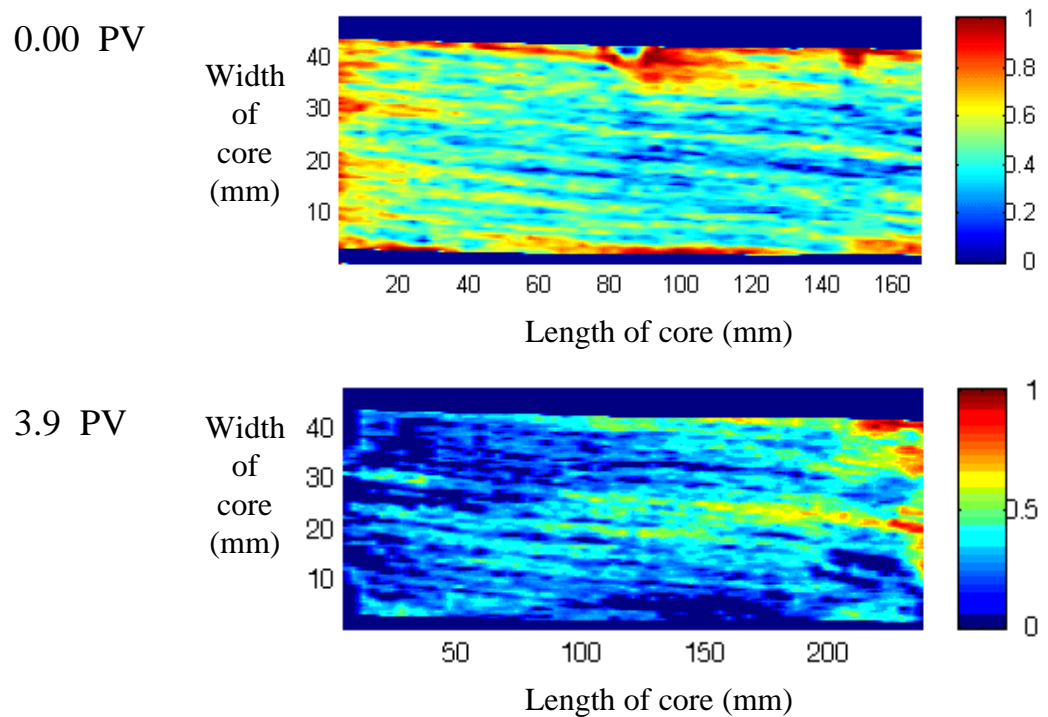


Figure 5.35 Water flooding of Core E (unfractured sandstone) to remove PCE. Vertical slices through the sandstone shown. Pore volumes injected indicated at the left of the images, and saturation of NAPL on the right bar, on a scale from 0 to 1.



Chapter 6

Three-Phase Flow in Fractured Media

6.1 Introduction

Three-phase flow conditions occur in the environmental context when a Non-Aqueous Phase Liquid (NAPL) infiltrates from the source of a spill or leak into the unsaturated zone, where usually both the air and water phases are initially present. Water is typically at low saturation if there has not been any recent recharge of the aquifer, but the soil may contain significant water saturation during certain seasonal events, resulting in a complex set of multiphase displacements. Another situation where three phases may be present is when a spill of NAPL that is less dense than water (LNAPL, e.g. most petroleum products) is large enough to infiltrate down to the water table, where it initially mounds and then spreads horizontally, “floating” over the water table. During seasonal water table recharge events, the water level rises or drops, creating conditions where either water displaces NAPL and air (rising water table or recharge, resulting in water imbibition), or air displaces NAPL and water (lowering of the water table or drainage). The contaminated aquifer may be composed of fractured consolidated material, resulting in three-phase flow in fractures. As we observed at the pore scale in Chapter 4, several double displacements can occur during NAPL infiltration or water table movement.

In addition, three-phase flow conditions may be generated during some remediation schemes, either by design or inadvertently. For example, during steam injection, the introduction of the steam phase to displace NAPL and the condensation of water when steam comes into contact with the cooler medium generates three-phase flow conditions. Steam injection may be undertaken to clean DNAPLs from fractured media. Three-phase flow conditions can also occur when active dewatering of the aquifer is undertaken to

lower the water table during Soil Vapor Extraction (Mutch and Scott, 1994), to improve the efficiency of the contaminant removal. SVE is then used to remove NAPL via volatilization and transport in the gaseous phase to a collection well. The NAPL may be an LNAPL trapped under the water table, or a dense NAPL (DNAPL, e.g. a chlorinated organic solvent) which is pooled at the bottom of the aquifer and may have flowed into the fractures of a clay or bedrock confining layer.

Three-phase flow conditions are also important in oil reservoir simulation and production. Many oil reservoirs have a gas cap overlying the reservoir and are in contact with an aquifer under the reservoir (Dake, 1978). Connate water is also almost invariably present in the reservoir, so as the reservoir is drained three-phase flow conditions may occur. In addition, most Enhanced Oil Recovery techniques such as injection of both water and gas (WAG process) or steam injection result in three-phase flow conditions. Many oil reservoirs are in either sandstones or shales, which are typically heavily fractured, resulting in significant three-phase flow in the fractures.

What is the significance of three-phase flow? As we observed at the pore scale (Chapter 4), the introduction of the gas phase into a two-phase situation can greatly reduce the NAPL “residual” saturation, by allowing it to flow in layers, even for many non-spreading NAPLs. DNAPL which had been disconnected under two-phase conditions (water-DNAPL) becomes mobilized and flows downward due to gravity. This may or may not be desirable. Although the saturation of NAPL is reduced, it has now been spread over a much larger area, and it has contaminated previously uncontaminated soil. On the other hand, the increased surface area to volume ratio of the NAPL blobs allows for faster volatilization of NAPL (if it is significantly volatile), and thus it may be removed via SVE. In the environmental field, mobilizing DNAPL farther into the fractured bedrock would be very undesirable, whereas for oil recovery the additional mobilization of oil would be very desirable.

Several experimental reports provide evidence of the reduction of the residual NAPL saturation during three-phase flow conditions compared to two-phase conditions,

including Wilson *et al.* (1990) and a compilation of 15 experiments by Mercer and Cohen (1990). Wilson *et al.* found that the residual NAPL saturations in the saturated zone ranged from 15 to 27%, for various soil and NAPL types, including LNAPLs (e.g. decane) and DNAPLs (e.g. tetrachloroethylene or PCE), with the variation depending mostly on soil type. In the unsaturated zone, with an average water saturation of 19.8 %, the residual NAPL saturation found by Wilson *et al.* ranged from 5.5 to 12.2%. The comparison of 15 experiments by Mercer and Cohen is not as clear because different researchers used different soil types, but there is a general trend towards lower residual NAPL saturations in the unsaturated zone. This comparison underscores the difficulty in determining residual saturation. The residual saturation is a function of soil type and the balance of gravity, viscous and capillary forces, so that experiments conducted at high water injection rate or with strong gravity effects are likely to result in lower NAPL saturations. In addition, under three-phase flow conditions, the “residual” NAPL saturation may continue to slowly decrease with time as NAPL slowly flows through the thin layers in the crevices. A short experiment will report a significantly higher NAPL saturation than an experiment where NAPL is allowed to drain for a longer time.

In a fracture, two- and three-phase residual NAPL saturations are expected to be much lower than in unfractured porous media. Even if NAPL is by-passed during two-phase flow conditions, it may eventually be displaced by water. If air is then introduced into the fracture, NAPL in the fracture will rapidly form a layer around the air bubble(s) and then travel along with the air phase. Fenwick and Blunt (1996) have estimated the theoretical conditions necessary for three phases to coexist in a pore space, which involves the ratios of interfacial tensions (at thermodynamic equilibrium) and capillary pressures. The capillary forces holding the NAPL in place are simply too small compared to gravity or viscous forces to prevent NAPL being swept out of the pore space, unless the fracture aperture is very small. But in very small fracture aperture regions we expect water to be the resident phase, since it is rather unlikely that it would be displaced by NAPL during the contamination process.

Micromodel observations of three-phase flow in a simulated fracture reveal that when air displaces NAPL which displaces water (double drainage), NAPL forms a layer around the air phase (Figure 6.1), and then the two phases travel together displacing water. The details of the micromodel setup are explained in Chapter 4. Because the interfacial tension between air and NAPL is typically considerably lower than the interfacial tension between air and water, when air contacts NAPL under three-phase conditions, air is more likely to displace NAPL than water, which is followed by NAPL layer formation around the gas phase. During double imbibition, where first NAPL displaces air and then water displaces NAPL, the air phase is continuously covered by a NAPL layer as it moves through either the porous media or the fracture, and once in the fracture, the combined air/NAPL bubbles can travel with relatively little interference from the surrounding water phase. Bubble or droplet flow regimes in fractures have been observed under two-phase conditions by Fourar *et al.* (1993), and in our micromodel observations under three-phase flow conditions (Figure 6.2) at higher capillary numbers ($> 10^{-5}$ in the fracture).

In this study, we image the NAPL, air and water saturations under a variety of three-phase flow conditions in different fractured cores, either with an impermeable matrix (granite cores) or a permeable matrix (sandstone cores). The saturation profile in the fracture and matrix after the displacements is acquired using a CT-scanner (described in detail in Chapter 2), to measure the effectiveness of the displacement process in reducing the saturation of the resident phase(s). We then compare these observations to simulations in a multiphase flow model (ECLIPSE), where the constitutive three-phase relative permeability-saturation-capillary pressure (K-S-P) relationships were constructed from the two-phase K-S-P functions using the method proposed by Parker and Lenhard (1990).

6.2 Theory

We use the general conservation of mass equation (Abriola and Pinder, 1985) presented in Chapter 5 to model three-phase flow :

$$\frac{\partial}{\partial t} \left[\sum_p \mathbf{f} x_{ip} \mathbf{r}_p S_p \right] + \sum_p [\nabla \cdot x_{ip} \mathbf{r}_p \bar{\mathbf{u}}_p] - \sum_p [\nabla \cdot \mathbf{f} \mathbf{r}_p D_{ip} \nabla x_{ip}] = \sum_p x_{ip} \mathbf{r}_p q_p \quad (6.1)$$

where:

S_p is the saturation of phase p

\mathbf{r}_p is the density of phase p

x_{ip} is the mass fraction of component i in phase p

\mathbf{f} is the porosity of the medium

$\bar{\mathbf{u}}_p$ is the velocity of phase p

D_{ip} is the dispersion/diffusion coefficient for component i in phase p

q_p is the source or sink term for phase p, per unit of bulk volume

We make the same assumptions as in Chapter 5, namely:

- the NAPL phase is insoluble in water.
- the mass sorbed relative to the mass in the NAPL phase is negligible for our analysis.
- dispersion/diffusion of dissolved contaminant is small compared to the advective flow in the fracture, at the time scale of advection.
- the time scale of the experiments is small enough that dissolution and volatilization is not significant, so we assume essentially immiscible flow. In fact, volatilization may be significant enough to affect the mass balance in some cases.
- the fluids are incompressible, or at least their compressibility is very small for the range of pressure changes in the experiments.
- the medium is incompressible.

With these assumptions, we can then write the equations governing three-phase flow in our experiments:

$$\mathbf{f} \frac{\partial S_w}{\partial t} + \nabla \cdot \bar{\mathbf{u}}_w = q_w \quad (6.2a)$$

$$\mathbf{f} \frac{\rho S_n}{\rho t} + \nabla \cdot \bar{\mathbf{u}}_n = q_n \quad (6.2b)$$

$$\mathbf{f} \frac{\rho S_g}{\rho t} + \nabla \cdot \bar{\mathbf{u}}_g = q_g \quad (6.2c)$$

where the subscripts w , o and g refer to the water, NAPL and gas phases.

We again assume that the relationship between flow velocity and pressure gradient is governed by a modified Darcy's law (Aziz and Settari, 1979):

$$\bar{\mathbf{u}}_p = \frac{kk_{r,p}}{\mathbf{m}} \nabla (P_p - \mathbf{r}_p gz) \quad (6.3)$$

where:

k is the absolute permeability of the medium

k_{rp} is the relative permeability of phase p

\mathbf{m}_p is the viscosity of phase p

P_p is the pressure in phase p

g is the gravitational constant

z is the position along the vertical axis

Three capillary pressure relationships exist:

$$P_{cow} = P_o - P_w \quad (6.4a)$$

$$P_{cgo} = P_g - P_o \quad (6.4b)$$

$$P_{cgw} = P_g - P_w = P_{cgo} + P_{cow} \quad (6.4c)$$

but only two of these relationships are independent. The saturation constraint is now:

$$\sum_{p=1}^3 S_p = 1 \quad (6.5)$$

Several multiphase flow simulators have been constructed based on these concepts, with different levels of complexity (e.g. Abriola and Pinder, 1985; Faust, 1985; Falls and Schulte, 1992; Huyakorn et al., 1994; Kaluarachchi and Parker, 1990; Kia, 1991; Van

Geel and Sykes, 1994; White et al., 1995). At issue is the functional relationship between relative permeability, saturation and capillary pressure (also known as the K-S-P functions).

6.2.1 Capillary Pressure

Given the extreme difficulty of measuring the three-phase K-S-P functions experimentally, there have been several approaches to construct these functions based on the two-phase relationships, which are more easily measured. One of the first attempts at developing three-phase saturation-capillary pressure (S-P) functions in porous media was the work of Leverett (1941). Leverett assumed that NAPL-water capillary pressure was only a function of effective water saturation (i.e. water saturation restricted to the range where water is mobile), and that total effective liquid saturation was a function of air-oil capillary pressure. The gas saturation can then be derived from the saturation constraint. Leverett and Lewis (1941) tested this hypothesis in a series of experiments, which appeared to corroborate their theoretical assumptions.

More recently, Parker and Lenhard (1987) and Lenhard and Parker (1987) have proposed a revised approach to Leverett's method to generate three-phase K-S-P functions from two-phase data. Based on van Genuchten's (1980) two-phase S-P function, and considering the same assumptions made by Leverett (1941), they propose the following scaled three-phase S-P function:

$$\bar{S}_j = \left[1 + (\mathbf{a}b_{ij} P_{cij} / \mathbf{r}_w g)^n \right]^{\frac{1}{n}-1} \quad (6.6)$$

where $\bar{S}_j = (S_j - S_m) / (1 - S_m)$ = scaled saturation of phase j

\mathbf{a} = a fitting parameter which varies with soil type, and possibly with saturation history, i.e. drainage or imbibition,

P_{cij} = capillary pressure between fluid i and j ,

$\mathbf{b}_{ij} = \mathbf{s}_{aw} / \mathbf{s}_{ij}$ = a scaling parameter for the different fluid pairs, from Parker and

Lenhard (1990),

\mathbf{r}_w = density of water,

g = gravitational acceleration constant,

n = a fitting parameter, related to soil type, possibly correlated with pore size distribution,

S_j = saturation of phase j ,

S_m = minimum water saturation (= S_{wc}),

\mathbf{s}_{ij} = interfacial tension between phase i and j .

In a series of experiments, Lenhard and Parker (1988), Lenhard (1992) and Busby *et al.* (1994) have tested the validity of the three-phase S-P model, by first measuring the two-phase S-P functions experimentally, then obtaining several points along the three-phase S-P curve and comparing the experimental work to the theoretical S-P relationship, with good agreement. The scaled two and three-phase S-P data points fall close to the scaled function (Equation 6.8), for different NAPLs and soils. Busby *et al.* (1994) found that the scaling parameter \mathbf{b}_{ij} is not accurately predicted by the ratio of interfacial tensions in all cases, when \mathbf{a} and n are considered constant for a particular soil and obtained from the air-water S-P curve. The scaling model is best for sands; materials that contain appreciable amounts of clay are not adequately modeled using \mathbf{b}_{ij} from the ratio of interfacial tensions. Parker and Lenhard (1990) do not consider the effect of contact angle (and thus wettability) in the scaling ratio, and this would appear to be a significant contributing factor to the scaling model which hasn't been incorporated. Ferrand *et al.* (1990) have also used a scaled three-phase S-P function constructed from two-phase relationships to model experimental results, also with good agreement for monotonic drainage.

To construct a scaled capillary pressure function for the fractured granite and sandstone cores (Core C, Core D and Core F from Chapter 2), we fit Equation 6.6 to the macroscopic P-S functions developed in Chapter 5 for two-phase flow. The graphical comparison is presented in Figure 6.3. The fitting parameter values are in Table 6.1. The fit is quite good for the higher saturations (a result partially due to the weighing in least-squares fitting), and is very good for the granite cores for saturations greater than 0.25. For the sandstone core (Core F, Figure 6.3c), the fit is only good for saturations greater than 0.6. The value of a is around two to three orders of magnitude greater than for the matrix in porous soils (Busby *et al.*, 1994; Parker and Lenhard, 1990; Lenhard and Parker, 1988), which reflects the much larger “pore” (aperture) size in the fracture compared with the porous matrix, and thus the much smaller capillary pressures in a fracture with respect to those in the matrix of soils. This is also reflected in the relative value of α between the three fractures, where a (Core D) > a (Core C) > a (Core F), which correlates well with their mean aperture. The exponent n ranges from 1.70 to 2.64 for the fractures, which is a fairly narrow range compared to the soils reported in previous studies, which may range from 1.3 to 6.97. The values found for the fractures are closer to those of the more complex, fine-grained soils such as loams, ($n = 1.3$ to 1.68) than for quartz sand ($n = 6.97$).

Table 6.1 Parameter values for Scaled Capillary Pressure-Saturation Functions

Parameter	Core C	Core D	Core F
a (m ⁻¹)	401	1312	224
n	2.41	2.64	1.70

S_m	0.0027	0.132	0.064
-------	--------	-------	-------

6.2.1 Relative Permeability

To construct three-phase relative permeability-saturation (K-S) functions, Corey *et al.* (1956) proposed using Burdine's (1953) method, based on the pore distribution and a simple power law model for two-phase S-P. Another widely used method in the petroleum engineering field for deriving three-phase K-S functions from two-phase data is that of Stone (1970, 1973), who has actually proposed two approaches. In the first model,

$$k_{ro} = S_o^* \left(\frac{k_{row}}{1 - S_w^*} \right) \left(\frac{k_{rog}}{1 - S_g^*} \right) \quad (6.7)$$

where k_{ro} = three-phase oil relative permeability

$k_{row} = f(S_w)$ = oil relative permeability in the presence of water only

$k_{rog} = f(S_g)$ = oil relative permeability in the presence of gas only

$$S_o^* = \text{effective oil saturation} = \frac{S_o - S_{om}}{1 - S_{wc} - S_{om}}$$

$$S_w^* = \text{effective water saturation} = \frac{S_w - S_{wc}}{1 - S_{wc} - S_{om}}$$

$$S_g^* = \text{effective gas saturation} = \frac{S_g}{1 - S_{wc} - S_{om}}$$

S_{om} = minimum oil saturation under three-phase flow conditions,

S_{wc} = connate water saturation.

The model is valid only if $k_{row}(S_w = S_{wc}) = k_{rog}(S_g = 0) = 1$, so that the three-phase relative permeability then collapses to the respective two-phase relative permeability. This model requires not only the two-phase relative permeabilities but also S_{om} , which may be a difficult parameter to obtain, since it is usually path-dependent (i.e. it depends on the imbibition and drainage history of the medium).

In the second model proposed by Stone (1973), S_{om} is not required:

$$k_{ro} = (k_{row} + k_{rw})(k_{rog} + k_{rg}) - (k_{rw} + k_{rg}) \quad (6.8)$$

Here, $k_{rw} = f(S_w)$ = water relative permeability,

$k_{rg} = f(S_g)$ = gas relative permeability.

In both models, the relative permeabilities of water and gas are assumed to depend only on their own saturation, and follow the two-phase relationship (Faust, 1985). Both of these methods are strictly empirical, and produce significantly different three-phase oil relative permeabilities, which has serious implications for multiphase flow modeling.

Parker *et al.* (1987) have proposed a three-phase K-S model based on Mualem's two-phase K-S model. The model is parameterized as follows:

$$k_{rw} = \bar{S}_w^{1/2} \left[1 - \left(1 - \bar{S}_w^{1/m} \right)^m \right]^2 \quad (6.9)$$

$$k_{ro} = (\bar{S}_L - \bar{S}_w)^{1/2} \left\{ \left[1 - \left(1 - \bar{S}_w^{1/m} \right)^m \right] - \left[1 - \left(1 - \bar{S}_L^{1/m} \right)^m \right] \right\}^2 \quad (6.10)$$

$$k_{rg} = (1 - \bar{S}_L)^{1/2} \left(1 - \bar{S}_L^{1/m} \right)^{2m} \quad (6.11)$$

where $m = 1/n$, obtained from the S-P function (Equation 6.6), and

$$\bar{S}_L = \frac{S_o + S_w - S_m}{1 - S_m} = \text{scaled total liquid saturation.}$$

Parker and Lenhard (1990) have evaluated these K-S functions against experimental results of water drainage by NAPL injection from two different soils, with a different NAPL in each soil. They compared experimental cumulative water flow out of the cores against a numerical simulation using Equations 6.9 - 6.11 with m obtained from capillary pressure measurements, and found a reasonably close match. Although this model is still empirically based, it has the advantage that the parameter values for the K-S-P relations can be more easily obtained from two-phase S-P experiments than the parameter values needed for Stone's methods.

We use here Parker and Lenhard's method to construct the three-phase relative permeabilities of the fractures, obtained from the study of the capillary pressure of the fractures, which in turn is based on the fracture aperture distribution, rather than on Stone's methods which are more data intensive. In Figure 6.4, k_{rw} and k_{rg} are plotted as a function of S_w and n . For the fractures in the granite cores, Equation 6.9 predicts a rather low k_{rw} for $S_w < 0.9$, and for the fracture in the sandstone core, k_{rw} is very low for $S_w < 0.8$. The opposite is the case for k_{rg} , where Equation 6.10 predicts essentially a linear relation between k_{rg} and S_w (or S_g) for the three fractures.

We explored the impact of the exponent n on k_{rw} and k_{rg} , to determine what value of the exponent would result in a linear relation between k_{rw} and S_w , given the modeling results from two phase flow, which indicate a linear relation between saturation and relative permeability for either phase. This occurs for $n \approx 0.7$, which is considerably lower than the exponent for any of the fractures.

For k_{ro} , we have to consider both S_w and S_L , or alternatively S_w and S_g . Interestingly enough, there is practically no variation in k_{ro} with n , for the range of interest ($n = 1$ to 7). In Figure 6.5 we present k_{ro} as a function of S_w and S_g . For $S_g = 0$, k_{ro} is close to linear with S_w (or S_o). As S_g increases, $k_{ro,max}$ decreases rapidly, reflecting the reduction in flow paths for the oil phase.

6.3 Experimental Observation of Three-Phase Flow

6.3.1 Experimental Method

For the three-phase flow experiments we used three cores, described in more detail in Chapter 2: a granite core with a simple fracture (Core C), a granite core with a complex set of fractures (Core D), and a sandstone core with a single fracture (Core F). The granite cores were chosen to represent fracture flow within an impermeable matrix, which allows us to isolate the processes involved in three-phase fracture flow, whereas the sandstone core involves the interactions between fracture and matrix and allows us to compare the flow dynamics of a permeable matrix with that of the granite cores. The core holder details are given in Chapter 5.

The cores were initially completely dry. After flushing with CO₂, water was allowed to imbibe until the cores were fully water saturated. Then there were three different displacement sequences, performed one after the other for each core:

- (1) PCE -> Air -> Water
- (2) Water -> PCE -> Air/Water
- (3) Air -> Water -> PCE/Air/Water

The first one follows the sequence of three-phase displacements typical of a NAPL spill into an unsaturated medium with some residual water. The second sequence parallels a water infiltration event into a PCE-contaminated unsaturated zone, or the sequence of three-phase flow displacements that occur when PCE is trapped as ganglia in the unsaturated zone and is displaced by a rising water table. The third sequence corresponds to either a falling water table, so that air reenters into the pore and fracture space, or active Soil Vapor Extraction of a NAPL pool.

In all cases, the liquid being introduced was pumped at 1.0 mL/min using HPLC pumps (Model 48-00, Rainin Instruments), and air was introduced at a constant pressure of 0.2 psi. The inlet and outlet pressures were measured with pressure transducers (Celesco DP-31 with demodulators model CD10B) to monitor any trends or abrupt

changes in pressure gradient. The outflow was collected and measured as a function of time, distinguishing between the two liquid phases.

Imaging three fluid saturations requires operating the scanner under dual-energy conditions, i.e. each location is sampled at a high and low x-ray energy, in order to solve for the three saturations. In fact, to obtain the three-phase saturation information, eight CT-scans are needed at each position (Burger, 1996): (a) a scan of the air-saturated core at energies 1 and 2, CT_{ar1} and CT_{ar2} ; (b) a scan of the water-saturated core at energies 1 and 2, CT_{wr1} and CT_{wr2} ; (c) a scan of the NAPL-saturated core at energies 1 and 2, CT_{nr1} and CT_{nr2} ; and (d) a scan of the core at a three-phase saturation, at energies 1 and 2, CT_1 and CT_2 . Sharma (1996), improving on the work by Vinegar and Wellington (1987), has derived the equations to calculate the saturation of each phase;:

$$S_o = \frac{(CT_1 - CT_{ar1})(CT_{wr2} - CT_{ar2}) - (CT_2 - CT_{ar2})(CT_{wr1} - CT_{ar1})}{(CT_{or1} - CT_{ar1})(CT_{wr2} - CT_{ar2}) - (CT_{or2} - CT_{ar2})(CT_{wr1} - CT_{ar1})} \quad (6.12)$$

$$S_w = \frac{(CT_2 - CT_{ar2})(CT_{or1} - CT_{ar1}) - (CT_1 - CT_{ar1})(CT_{or2} - CT_{ar2})}{(CT_{or1} - CT_{ar1})(CT_{wr2} - CT_{ar2}) - (CT_{or2} - CT_{ar2})(CT_{wr1} - CT_{ar1})} \quad (6.13)$$

$$S_a = 1 - S_o - S_w \quad (6.14)$$

To choose the high and low energy levels, several factors need to be considered. The difference between the high and low energy levels should be as large as possible, to have a smaller error in the calculation of the three saturations. There must be enough energy transmitted at the low energy to obtain a clear image; if the energy is too low, it is quite possible to have an “energy-starved” image with dark lines, indicating that some detectors received no signal since all the x-ray energy was reflected or absorbed by a dense region in the sample. If the high level energy is too high, the scanner can easily overheat, requiring very long cooling periods between scans, and it also shortens the life

of the x-ray lamp. After evaluating the quality of the low energy images, the cooling time at the high energy level and the resulting difference in the two images (high and low level), we choose to work at 140 kV and 80 kV, both at a current of 80 mA. All other scanner parameters are as described in Chapter 2.

The images of the rock with only air were taken at the beginning of the studies. The core saturated with water was imaged at both energies after imbibition into the CO₂ filled core. For the PCE-saturated core, first all of the experiments were performed (two- and three-phase) and then the core was steam cleaned, dried with hot air, then cooled, before PCE was injected into the CO₂ filled core. The CO₂ was allowed to dissolve in PCE for 24 hr before additional PCE was injected to flush the core filled with the PCE/CO₂ mixture. The PCE-saturated core was then imaged at both energies. The images with three-phase saturation were taken at the end of each displacement. In all cases the images were taken with a spacing of 3 mm between “slices” perpendicular to the core’s longitudinal direction. The main fracture plane of all the cores was horizontal, so that flow was mostly in a horizontal plane, except in the case of the complex fracture network of Core D. The two- or three-dimensional image of the saturation of each phase was then reconstructed from these slices using Equations 6.12, 6.13 and 6.14.

Burger (1996) has estimated the error for the saturation calculations using Equations 6.12, 6.13 and 6.14, and has found that the error can vary from 2.9% up to 11.5%, depending on the sample and the difference between energy levels. This is important when trying to discern a particular phase at very low saturation, where the error may be of the same magnitude as the mean saturation value. For the phase(s) at high saturation, the error in saturation is not as significant, since we seek mostly to detect the presence and location of the phases.

6.3.2 Saturation profiles

We first studied the three phase displacements in the simplest granite core, C. This core has only a single horizontal fracture, but with significant variability in fracture aperture, as described in Chapter 2. In Figure 6.6 we present the NAPL (PCE), water and air saturations after PCE has been injected into the unsaturated core (air has displaced most of the water). Although only PCE was been produced in the outlet, and more than two pore volumes had been injected, it appeared that PCE had found some preferential channels and displaced only some of the air, trapping the rest in the fracture. Water saturation was quite low in most of the fracture. Subsequent water flooding of the core (Figure 6.7) practically removed all the air and most of the NAPL. In fact, PCE outflow contained at first a significant number of air bubbles. The injection of air at low pressure to displace the water/PCE/air phases in the core reduced significantly the water saturation, and PCE was only detected as small, disconnected drops (Figure 6.8). The pore volumes injected for each displacement are presented in Table 6.2.

After PCE injection into the unsaturated core (C), the average NAPL saturation is 39.5%. The NAPL saturation decreases to 7.5% after water flooding, and drops to 1.6% after air injection. These low residual saturations are consistent with our observations of flow at the pore scale, which results in very low NAPL saturations.

Table 6.2 Experimental Conditions for Three-Phase Experiments

Pore Volumes injected	Core C	Core D	Core F
PCE -> Air -> Water	1.25 PV	1.25 PV	1.1 PV
Water -> PCE -> Air/Water	1.25 PV	1.25 PV	2.5 PV

Air -> Water -> PCE/Air/Water	1.25 PV	5 PV	*
-------------------------------	---------	------	---

* CT-scan data indicates misalignment of core versus original position, rendering the analysis fruitless.

Core D is a granite core with two main fractures, one oriented horizontally along the longitudinal axis of the core, and the other vertical and almost perpendicular to the first, near the core outlet (right hand side on the saturation images). We present the situation at the end of each displacement for the horizontal fracture plane (as seen from the “top” view of the fracture) and as a reconstructed “side” view of the core, to observe vertical flow. The vertical fracture is at an angle with respect to the longitudinal direction, so that even though it has a small average aperture, on the images it appears as a much larger feature. For PCE displacing air and water in the unsaturated core (Figure 6.9), we observe a more complete displacement by PCE of the air phase than for Core C, resulting in few trapped air bubbles. Subsequent displacement of PCE via water flooding results in a high water saturation (Figure 6.10) but also in considerable trapping of PCE. Air saturation was rather low, with only a few trapped bubbles, since this is already the second displacement of air, first by PCE then by water displacing PCE. In the final displacement, air is injected to displace water and PCE (Figure 6.11). PCE is removed to leave behind only a very low saturation, mostly in disconnected drops; some of the PCE remains at the bottom of the vertical fracture. Water is mostly along the edges, where we have the narrowest apertures, and in the vertical fracture, where air is less likely to enter to displace either liquid phase, due to gravity effects.

In the case of Core D, the initial injection of PCE into an unsaturated core results in a final NAPL saturation of 68.4%, which is significantly higher than for Core C, which reflects the larger apertures in Core D and thus the easier displacement of the resident phases. Also, since PCE can displace water from the vertical fracture (due to their density difference), a greater PCE saturation can be achieved. After subsequent water flooding, average PCE saturation drops to 18.2%; water is not very effective in removing PCE from the vertical fracture. After air displaces both water and PCE (and probably some

volatilization occurs), average PCE saturation is down to 5.4%, again reflecting a relatively low NAPL saturation under three-phase flow conditions.

In the fractured sandstone core F, the matrix plays a significant role. We present a horizontal “slice” through the middle of the core, reconstructed from 76 scans along the core length, as well as a vertical “slice”, perpendicular to the fracture plane. For PCE displacing Air that displaces water (i.e. PCE entering a partially saturated fractured porous media), PCE is seen to travel mostly at the bottom of the core, below the fracture plane (Figure 6.12). This is seen most clearly on the vertical slice presenting the NAPL saturation. NAPL saturation in this region is relatively high. The horizontal slice presenting NAPL saturation indicates that at the middle of the core the NAPL saturation is fairly low (25 to 50%) and mostly on one side of the core. A significant amount of water is in the upper region of the core, although air saturation is more evenly distributed along the core. The fracture appears to separate the upper, water-saturated region, from the lower PCE-saturated region.

In the next displacement in Core F, water displaces PCE which displaces air (Figure 6.13). Air saturation is very nearly the same as in the first displacement, suggesting that the air is mostly trapped. Water saturation is now more evenly distributed in the core, although the lower region of the core (as seen in the vertical slice) still contains more PCE. The highest water saturation is apparently near the fracture, which is near the middle of the core in the vertical slice.

6.3.3 Steam Injection

Steam injection was used in these experiments to clean the granite and sandstone cores between one study and the next, which results in three-phase flow conditions (steam, water and NAPL). Steam injection has been proposed as a means of cleaning up underground contamination (EPA, 1995; Clarke *et al.*, 1994; Falta *et al.*, 1992; Udell and Stewart, 1989), and is commonly used to enhance oil recovery (Matheny, 1980). Several

processes are at work during steam injection. The mobility of NAPL is increased by reducing its viscosity (Willman *et al.*, 1961) and in some cases the interfacial tensions (Akatsuka *et al.*, 1995), as the temperature of the fluids rises. A hot water bank forms ahead of the steam front, which displaces NAPL ahead of it (Prats, 1986). NAPL can more easily volatilize into the gas phase, where it can then be removed in the outlet.

A major concern during steam injection into consolidated material is the amount of energy required to heat up the rock and resident fluids. Marx and Langenheim (1959) and Lauwerier (1955) have developed analytical methods to approximate the heat requirements for a simple geometry in porous media, based on an energy balance. The energy required can then be estimated from the heat capacities of the rock and fluids, as well as the enthalpy of the injected steam.

For steam injection into fractured rock, steam enters first through the fracture, but rapidly condenses as the steam loses heat to the surrounding rock matrix. Steam will continue to condense until the surrounding matrix is at least at the steam's temperature and pressure. This mechanism ensures that all of the fracture and a significant fraction of the matrix is heated, rather than having steam travel very fast through the fracture to the outlet (or producing well).

The setup used in these experiments is shown in Figure 6.14. Deionized, distilled water at a constant flow rate is pumped through the steam generator, and then into the core inlet through insulated steel tubing. A four-way valve at the core's inlet allows for the removal of condensed water from the inlet line, so that only steam is pumped into the core. Steam pressure and temperature are measured right before the core's inlet and at the core's outlet. The temperature at five equidistant points along the longitudinal axis of the core is also measured using thermocouples, and recorded directly into a computer file using LabView.

The temperature profile of a typical run in the fractured sandstone Core F is shown in Figure 6.15. The inlet temperature rises rapidly, with a very sharp profile. The temperature profiles inside the core rise less rapidly, indicating that the steam/hot water

front becomes more diffuse as it travels through the core. Similar behavior is observed in the granite cores, indicating that it is the heat front that becomes more diffuse with time.

CT scans of the core during steam injection were made. However, the hot water front rapidly displaces all of the resident fluids in the fracture, so the scans reveal practically only water saturation, until the steam front displaces the hot water. Reconstruction of the CT scans with the core fully heated by steam indicate that the core has practically only steam, which appears as gas, with only a few cooler points (Figure 6.16 for Core C). A large water droplet is still observable near the outlet.

An important result obtained during steam injection was the comparison between the behavior of the unfractured sandstone Core E and the fractured sandstone Core F, which were otherwise identical. At the same steam flow rate, the pressure gradient across Core E was much higher than for Core F, with an average pressure drop of 29 psi in Core E compared to a pressure drop of 0.44 psi in Core F, at a flow rate of 1.25 mL/min. Each core was approximately 241 mm in length. However, Core F heated much faster than Core E, taking approximately 90 minutes to achieve complete heating to a uniform 102 ± 4 °C in Core F, compared with incomplete heating of Core E even after 300 minutes. This is due to (1) the larger surface area through which the heat can be transferred; and (2) the continual replacement of fluids in the fracture, with “fresh” hot steam displacing hot water which in turn displaces colder water, as opposed to the movement as a single front in the unfractured core, which dissipates much more heat to the surroundings.

6.4 Modeling of Three-Phase Flow in Fractured Media

To model three-phase flow in fractured porous media we use the ECLIPSE simulator, with the same input parameters as in Chapter 5 (c.f. Table 5.1), modifying the three-phase relative permeabilities and capillary pressures as indicated in section 6.2. For simulation purposes, the “residual” saturations considered for the matrix are 0.03 for

NAPL, 0.05 for water and 0.08 for air. We use the same dimensions and grid, namely a core with 180 x 50 x 50 mm (L x W x H), discretized with 60 x 1 x 51 blocks, with the fracture running in the middle of the core, along the horizontal direction. The fracture is modeled as a region of 60 x 1 blocks, with a homogenous aperture (and permeability) field. We attempted to model the heterogeneous permeability field obtained from the fracture aperture distribution, but it led to extreme instability of the ECLIPSE model, due to the large saturation changes in the small aperture regions. Even with a constant aperture, ECLIPSE required a very small time step for most simulations, to reduce the saturation changes due to the very high fracture permeability relative to the matrix.

The results obtained here are instructive for understanding the behavior that a fracture has in terms of three-phase flow in porous media, in particular with respect to the transfer between matrix and fracture due to capillary and viscous forces. We assume that the capillary forces in the matrix are two orders of magnitude greater than in the fracture. This assumption is valid for the larger aperture regions, but may in fact not be true in the small aperture regions, which compete in dimensions with the pores in the matrix. Only the front and rear faces are flow boundaries, with a constant inlet flow rate, and the outlet a constant (atmospheric) pressure boundary. In all of the simulations, we present the situation in the core after less than one pore volume has been injected, to evaluate the shape of the displacement fronts.

We first simulate injection of PCE into an unsaturated, fractured sandstone matrix (Figure 6.17), where the initial water saturation is 15% and the simulated connate water saturation is 14%. The PCE front is fairly sharp, leaving behind a high PCE saturation which basically displaces all of the air and mobile water. This is in direct contrast with the saturation profile acquired using CT-scanning, where a significant air saturation was still present (20-30%) after PCE injection. It is not difficult to modify the relative permeability relationship of the gas phase to leave behind a residual; however, it is difficult to predict *a priori* the residual gas saturation. Of particular interest is the shape of the water saturation, which is more affected by the fracture and capillary pressure than NAPL or gas

saturation. A small bank of water forms along the edges of the core, with better water displacement (by PCE) near the fracture.

For comparison between a fractured and unfractured core, we simulate the same core as before but without a fracture (Figure 6.18). We again observe very sharp PCE and air fronts, almost as predicted by Buckley-Leverett theory (for one-dimensional, two-phase flow). The water front is smeared over a larger part of the core, mostly by capillary pressure.

Next we analyze the injection of water into a fractured sandstone core which has a high initial (and homogeneous) PCE saturation, with gas and water near their residual saturations (Figure 6.19). In this case, water imbibes readily into the matrix displacing PCE. The fracture appears to facilitate the entry of water, which displaces both PCE and gas. Gas is displaced quite readily, and forms a very sharp front, while the PCE and water fronts are much more affected by both capillary pressure and the fracture. The effect of the fracture is more noticeable when comparing to an unfractured sandstone core (Figure 6.20), which presents very sharp fronts for PCE and air, and only some smearing of the water front due to capillary pressure.

The third analysis is gas injection into a fractured sandstone with a high initial water saturation, and a low PCE and gas saturations (Figure 6.21). In this case, NAPL is displaced preferentially near the fracture, but water is displaced along a fairly sharp front, which is almost unaffected by the fracture. The saturation profiles in the equivalent unfractured core (Figure 6.22) are all rather sharp, since capillary pressure actually tends to self-sharpen the water saturation profile.

6.5 Summary and Conclusions

We have observed the flow of three phases in fractured granite and sandstone cores, using CT-scanning. In general we find that the three-phase displacements, where an

injected phase displaces two other resident phases, are not entirely effective in terms of complete displacement, and in general result in residual saturations of the two displaced phases. However, NAPL saturations can be quite low after water flooding in the presence of air, much lower than typically achieved under a two-phase (water-NAPL) water flood.

The effectiveness of NAPL displacement by water flooding under three-phase conditions is complicated when multiple fractures are present, which results in more trapped NAPL than for the single fracture geometry. The presence of a porous matrix (e.g. sandstone cores) again complicates the interpretation of three-phase flow in the fracture, because the fracture-matrix capillary interactions are very significant.

We used steam injection to remove NAPL from the cores, with very good results for the fractured cores. In the granite cores, steam injection was effective in removing practically all remaining NAPL, and in achieving quite uniform heating. In the sandstone cores, uniform heating and complete NAPL removal was only achieved in the fractured core, but not in the unfractured core. The fracture is an effective means of delivering energy to heat up the porous matrix, which then results in mobilization, vaporization and removal of NAPL from the matrix.

Measuring three-phase K-S-P relationships in fractured media is extremely complicated, and we may only be able to infer these K-S-P functions from inverse modeling of controlled experiments. Our attempt here was to use existing methods for constructing three-phase K-S-P functions, and then apply them in a numerical (continuum) model to interpret our experimental observations. The CT-scanning data for three-phase flow in general, and in fractures in particular, is not yet clear enough to prove or disprove a particular method of constructing the K-S-P functions. Hence we only evaluated the potential role of a fracture in porous media during three-phase flow conditions using Parker and Lenhard's method for constructing the K-S-P functions, without attempting to determine if this is the best method.

To model the presence of a region of very high permeability and very low volume (i.e. the fracture plane) relative to the matrix in the numerical simulations requires very

small time steps, since the saturation changes in this region are very large, and the simulator might not otherwise converge. Adding the variability in fracture aperture to the simulator caused extreme instability, and the simulator could not converge. Therefore, comparing the experimental results to the numerical simulations was not feasible. We are then not able to model the potential for preferential paths within the fracture plane, nor the possibility for by-passing the non-wetting phase, and leaving behind some non-uniform saturation of gas, NAPL or water. We opted to illustrate the behavior of a very simple, “parallel-plate” fracture in a porous matrix, to gain some insights into the balance of forces that may occur during the various three-phase flow combinations.

The modeling results in this chapter illustrate that the presence of a fracture is more important in some displacement sequences than in others. In addition, the effect of the fracture is sometimes magnified by the role that high capillary pressure in the matrix (relative to the capillary pressure in the fracture) plays in sharpening or spreading the displacement front. For example, in the case of PCE movement into a fractured, unsaturated sandstone, the three fronts (PCE, water and air) are quite sharp and almost independent of the presence of a fracture or capillary forces. In contrast, for water flooding into a fractured core with high PCE saturation and some residual air, or air entrance into a fractured porous core with high water saturation and some PCE almost at residual, both the fracture and capillary forces play a significant role in the shape of the displacement fronts.

Further studies, both experimental and numerical, are needed to determine the three-phase K-S-P functions. These functions are likely to depend on many factors, such as the spreading coefficient (as inferred from the micromodel work in Chapter 4), the properties of the media (e.g. pore size distribution, surface wettability and heterogeneity), and the particular path of the displacement, i.e. whether it is an imbibition or a drainage process, or a combination of drainage and imbibition sequences. Therefore, understanding the behavior of the three-phase K-S-P relationships will require an extensive effort.

6.6 References

- Abriola, L. M. and G. F. Pinder, 1985: A multiphase approach to the modeling of porous media contamination by organic compounds, 1. Equation development, *Water Resources Research*, **21**:1, 11-18
- Akatsuka, S., H. Yoshigiwa and Y. H. Mori, 1995: Temperature dependencies of spreading coefficients of hydrocarbons on water, *J. Colloid and Interface Science*, **172**, 335-340
- Aziz, K. and A. Settari, 1979: *Petroleum Reservoir Simulation*, Applied Science, London
- Burdine, N. T., 1953: Relative permeability calculations from pore size distribution data, *Trans. Am. Inst. Min. Metall. Pet. Eng.*, **198**, 71-77
- Burger, J., 1996: *CT Development Guide*, Dept. of Petroleum Engineering, Stanford University, Stanford, CA
- Busby, R. D., R. J. Lenhard and D. E. Rolston, 1994: An investigation of saturation-capillary pressure relations in two- and three-fluid systems for several NAPLs in different porous media, *Ground Water*, **33**:4, 570-578
- Clarke, A. N., D. J. Wilson and P. R. dePercin, 1994: Thermally enhanced vapor stripping, in *Hazardous waste site soil remediation*, Wilson, D. J. and A. N. Clarke, eds., Marcel Dekker, New York, New York
- Corey, A. T., C. H. Rathjens, J. H. Henderson and M. R. J. Wyllie, 1956: Three phase relative permeability, *Trans. Am. Inst. Min. Metall. Pet. Eng.*, **207**, 349-351
- Dake, L. P., 1978: *Fundamentals of reservoir engineering*, Elsevier, Amsterdam
- EPA, 1995: In-Situ steam enhanced recovery process, Hughes Environmental Systems, Inc., Innovative Technology Evaluation Report, *United States Environmental Protection Agency EPA/540/R-94/510*, Office of Research and Development, Washington, D. C.
- Falls, A. H. and W. M. Schulte, 1992: Theory of three-component, three-phase displacement in porous media, *SPE Reservoir Engineering*, **8**, 377-384
- Falta, R. W., K. Pruess, I. Javandel and P. A. Witherspoon, 1992: Numerical modeling of steam injection for the removal of nonaqueous phase liquids from the subsurface, 1. Numerical formulation, *Water Resources Research*, **28**:2, 433-449
- Faust, C. R., 1985: Transport of immiscible fluids within and below the unsaturated zone: a numerical model, *Water Resources Research*, **21**:1, 587-596
- Fenwick, D. H. and M. J. Blunt, 1996: Three dimensional modeling of three phase imbibition and drainage, *Advances in Water Resources*, (in press)
- Fourar, M., S. Bories, R. Lenormand and P. Persoff, 1993: Two-phase flow in smooth and rough fractures: measurement and correlation by porous-medium and pipe flow models, *Water Resources Research*, **29**:11, 3699-3708
- Huyakorn, P. S., S. Panday and Y. S. Wu, 1994: A three-dimensional multiphase flow model for assessing NAPL contamination in porous and fractured media, 1. Formulation, *J. of Contaminant Hydrology*, **16**, 109-130
- Kaluarachchi, J. J. and J. C. Parker, 1990: Modeling multicomponent organic chemical transport in three-fluid-phase porous media, *J. of Contaminant Hydrology*, **5**, 349-374
- Kia, S. F., 1991: Subsurface multiphase flow of organic contaminants: model development and validation, *Water Resources*, **25**:10, 1225-1236
- Lauwerier, H. A., 1955: The transport of heat in an oil layer caused by injection of hot fluid, *Applied Scientific Research*, **A5**, 145-50
- Lenhard, R. J., 1992: Measurement and modeling of three-phase saturation-pressure hysteresis, *J. Contaminant Hydrology*, **9**, 243-269
- Lenhard, R. J. and J. C. Parker, 1987: A model for hysteretic constitutive relations governing multiphase flow: 2. Permeability-saturation relations, *Water Resources Research*, **23**:12, 2197-2206
- Leverett, M. C., 1941: Capillary behavior in porous solids, *Trans. Am. Inst. Min. Metall. Pet. Eng.*, **142**, 152-169
- Leverett, M. C. and W. B. Lewis, 1941: Steady flow of gas-oil-water mixtures through unconsolidated sands, *Trans. Am. Inst. Min. Metall. Pet. Eng.*, **142**, 107-116
- Matheny, S. L. Jr., 1980: EOR methods help ultimate recovery, *Oil and Gas J.*, March 31, 74-124

- Marx, J. W. and R. H. Langenheim, 1959: Reservoir heating by hot fluid injection, *Transactions AIME*, **219**, 312-315
- Mercer, J. W. and R. M. Cohen, 1990: A review of immiscible fluids in the subsurface: properties, models, characterization and remediation, *J. of Contaminant Hydrology*, **6**, 107-163
- Mutch, R. D. and J. I. Scott, 1994: Problems with the Remediation of Diffusion-Limited Fractured Rock Systems. *Hazardous Waste Site Soil Remediation: Theory and Application of Innovative Technologies*. New York, Marcel Dekker, Inc.
- Parker, J. C., R. J. Lenhard and T. Kuppasamy, 1987: A parametric model for constitutive properties governing multiphase fluid flow in porous media, *Water Resources Research*, **23**, 618-624
- Parker, J. C. and R. J. Lenhard, 1987: A model for hysteretic constitutive relations governing multiphase flow: 1. Saturation-pressure relations, *Water Resources Research*, **23**:12, 2187-2196
- Parker, J. C. and R. J. Lenhard, 1990: Determining three-phase permeability-saturation-pressure relations from two-phase system measurements, *J. Pet. Sci. and Eng.*, **4**, 57-65
- Prats, M., 1986: *Thermal recovery*, Soc. Pet. Eng. Monograph vol. 7, New York, NY
- Sharma, B., 1996: CT imaging techniques for two-phase and three-phase in situ saturation measurements, M. Eng. Dissertation, Stanford University, Stanford, California
- Stone, H. L., 1970: Probability model for estimating three phase relative permeability, *J. Pet. Technology*, **249**, 214-218
- Stone, H. L., 1973: Estimation of three-phase relative permeability and residual oil data, *J. Can. Pet. Technology*, **12**, 53-61
- Udell, K. S. and L. D. Stewart, 1989: Field study of an in situ steam injection and vacuum extraction for recovery of volatile organic solvents, *UCB-SEEHRL Rep. 89-2*, Univ. of California, Berkeley
- Van Geel, P. J. and J. F. Sykes, 1994: Laboratory and model simulations of a LNAPL spill in a variably-saturated sand, 2. Comparison of laboratory and model results, *J. of Contaminant Hydrology*, **17**, 27-53
- van Genuchten, M. T., 1980: A closed-form equation for predicting the hydraulic conductivity of unsaturated soils, *Soil Sci. Soc. Am. J.*, **44**, 892-898
- Vinegar, H. J. and S. L. Wellington, 1987: Tomographic imaging of three-phase flow experiments, *Rev. Sci. Instrumentation*, **58**, 96-107
- White, M. D., M. Oostrom and R. J. Lenhard, 1995: Modeling fluid flow and transport in variably saturated porous media with the STOMP simulator, 1. Nonvolatile three-phase model description, *Advances in Water Resources*, **18**:6, 353-364
- Willman, B. T., V. V. Valleroy, G. W. Runberg, A. J. Cornelius and L. W. Powers, 1961: Laboratory studies of oil recovery by steam injection, *J. Pet. Tech, Transactions AIME*, **222**, 681-690
- Wilson, J. L., S. H. Conrad, W. R. Mason, W. Peplinski and E. Hagan, 1990: Laboratory investigation of residual liquid organics from spills, leaks and the disposal of hazardous wastes in groundwater, EPA/600/6-90/004, Environmental Protection Agency, R. S. Kerr Env. Res. Lab., Ada, Oklahoma

Figure 6.1 Observation of three-phase flow in a fracture, simulated with a micromodel.



decane flowing in the fracture, displacing water

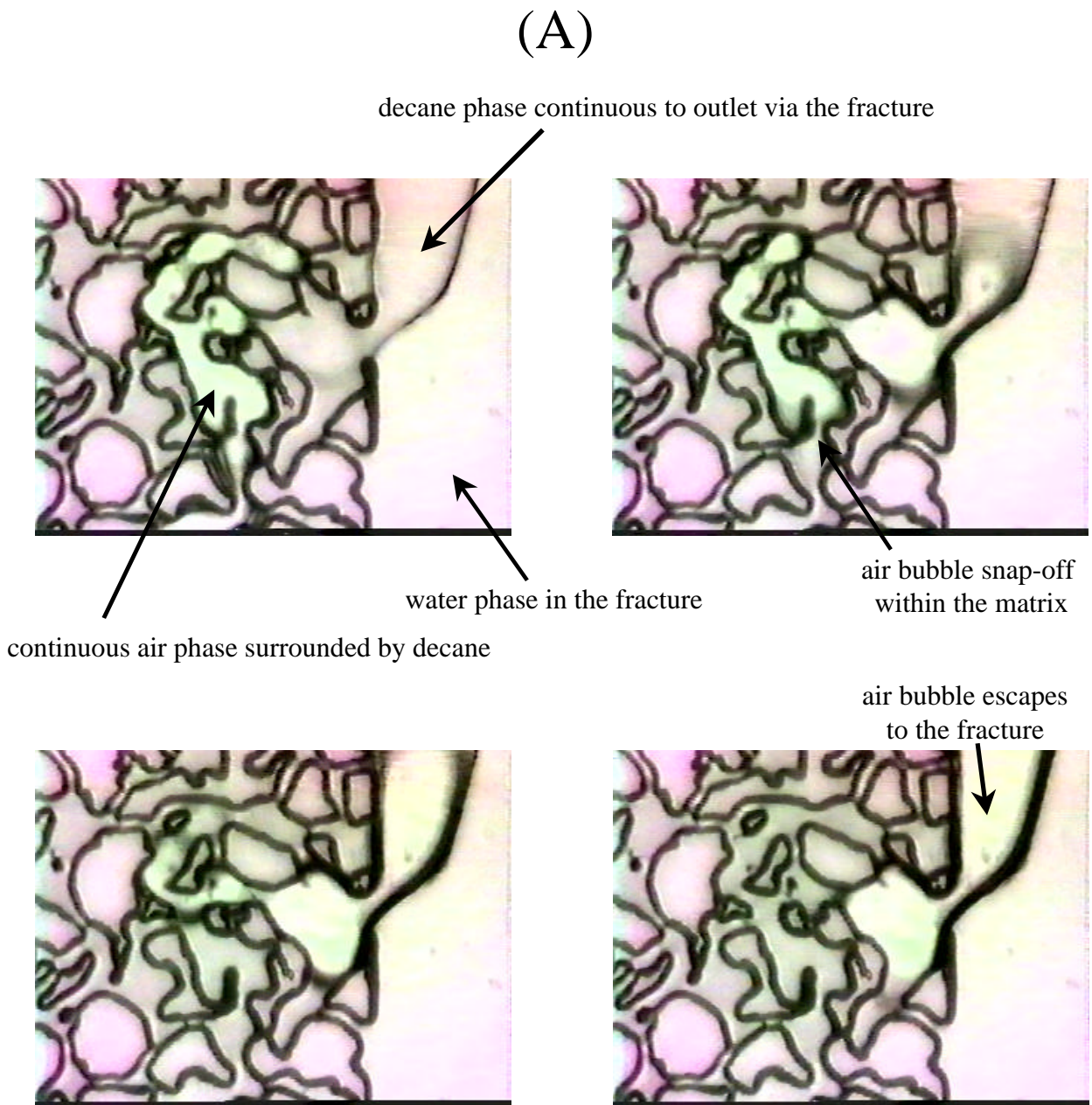


air moves through the fracture displacing decane; neither decane nor air enter the water-saturated matrix



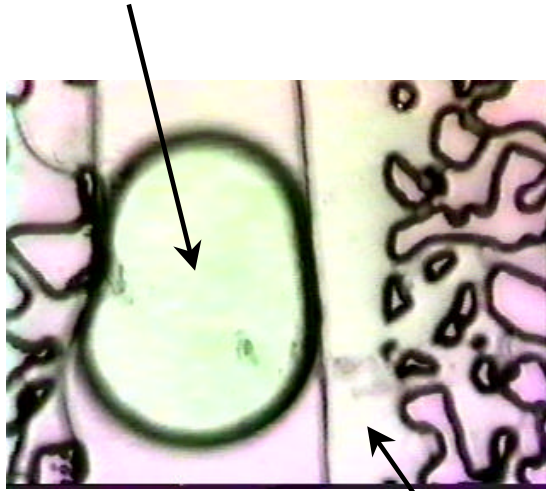
air displaces decane in the fracture and only a layer of decane covers the air bubble

Figure 6.2 Three sequences of air bubbles traveling inside the decane phase which is surrounded by water in a fracture: (A) Generation of snapped-off air bubble within the porous matrix and travel into the fracture; (B) air bubble traveling through wide decane channel in fracture; (C) air bubble traveling through narrow decane channel in fracture.



(B)

air bubble in decane phase



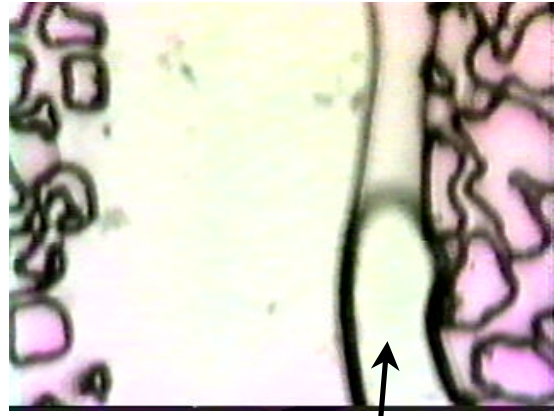
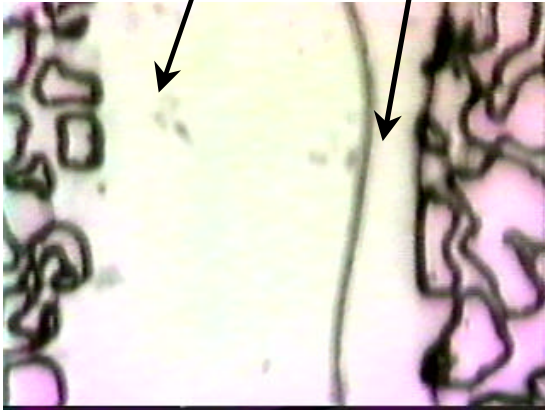
water phase in the fracture



(C)

water phase in the fracture

continuous decane in fracture



air bubble traveling in continuous decane phase, adjusting to the flow channel

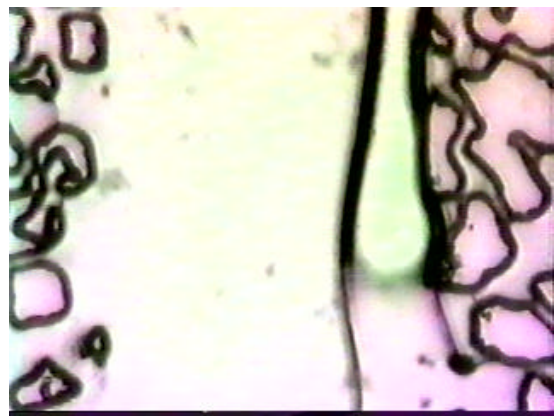


Figure 6.3 Air-water Capillary Pressures vs Scaled Saturations for (a) Core C (granite); (b) Core D (granite); and (c) Core F (sandstone). The scaled capillary curve from the network model is in black; the fitted function using the modified van Genuchten model is in gray.

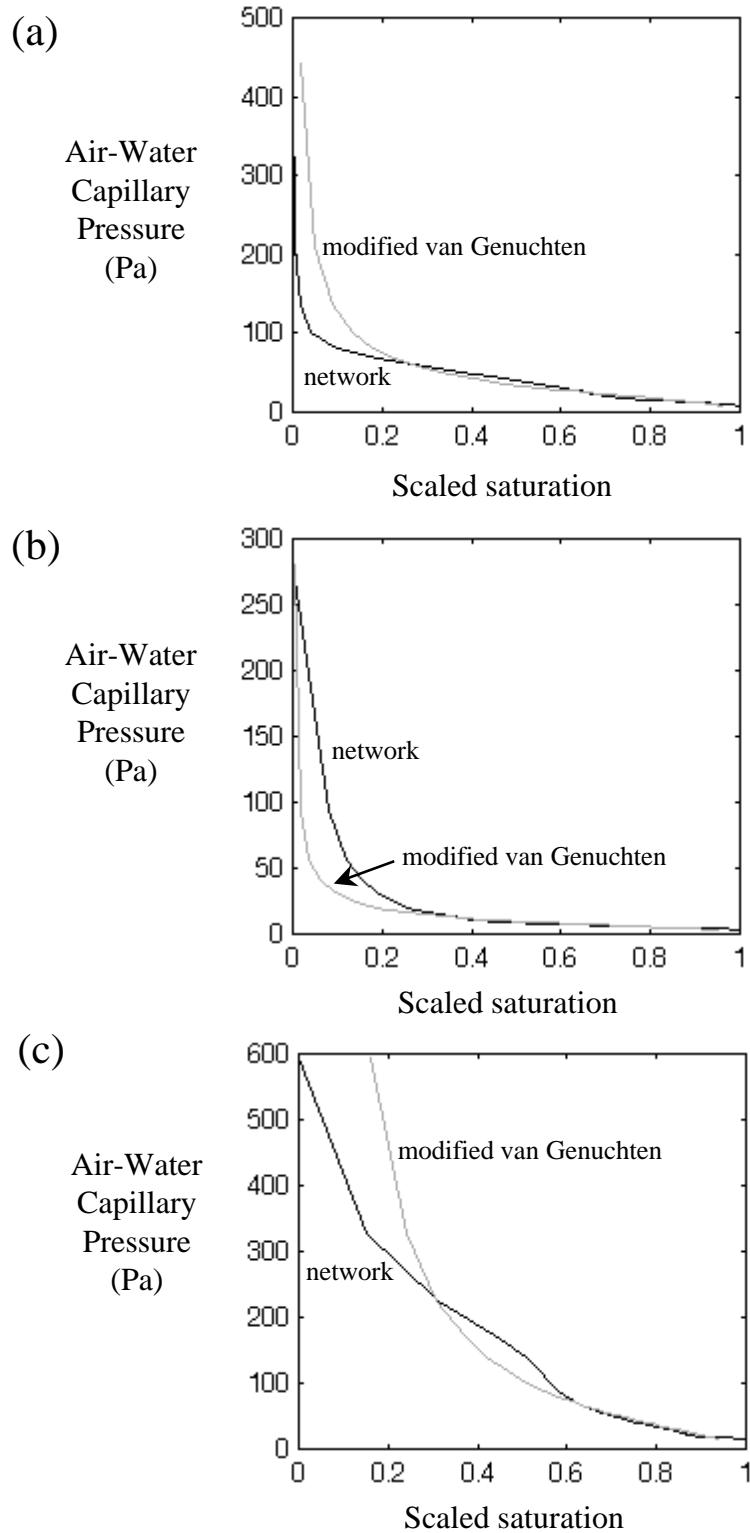


Figure 6.4 Three-phase relative permeabilities vs scaled water saturations for (a) k_{rw} and (b) k_{rg} , using equations 6.9 and 6.10. The exponent n ($= 1/m$) varies from 0.5 to 2.64 as indicated next to each curve.

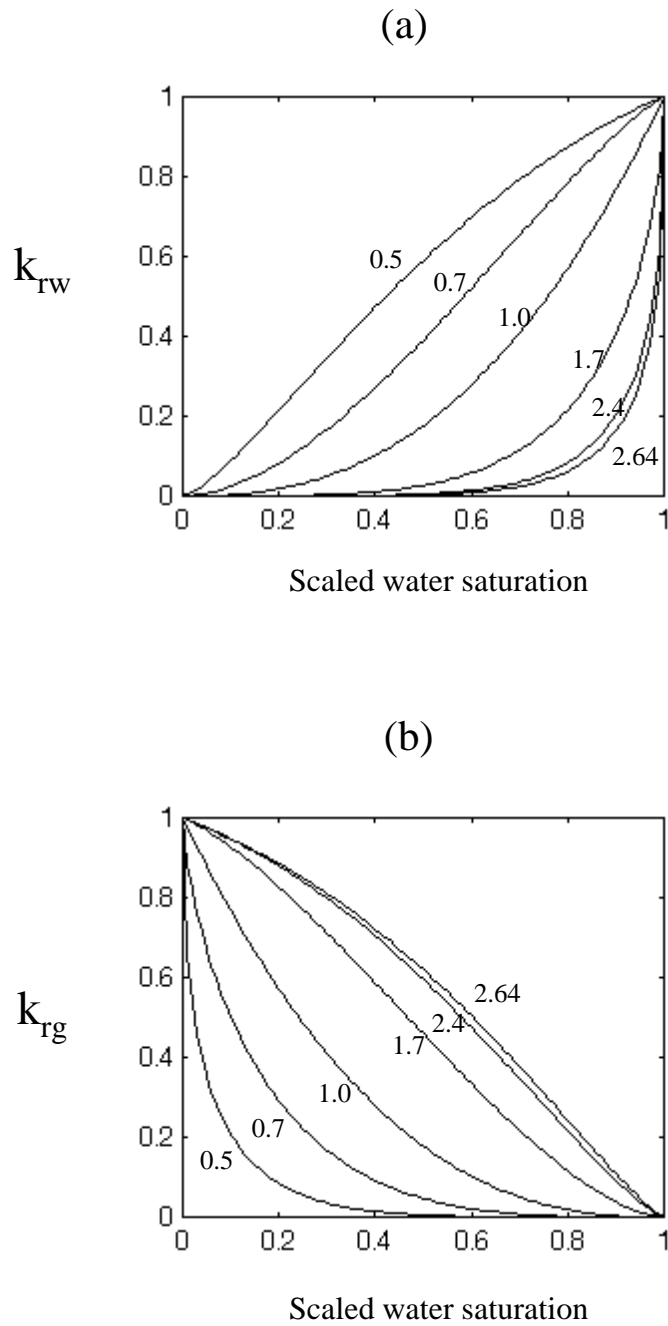


Figure 6.5 Three-phase relative permeability vs scaled water saturation for k_{ro} using equation 6.11. The scaled gas saturation varies from 0 to 0.8 as indicated next to each curve.

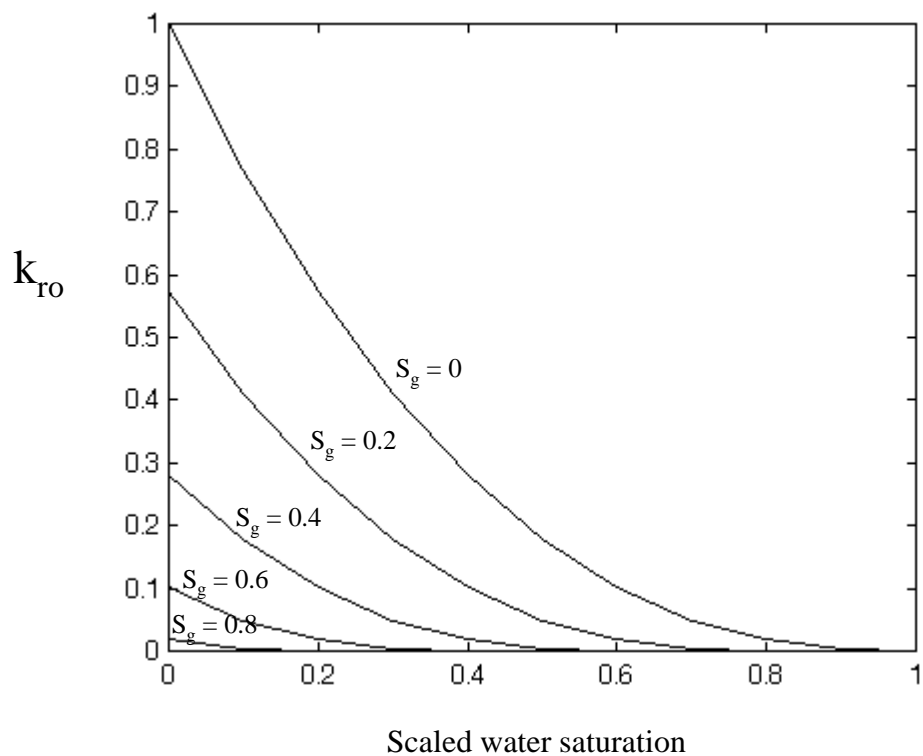
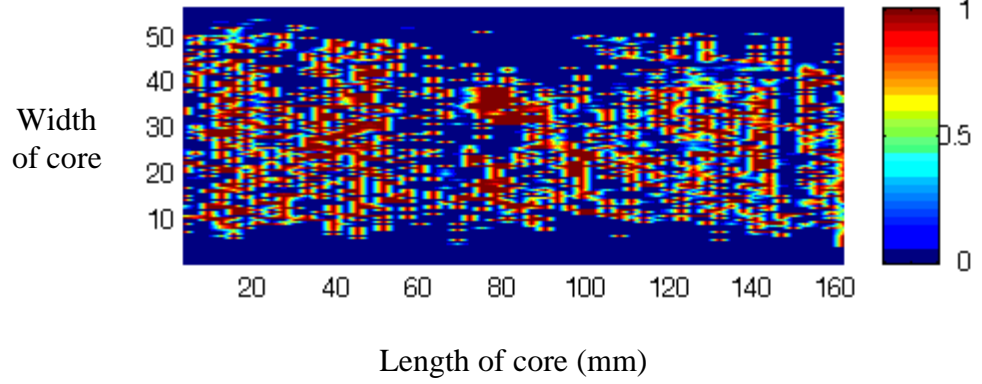
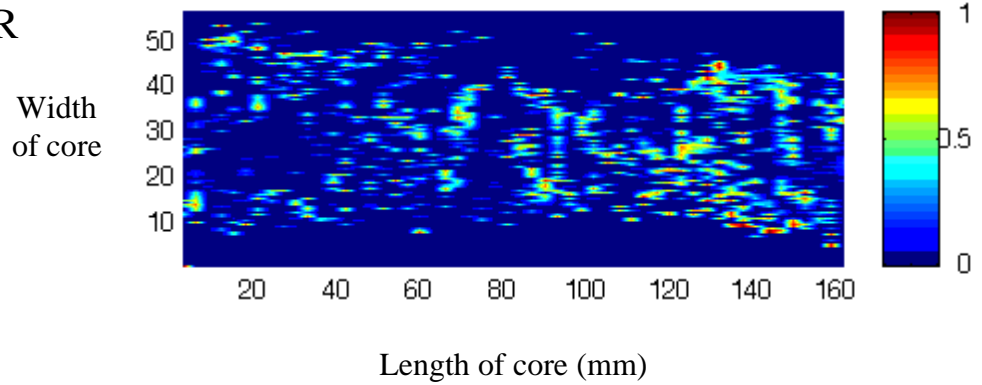


Figure 6.6 PCE displaces Air that displaces Water in Core C. Flow is on a horizontal plane, with the inlet on the left side of the images. The bar at right represents saturation of the corresponding fluid, on a scale from 0 to 1.

NAPL



WATER



AIR

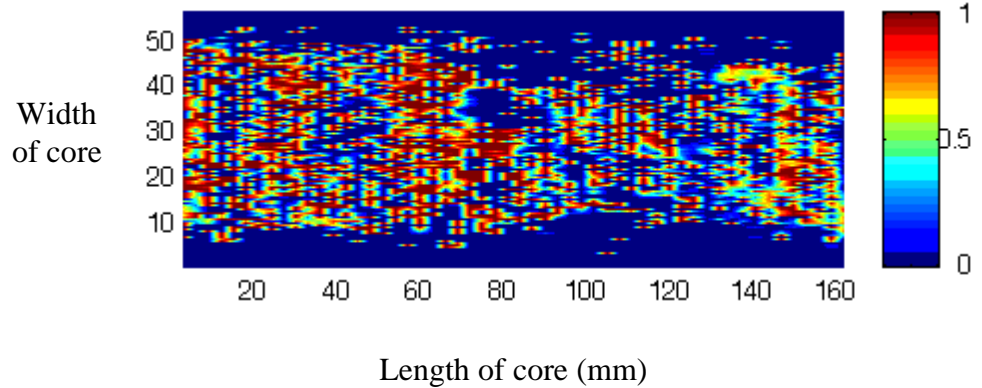


Figure 6.7 Water displaces PCE that displaces Air/Water in Core C. The core was initially at low water saturation, with air filling most of the pore space, then PCE was injected and then water displaces the other two phases. Flow is from left to right.

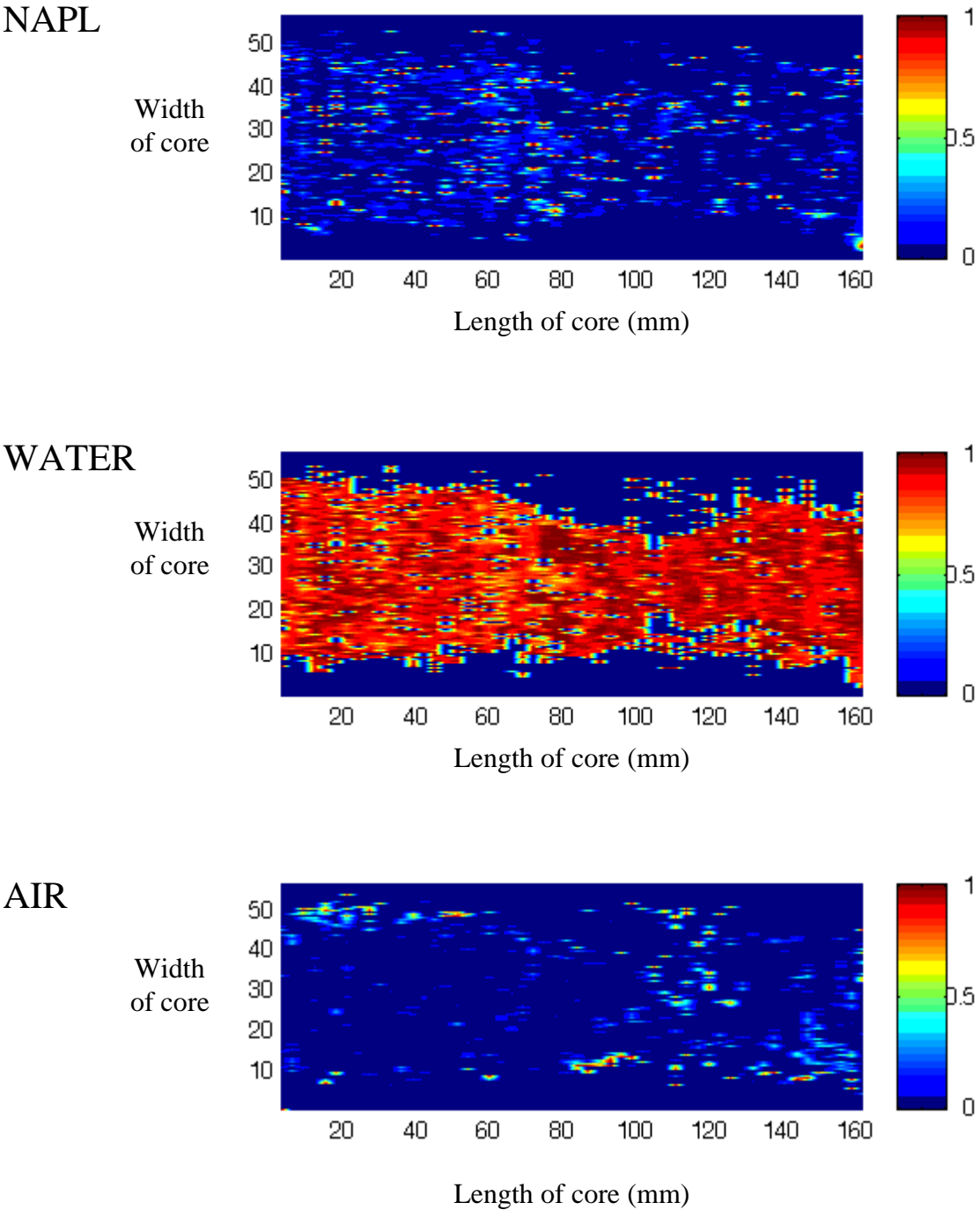


Figure 6.8 Air displaces Water that displaces PCE/Air/Water in Core C.

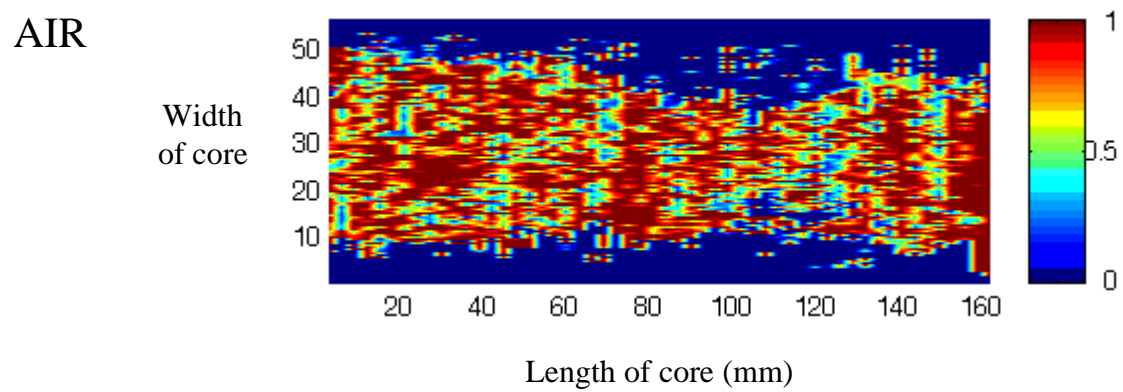
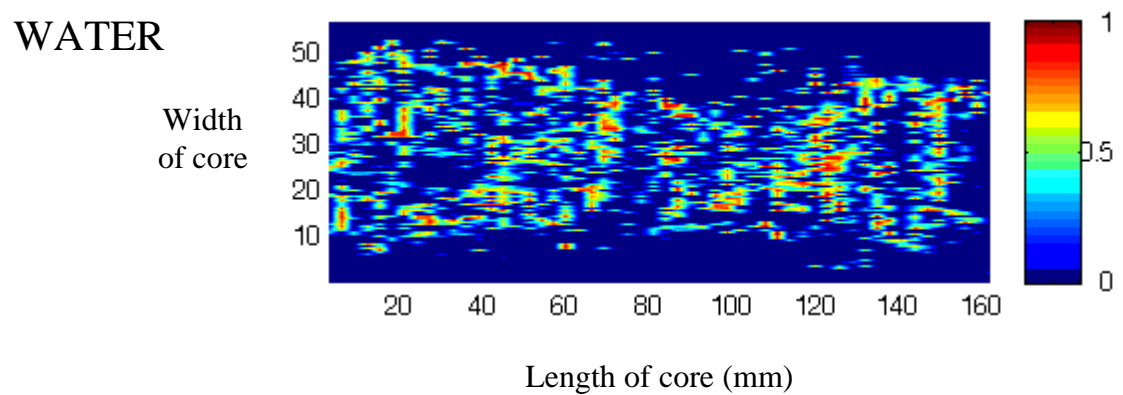
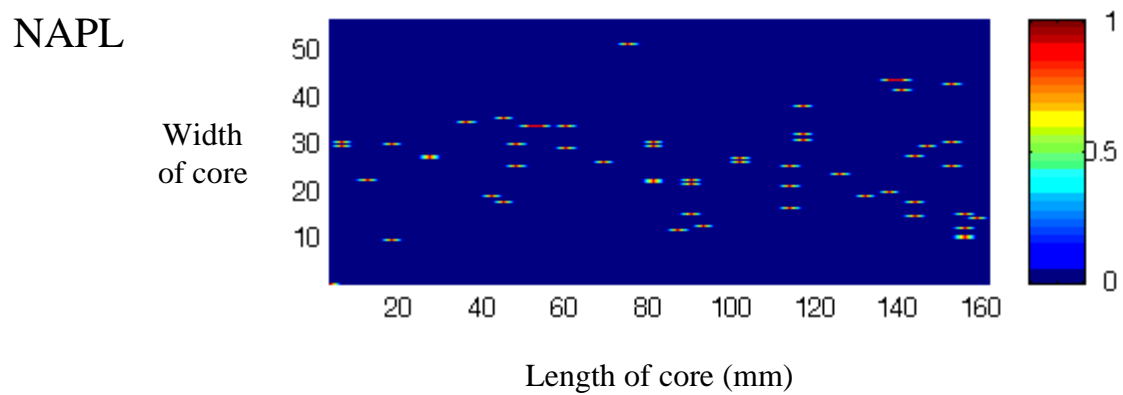
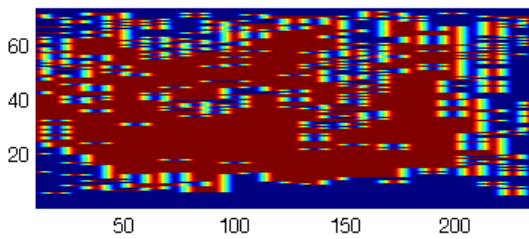


Figure 6.9 PCE displaces Air that displaces Water in Core D. The images on the left present the horizontal fracture plane from the top; the images on the right show a side view of the core and fracture planes. The bar at right represents saturation of the corresponding fluid, on a scale from 0 to 1.

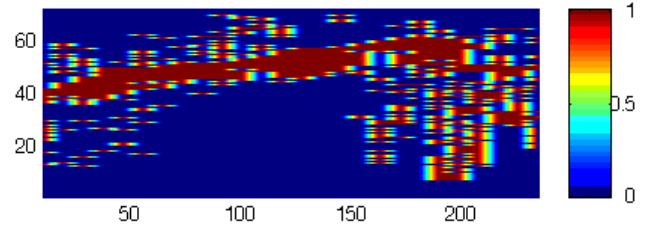
TOP VIEW OF FRACTURE

SIDE VIEW OF FRACTURE

NAPL

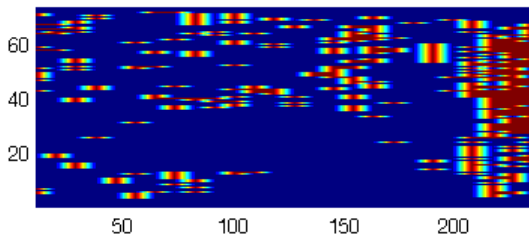


Length of core (mm)

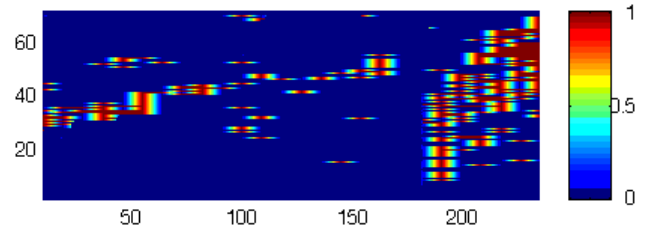


Length of core (mm)

WATER

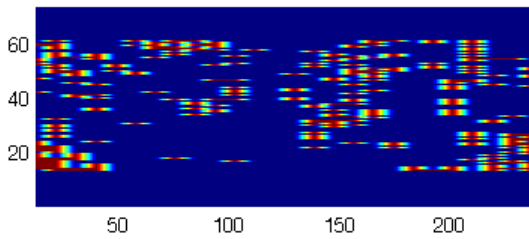


Length of core (mm)

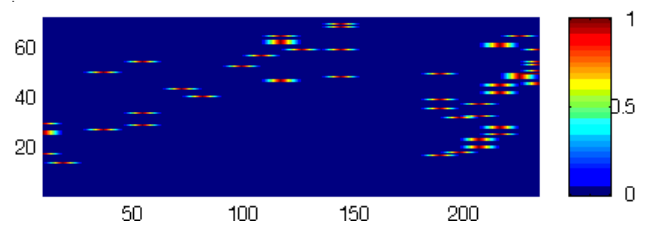


Length of core (mm)

AIR



Length of core (mm)



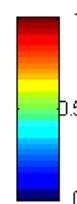
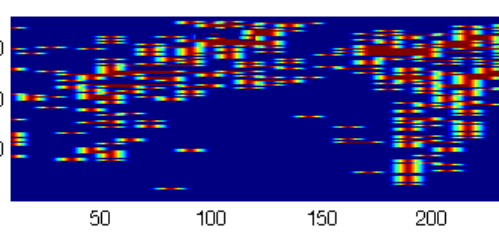
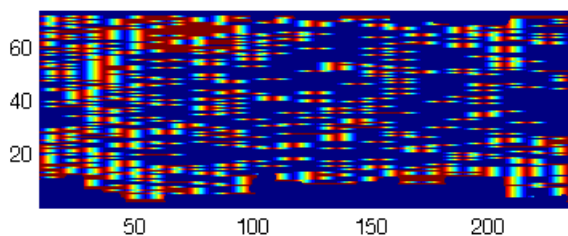
Length of core (mm)

Figure 6.10 Water displaces PCE that displaces Air/Water in Core D. The images on the left present the horizontal fracture plane from the top; the images on the right show a side view of the core and fracture planes.

TOP VIEW OF FRACTURE

SIDE VIEW OF FRACTURE

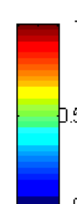
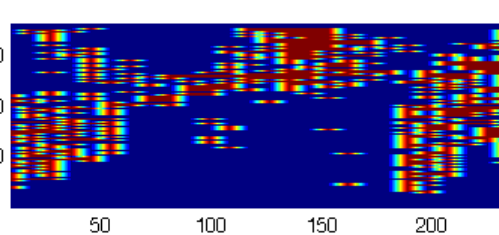
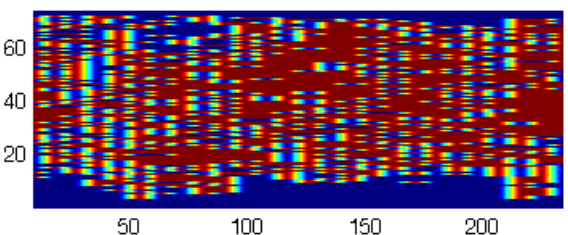
NAPL



Length of core (mm)

Length of core (mm)

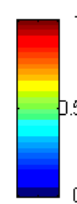
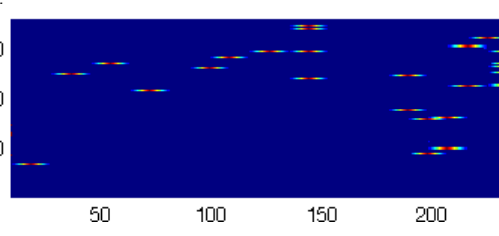
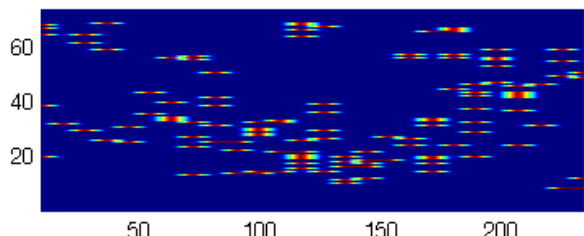
WATER



Length of core (mm)

Length of core (mm)

AIR



Length of core (mm)

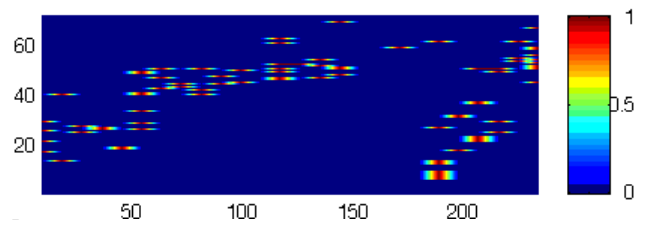
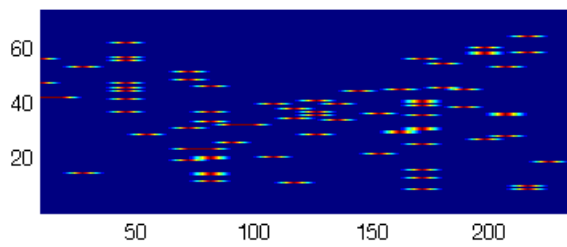
Length of core (mm)

Figure 6.11 Air displaces Water that displaces PCE/Air/Water in Core D. The images on the left present the horizontal fracture plane from the top; the images on the right show a side view of the core and fracture planes.

TOP VIEW OF FRACTURE

SIDE VIEW OF FRACTURE

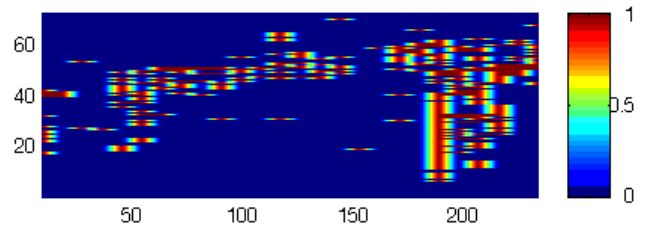
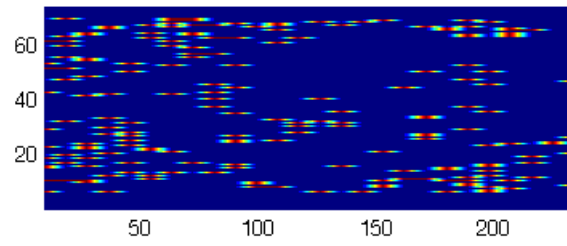
NAPL



Length of core (mm)

Length of core (mm)

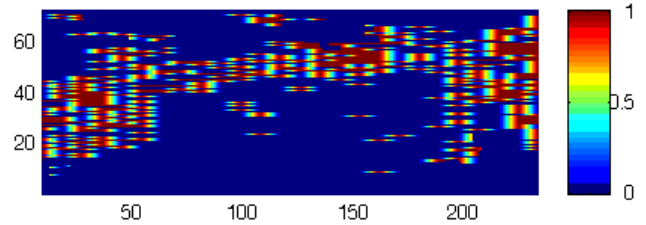
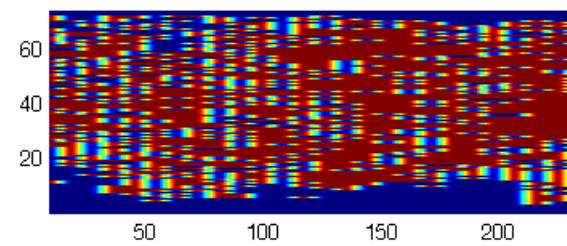
WATER



Length of core (mm)

Length of core (mm)

AIR



Length of core (mm)

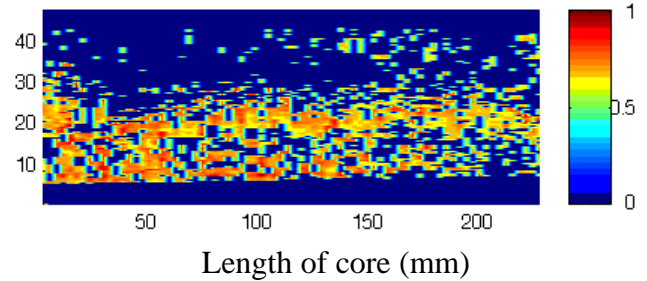
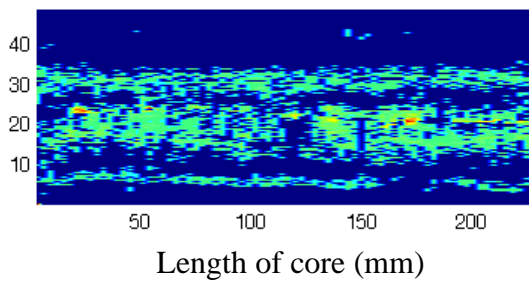
Length of core (mm)

Figure 6.12 PCE displaces Air that displaces Water in Core F. The images on the left present a horizontal “slice” through the middle of the core; the images on the right show a vertical “slice”. The bar at right represents saturation of the corresponding fluid, on a scale from 0 to 1.

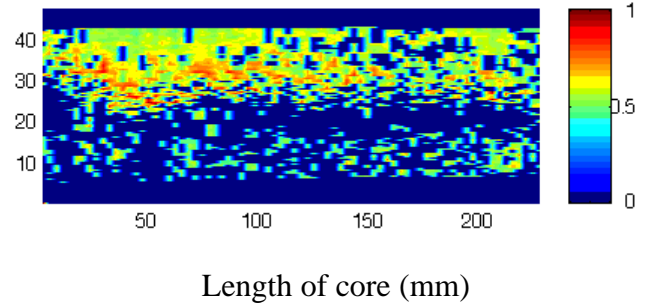
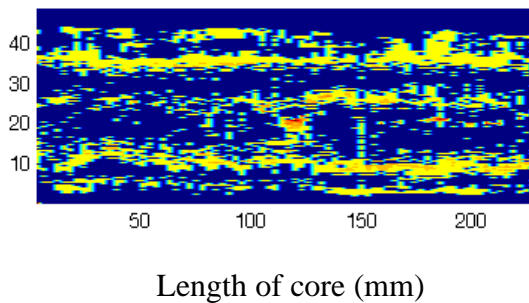
HORIZONTAL SLICE

VERTICAL SLICE

NAPL



WATER



AIR

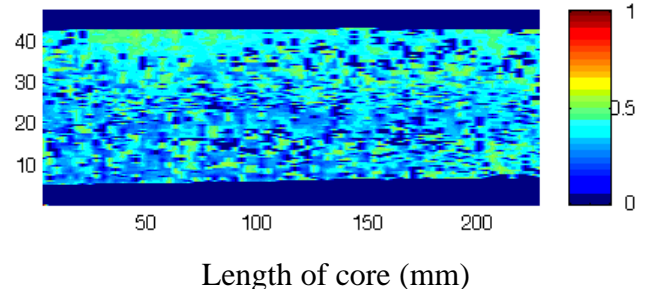
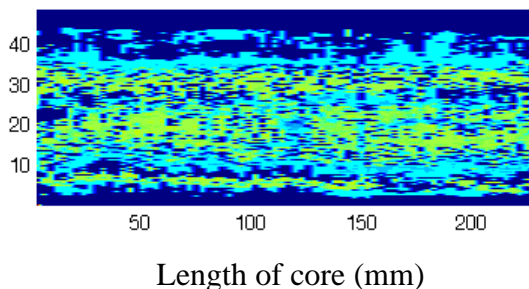
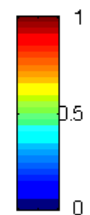
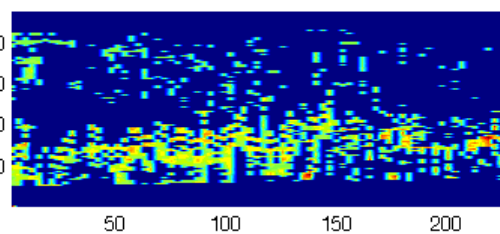
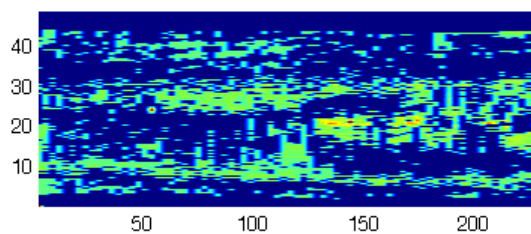


Figure 6.13 Water displaces PCE that displaces Air in Core F. The images on the left present a horizontal “slice” through the middle of the core; the images on the right show a vertical “slice”. The bar at right represents saturation of the corresponding fluid, on a scale from 0 to 1.

HORIZONTAL SLICE

VERTICAL SLICE

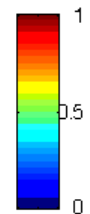
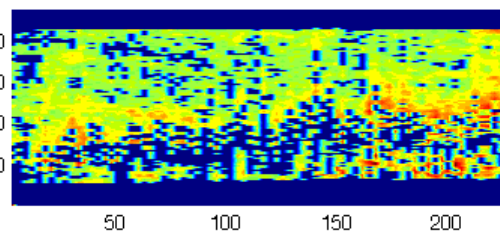
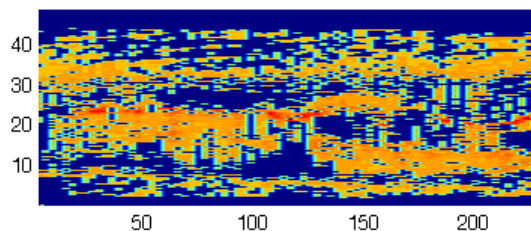
NAPL



Length of core (mm)

Length of core (mm)

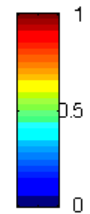
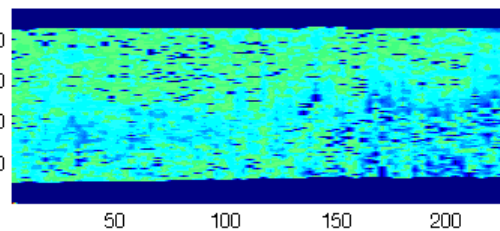
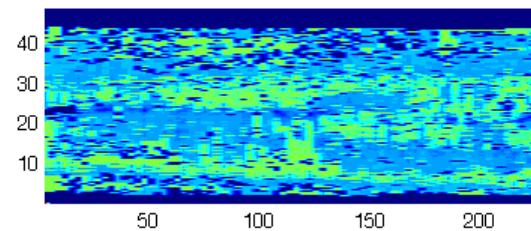
WATER



Length of core (mm)

Length of core (mm)

AIR



Length of core (mm)

Length of core (mm)

Figure 6.14 Steam Injection Setup

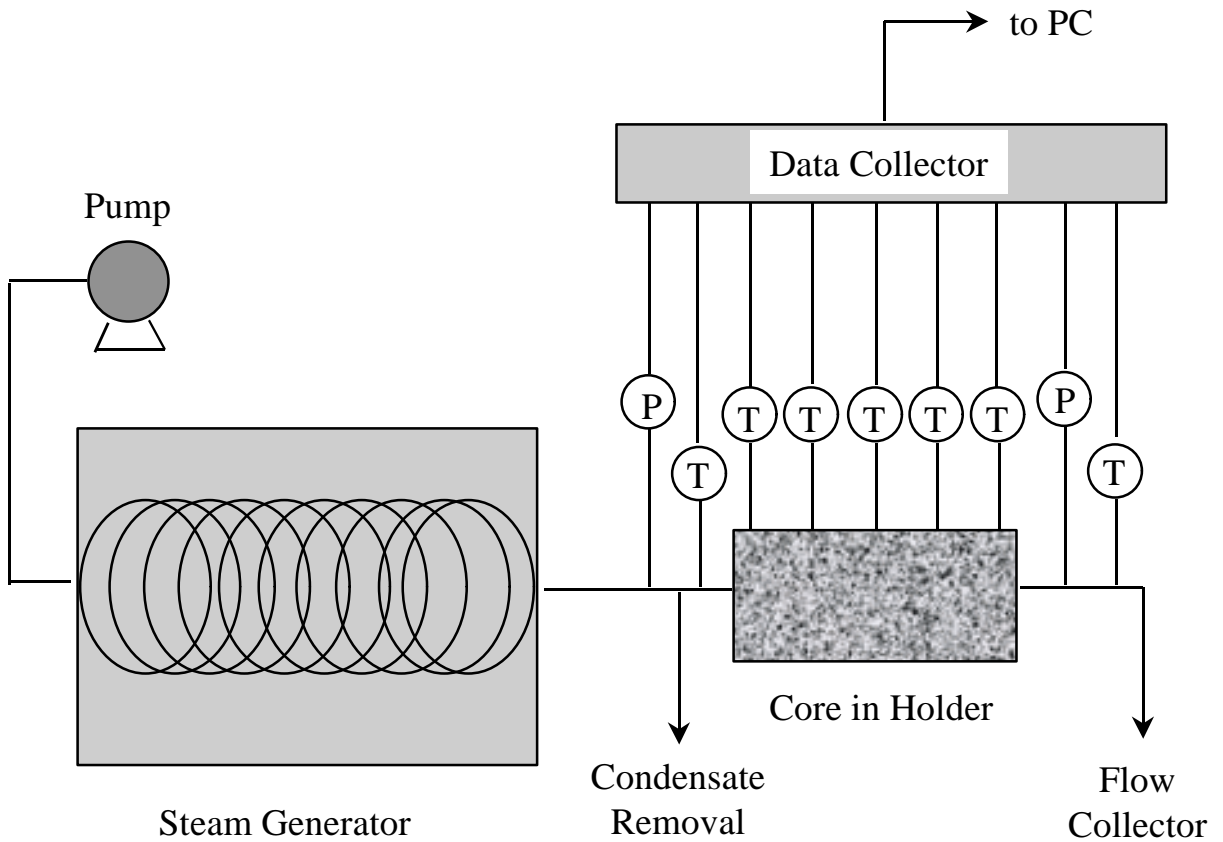


Figure 6.15 Temperature profile during steam injection of the sandstone Core F.

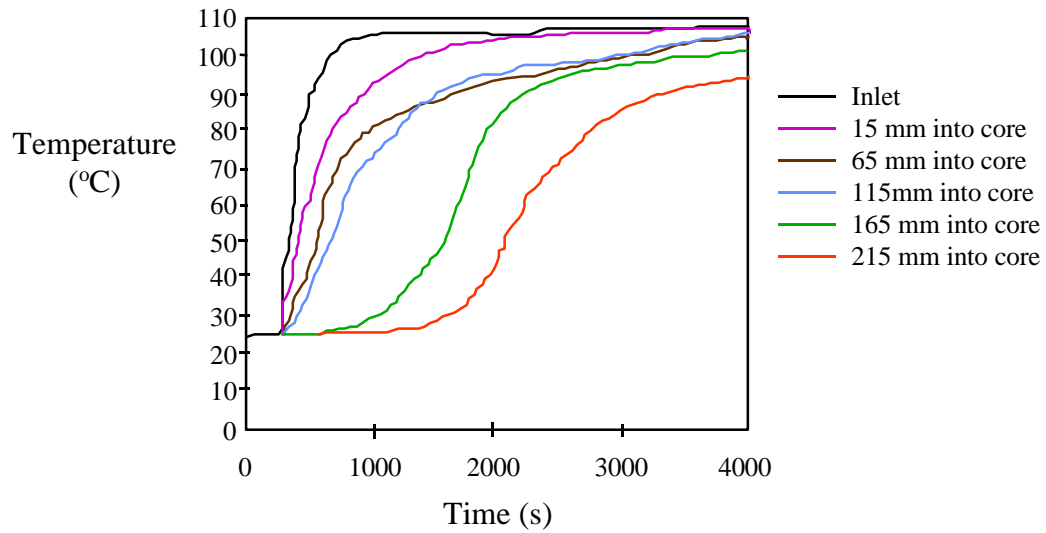


Figure 6.16 Reconstructed top view of the steam/water saturation in Core C after the temperature profile stabilizes. The bar at the right indicates water saturation, where 0 = steam and 1 = water

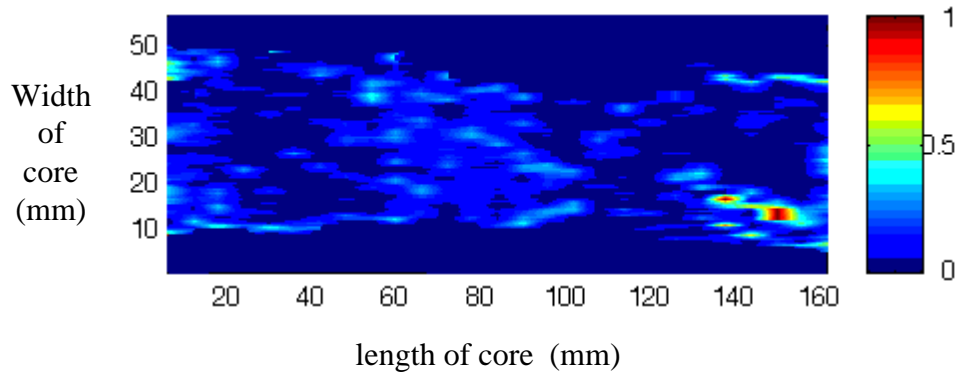


Figure 6.17 Numerical simulation of PCE injection into an unsaturated sandstone matrix with a fracture along the length of the core. The bar at right represents saturation of the corresponding fluid.

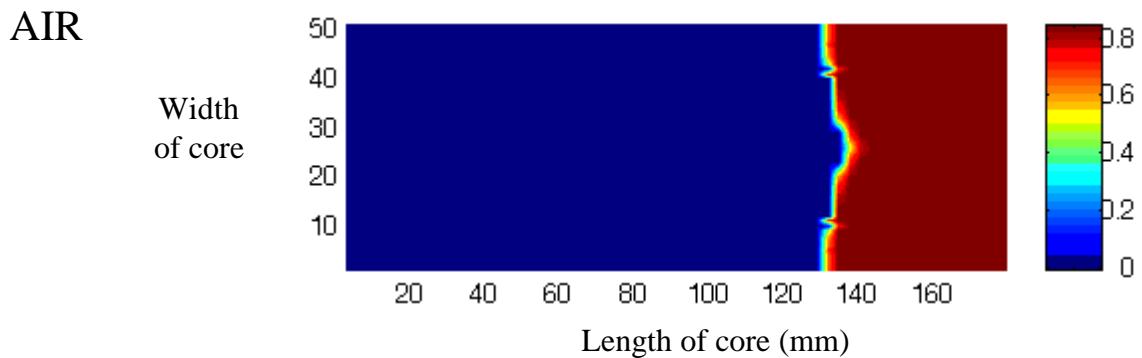
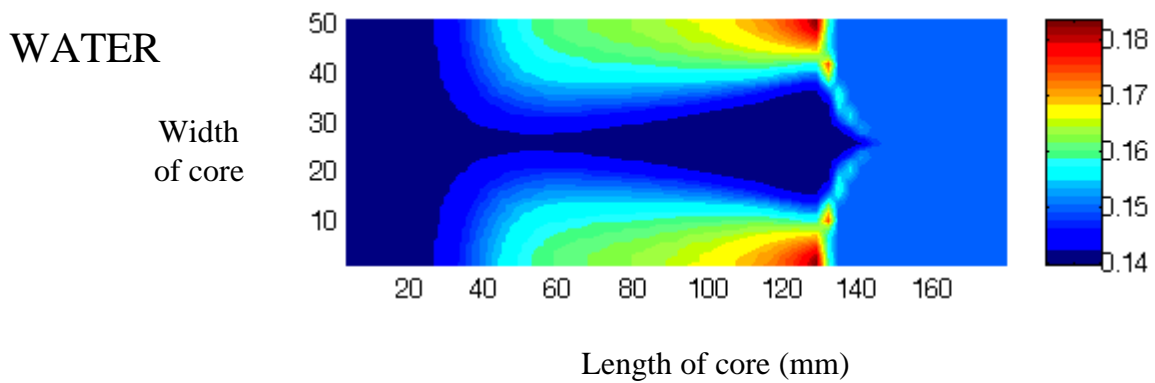
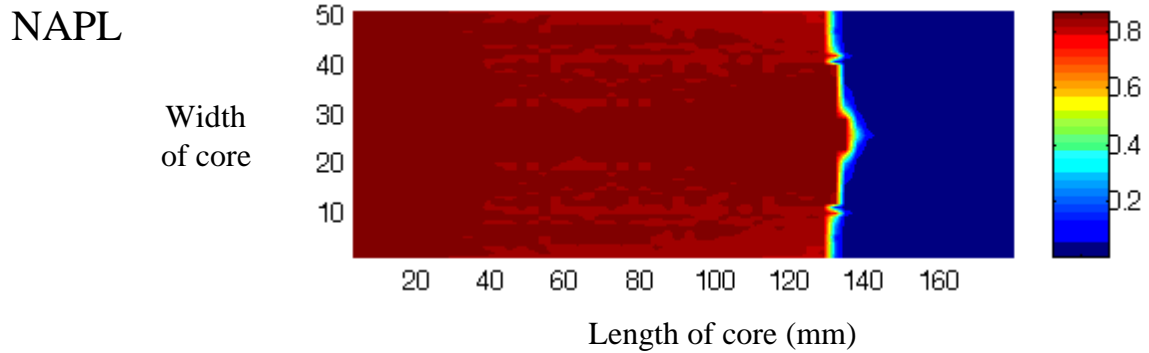


Figure 6.18 Numerical simulation of PCE injection into an unsaturated sandstone matrix with no fracture. The bar at right represents saturation of the corresponding fluid.

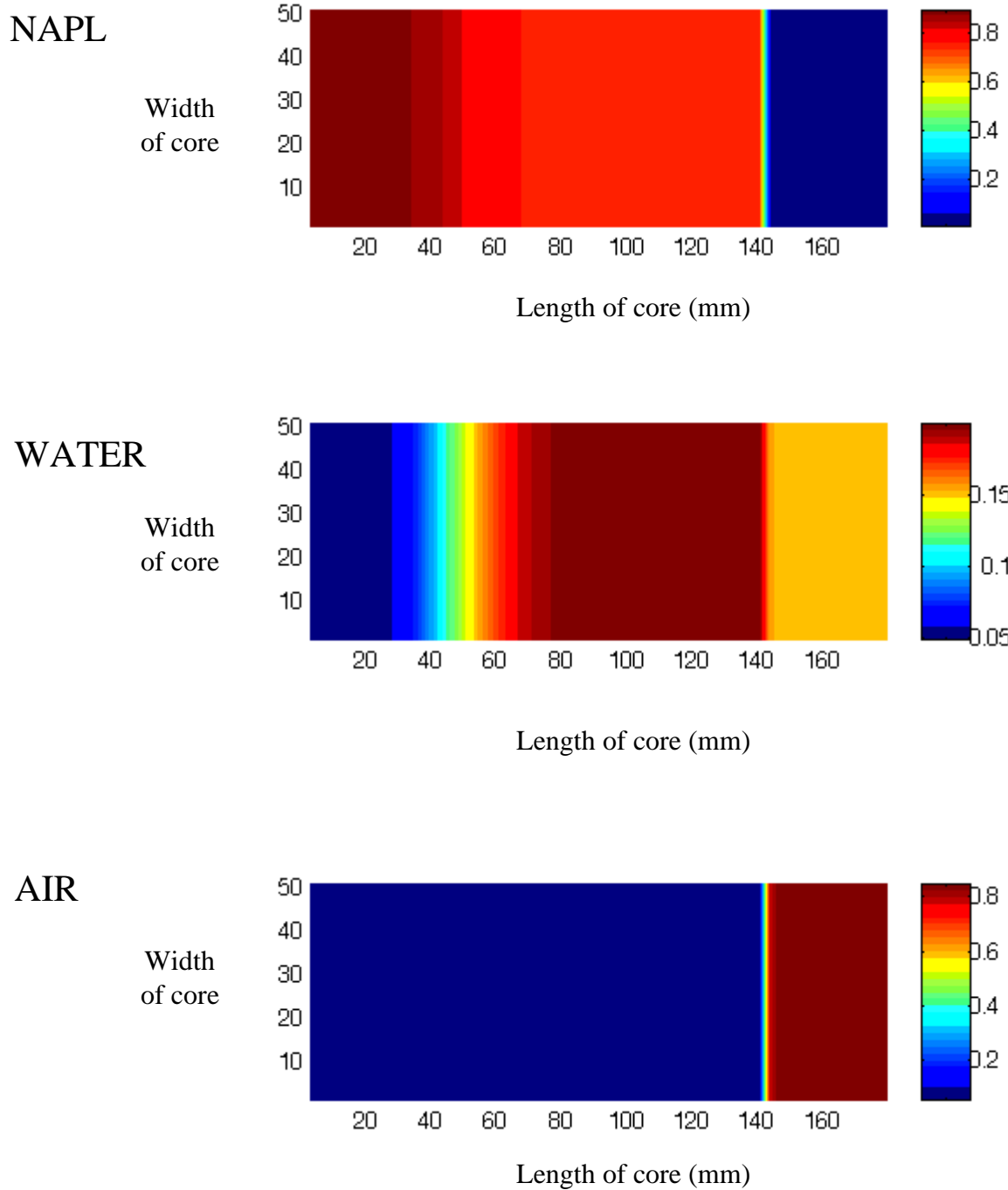


Figure 6.19 Numerical simulation of water injection into a fractured sandstone matrix with a high initial saturation of PCE, and water and gas near residual saturations. The bar at right represents saturation of the corresponding fluid.

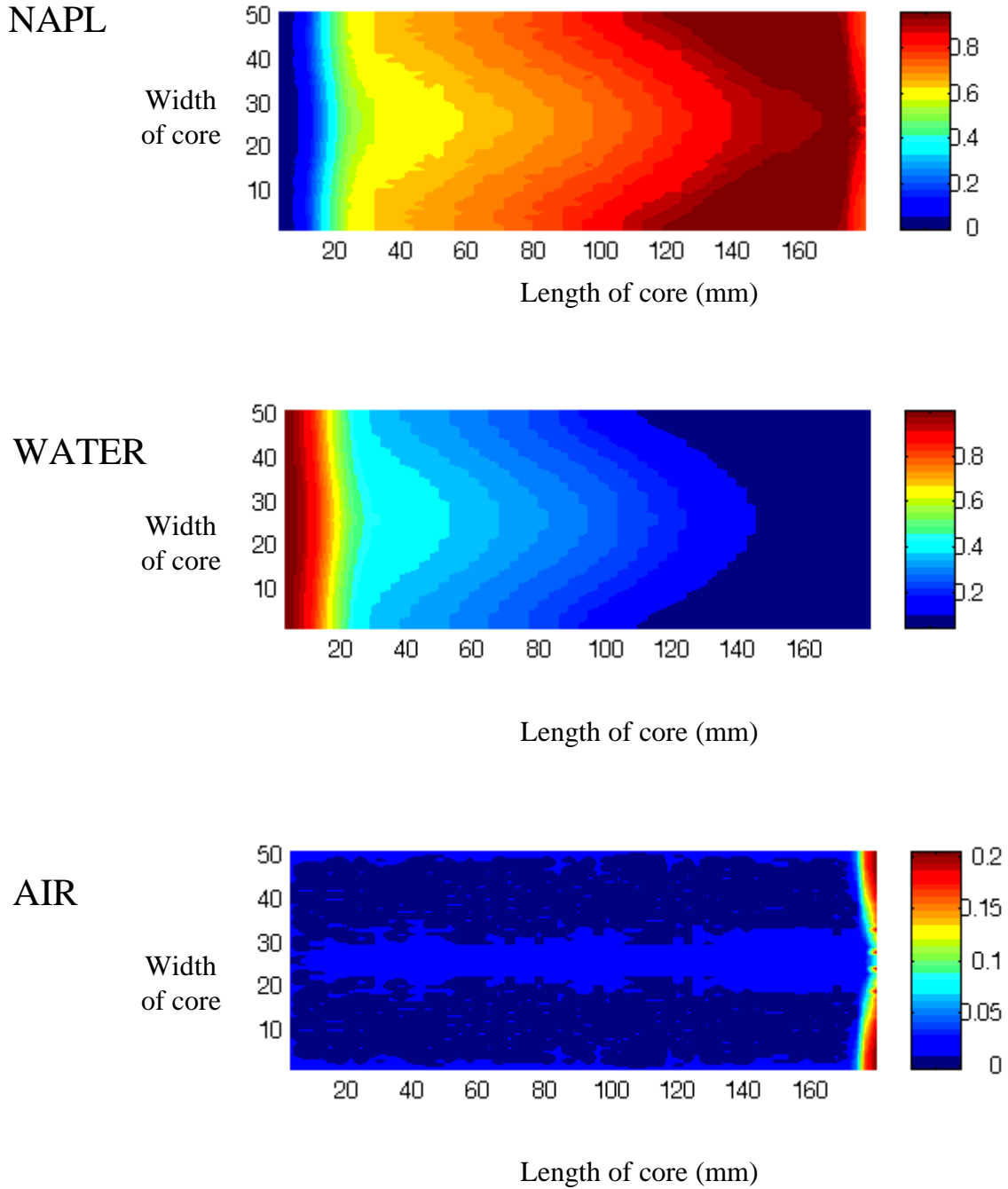


Figure 6.20 Numerical simulation of water injection into an unfractured sandstone matrix with a high initial saturation of PCE, and water and gas near residual saturations. The bar at right represents saturation of the corresponding fluid.

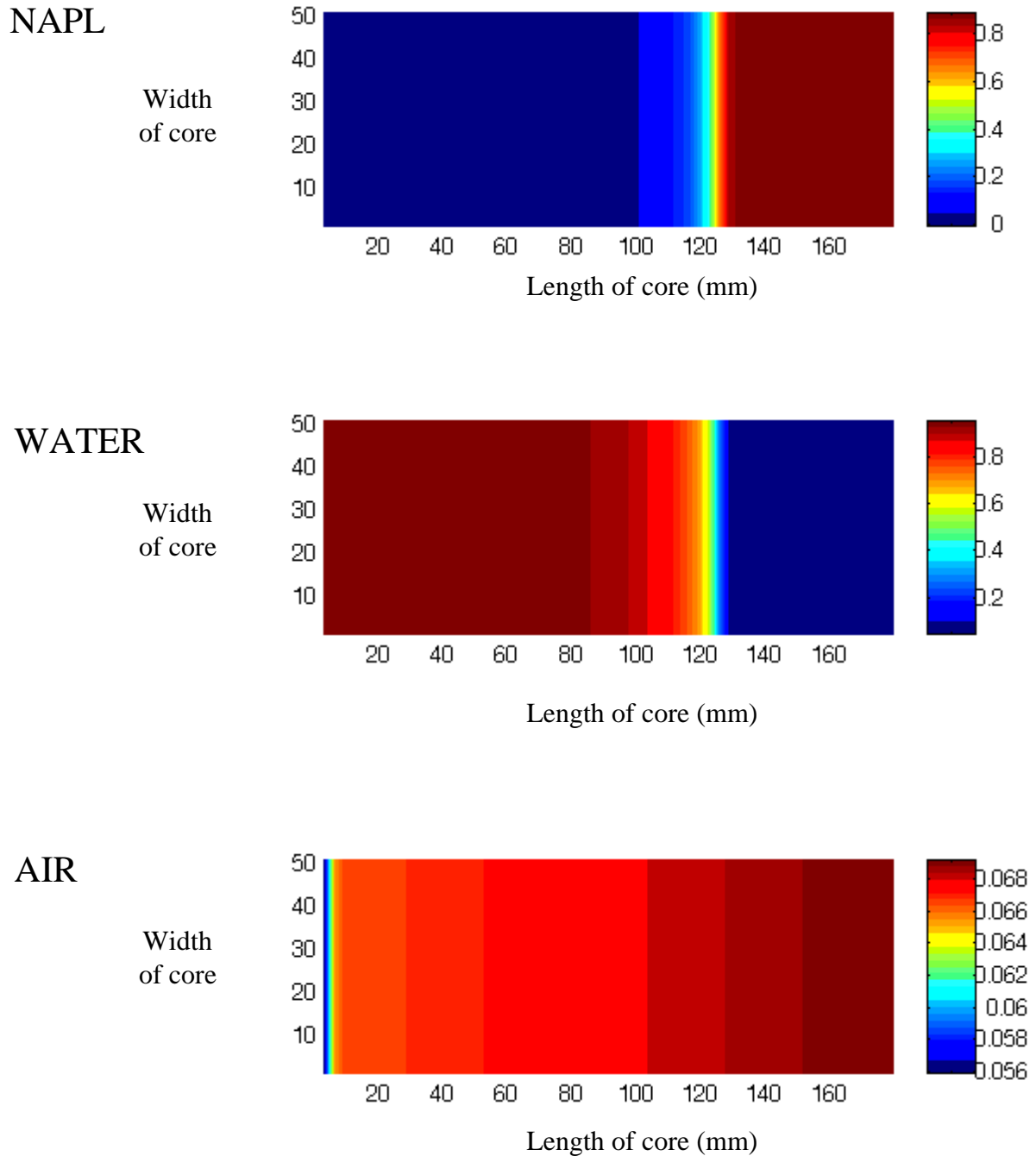


Figure 6.21 Numerical simulation of gas injection into a fractured sandstone matrix with a high initial saturation of water, and PCE and gas near residual saturations. The bar at right represents saturation of the corresponding fluid.

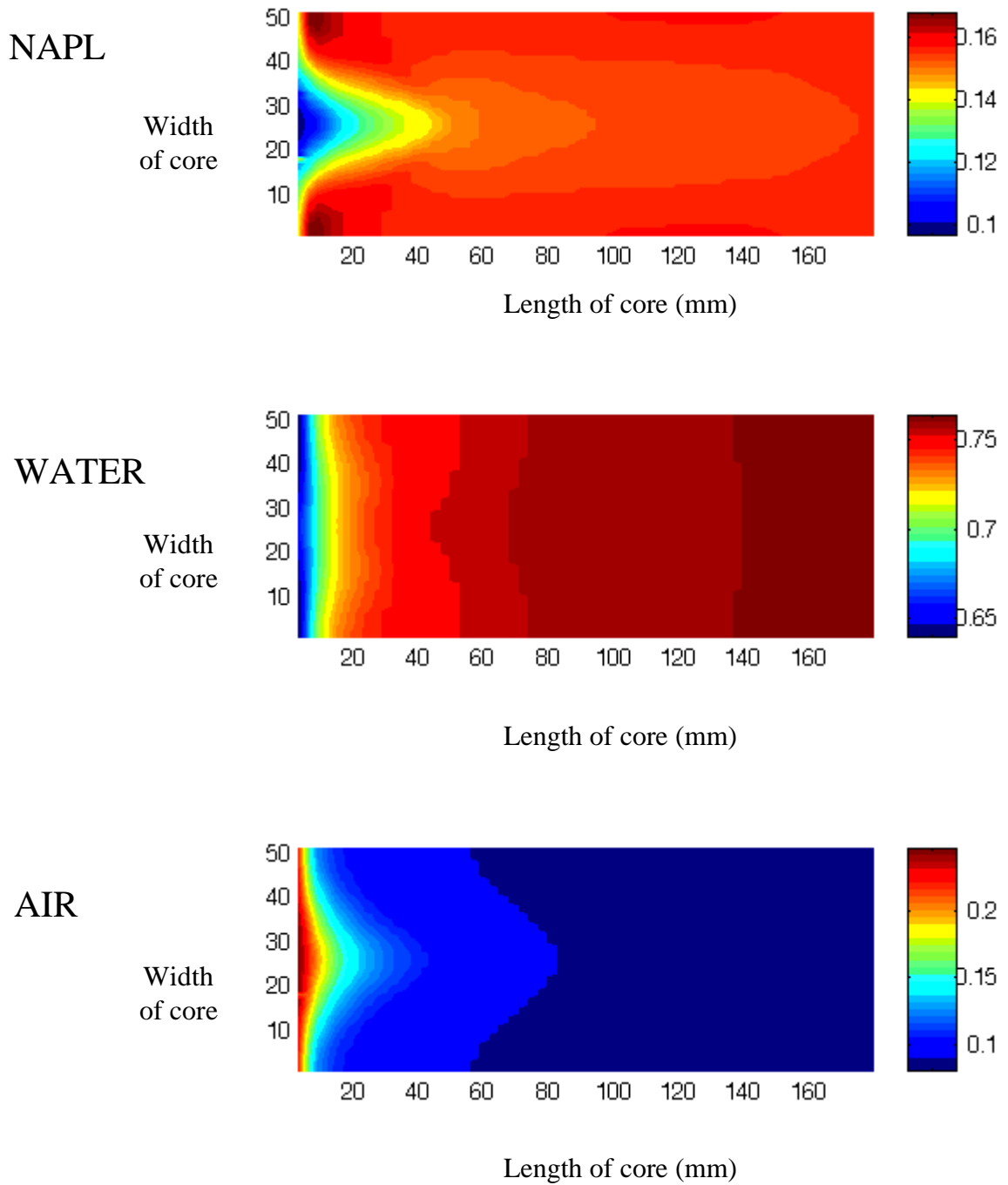
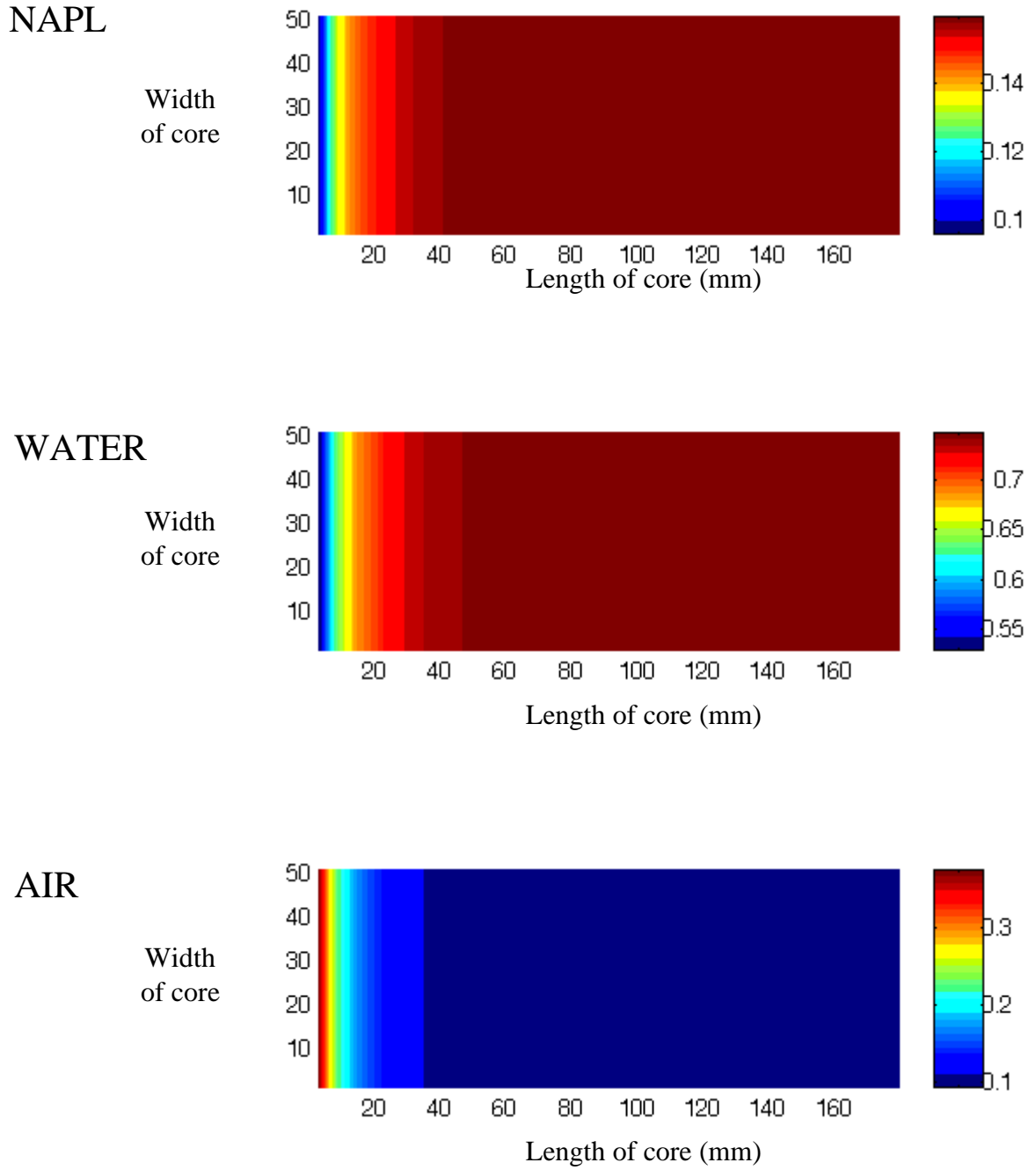


Figure 6.22 Numerical simulation of gas injection into an unfractured sandstone matrix with a high initial saturation of water, and PCE and gas near residual saturations. The bar at right represents saturation of the corresponding fluid.



Chapter 7

Engineering Significance

This investigation is centered on understanding the physical processes that govern flow at the pore and core scale for single and multi-phase flow. To be of significance in solving engineering problems, these results have to be scaled up to a level where they can be applied as predictive tools, in particular in a numerical modeling framework. I will first discuss the upscaling of the micromodel observations, followed by a discussion on the scaling up of the insights at the fractured core level.

7.1 Pore Scale Observations

We have observed the presence of water and NAPL layers under multiphase flow conditions at the pore scale, even for systems with a negative equilibrium spreading coefficient. Water and NAPL layers provide additional paths for the corresponding phases to flow under two- and three-phase conditions. In the case of two-phase flow, water layers allow by-passed water a drainage path, reducing the saturation of water to the point where capillary forces are too large for additional drainage (i.e. in the very small pore throats and crevices). Drainage through these water layers is slow, since the thickness of these layers is on the order of a micrometer, but significant enough in a time scale of weeks to months, over length scales of tens of centimeters to meters.

In three-phase flow conditions, both water and NAPL layers play a role in reducing the corresponding “residual” saturations. Water behaves under three-phase flow conditions in a manner similar to two-phase flow, draining out through wetting layers. The behavior of NAPL under three-phase flow conditions is drastically different than under two-phase flow conditions. In two-phase flow, NAPL (or the non-wetting phase) can

easily be trapped due to snap-off and by-passing. Once trapped, it is very difficult to mobilize the non-wetting phase, requiring very high viscous or gravity forces to overcome the capillary forces holding the discontinuous non-wetting phase in place. Under three-phase conditions, by-passed NAPL can flow out through NAPL layers in the crevices, at slow but measurable rates. Our findings are applicable to DNAPLs and LNAPLs, since the formation of layers depends only on the ratio of capillary forces and interfacial tensions, or the contact angle and the crevice angle; at the pore scale, gravity forces are small compared to capillary forces. The results obtained in a two-dimensional representation of the pore space are valid in the real three-dimensional porous structure, since one is likely to find crevices for layer flow in most porous media.

To scale up these results, relative permeabilities can be constructed to capture the role of layers in two- and three-phase flow, by allowing for layer flow in a network model. The resulting relative permeabilities indicate that even at very low saturation, layer flow results in a finite relative permeability, albeit with very low values, implying that layer flow is orders of magnitude slower than flow through the main pore cross-section. The significance in terms of designing an engineering solution to a three-phase problem is that when the contaminant has been trapped for a long time (weeks to months to years), additional flow can occur to reduce NAPL saturations to very low values. The same conclusions are valid for three-phase flow conditions in oil recovery, indicating the potential for producing additional oil by forcing a change from two- to three-phase conditions.

The shape of the relative permeability curve is probably quite a bit more complicated since it is likely to depend on several factors, for example the equilibrium spreading coefficient, the contact angles of the various phases (and thus wettability of the surface) and the history of the imbibition and/or drainage processes. Under two-phase flow conditions, we observe the entrapment of non-wetting phase due to snap-off and by-passing during imbibition. Subsequent drainage will follow a different path through the

pore channels, resulting in hysteretic behavior. Hysteresis also occurs for primary drainage followed by imbibition.

Under three-phase flow conditions, the possibility of hysteresis (i.e. path dependence of the relative permeabilities) is even higher, given the larger number of possible combinations of phase displacement, i.e. double drainage, double imbibition or the other drainage-imbibition combinations observed at the pore scale in this study. The relative permeability functions may represent a surface rather than a single curve. This has significant implications for trying to determine a “simple” functional relationship between relative permeability and saturation, such as those presented in Chapters 5 and 6.

7.2 Fracture Aperture

Throughout this dissertation I have pointed out the circumstances that lead to single, two- and three-phase flow in fractures, and have stressed the importance of fractures due to their prevalence in natural and man-made materials. To understand flow in fractures, we have to know about the location and spatial variability of fractures, the nature of the material (i.e. its properties), its geologic history, and the possible range of fracture apertures, fracture spacing and fracture density. Characterizing the subsurface will continue to be a very active area of research for geophysical scientists in the future, and a concern to environmental and petroleum engineers.

In these studies I focused on a smaller scale, to gain insights about the range of fracture aperture variability in a few fracture planes and their junctures, using a high resolution CT-scanner, since it is not feasible to sample aperture variability at high resolution in the field. I found that the aperture variability was significant even for small cores, and that it is due to this variability that flow and transport in fractures is considerably less predictable than in unfractured porous media. Modeling flow in the

fractures as if they were parallel plates with constant spacing (aperture) will clearly result in erroneous results. Throughout these studies, aperture variability was the dominant factor in determining the flow behavior, whether it was the formation of fast streamlines or channels through the fracture, or the paths followed by the wetting and non-wetting phases during two- and three-phase displacements.

In terms of characterizing the fracture aperture distribution, I found in this study that the distribution appears lognormal, corroborating previous studies. In addition, I found that the correlation length is small, on the order of millimeters, relative to the scale of the cores sampled, indicating only short range structure in the variability. With this knowledge, and a determination of the mechanical and hydraulic aperture from field scale pumping and tracer tests, we may obtain a measure of the variance for a large scale fracture plane. This information may be used to roughly (within an order of magnitude) estimate the dispersivity of the fracture or to construct capillary pressure curves for the fracture plane. These scaled-up functions can then be used in a numerical modeling framework. Larger scale studies corroborating these results are needed before we can determine the validity of these methods.

7.3 Single Phase Flow in Fractures

These studies indicate that channeling dominates the transport of a dissolved contaminant in a fracture, even at the small core scale, due to the high variability in fracture aperture within the fracture plane. This results in very early breakthrough, compared to an equivalent parallel plate analog. Channeling also has implications for dissolved contaminant removal even in impermeable matrices (e.g. granite or other crystalline rocks), since the movement of dissolved contaminants through the slower streamlines will represent a continuous “source” of contamination for a longer time than would be the case in the parallel plate analog.

Scaling up these results is in principle straightforward, since channeling has been observed in field scale studies. However, characterizing the subsurface environment is still the main challenge in terms of designing engineering solutions to contaminant transport problems. The high resolution information obtained in this study is unlikely to exist for any field scale study. Moreover, my comparison of experimental tracer breakthrough to the predictions of stochastic theory indicates that the theory is valid only as an order of magnitude estimator of dispersivity, even with knowledge of the fracture aperture distribution at high resolution. Another complication in field scale modeling is the additional mixing that may occur at fracture intersections, which I have not studied here. However, from an analysis of the fracture aperture in the complicated fracture network of Core D, one can see that the larger apertures at fracture intersections are bound to create zones where mixing may occur, increasing the dispersion of the contaminant.

7.4 Multiphase Flow in Fractures

Although capillary forces within a fracture are much smaller than capillary forces in the matrix (given the relative magnitude of pore sizes), they still play a significant role in determining the pathways that the wetting and non-wetting phases follow during imbibition and drainage. For fracture flow which is capillary-dominated (compared to viscous and gravity forces), a significant amount of non-wetting phase (either NAPL or gas) can be trapped during water imbibition, leaving behind a large “residual” saturation. In most cases, flow through the fracture will actually be in a regime where viscous or gravity forces are larger than the capillary forces, resulting in removal of the trapped non-wetting phase. This underscores the need to engineer a sufficiently large pumping rate to dislodge NAPL from the fracture, overcoming the capillary pressure, which may or may not be feasible, depending on the size of the pumping domain and the transmissivity of both the fractures and the matrix.

Under most circumstances where DNAPL displaces water out of a water-saturated fractured porous media, DNAPL will travel mostly through the fracture, since it is unlikely that it would have enough entry pressure to dislodge water from the matrix. This has the advantage that DNAPL is for the most part localized within the fracture network, but on the other hand, it means that for a spill of a given volume, DNAPL will travel much farther through the fracture network than if we were dealing with a spill in an equivalent unfractured porous media.

If the porous matrix is unsaturated before NAPL contamination, then three-phase flow conditions occur. In this case, NAPL can readily move into the matrix and displace the air, as well as water which is not in the smallest pores. The fracture plays a minor role in this situation, since the NAPL front moves almost uniformly through the media; this may be the result of conducting the experiments in relatively homogeneous sandstone. Although not the subject of my experimental investigation, low permeability barriers (such as tighter sands, clay lenses or unfractured consolidated materials) will have a significant role in redirecting the NAPL front, horizontally and vertically, and fractures may play a larger role in providing a preferential flow path.

Water flooding to dislodge NAPL from the matrix and fracture will only be partially successful under two-phase conditions. Large volumes of water (several pore volumes) will be required to reduce NAPL saturation, thus creating a huge above-ground treatment problem. Under three-phase flow conditions, NAPL is expected to flow through layers to very low saturations, which implies that either soil venting (in the unsaturated zone) or water flooding (in the saturated zone) will be more successful in removing the contaminant, since there is a larger interfacial area for volatilization or dissolution. However, some contaminants may have very low vapor pressure and/or solubility, such that only thermal methods (e.g. steam injection) may succeed in removing them from both the fracture and the matrix. My experimental observation of PCE removal from both the fracture and the matrix using steam injection indicates that this may be a plausible alternative. The fractures in the matrix actually help to provide additional surface area for

heat transfer, as well as a means of displacing the hot water front ahead of the steam front, such that it is easier to heat a fractured core than an unfractured core. Scaling up these results requires additional experimentation at the core and field scale, before it can be demonstrated that steam injection into fractured media is a valid alternative. If it is proven effective, then we can engineer hydro- or pneumatic-fracturing of the contaminated zone prior to steam injection, to improve heat transfer.

7.5 Conclusions

Fractures play a significant role in transporting contaminants through the subsurface, whether as dissolved species in the aqueous phase or in their own phase, by providing a preferential pathway. Neglecting the presence of fractures is likely to result in underestimation of the travel time of the contaminant to a location at risk (e.g. a producing well or a water-supply aquifer). Considering the medium as an “equivalent” porous media with increased permeability due to the fractures is at best a crude representation of the role of fractures. However, attempting to model all the fractures present in a field scale situation is practically impossible. Perhaps our best strategy is to detect the major fracture planes via pumping and tracer tests (in the unsaturated and saturated zone), and then apply our understanding of flow in fractures from these and similar laboratory experiments.

7.6 Future Work

I have pointed out above some necessary extensions of this work to prove the reliability of these methods. In particular, I feel that research should be directed to:

- Studying the formation of NAPL layers for other systems under three-phase flow conditions, in particular chlorinated solvents, as well as under various wetting regimes.
- Evaluating at larger scales and in heterogeneous systems the effect that layer flow (in three-phase conditions) has on residual saturations, in particular for the longer time frames, since this has significant implications for environmental and petroleum applications.
- High resolution characterization of many more fractures in various materials, which have been fractured in different stress modes, to be able to generalize the results about the fracture aperture distributions.
- Tracer experiments within a fracture network, to study mixing at the intersections, as well as the transport of tracer into a porous matrix. This may eventually require much larger scale “cores” or even a well characterized field site.
- Multiphase flow experiments under conditions that permit an instantaneous “snapshot” of the various saturations, to compare against the network and numerical models.
- Construction of a fracture network model that incorporates flow of “bubbles” under two- and three-phase flow conditions, since this regime is likely to exist in fractures due to the higher capillary numbers that can be obtained. The model can then be used to determine relative permeabilities for the fracture, and can be compared to experimental observations. For three-phase flow, the model also has to include flow through NAPL layers.
- Incorporating the variable fracture aperture (and its effect both on permeability and “pore volume”) in a continuum simulator, to evaluate the effect of fracture and matrix interactions due to the balance of capillary, viscous and gravity forces.